Development of Novel Low Activation Refractory High Entropy Alloys for Nuclear Fusion Applications

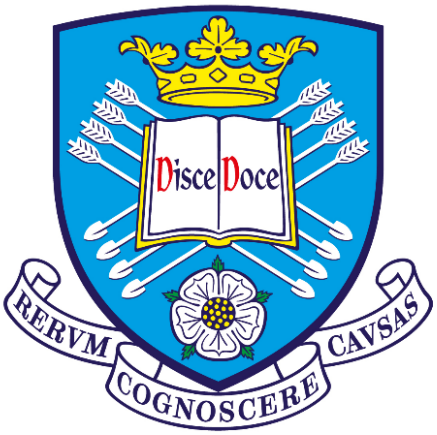

The University Of Sheffield.

Dhinisa Patel

Department of Materials Science and Engineering

University of Sheffield

This thesis is submitted as a requirement for the degree of

Doctor of Philosophy

Submitted September 2021

Abstract

Nuclear fusion power has the potential to meet the growing global energy demand. However, for commercial fusion energy to be realised, serious reactor design concerns need to be addressed. Suitable materials for the first wall of the reactor need to be able to withstand harsh conditions including: extreme heat loads (0.25-0.5 MWm^{-2}), significant transient heat fluxes between 10-20 MWm^{-2}, and high energy neutron bombardments (14 MeV). A novel class of materials, high entropy alloys, have recently been identified to have interesting properties including high temperature capabilities and the self-healing effect upon irradiation.

Preliminary findings, reported in this thesis, demonstrated the excellent radiation damage resistance of the refractory high entropy alloy $V_{2.5}Cr_{1.2}MoWCo_{0.04}$ in the as-cast condition. This metastable BCC phase showed no microstructural difference upon 5 MeV Au^{2+} ion implantation at room temperature. Despite this, after a prolonged heat treatment at intermediate temperatures the phase transformation to a mixture of phases including a BCC, tetragonal, and an orthorhombic phase was observed.

Computational alloy design tools were implemented for the development of novel low activation refractory high entropy alloys for consideration as plasma-facing materials. High entropy alloy empirical parameters for the prediction of a BCC solid solution, and Thermo-Calc simulations for the reduction of intermetallic phases were used for the design of five novel refractory low activation high entropy alloys: $V_{35}Cr_{33}Mn_2Fe_{12}W_{18}$, $V_{46}Cr_3Mn_1Ta_{10}W_{40}$, $V_{21}Cr_{18}Mn_9Fe_{17}Ta_{20}W_{15}$, $V_{36}Cr_{18}Fe_8Ta_{17}W_{21}$, and $V_{26}Cr_{17}Fe_{32}Ta_{25}$. The thermal stability of these alloys was assessed, and the elemental segregation of the alloys could not be reduced due to insufficient homogenisation time. Additionally, only VCrMnTaW and VCrMnFeW displayed BCC phases which were retained upon thermal treatment. From these results, the deficiencies of the design tools were highlighted. Vickers microhardness studies also showed a strong correlation between atomic size difference and as-cast hardness values.

The most promising alloy, $V_{35}Cr_{33}Mn_2Fe_{12}W_{18}$ displayed strong microstructural similarities to $V_{2.5}Cr_{1.2}MoWCo_{0.04}$, so potential for radiation resistance in the as-cast condition may result. Further high temperature X-ray diffraction experiments on $V_{35}Cr_{33}Mn_2Fe_{12}W_{18}$ showed the formation of a σ phase at 750 °C which was irreversible upon cooling to room temperature.

In this work, the investigation of novel low activation refractory alloys and their potential as plasma-facing materials is assessed and insight is given into the design process of high entropy alloy systems with BCC solid solutions.

Acknowledgements

First and foremost, I would like to express my sincerest gratitude to my supervisor Dr Amy Gandy, for her unwavering support, advice, and encouragement throughout the course of my Ph.D. I am incredibly fortunate to have you as my supervisor, without your direction and invaluable wisdom this research and thesis could not have happened. I would also like to thank my secondary supervisor Dr Russell Goodall for all his help, guidance, and expertise. Many thanks go to my industrial supervisor Mark Richardson and my sponsor Culham Centre for Fusion Energy for their support and for funding this project.

I would like to pass on my sincerest thanks to the many technicians and members of staff who helped me in all my work, in particular Lisa Hollands and Neil Hind in the foundry for their constant support and technical expertise. Special thanks go to Claire Utton for her help and assistance with Thermo-Calc, and to Rob Snell for his guidance on the design process for high entropy alloys. I would also like to express sincere gratitude to Stavrina for all her help navigating the python script and to Zhao for his expertise and assistance with vacuum arc melting. From the XRD SRF, I would like to thank Nik Reeves McLaren for his important guidance and assistance with conducting the various XRD experiments and for all his help with the subsequent analysis.

To the Centre of Doctoral Training - I am grateful for the staff and the academic members for this incredible opportunity and to my fellow cohort members who made this journey thoroughly enjoyable.

I would like to personally acknowledge the support of my parents and my sister, who always pushed me in everything I have pursued. Thank you for your never-ending support and love and especially for taking care of me over lockdown. Lastly, and most importantly - I am extremely grateful for Liam. Thank you for being on this journey with me, I couldn't have done it without you.

This work has been carried out within the framework of the EUROfusion Consortium and has received funding from the Euratom research and training programme 2014-2018 and 2019-2020 under grant agreement No 633053 and from the RCUK [grant number EP/T012250/1]. The views and opinions expressed herein do not necessarily reflect those of the European Commission.

Publications

Patel, D., Richardson, M.D., Jim, B., Akhmadaliev, S., Goodall, R. and Gandy, A.S., 2020. Radiation damage tolerance of a novel metastable refractory high entropy alloy V2. 5Cr1. 2WMoCo0. 04. Journal of Nuclear Materials, p.152005.

Gandy, A.S., Jim, B., Coe, G., Patel, D., Hardwick, L., Akhmadaliev, S., Reeves-McLaren, N. and Goodall, R., 2019. High temperature and ion implantation-induced phase transformations in novel reduced activation Si-Fe-V-Cr (-Mo) high entropy alloys. Frontiers in Materials, 6.

Conference Attendance

2021

PhD Showcase Culham Centre for Fusion Energy – Online Presentation

2019

National Student Conference Advanced Metallic Systems (Chair)
Eccomas Young Investigators Conference (Krakow, Poland) – Presentation
Universities' Nuclear Technology Forum (Surrey) - Presentation

2018

National Student Conference Advanced Metallic Systems – Presentation
EuroMat (Budapest, Hungary) – Poster
International Conference on High Entropy Materials (Jeju Island, South Korea) - Presentation

2017

National Student Conference Advanced Metallic Systems - Poster
Energy 2050 Symposium - Poster

Prizes

National Student Conference Advanced Metallic Systems 2018 - Best Oral Presentation

Energy 2050 Symposium 2017 - Best Poster Presentation

Table of Contents

Chapter 1: Introduction

1.1. Introduction to Fusion Energy

The global demand for energy is projected to more than double by 2050, to an anticipated 25-60 TW, and is set to triple by the end of the century. The requirement for greater energy consumption is due in part to the increase in the world's population [1]. Our reliance on fossil fuels raises serious environmental concerns; the burning of fossil fuels releases around 21.3 billion tonnes of CO_2 per year contributing to global warming and ocean acidification. As such, a global effort is underway to generate low carbon renewable energy in hopes of reducing greenhouse gas emissions. Figure 1.1 shows an estimation of electricity generation capacity reflecting the projected increase in reliance on nuclear energy and offshore wind energy.

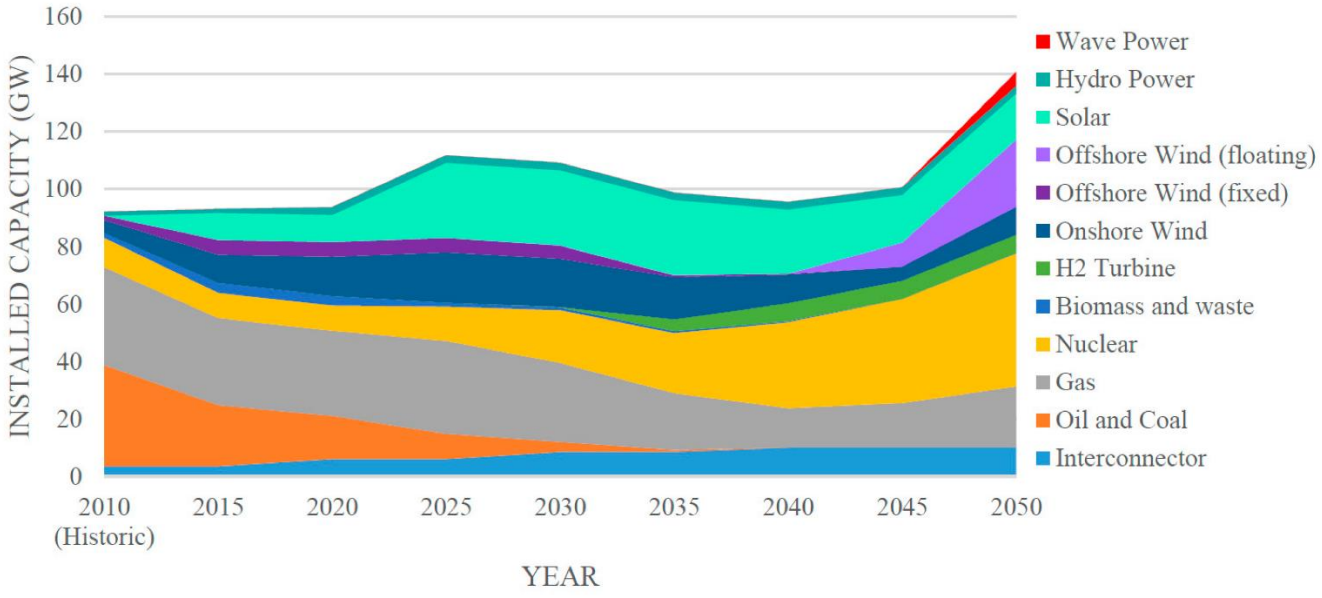

Figure 1.1: Projected global energy production of different technologies showing an increased capacity from nuclear energy and other renewable sources, with less reliance on oil and coal in 2050 [2].

Nuclear power is currently the second-largest source of low-carbon electricity, equating to 10% of global electricity generation, and remains the focus of worldwide research towards greater efficiency and safety. Nuclear fission is the process currently utilised in nuclear power plants and there are approximately 450 nuclear fission reactors in operation in 30 countries

around the world [3]. Future advanced reactor concepts focus on the implementation of improved safety, improved fuel efficiency, and cost-effective simpler designs [4].

Whilst fission energy is already an established means of producing electricity, nuclear fusion research is still in the developmental stage. The foundation of nuclear fission is the bombardment of an unstable isotope by neutrons, causing the target nucleus to break into smaller isotopes. This also releases a large amount of energy which is harnessed as electricity. Fusion reactions, on the other hand, occur via fusing isotopes of hydrogen into helium; a process that powers the Sun.

Unlike fission power, fusion energy cannot produce any runaway nuclear chain reactions, nor does it produce large amounts of hazardous radioactive waste, therefore large-scale nuclear accidents are not possible. As well as providing a safe and economical alternative, fusion power is expected to yield a substantially greater energy per unit mass of fuel in comparison to any fuel-consuming energy source currently in use, with the capability of utilising one kilogram of fuel to produce the same amount of energy that would require 10 million kilograms of fossil fuels [5].

Currently, fission power is more attainable due to the extreme parameters required for fusion nuclei reactions to occur and the challenging environment of the reactor, including chemical compatibility, radiation, heat fluxes, and thermomechanical stresses [6]. This is explained in further detail in the plasma-facing components section (Chapter 2.1: Plasma-Facing Components).

A common theme for all solar, fission, and fusion energy technologies is the demand for greater materials research to improve capabilities and feasibility for reliable baseload power [6]. Alongside advances in plasma physics, there needs to be a development of advanced structural fusion materials able to withstand high neutron irradiation and heat fluxes for fusion to be a realistic candidate energy option for the near future.

1.2. Fusion Principles

1.2.1. Background

For decades, researchers have been trying to harness the energy that is released in the core of every star. The first fusion experiments were conducted during the 1930s, and since then, fusion research has made progress towards fusion becoming a viable source of energy generation. However, the goal of fusion power providing electrical energy for a competitive market still requires substantial advances in materials science and plasma physics.

Nuclear fusion is the reaction between two (or more) light atomic nuclei which are fused together generating one (or more) heavier atomic nuclei and subatomic particles (either neutrons or protons). The difference in mass between the reactants and products is released as kinetic energy of the reaction products in accordance with Einstein's equation:

$$\Delta E = \Delta m c^2 \qquad \textit{Equation 1.1}$$

Where ΔE is the change in energy, Δm is the total change in mass of the nucleons, and c is the velocity of light. A nucleus comprises positively changed protons and neutrons that have no charge. Protons and neutrons are collectively known as nucleons.

The graph shown in Figure 1.2 represents the binding energy per nucleon with respect to the mass number of the element. If you determined the mass of a nucleus and the combined mass of the individual nucleons comprising that nucleus, you would find a disparity between the two values, with the mass of the nucleus being less than the sum of the nucleons. This "mass defect" represents the energy that was released when the nucleus was formed, and therefore the energy that can be released when fusing together two light nuclei. From Figure 1.2 the fusion process will occur for products of nuclei that are lighter than iron-56 (the element with the highest binding energy). For all nuclei with an atomic number lower than iron-56, energy is released during fusion reactions and for heavier nuclei (with a mass number greater than 60) energy is released during fission reactions.

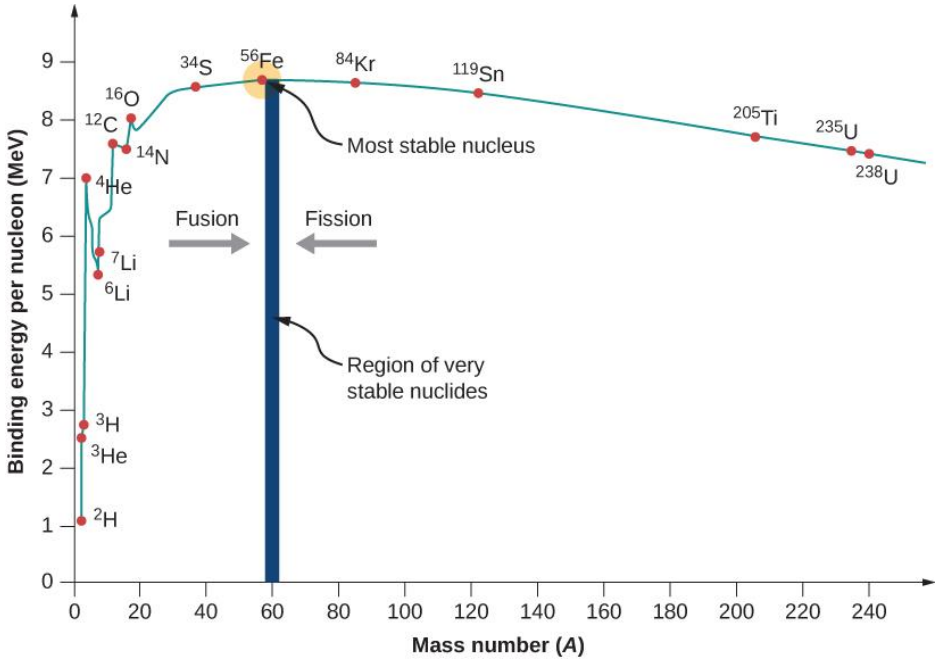

Figure 1.2: Binding energy per nucleon as a function of the element's mass number [7].

Extremely high temperatures, around 100 million K, are required for fusion reactions in order to overcome the Coulomb repulsion between the positively charged protons. There are several possible reactions that can occur between light atomic nuclei (with mass numbers below 60). In deciding which nuclei should be used as the fuel in a commercial nuclear fusion power plant, the reaction cross section of the reaction must be evaluated. The reaction cross section (σ) is a measure of the probability of a fusion reaction as a function of the kinetic energy (T) of the reactant nuclei. The reaction cross sections for three fusion reactions (D-T, D-D, and D-3He) are plotted in Figure 1.3 where the D + D reaction has two possible avenues with the denoted line representing an average of both processes.

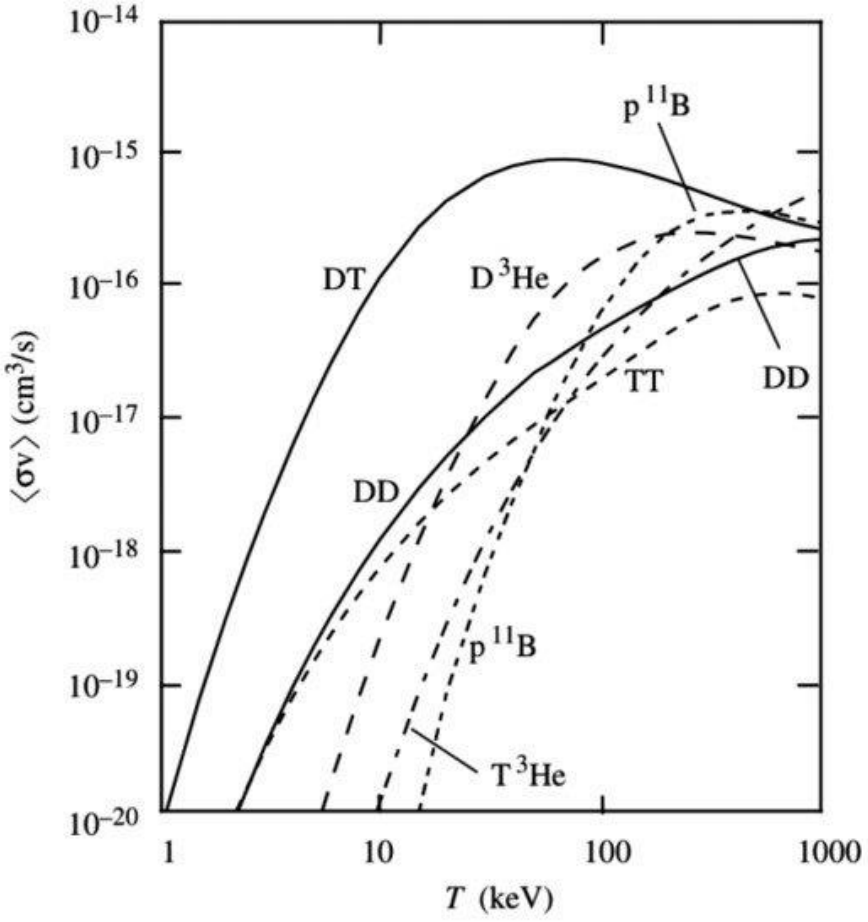

Figure 1.3: The reaction cross section of three candidate fusion reactions as a function of their kinetic energy [8].

1.2.2. Nuclear Reaction

The most attainable means of achieving sustainable fusion on Earth is best described by the D-T reaction – the nuclear reaction where deuterium and tritium ions (both isotopes of hydrogen) overcome electrostatic repulsion and fuse together. This has the fastest reaction rate and has the largest cross section which peaks at the lowest temperature compared to other reactants commonly considered for fusion energy (as shown in Figure 1.3). From this figure, temperatures more than 100 million K (ITER aims to operate at 150 million K) are required to allow the reactants to have enough kinetic energy to overcome the Coulomb barrier and fuse together. Upon this reaction the release of a neutron, a helium nucleus and 17.6 MeV of energy occur:

$$^{2}D + ^{3}T \rightarrow ^{4}He\ (3.5\ MeV) + ^{1}n\ (14.1\ MeV) \qquad \textit{Equation 1.2}$$

During this process, energy and momentum are conserved and so neutrons with an energy of 14.1 MeV are released and the resultant energy generated, in principle, could be utilised in heating water to rotate turbines for the generation of electricity.

Lawson's criterion quantifies the conditions for a nuclear fusion reactor to obtain a net yield energy from the fusion reaction and is usually defined in terms of ion density and confinement time. In 1957, J. D. Lawson determined that the product of ion density and confinement time determined the minimum conditions for productive fusion [9]. Commonly quoted figures for Lawson's criterion for the D-T reaction is $n\tau \geq 10^{14}$ s/cm^3 which is the product of n the plasma (electron) density, and τ is the energy confinement time required for the net energy output.

1.2.3. Fuels

The raw materials required for the fuel for fusion are in abundant supply: deuterium is available from seawater, and tritium, a rarer isotope, will be bred in the breeder blanket system behind the first wall of the reactor vessel from the reaction of neutrons with the common element lithium (Li), an alkali metal which can be extracted from the Earth's crust. The available lithium reserves could sustain fusion power plants for around 250-600 years with further potential to extract lithium from seawater which would render the fuel supply as potentially limitless. As seen in Equation 1, the waste product from this reaction is a helium nucleus (an alpha particle) which, on interaction with electrons, becomes an inert helium gas atom. There is an adequate global supply of deuterium and lithium resources to fulfil energy demands for millions of years [8].

The Li-containing blanket also serves to extract excess heat from the plasma by absorbing energy from colliding high-energy neutrons and charged particles. This kinetic energy is then transferred through a coolant into a working fluid and the resultant steam is then used to produce electricity using traditional turbines. Another proposed means of power production includes direct conversion which transfers the kinetic energy into voltage. The exact method of energy production from fusion is still under development and depends on the reactor design chosen.

1.3. Reactor Design

To reach the remarkably high temperatures (over 100 million degrees Kelvin) needed for the D-T nuclear reaction to occur, the fuels must be kept in an ionised gaseous state – where the ions of gas atoms have had some of their orbital electrons removed and co-exist with the free electrons is termed the plasma-state. A method of plasma confinement is needed to achieve the temperatures and pressures necessary for the fusion reaction to take place.

The hot plasma must be contained for sufficiently long enough to undergo the nuclear fusion reaction and designing a system with such requirements has proven to be a great challenge in the development of fusion power. Current approaches exploit the use of either magnetic confinement fusion (MCF) or inertial confinement fusion (ICF) to ensure that the plasma can be heated and held at a sufficient density to ensure particle collision.

Inertial confinement uses high intensity converging laser or ion beams to rapidly heat and compress the hydrogen plasma which is in the form of a deuterium/tritium fuel pellet. A weak laser beam is created, split, and sent to preamplifiers to increase the pulse energy before being passed back and forth through several power amplifiers before finally hitting the pellet which is placed in the centre of a vacuum chamber. The surface layer of the fuel pellet ablates causing the material to contract therefore compressing and heating the fuel. Once compressed to densities greater than ten times that of elemental lead, the deuterium and tritium in the core of the pellet encounter each other and react.

The largest working experimental ICF system is the National Ignition Facility (NIF) which is located at the Lawrence National Laboratory in Livermore, USA. NIF is the world's most precise laser system and is host to 192 laser beamlines, generating temperatures more than 180 million degrees Fahrenheit. After compressing the pellet to a high density, short-pulsed lasers supply enough energy for ignition to occur, where the self-sustaining fusion reaction is triggered. In this scenario, the power station produces pulsed power at higher pressures than MCF, and one pulse only takes around a billionth of a second. Contrarily, in magnetic confinement, the plasma is confined for much longer periods of time, on the order of seconds [10].

Magnetic confinement uses strong magnetic fields to isolate the hot, conductive plasma within a vacuum chamber. The plasma cannot simply be confined in a material vessel as any contact

with the walls will result in rapid cooling, therefore magnetic confinement also reduces thermal losses. There are two proposed designs for magnetic confinement: tokamaks and stellarators.

A tokamak adopts the use of magnetic confinement and is established as the most developed approach to fusion. Figure 1.4 shows the schematic of the components of a tokamak which adopts a magnetic confinement method.

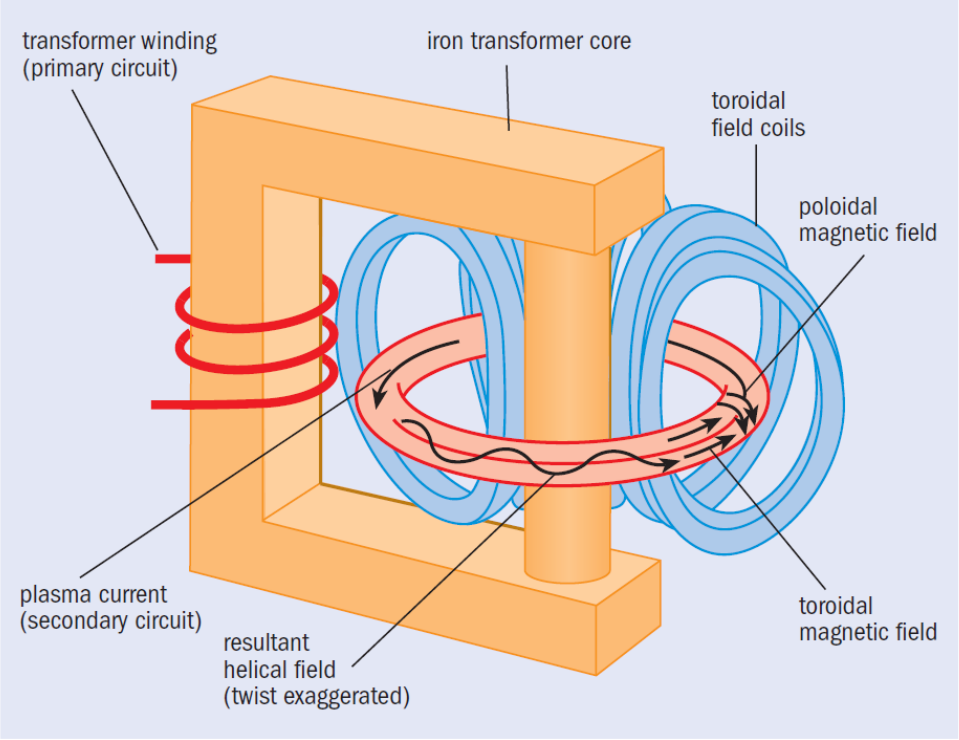

Figure 1.4: Schematic of the conventional tokamak design. The toroidal field coils and plasma current are used to create the core toroidal and poloidal magnetic fields which contain the fusion plasma [11].

It comprises a toroidal vessel surrounded by a helical magnetic field produced from D-shaped toroidal field coils. This doughnut-shaped chamber, or torus, contains the hot plasma and the toroidal field coils are produced by large superconducting magnets. The transformer action gives rise to a poloidal magnetic field and the coils create a toroidal magnetic field. The helical field gives rise to stability of the tokamak plasma. The transformer action generates a pulsed mode, however due to the self-sustaining mechanism of the plasma it is hoped that future power stations could operate in a near-continuous mode [12].

Alternatively, the stellarator design, the US contender in the 1960s, only uses the field coils to induce helicity to the plasma without the use of the transformer action. This results in a steady-state mode being achieved with higher plasma densities and less instabilities occurring. As expected, this requires the design of complex field coils, resulting in an intricate reactor needing to be built. The most notable nuclear reactor is the Wendelstein 7-X stellarator in Germany [13].

1.4. Roadmap to Commercial Fusion

Many scientific hurdles must be overcome before a commercial nuclear fusion power plant is feasible. In the 1970s a European collaboration to construct the world's largest operational magnetically confined nuclear reactor – the Joint European Torus (JET) began, located at the Culham Centre for Fusion Energy, in Oxfordshire, UK. Since its first operation in 1983, it has since become the first reactor to use a 50-50 mix of tritium and deuterium fuel [14]. No fusion reactor, including JET, has yet to achieve net energy output, an issue which JETs successors aim to address.

The construction of ITER, a pilot reactor, located in Provence, southern France will take over from JET as the world's largest experimental fusion tokamak. The ITER project has seven partners including China, Korea, India, Russia, Japan, the USA, and the European Union (and the UK) who have dedicated scientific and financial resources to establish fusion power as a viable energy source. ITER will be the first facility to produce net energy from the D-T reaction, with sustained pulses as long as 300 to 5000 seconds [15]. This unprecedented move will prove the technical feasibility of self-sustained plasma burn for electricity production. The construction of ITER serves to solve fundamental constraints including the testing of tritium breeding technology, sustainability of the hydrogen plasma by internal heating, and to evaluate safety protocols of the fusion reactor.

ITER will be the first fusion device to incorporate an actively cooled lithium blanket technology, with the coolant designed to remove up to 736 MW of thermal power [16]. Designed to be much bigger and thirty times more powerful than JET, ITER will produce approximately 500 MW of fusion power sustained for up to 1,000 seconds compared to its predecessor's 16 MW for less than second [17]. Figure 1.5 compares large confinement facilities using different metrics. There is clearly a significant distinction between ITER and DEMO (the DEMOnstration power plant; ITER's successor) with an increase of 30-50x in nuclear damage and highlights

the push into the commercial fusion power. These challenging conditions will also serve to test material requirements: lifetime of the materials, use of low activation materials, and increased nuclear constraints.

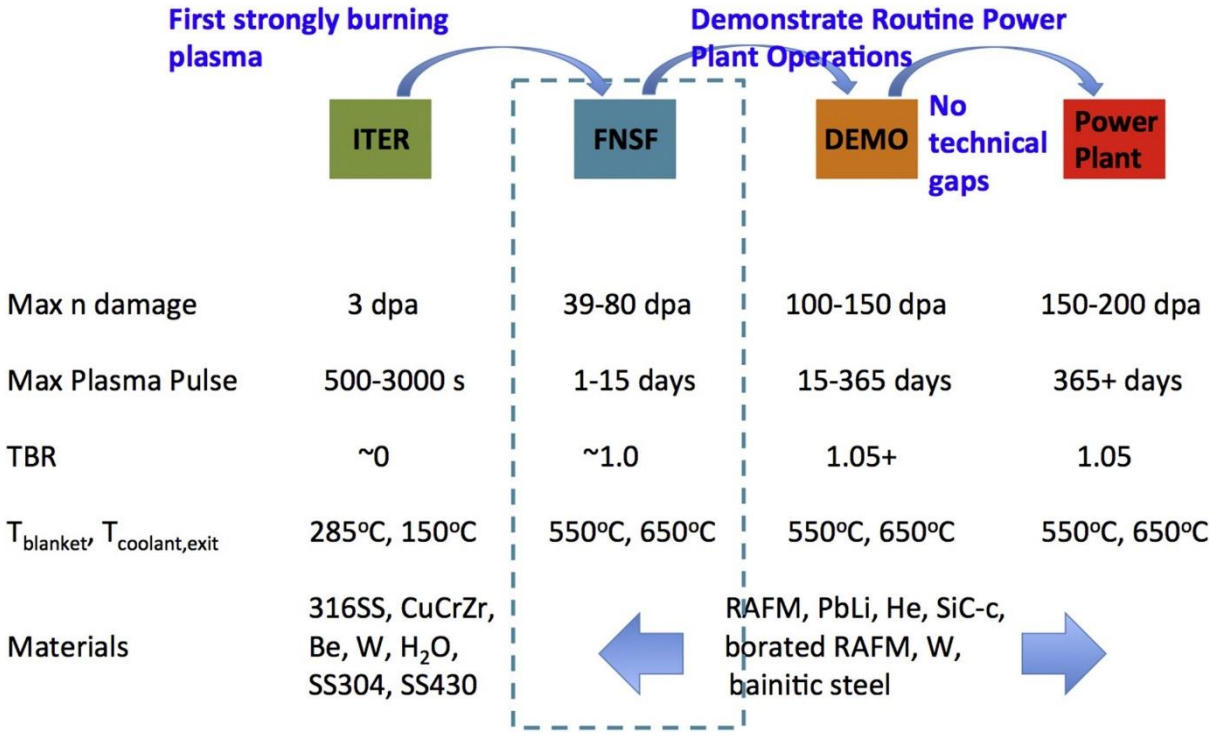

Figure 1.5: Comparisons of descriptive metrics for different nuclear reactor facilities including an estimation of radiation damage that the materials of the reactor are expected to experience [15].

JET has installed an ITER-like wall (ILW) to investigate plasma-facing materials for ITER. The previously used carbon fibre composite (CFC) tiles in the vacuum vessel were replaced with materials which combine low activation beryllium and high atomic number tungsten [18]. For the divertor a combination of bulk tungsten and tungsten-coated CFC divertor tiles are used and for the main chamber there are bulk beryllium tiles and beryllium-coated Inconel-625 between limiters where there is lower heat flux. Whilst materials for ITER have been chosen for the optimum conditions within its fusion reactor, the environment within a commercial power plant will be much more demanding; there will be an increase in operating temperature and the neutron fluence and heat loads will be orders of magnitude higher (Figure 1.5) [19]. For this reason, further advanced materials with improved mechanical performance need to be evaluated to accommodate the intense conditions of the reactor.

Demonstration power plant (DEMO) is ITER's planned successor and is projected by 2050. DEMO is anticipated to be the first fusion reactor to generate electricity and is projected to be 15% larger than ITER with a 30% greater plasma density. It is projected to build upon and improve the technological concepts of ITER to make fusion energy available by 2033. Following ITER, DEMO is the next step for the preparation for a reliable, economical credible fusion power plant.

Announced in October 2019, Spherical Tokamak for Energy Production (STEP) is a concept proposed by the United Kingdom Atomic Energy Authority (UKAEA) for the aim of producing net electricity from fusion energy by 2040. STEP will be a UK-based facility based on the spherical tokamak design and will be heavily influenced by UKAEA's Mega Ampere Spherical Tokamak (MAST) Upgrade spherical tokamak. Compared to ITER, STEP will be considerably smaller in size (with a diameter of approximately 10 m) and so will be much more cost effective. However, due to the comparatively smaller size the hot dense plasma in a smaller device will apply a higher stress on the materials used for the reactor and so the components will need to be replaced more frequently. Furthermore, STEP is unlikely to be capable of breeding tritium inside the device as the technology cannot be implemented in such a short time frame. One of the primary objectives of STEP is to demonstrate the commercial viability of fusion energy and will include features of a fully operational power station such as infrastructures associated with research and development and component testing facilities.

1.5. Plasma-Facing Components

Figure 1.6 shows the first wall panels, divertor, and test blanket modules (TBM) which are all part of the vacuum vessel of the tokamak reactor and are directly exposed to the hot plasma and are termed plasma-facing components (PFCs).

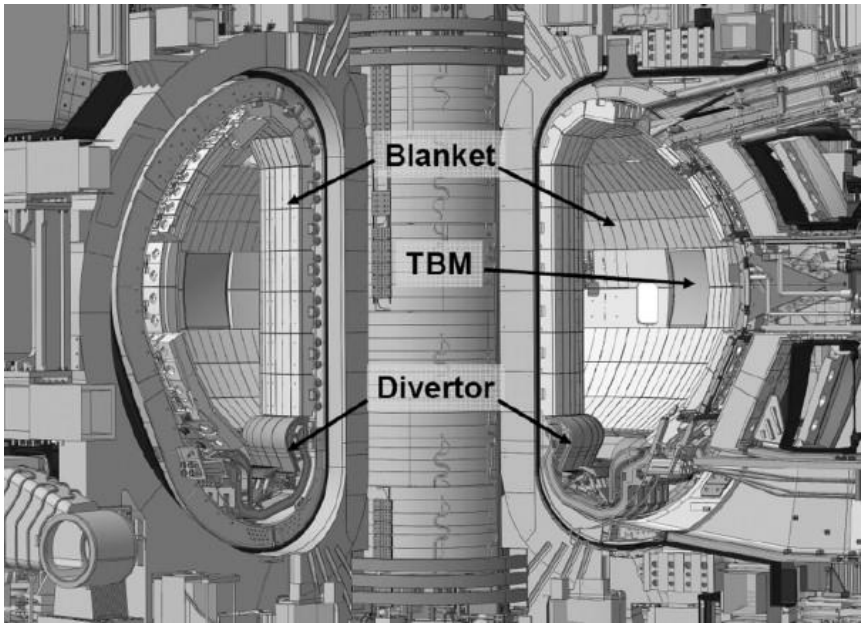

Figure 1.6: ITER plasma-facing components [20].

For the safe operation of a successful nuclear reactor, advanced high temperature materials with resistance to irradiation with preservation of mechanical performance in extreme conditions must be chosen. It is essential that the plasma-facing materials (PFMs) minimise any possible contamination with the plasma as this could affect plasma confinement stability, fuel dilution, and radiation losses. Additionally, the structural materials must also be compatible with the intense, fluctuating field lines, other materials, and coolants [21]. As shown in Figure 1.6, the main PFCs are the test blanket modules (TBM) and divertor components.

1.5.1. First Wall

Figure 1.7 displays the structure of the first wall component fingers, comprised of different materials. The fingers consist of a ‘sandwich’ structure of beryllium, copper, and Cu-Cr-Zr alloy.

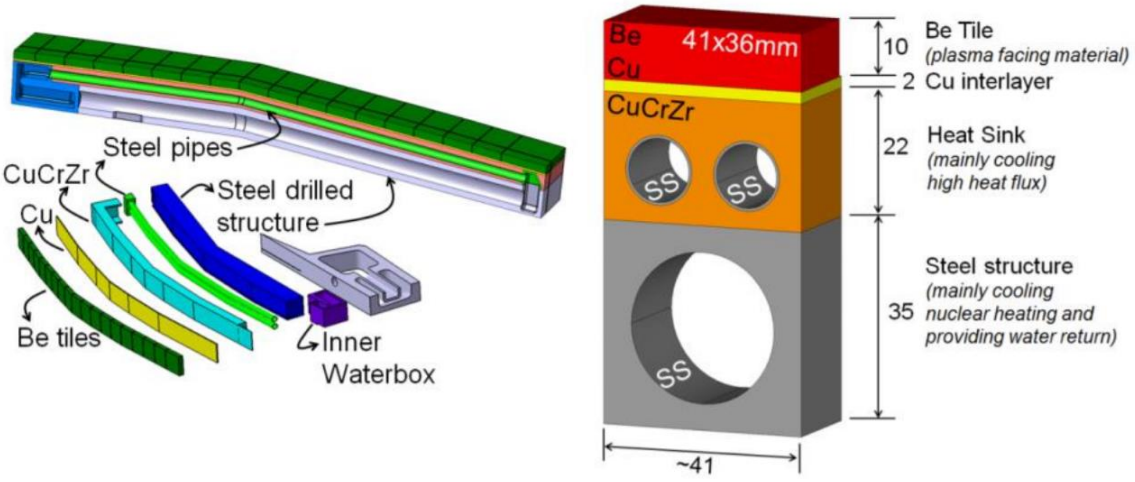

Figure 1.7: First wall panel design, composed of different layers of material for the ITER procurement [22].

The blanket module's primary role is to breed tritium for the D-T reaction but also serves to shield the rest of the vacuum vessel and superconducting magnets from the extreme heat loads of 0.25-0.5 MWm^{-2} and high energy neutron bombardment. Even so, the detachable, front-facing first wall panels face additional challenges compared to the blanket components. It is crucial that they can withstand the high heat flux from the plasma (the amount of which is dependent on their positioning within the vacuum vessel). Not only are there high thermal loads, but due to the design of the tokamak the PFCs must be able to endure the extreme heating and cooling cycles from the pulsed nature of the plasma environment. The panels are composed of 'fingers' (Figure 1.7) attached to a structural beam which holds the cooling water channels. At the end of the materials lifetime, it is expected that they will be serviced and replaced remotely with robotic assistance due to the severe radioactive environment within the vessel. This is expected to take up to 6 months so the components must last at least 2 years under these conditions.

1.5.2. Divertor

As neutrons have neutral charge, they are unaffected by the magnetic field and so they are emitted in all directions of the plasma. These fast neutrons will interact with the lithium blanket to generate tritium. The other product of the D-T reaction is the helium nucleus which, as a charged particle, is trapped by the magnetic confinement. This allows for energy to be retained

[11] and ‘self-sustain’ the plasma allowing for the reactor to operate in ignition mode. Once this energy has transferred, the heavy ions become helium ash and begin to dilute and rapidly cool the plasma. The waste helium gas must be extracted from the plasma to prevent the risk of reducing the D-T reaction rate and to protect the surrounding walls from thermal and neutronic loads. This is achieved by employing the use of a divertor, placed at the bottom of the torus, which also absorbs residue, allows the passage of heat flux, and traps unwanted contaminant ash particles. This presents a key materials challenge due to exposure from the harshest conditions within the reactor and requirements of the divertor include stability from intense particle bombardment at high temperatures. Specifically, the operating conditions of the divertor predicted for ITER, not only include the high neutron fluxes of up to 14 MeV in energy, but also extreme transient heat fluxes between 10-20 MWm^{-2}.

In ITER, the divertor is composed of 54 ten-tonne cassette assemblies, where each part has a supporting stainless steel structure and 3 PFC parts - the inner and outer vertical targets and the dome. Tungsten, the highest melting temperature metal, was proposed as the main component of the armour material following promising prototype testing. The advantageous properties of tungsten, including low sputtering at low plasma temperatures, low vapour pressure, and high melting point, render this refractory metal as the most suitable material for the first wall in DEMO and future advanced reactors. An alternative PFM for future reactors was liquid metal layers on either graphite or tungsten-based tiles. Liquid lithium is a low atomic number alkali metal that has been suggested to enclose the fusion plasma to address the challenges involved with solid PFMs. Liquid metals have the capacity to withstand the 50 MWm^{-2} heat loads and can also absorb high energy neutrons and convert this kinetic energy for the generation of electricity. Furthermore, lithium impurities in the plasma are well below 1% as the susceptibility of damage to the component causing contamination to the plasma are reduced. Liquid lithium coatings added to the PFC of the Tokamak Fusion Test Reactor in the Lithium Tokamak Experiment (TFTR, in 1996) showed promising results, however further investigation of the physical limitations of safely using multi-layered liquid lithium compounds for greater heat loads and neutron flux is needed.

The overall requirements for PFMs are as follows:

- Result in only low-level radioactive waste 100 years after the shutdown of the nuclear reactor thereby limiting the impact on the environment. This is to ensure the safe

disassembly of the reactor and to minimise the burden of handling and disposing of the used material. This means that only low activation elements can be used.

- Withstand steady state and transient thermal loading as a result of plasma instabilities
- Maintain high strength at elevated temperatures
- Display adequate ductility for the fabrication of complex cassette assemblies
- Tolerate charged particle bombardment and neutron irradiation. Damage to the material includes hardening and embrittlement which will affect the mechanical performance of the component.
- Contain low Z elements to minimise disruption of the plasma if contamination occurs.
- Have a high thermal conductivity to allow the high heat flux to pass through
- High resistance to thermal shock and fatigue
- Low tritium retention, as tritium levels in the plasma must remain constant so the D-T reaction rate is not affected

The ideal material, which can accommodate all of these complex criteria in the harsh environment of the reactor, does not currently exist as a conventional engineering alloy. For example, high strength at high temperatures would have to be compromised by the ductility needed for manufacturing of the complex component. Development of suitable PFMs would need to account for these specifications in addition to the extreme conditions of the reactor. Further insight into the challenging requirements for PFMs, the current material selection for PFCs and their constraints, and the obstacles faced when designing novel structural alloys is discussed in Chapter 2.1: Plasma-Facing Materials.

1.6. High Entropy Alloys as a PFC candidate

High entropy alloys (HEAs) are a relatively new class of materials which are principally based around multiple elements rather than one or two. They have been shown to possess excellent properties including high strength, hardness, and wear resistance and have recently shown potential as structural fusion materials due to their high radiation damage tolerance [23]. Most previously studied HEAs have focused on high-activation elements, but for fusion applications this would create high level radioactive waste material which would require specialised disposal after the shutdown of the reactor. It is at the forefront of this research to study HEAs composed of low-activation elements to establish their viability as structural materials for use in fusion reactors.

1.7. Aims and Objectives

The primary aim of this work is to determine the potential of low activation high entropy alloys for their suitability as plasma-facing components for nuclear fusion applications. This can be achieved by investigating the thermal stability of the equilibrium phases of the novel high entropy alloys at in-service temperatures. The following objectives of this work can be identified as:

1. Conduct preliminary investigations of the high entropy alloy VCrWMo(Co), where all the constituents have a BCC crystal structure, to determine if this promotes a BCC solid solution. In this study the objective is to determine whether the alloy was stable upon a) ion implantation and b) thermal annealing.
2. Highlight potential low activation/refractory elements with promising material properties which would not only be suitable for use as plasma-facing components, but also encourage the formation of a BCC solid solution.
3. Design of alternative high entropy alloys consisting of only low activation elements (removal of high activation molybdenum).
4. To characterise the designed series of low activation refractory high entropy alloys. In this work the evaluation of phase stability, especially upon thermal annealing, is integral in assessing the suitability of these alloys as plasma-facing components.
5. To highlight any promising candidate high entropy alloys for further specialised analysis, specifically to probe the thermal stability of the as-cast phases formed to determine their ability to perform as plasma-facing materials.

1.8. Thesis Overview

This thesis is formed of eight chapters including this Chapter 1: Introduction; an outline of the chapters in this work is given below:

Chapter 2 is a survey of the relevant literature to date. Firstly, a brief background of the mechanisms involved in radiation damage process in materials is included. A comprehensive review of the past and current candidate plasma-facing alloys and the issues associated with irradiated fusion armour materials is given. An introduction of the new class of materials termed high entropy alloys and the work pertaining to the design of stable solid solutions is also given.

Chapter 3 includes a detailed experimental methodology used in this work including the alloy fabrication methods (and subsequent special considerations for these alloys), alloy design processes, sample preparation and characterisation techniques, and mechanical testing procedures.

Chapter 4 includes a published paper for the preliminary investigation of the alloy $V_{2.5}Cr_{1.2}WMoCo_{0.04}$. In this paper, a refractory high entropy alloy was designed to form stable BCC solid solution and was evaluated using ion implantation and thermal annealing treatments to determine the stability of the as-cast phases.

Chapter 5 begins by highlighting potential low activation refractory elements with promising material properties. This chapter gives an overview of the design processes and modelling simulations evaluated in this work for the development of new low activation high entropy alloys.

Chapter 6 encompasses the main body of work in this thesis by evaluating the newly developed alloy compositions through experimental characterisation. Analysis is conducted to determine the phase structures, thermal stability, and mechanical properties of each alloy for the assessment of their suitability as plasma-facing materials.

Chapter 7 shows further experimental characterisation of the promising high entropy alloy, VCrMnFeW. In particular, examination of the thermal stability of the as-cast phases is required for the determination and extent of unfavourable phase formation which may prove detrimental in-service conditions.

Chapter 8 summarises the findings of this thesis and concludes with suggestions for future work based on the results ascertained in the past few chapters.

1.9. References

[1] Stringer, J. and Horton, L., 2003. Basic Research Needs to Assure a secure energy future. Oak Ridge, Tenn.: Oak Ridge National Laboratory: pp. A-97-A-101.

[2] Stegman, A., De Andres, A., Jeffrey, H., Johanning, L. and Bradley, S., 2017. Exploring Marine Energy Potential in the UK Using a Whole Systems Modelling Approach. Energies, 10(9), p.1251.

[3] Cobb, J., 2020. Highlights of the World Nuclear Performance Report 2020.

[4] Kelly, J.E., 2014. Generation IV International Forum: A decade of progress through international cooperation. Progress in Nuclear Energy, 77, pp.240-246.

[5] Jepson, J., 2016. Importance of Grad-Shafranov Re-Solves Towards Accurately Modeling an ITER Equilibrium in NIMROD.

[6] Zinkle, S.J., 2005. Fusion materials science: overview of challenges and recent progress. Physics of Plasmas, 12(5), p.058101.

[7] Ling, S.J., Sanny, J., Moebs, W., Friedman, G., Druger, S.D., Kolakowska, A., Anderson, D., Bowman, D., Demaree, D., Ginsberg, E. and Gasparov, L., 2016. University Physics Volume 2.

[8] Ongena, J.P.H.E. and Oost, G.V., 2012. Energy for future centuries: prospects for fusion power as a future energy source. Fusion Science and Technology, 61(2T), pp.3-16.

[9] Lawson, J.D., 1957. Some criteria for a power producing thermonuclear reactor. Proceedings of the physical society. Section B, 70(1), p.6.

[10] Lindl, J.D., McCrory, R.L. and Campbell, E.M., 1992. Progress toward ignition and burn propagation in inertial confinement fusion. Phys. Today, 45(9), pp.32-40.

[11] Nuttall, W.J., 2008. Fusion as an energy source: Challenges and Opportunities.

[12] Freidberg, J.P., 2008. Plasma physics and fusion energy. Cambridge university press.

[13] Feist, J.H., Bramow, H.J., Brockmann, R., Gliege, G., Grünberg, D., Kluck, T., Pohle, D., Schroeder, M., Schult, R. and Vilbrandt, R., 2007. Quality management for WENDELSTEIN 7-X—Lessons learned. Fusion Engineering and Design, 82(15-24), pp.2838-2843.

[14] Keilhacker, M., Gibson, A., Gormezano, C., Lomas, P.J., Thomas, P.R., Watkins, M.L., Andrew, P., Balet, B., Borba, D., Challis, C.D. and Coffey, I., 1999. High fusion performance from deuterium-tritium plasmas in JET. Nuclear Fusion, 39(2), p.209.

[15] Kessel, C.E., Blanchard, J.P., Davis, A., El-Guebaly, L., Garrison, L.M., Ghoniem, N.M., Humrickhouse, P.W., Huang, Y., Katoh, Y., Khodak, A. and Marriott, E.P., 2017. Overview of the fusion nuclear science facility, a credible break-in step on the path to fusion energy. Fusion Engineering and Design.

[16] Raffray, A.R. and Merola, M., 2012. Overview of the design and R&D of the ITER blanket system. Fusion Engineering and Design, 87(5-6), pp.769-776.

[17] Llewellyn-Smith, C. and Ward, D., 2005. Fusion power. European Review, 13(3), pp.337-359.

[18] Matthews, G.F., Beurskens, M., Brezinsek, S., Groth, M., Joffrin, E., Loving, A., Kear, M., Mayoral, M.L., Neu, R., Prior, P. and Riccardo, V., 2011. JET ITER-like wall—overview and experimental programme. Physica Scripta, 2011(T145), p.014001.

[19] Duffy, D.M., 2010. Fusion power: a challenge for materials science. Philosophical Transactions of the Royal Society of London A: Mathematical, Physical and Engineering Sciences, 368(1923), pp.3315-3328.

[20] Merola, M., Loesser, D., Martin, A., Chappuis, P., Mitteau, R., Komarov, V., Pitts, R.A., Gicquel, S., Barabash, V., Giancarli, L. and Palmer, J., 2010. ITER plasma-facing components. Fusion Engineering and Design, 85(10-12), pp.2312-2322.

[21] Neu, R., Rohde, V., Geier, A., Krieger, K., Maier, H., Bolshukhin, D., Kallenbach, A., Pugno, R., Schmidtmann, K., Zarrabian, M. and Team, A.U., 2001. Plasma operation with tungsten tiles at the central column of ASDEX Upgrade. Journal of nuclear materials, 290, pp.206-210.

[22] Kirk, S., Porton, M., Perez, G., Vizvary, Z., Luzginova, N., Eaton, G., Banetta, S. and Cicero, T., Preliminary study into the repair of ITER normal heat flux first wall panels.

[23] Xia, S.Q., Zhen, W.A.N.G., Yang, T.F. and Zhang, Y., 2015. Irradiation behavior in high entropy alloys. Journal of Iron and Steel Research, International, 22(10), pp.879-884.

Chapter 2: Literature Review

Chapter 2.1: Radiation Damage in Materials

In Chapter 1: Introduction, the environment of proposed commercial fusion reactors was described, specifically the exceedingly high temperatures of plasma (around 150 million K), high neutron fluxes of up to 14.1 MeV in energy, and extreme transient heat fluxes between 10-20 MWm^{-2}. Arguably, the most complex challenges faced by PFCs are the different effects of neutron irradiation, specifically neutron sputtering and absorption. There are critical requirements for reactor materials including resistance to void swelling and thermal stability, as well as retainment of mechanical properties (good tensile strength, ductility, and fracture toughness). Favourable radiation damage tolerance including reduced irradiation-induced embrittlement and hardening is also required. In this section, an overview of the fundamental displacement damage process in materials is given, as well as the physical effects of these mechanisms including phase stability of the alloys.

2.1.1 Displacement Damage in Materials

The profound effects of neutron irradiation can be discerned from the fundamental processes that govern the displacement of atoms from their lattice sites due to interactions with neutrons. The process of devising new radiation-tolerant materials arises from the need for higher efficiency materials which can comply with the increasing demands of nuclear reactors (for example the increasing neutron fluxes experienced by components in future advanced reactors). Fundamentally, this rests on the mitigation of the physical deterioration of the irradiated materials resulting from detrimental effects such as swelling, growth, phase change, and segregation [1]. Many of the damage processes that occur in nuclear fission reactors are relevant for nuclear fusion. Typically, nuclear materials will undergo changes in properties including increased volume and hardness, reduction in ductility, increased embrittlement, and stress corrosion cracking. Novel to nuclear fusion and for PFMs are the impacts of the high flux, high energy (14.1 MeV) fusion neutrons on material properties. This section describes the fundamental damage processes relevant to both fission and fusion, as well as the unique challenges posed by nuclear fusion.

High energy neutrons, formed from the nuclear fusion reaction, can be projected from the plasma onto the surface of the PFM. This event results in the interaction of the energetic incident particle (in this case, a neutron) with a lattice atom of the material. These atom-neutron interactions can result in two main effects: (1) scattering, where the neutron displaces the atom from its lattice site if sufficient kinetic energy has been transferred; and (2) absorption, which results in transmutation of the lattice atom [2].

In this section, we will consider only neutron scattering, as the ion implantation experiments carried out during this work were used only to simulate neutron scattering. During neutron scattering, we can consider both the neutron and lattice atom to be two hard spheres. In this "hard sphere model" [3] it is assumed that collisions are approximately head on, and that kinetic energy and momentum are conserved. Therefore, we consider these interactions to be "elastic". If the neutron produces an inelastic reaction, then transmutation occurs which generates light atoms as helium and hydrogen. Transmutation effects are beyond the scope of this work however, some of these effects are further discussed in Section 2.2.3.4.

For an atom to be displaced from its lattice site, sufficient kinetic energy must be transferred from the neutron to the atom, called the displacement energy, E_d. If the neutron transfers less than the displacement energy to the atom, then the atom will vibrate about its lattice site, but will not be displaced. If the neutron transfers greater than E_d, then the atom will be displaced from its lattice site and move through the material, where the atom itself can cause further atomic displacements. This atom, called the primary knock-on atom (PKA), leaves behind a vacancy if the PKA has sufficient kinetic energy to cause a series of displacements, this is called a collision or displacement cascade, where point defects (vacancies and interstitials) are created by the PKA, until it finally comes to a rest in an interstitial position [4]. The vacancy-interstitial pair is called a Frenkel pair and can, along with other phenomena, be responsible for the physical effects of irradiation. During the collision cascade, many of the vacancies and interstitials recombine, facilitated by the kinetic energy possessed by the interstitials, enabling them to diffuse through the material increasing the probability that they will encounter a vacancy. The migration, agglomeration, and annihilation of the collection of point defects that occurs during the collision cascade, approximately 10^{-11} s in duration, is termed "dynamical annealing" [5]. The point defects that remain following dynamical annealing result in the observable effects of irradiation, such as radiation induced hardening.

The amount of damage that occurs because of this process can be calculated for a given material. Two essential variables: σ, the transfer of energy from the incoming particle to the PKA and υ, the total number of displacements that the PKA creates, together express the total number of displacements resulting from the incoming neutron. Equation 1 summarises this relationship [6]:

$$dpa = t_e \phi_{tot} \int dE \sigma_d(E) \Psi(E) \qquad \textit{Equation 2.1}$$

where ϕ_{tot} is the time dependent neutron flux intensity as a function of neutron energy, E. And σ_d is the atomic displacement cross-section for a particular material and $\Psi(E)$ is the normalised flux spectrum integrated over energy.

The universal standard for quantifying the displacement cascade damage is measured in displacements per atom (dpa) and is often used instead of neutron fluence. Dpa is used to normalise the amount of radiation damage that different reactors produce. For example, fluence cannot be used when the neutron spectrum is different from the experiment as the damage cascade is dependent on neutron energy and the target material [7]. The detrimental effects mentioned previously, causing property changes within the material, is dependent on the amount and type of displacement damage – the extent of which varies on temperature. Figure 2.1 shows the operating temperature windows for various structural materials used in nuclear energy systems for damage levels from 10-50 dpa. From this figure it can be observed that at lower temperatures the reduced ductility is associated with radiation embrittlement. Whereas for higher temperatures thermal creep dominates.

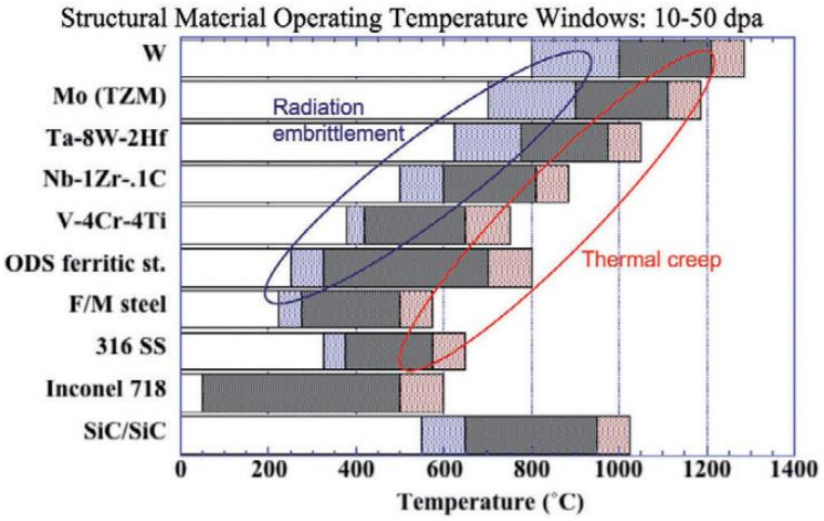

Figure 2.1: Comparison of several structural materials in comparison to their operating temperature window and the resultant radiation-induced effects [8].

Frenkel defects created by the high energy neutron-lattice atom collision can be lost by recombination of the vacancy and interstitial or by interaction with a defect sink. Defect sinks, for vacancies and interstitials, can be classed into different categories: neutral, biased, or variable. Neutral sinks display no preference for trapping any defect and are typically voids/gas bubbles and incoherent precipitates [9]. Incoherent precipitates are distinguished from the matrix as not having a matching interface. Biased sinks show preferential attraction for a particular defect type. Finally, variable bias sinks trap and preserve defects until an opposite defect approaches and annihilation occurs. This process is facilitated by the coherency between the trap and the lattice which relieves the strain field produced by the difference in lattice parameters. They possess the ability to vary their preference for point defects depending on the relative sink strengths in the bulk material. Examples of these sites include coherent precipitates, which has a perfect registry with the matrix lattice, or impurity atoms.

2.1.2 Phase Stability

Upon irradiation, the displacement cascade event causes the creation of point defects, which can induce the formation, or dissolution, of phases by forming regions enriched or depleted of alloying elements, thus changing the local composition of the alloy. This has a profound effect on the mechanical properties of the bulk alloy and so must be fully investigated for structural

fusion components. The mechanisms by which this phenomenon can occur are discussed in this section.

2.1.2.1. Radiation-Induced Segregation

Point defects and defect clusters produced by irradiation can either recombine or move to discrete sinks such as dislocations, grain boundaries, precipitates, etc. Depletion or enrichment of elements at the grain boundaries can cause local chemical and microstructural changes which affect the mechanical stability of the component. This process, termed radiation-induced segregation (RIS), is a non-equilibrium process that occurs at intermediate temperatures (T_m=0.3-0.5) and poses an important problem for structural nuclear components [10]. These effects are driven by the defect fluxes (as the motion of defects are affected by the motion of atoms) which induce an elemental concentration gradient. For example, the flux of vacancies corresponds with an equal flux of elemental atoms in the reverse direction providing a net loss of this element at the boundary and a net gain of the remaining elements at the boundary. For interstitial fluxes this too is dependent on atomic fluxes; if the concentration of one element is greater in the interstitial flux than in the overall fraction of the alloy then there is elemental enrichment at the boundary (and vice versa).

An interesting outcome of this type of segregation is the effect of localised concentration changes. When irradiation-induced elemental segregation leads to a higher concentration of a particular element (in comparison to the bulk of the alloy) that exceeds the solubility limit, then precipitation of a different phase will occur. Additionally, irradiation can also induce and preserve precipitation of phases that would normally not be present in thermodynamic equilibrium. An example of radiation-induced precipitation was observed in high-purity 304 + Si stainless steel implanted with 2 MeV protons at a dose of 5dpa at 360 °C. Atom probe tomography identified Ni/Si-rich precipitates likely to be precursors of γ’ or other high-Si, high-Ni phases [11]. Alternatively, if a second phase is already present pre-irradiation, then depletion of a solute, if steered below the solubility limit, can cause the decomposition of this phase upon irradiation. In situ electron irradiations performed on Ni_2Al_3 revealed that at high doses precipitation of aluminium from the B2 matrix occurs due to radiation-induced segregation [12].

2.1.2.1.1. Solute size effect

The difference in size between impurity atoms, which act as traps for defects, is an important factor when calculating the direction and degree of elemental segregation. For example, oversized solute atoms show preference for substitutional sites and so will move to (or remain) in these positions - unless vacancies can be exchanged with these atoms. On the other hand, undersized solute atoms will remain in interstitial sites to reduce strain energy in the lattice [13]. Upon irradiation, repositioning of solute atoms, due to variance in defect fluxes, causes an enrichment of undersized solutes, and a depletion of oversized solutes near defect sinks.

2.1.2.1.2. Temperature Dependence

At elevated temperatures, increased diffusion rates lead to high defect recombination rates and so defect fluxes are reduced, and the degree of elemental segregation is accordingly diminished [14]. Similarly, at lower temperatures, there is a reduced amount of segregation again due to higher rates of defect recombination. However, this process is due to lowered vacancy mobility which results in a higher radiation-induced excess vacancy concentration. At intermediate temperatures, radiation-induced segregation dominates as both the thermal vacancy concentration and radiation-induced excess vacancy concentration are low.

2.1.2.1.3. Dose Rate

Segregation is also dependent on the dose rate of the irradiation as this influences the effect of the temperature dependence [15]. Decreasing the dose rate shifts the temperature dependence of the segregation to lower temperatures. In this case, the lower dose rates give rise to lower amounts of point defects being formed, however their mobility remains the same and so this increases the probability of the defects migrating to the sink rather than recombining. This increases the amount of segregation occurring at a given temperature. Increasing the temperature exacerbates the importance of sinks over irradiation-induced vacancies and so segregation decreases with decreasing dose rate.

2.1.2.1.4. Local Composition and Diffusion

Diffusion of elements is also an important process that affects the extent of RIS as elemental composition changes at the grain boundary, so does the diffusivities of each element. An example of this can be demonstrated by the experimental studies of the Fe-Cr-Ni system where chromium (a fast diffuser) tends to deplete and nickel (a slow diffuser) tends to enrich.

Figure 2.2 shows the depletion of chromium and enrichment of nickel at the grain boundary of an irradiated stainless steel.

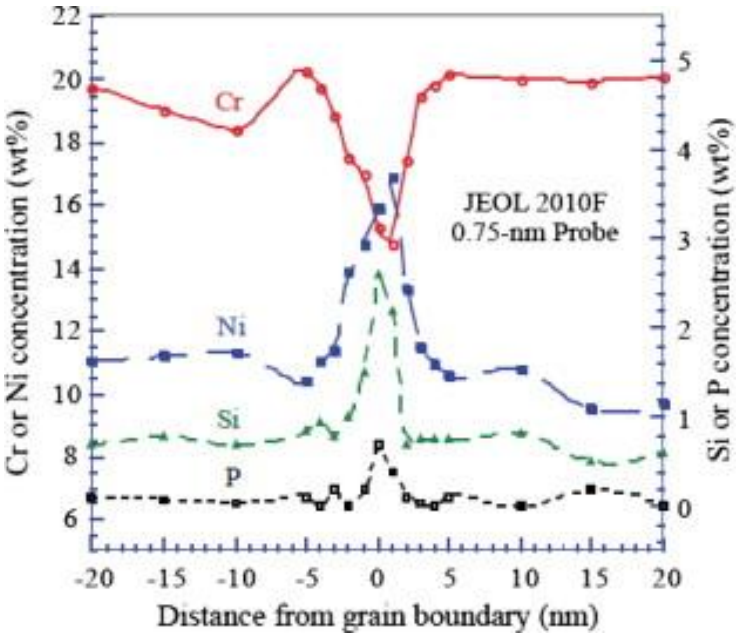

Figure 2.2: Radiation induced segregation of Cr, Ni, Si, and P in relation to distance from grain boundary for a stainless steel alloy irradiated at 300 °C [16].

The role of iron depends on the concentrations of the other element. For instance, when the concentration of nickel is greater than chromium, iron will deplete at the grain boundary to compensate for the lack of chromium. This process is reversed for when chromium concentrations exceed nickel and so iron will tend to enrich at the grain boundary.

2.1.2.1.5. Austenitic and Ferritic Steels

Exhaustive phase stability studies have been carried out for austenitic steel engineering alloys used in the cores of advanced reactor systems over the last 20 years. As mentioned previously, chromium depletes at the grain boundary upon irradiation. A typical example of this is represented in irradiated FCC austenitic steels where the depletion of chromium at the grain boundaries induces intergranular stress corrosion cracking (ISCC) due to the loss/reduction of passivity of chromium by Cr_2O_3 [17].

Three categories of phases found in these steels are affected by irradiation: radiation-induced, radiation-modified, and radiation-enhanced. Radiation-induced phases are only formed upon irradiation and do not appear in thermal states. Radiation-modified phases appear under both

thermal and irradiation conditions whilst radiation-enhanced phases develop during thermal operations but form more rapidly at lower temperature irradiation. For 316 austenitic stainless steels irradiated in the range 400 °C - 500 °C the radiation-induced γ' Ni_3Si phase rapidly forms, where the volume fraction is a function of the Si and Ti concentrations [18]. At higher temperatures, between 500 °C and 600 °C, radiation-enhanced and radiation-modified phases overtake in the form of G-phases ($M_6Ni_{16}Si_7$), M6C Laves, phosphides, and silicides. The precipitation of these phases is representative of the phase stability upon irradiation. Radiation-induced segregation causing areas of sinks to be abundant in solutes results in the production of precipitates. Alternatively, radiation-enhanced diffusion can affect precipitation growth under thermal conditions.

2.1.3 Mechanical Properties - Irradiation Hardening

Irradiation of both FCC and BCC metals, causes an increase in yield strength, reduction of fracture toughness, and a decrease in ductility [19]. Even at lower temperatures, BCC materials exhibit brittle behaviour when exposed to high fluence. Hardening occurs due to the formation and accumulation of irradiation-induced defects (including precipitates, dislocation loops and lines, voids and bubbles, and defect clusters) [20]. In irradiated materials, the motion of dislocations through a crystal lattice are impeded by the radiation-induced obstacles resulting in the pinning of dislocations which causes hardening of the material. For example, in alloys where incoherent precipitates are present this act as a physical obstruction for dislocations moving along a slip plane and causes a short-range interaction. Bowing of the dislocation between the obstacles can occur when the applied stress is significant and can continue until annihilation occurs and a dislocation loop is created. The obstacle is left behind and is surrounded by a dislocation loop creating a stronger dislocation obstruction and the dislocation is then free to move on until the process repeats again. Creation of the dislocation loop provides strengthening from the obstacles. Radiation hardening can lead to an upward shift in ductile to brittle transition temperature (DBTT), particularly observed by vanadium and tungsten alloys after irradiation at below 400 °C [21]. A further effect of radiation hardening is the dramatic decrease in fracture toughness and tensile elongation of refractory alloys at low temperatures. For example, Ta alloys exhibit significant radiation hardening and loss of uniform elongation [22]. However, there have only been a few reported fracture toughness studies post-neutron irradiation [23]. It has been suggested that for refractory alloys (alloys

containing substantial amounts of refractory elements) exposed to neutron irradiation, temperatures should be kept above $0.3T_m$ to minimise irradiation-induced embrittlement [24].

2.1.4 Heavy Ion Implantation as an Analogous Study for Neutron Irradiation

There are several particle irradiation types: electron, proton, neutron, and ion - they all can displace material atoms from their lattice sites. However, due to their contrasting masses they form different damage cascades, and this results in the production of different types of damage morphology. Lighter species (such as electrons and protons) generate more isolated and widely spaced Frenkel pairs in smaller clusters, whereas heavier ions and neutrons create denser damage cascades culminating in large clusters which promote increased recombination [25].

Neutron irradiation studies of candidate structural nuclear materials are important in assessing how the first wall components respond to harsh environments. Gaining insight into the deterioration of mechanical and physical properties over the in-service lifetime is important for the advancement in the design of advanced nuclear reactors [26]. Testing of materials is imperative due to them displaying different behaviours under similar irradiation conditions and due to different areas of the reactor experiencing a diverse range of flux and spectrum of neutrons. Materials testing in reactors takes around 1-3 years to reach a fluence needed for experimental analysis [1]. During this time, variation of irradiation parameters (including dose, temperature, etc.) cannot be altered and so further testing is required to refine these parameters - this increases the total time needed for irradiation experimentation. Another drawback of neutron irradiation testing is that the samples post-irradiation needs to be handled with special precautions due to residual radioactivity. Most importantly, the primary flaw of fusion materials testing results from fission reactors only possessing, on average, 2 MeV energy neutrons [27]. Currently available neutron sources tend to be on the order of one order of magnitude lower in flux for 14 MeV energy neutrons and so do not accurately represent the conditions within a fusion reactor. Nonetheless, neutron irradiation facilities are important for the study of transmutation nuclear reactions. For all these reasons, the costs and time needed for each irradiation cycle can be very high and so finding a replacement method for the testing of materials is required.

Ion implantation is widely used as a surrogate for neutron irradiation studies to mitigate some of the deficiencies of using neutrons. This method involves the bombardment of the material's surface with a chosen charged ion of a given energy to replicate the fusion environment, where high energy neutrons are projected onto the material [28]. The energy of the ion, whether hundreds of keV or several MeV, and ion type will determine the depth of the distribution of the implanted ions. The ions travel through the material and cluster at a given depth, leaving a portion of the surface lean in the implanted ion. This is advantageous in that this lean area can then be analysed for the damage occurred due to the implantation without the contamination of the implanted ion.

To reach the same levels of neutron fluence (which requires years of irradiation) ion implantation only takes in the order of tens of hours to reach 1-10 dpa. Generally, samples after ion implantation have no radioactivity (dependant on the implantation ion) and so can be handled with routine care, this reduces the cost and time of testing compared to neutron irradiation. Samples implanted with heavy ions do not directly undergo transmutation reactions, unlike materials exposed to neutron environments. However, this phenomenon can be evaluated using He and H ion implantation to evaluate when gas is generated during transmutation.

The suitability of ion implantation as an analogous method for neutron irradiation must be evaluated if comparable conclusions are to be drawn. Measuring the extent of radiation effects in materials (for example, elemental segregation, formation of dislocation loops, and hardening) using analytical techniques can be used to determine the comparable effects of both neutron and ion irradiation [29]. Ion implantation can provide a quick, low-cost option for the rapid screening of a range of novel materials.

Variation of irradiation parameters, including particle type, energy, dosage, temperature, dose rate, etc., allows for the examination of the resulting microstructure and damage state from basic damage processes. Ion implantation is often used to emulate neutron irradiation, to not only mitigate some of the negative consequences of using neutrons, but also to gain a deeper understanding of the fundamental physical process that occurs during irradiation. The challenge lies in determining the optimum variables which best replicate the neutron environment within a nuclear fusion reactor.

To further complicate the process of finding the most fitting irradiation parameters for ion implantation, the realistic environment within a nuclear fusion reactor has proven challenging

to quantify. For example, in an advanced nuclear fusion reactor it is difficult to determine the exact temperature and dpa the plasma-facing components experience and so neutronic models are often relied on. This means that even though ion implantation studies can be easily controlled, difficulty arises when assessing the best parameters which most accurately emulate the conditions experienced by the components within a nuclear reactor.

There are some major differences between ions and neutrons that need to be considered when ascertaining the irradiation damage of materials. Firstly, the production of ions and neutrons vary - neutrons in a fusion reactor have energies around 14 MeV whereas ions are generated in an accelerator and have a smaller range of energies. Secondly, the penetration depth of ions and neutrons into the subject material vary greatly due to the additional loss of charged particle energy by electronic excitation as well as from elastic collisions [30]. For ions, the distance travelled into the surface of the material is typically up to 100 microns, whereas neutrons, due to their neutral charge, come to a rest after travelling millimetres into the material. Additionally, as neutrons have a larger mean free path, the neutron damage energy is low but constant over their distances of travel.

A further benefit of ion implantation is the availability of simulation software to allow for the modelling of interactions to predict the physical effects of irradiation, including the penetration depth of ions into a given material. The Stopping and Range of Ions in Matter (SRIM) is a computer software program used for ion implantation studies to define the interaction of ions with materials [31]. The user inputs a desired ion type and energy and defines the material to be implanted. The program is based on a Monte Carlo simulation method and simulates the bombardment of ions onto the selected material. The simulation plots the distribution of ions in the material and the target atoms cascades and outputs information including penetration depth of the material, sputtering rate, concentration of vacancies, energy deposition rate, etc. However, there are some features that SRIM cannot compute, for example, defect clustering and irradiation-induced amorphization cannot be evaluated. SRIM also assumes that the sample is amorphous and at absolute zero Kelvin therefore no annealing is calculated - hence it always overestimates damage levels.

Compositional changes can happen during ion implantation due to the damage cascades that occur when ion bombardment ensues. Sputtering occurs when atoms of the alloy are given enough energy from the incident ion to eject the outer surface [32]. Each element will physically sputter at different rates; elements with higher atomic numbers (Z) and surface

binding energies affects the amount of energy and momentum transferred to the atom. As elements are ejected from the material, this also means that sputtering affects the surface composition of the alloy.

Radiation-induced segregation (RIS) is an effect which relies only on the mechanism of point defects and so can be studied without having to consider the complex consequences of agglomeration. For this reason, the extent of RIS in light-water reactor (LWR) core materials has been measured using different irradiation sources to quantify the equivalence between ion and neutron irradiation as mentioned previously. The amount of depletion of chromium at the grain boundaries is determined in post-irradiated samples tested at a range of different irradiation parameters considering displacement efficiencies between irradiated particle types. For novel materials, in particular classes of alloys which have not been greatly studied for nuclear applications - including high entropy alloys, benchmarking studies need to be conducted to establish comparable techniques.

2.1.5. Summary

In this section the theory of radiation damage in materials was discussed. The radiation damage event is outlined where energetic neutrons produce displacement cascades which accumulate several displaced atoms to form Frenkel pair defects which will eventually deposit damage on the material. Irradiation-induced defects, such as interstitial clusters, dislocation loops, or vacancy-type voids can act as barriers to dislocation movement thus producing significant hardening and a reduction in ductility.

Irradiation-induced defect evolution and microstructural changes are of great importance when investigating the irradiation performance of materials. Understanding the mechanisms of defect evolution, irradiation-induced microstructure changes, void swelling, phase stability, and mechanical properties under irradiation is integral when evaluating components exposed to constant bombardment of high energy neutrons, high temperatures, and cyclic stresses.

Neutron irradiation inherently induces transmutations and nuclear activation, therefore produces samples which are difficult to analyse. Heavy ion implantation studies have been used to emulate neutron irradiation however, differences between these two techniques means that consideration must be considered concerning shallow depth of irradiation, higher dose rates, and lack of transmutation of ion implantation. In conclusion, heavy ion implantation

is a useful method for the investigation of radiation damage tolerance for materials considered for plasma-facing components subjected to the harsh environment of a nuclear fusion reactor.

2.2: Plasma-Facing Materials

This section will primarily focus on the discussion of the strict requirements of plasma-facing materials (PFMs) in terms of material degradation due to the extreme reactor environment. The effects of the radiation damage processes caused by the high energy neutrons is also discussed in terms of material specifications. Alongside this is an in-depth evaluation of the previous and current prospective candidates, including carbon composites, beryllium, and tungsten, for JET, ITER, DEMO, and future advanced reactors.

2.2.1 Plasma-Facing Components

Figure 2.3 shows the key components of a tokamak reactor. The inner lining armour of the toroidal magnetic chamber, termed the plasma facing components (PFCs), protects the outer mechanical components and superconducting magnets from plasma damage. The hot plasma contains energetic helium particles and neutrons which can escape and interact with the surface of the PFCs resulting in surface erosion and neutron induced damage.

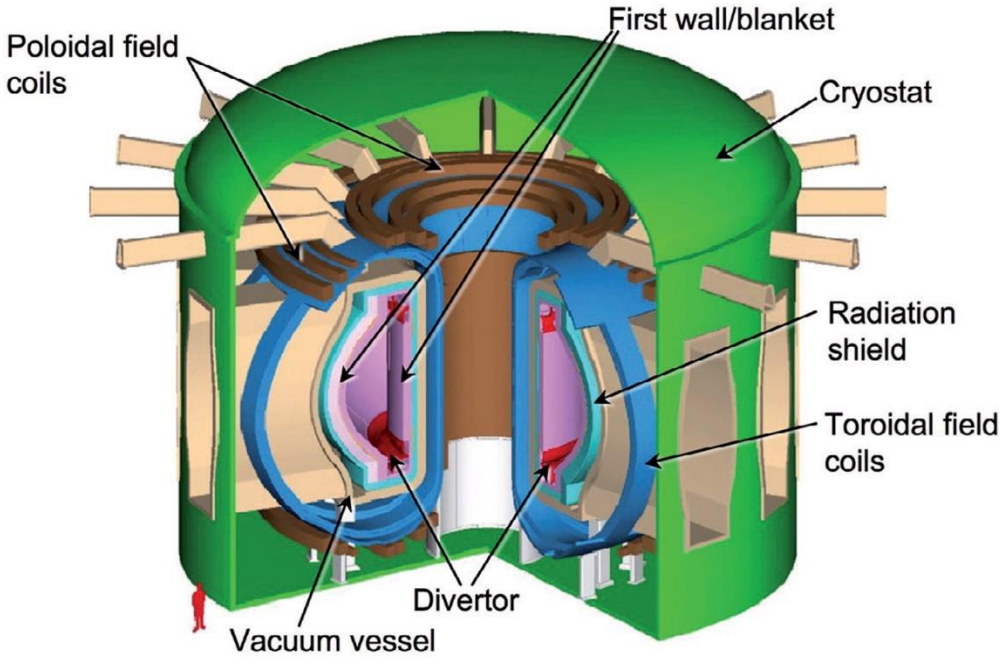

Figure 2.3: Schematic of the components in a magnetically confined tokamak fusion reactor [8].

These processes have significant implications for plasma stability and material performance and are described in Sections 1.5. and 2.1, respectively. The plasma-facing material (PFM) and the plasma form a complex coupled system where the components will have to endure

extreme physical conditions which will consequently impact the lifetime of the first wall. In view of the plasma-wall interactions, which are associated with the high particle and heat fluxes, a set of new challenges must be met for advanced fusion devices.

Key concerns for materials selection for the first wall of a nuclear fusion reactor include:

- Favourable resistance to radiation damage. Neutron irradiation of the PFCs is expected to withstand substantial damage up to 150 dpa during the lifetime of the reactor. This has a significant effect on the mechanical performance of these components. Increased defect production and transmutation will severely degrade the material and in turn this can further lead to crack formation and melting which can aid erosion losses and dust formation – this is detrimental to the lifetime of the component and can also negatively affect the plasma [26].
- Longer lifetimes. This is due to the difficulty in physically replacing the components and for the extended operational times for the future fusion reactors with longer pulse lengths leading to steady-state operation [33]. This ultimately increases the neutron fluence and heat loads on the first wall components as explained further in the next section.
- Compatibility with coolant and other structural materials. Due to the increasing demands of the first wall, resultant from intense thermal loads and longer discharge durations, coolants such as water or helium, are needed to enable safe operation.
- Acceptable mechanical properties at elevated temperatures. High neutron fluxes deteriorate the thermal conductivity of the first wall material which consequently affects the heat removal efficiency of the armour. Additionally, neutron-induced degradation occurs in the form of an increased ductile to brittle transition temperature which ultimately reduces the temperature operation window (where the material demonstrates sufficient ductility) [34].
- Low radioactivity and radioactive heat decay (this is discussed further in Section 2.2.2.)
- Deuterium and tritium can diffuse into the surface of the first wall material where they can become trapped in neutron-induced defects and subsequently cause embrittlement of the material and additionally cause a significant increase in the tritium inventory of the first wall.
- Safety of waste disposal and maintenance (this is discussed further in Section 2.2.2.).
- Availability and cost of materials as well as ease of design and fabrication of the PFC.

An important challenge in the advancement of fusion structural materials is the extreme environment within the fusion reactor; the presence of high energy neutron (14.1 MeV) irradiation, high neutron fluxes (around 8.25 x 10^{14} n $cm^{-2}s^{-1}$ in the first 2 cm of the first wall armour [35]) and high heat fluxes (up to 20 MWm^{-2}) are key constraints when considering potential candidate materials. Due to the expected short transient thermal loads, plasma-facing components are expected to reach a maximum surface temperature 1100, 1500, and 2300 °C for the three discharges. Therefore, temperature and radiation-induced structural transformations and associated property changes of candidate materials need to be fully understood for the successful development of advanced materials for fusion. The following is a discussion of the material requirements for PFMs, current candidate materials, their limitations, and the need to develop novel alloys.

2.2.2 Radiation Damage and Effects

The plasma is confined within the vacuum vessel, a high vacuum stainless steel container, using superconducting magnets so the spiralling plasma does not touch the walls. Despite this, energetic plasma particles and high energy neutrons can escape the plasma and penetrate the surface of the plasma-facing components. This interaction can cause atomic displacement cascades and transmutation nuclear reactions within the materials in the first wall as discussion in Section 2.1. The impact of neutron damage on the plasma-facing material has substantial effects particularly due to the neutron flux and energies produced in a fusion reactor which are significantly greater than in any current nuclear fission power reactor. Figure 2.4 shows the neutron-energy spectra for both nuclear fusion and fission reactors [35]. It can be observed that for the fusion spectrum there is a significant flux of neutrons in the 12 - 15 MeV neutron energy range. A proportionally higher flux of high energy neutrons is responsible for the higher dpa levels of fusion reactors in comparison to fission reactors of similar thermal power.

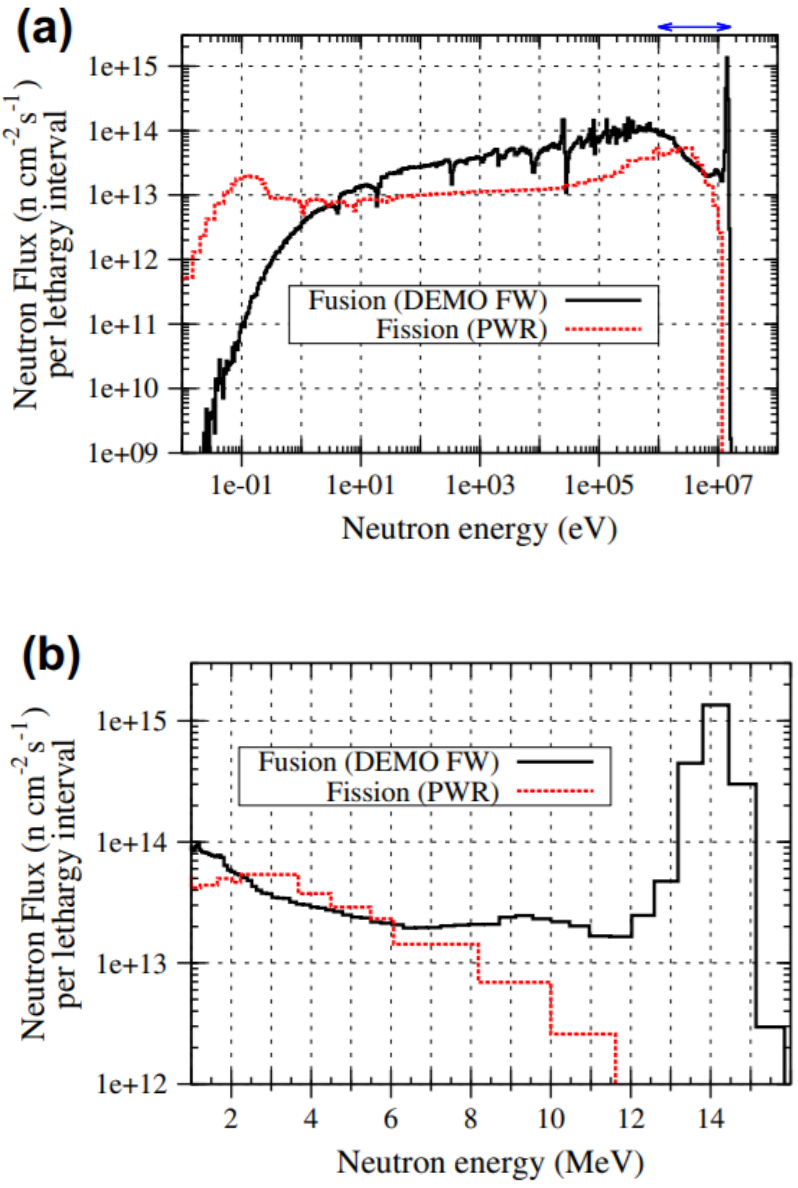

Figure 2.4: Comparison of the neutron fluxes and energies in both nuclear fusion and fission reactors experienced by the first wall, where a) shows the full energy range of the spectra and b) shows the spectra above 1 MeV [35].

Due to the higher energy neutron bombardment, there are both elastic and inelastic collisions of high energy ions and neutrons. Resultant from the inelastic collisions, due to the neutron absorption cross-section, the high energy fusion neutrons can be absorbed by common elements used in current nuclear fission materials, resulting in their transmutation to radionuclides [36]. Tungsten transmutes to rhenium, tantalum, and osmium, this is discussed in Section 2.2.3.4.

On the other hand, elastic collisions result in high recoil energy reaction products and lead to the production of displacement damage, this is discussed in greater depth in Section 2.1. At elevated temperatures, the mobile primary defects (interstitials and vacancies) can recombine or form dislocation loops, vacancy clusters, and large voids.

2.2.2.1 Crystal Structure

Whilst alloying additions can have a strong effect on the radiation damage tolerance of a material, in this work we have chosen to focus primarily on medium atomic weight BCC metals (V, Fe) as a large component of the plasma-facing material as they are often found to have a greater radiation damage resistance compared to FCC elements. Under similar irradiation conditions, void concentration in BCC metals (Fe, V, Nb, Ta, Mo, W) can be up to 2 orders of magnitude higher than in FCC metals. The voids produced in BCC materials are also considerably smaller and more-finely dispersed. However, in BCC materials the smaller voids have an increased probability of undergoing vacancy-interstitial recombination during ion implantation [37]. This results in BCC materials displaying reduced irradiation-induced structural changes compared to FCC structures; it is for these reasons that BCC materials are favoured for fusion environments.

2.2.2.2. Ductile to Brittle Transition Temperature

A compromise between ductility and strength is often required for structural materials, as high strength materials (e.g., BCC metals) tend to have lower ductility. Work hardening, where materials become stronger when plastically deformed, is favourable in materials exposed to external stresses. Additionally, these high strength BCC metals have a characteristic ductile to brittle transition temperature, where there is a lower temperature region (where the material will undergo brittle fracture) clearly distinct from a higher temperature ductile fracture regime. At temperatures lower than the DBTT, the material tends to become overly brittle and so for structural purposes it is important to ensure the operational temperature of the component is above the DBTT. Furthermore, an increase in DBTT and decrease in ductility is also resultant from an increase in lattice defects upon neutron irradiation which causes irradiation-induced hardening.

Table 2.1 summaries the radiation damage processes and the irradiation conditions (with respect to melting temperature T_m) required for them to occur.

Table 2.1: Physical and mechanical effects of radiation damage [37].

Radiation Damage Process	Irradiation Conditions (Temperature)	Irradiation Conditions (dpa)
Radiation Hardening	<0.4 T_m	>0.1
Fracture and Embrittlement	<0.4 T_m	>0.1
Radiation-Induced Precipitation and Segregation	0.3-0.6 T_m	>10
Volumetric Swelling from Void Formation	0.3-0.6 T_m	>10
Helium Embrittlement	>0.5 T_m	>10

At lower temperatures, the yield stress is increased, and the ductility of the alloy is reduced due to the defects inhibiting the gliding of dislocations. This low temperature radiation hardening results in the change of the ductile to brittle transition temperature to below where the yield stress exceeds the cleavage stress. This increase in DBTT of tungsten to above room temperature upon irradiation has the adverse resultant effect of narrowing the operational temperature window [38].

2.2.2.3. Transmutations and Fuel Retention

At higher temperatures, transmutation of elements resulting in the generation of helium, which is insoluble in metals, causes precipitation of bubbles which can grow to form cavities. Helium is formed because alpha particles are produced during transmutation reactions. Formation of these void-like cavities causes embrittlement in the materials and formation at grain boundaries results in intergranular failures. At lower temperatures hydrogen embrittlement can

also be expected due to the poor solubility of hydrogen isotopes in metals and therefore is important for the consideration of fuel implantation at the material surface. Trapping of tritium at damage sites, formed from inherent lattice imperfections from ions and neutron irradiation causes tritium retention in the material where the amount retained is a function of temperature. In the fusion environment there is also a high flux of deuterium which can cause damage to the PFMs [39]. Trapping of deuterium in the surface of the PFM can cause unwanted localised stress which culminates in blistering, exfoliation, and cracking. Blisters on the surface of the component can further disrupt the diffusion of deuterium [40].

2.2.2.4. Sputtering

PFMs are subjected to high fluxes of neutrons and other charged particles resulting in sputtering of atoms from the surface of the material. The process of sputtering occurs when material particles are ejected from the PFC due to the neutron and ion bombardment of the target. Sputtered impurity atoms from the PFM can then be transported to the plasma and subsequently ionised and redeposited on further components of the vacuum vessel [41]. When the plasma is exposed to impurities from the armour material, this can cause rapid unwanted cooling and decreases plasma stability which in turn can reduce the effectiveness of the D-T reaction [42]. Materials composed of high atomic number (Z) elements (such as tungsten) increases this radiative loss of the plasma and so poses an unfavourable impact on the plasma performance. To minimise these effects, low Z elements are typically favoured (C, Be) for the wall, however, high Z elements (W) are often preferred due to their high temperature capabilities. Therefore, if high Z elements are used in the PFM, it is imperative that these higher Z ions are not allowed to contaminate the plasma.

2.2.2.5. Erosion

A further detrimental effect includes erosion of the PFM where enhanced material erosion is due to the heat and plasma loading on the neutron-damaged armour material. This can cause significant material loss, where the erosion yield is measured by weight-loss of the material and has detrimental effects including a reduction of the lifetime of the component. The generation of dust, as a direct consequence of the erosion mechanism, is a process that requires further research [43]. The erosion/redeposition process is governed by several material characteristics: material mass, binding energy, and atomic density [41]. Figure 2.5 shows the self-sputtering yields for some refractory elements computed by ITMC-DYN

calculations [44]. From these simulations, molybdenum and tungsten have almost identical sputtering yields, whilst zirconium and niobium have similar yields.

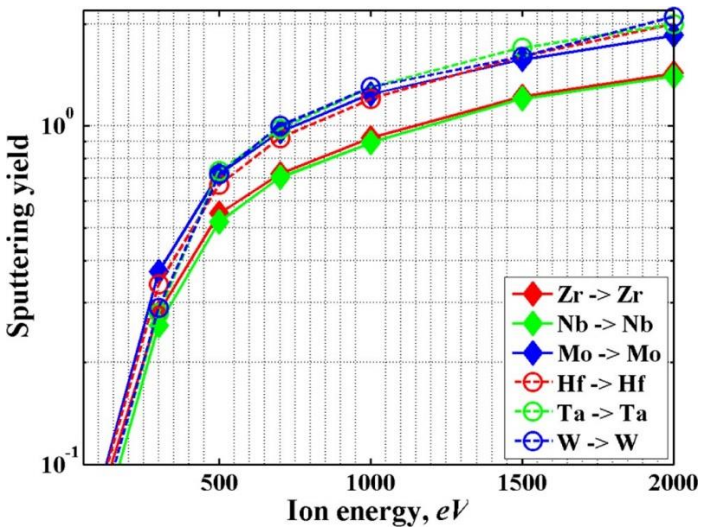

Figure 2.5: Self-sputtering comparison of candidate high Z materials [44].

However, it is important to note that further studies of material's sputtering yields in D-T and He rich environments and for mixed-material surfaces are required to make a reasonable assessment of PFMs. The erosion rate of the first wall of ITER is expected to be on the order of approximately 0.05 mm/burn-year [45] and so therefore is a need to investigate advanced wall materials that can further reduce the sputtering yields.

2.2.3. Reduced Activation Elements

Unlike the processes that occur in nuclear fission reactors, the products of the nuclear fusion reaction (3.5 MeV helium nuclei and 14.1 MeV neutrons) are not inherently radioactive. However, the 14 MeV neutrons can activate the armour material and generate radioactive and volatile materials by the end of the first wall operational lifetime, thus resulting in long-lived radioactivity [46]. Due to the neutron absorption cross-section, the high energy fusion neutrons can be absorbed by common elements used in current nuclear fission materials, resulting in their transmutation to radionuclides, some of which have long half-lives, beyond the reduced activation criterion of 100 years.

When considering the primary components of materials for the first wall it is important to choose a chemical composition that is based on low activation elements, limiting higher activation elements, to reduce the overall radioactivity of the material. Figure 2.6 shows that the degree of activation an element possesses can be defined by the calculated radioactivity of a selected element with regards to time spent exposed to a typical neutron spectrum.

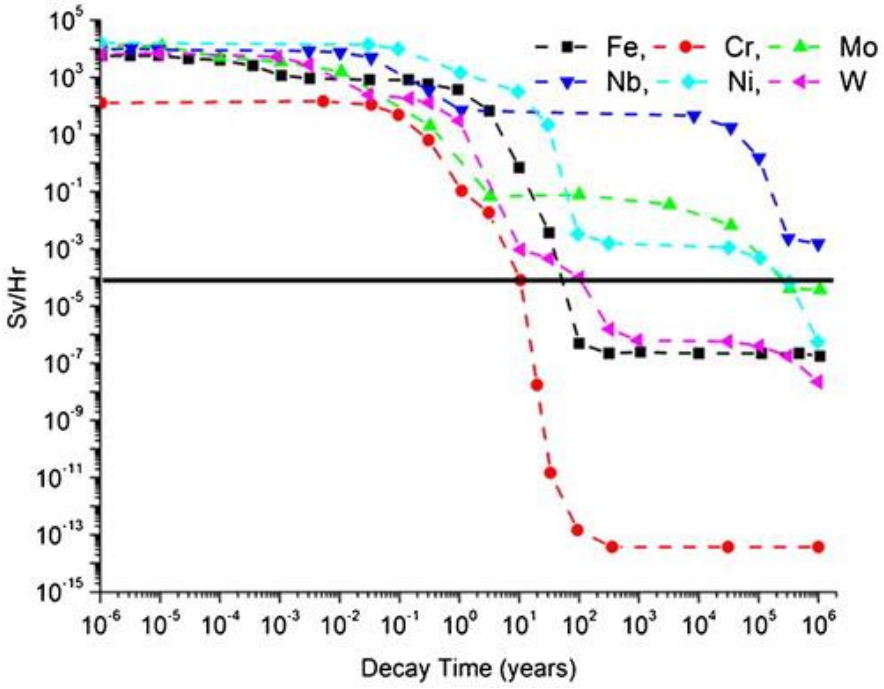

Figure 2.6: The level of irradiation for several elements as a function of time after removal from a 3.6 GW fusion reactor following 5 years of irradiation. The black line represents the ITER limit for hands-on maintenance [46].

From this figure many commonly used elements, such as Ni, Nb, and Mo, do not meet the desired low-level radioactivity in sufficient enough time to be considered safe to use as plasma-facing materials. For example, upon neutron irradiation nickel transmutes to ^{60}Co which leads to a highly activated product ($_{t1/2}^{60}Co = 5.27\ year$) [47].

To avoid disposal challenges, the exclusion of elements such as Ni, Cu, Co, Nb, and Mo is imperative for the reduced activation requirement and therefore conventional high-temperature alloys are rendered unsuitable for structural fusion components. For example, austenitic stainless steels were previously studied to investigate the effects of a helium environment within a fission reactor. However, due to the inclusion of Nb (and other higher activation elements), these steels display long-lived radioactivity [48]. Therefore, any

candidate PFM must comprise elements that are reduced activation so that if they do undergo neutron induced transmutation, they, or any other radionuclides along the decay chain, will not be radioactive for longer than 100 years following neutron irradiation.

It is expected that there will be a legislative criterion that all materials used in a commercial fusion reactor need to be recycled or disposed of safely (without the need for special consideration) when plant decommissioning occurs. Furthermore, any material used in the construction of a commercial fusion reactor must not be sufficiently radioactive (i.e., activity must be below safe handling limits) approximately 100 years after removal of the material from the reactor, to avoid the need to dispose of high-level radioactive waste [41]. Specialised handling of highly active and toxic nuclear waste possesses challenges including separation of materials that constitute the structural and functional components of the first wall, and construction of recycling plants including development of new recycling techniques for novel waste streams not produced by nuclear fission. Figure 2.7 summarises the length of time it would take each element of the periodic table to become low level waste.

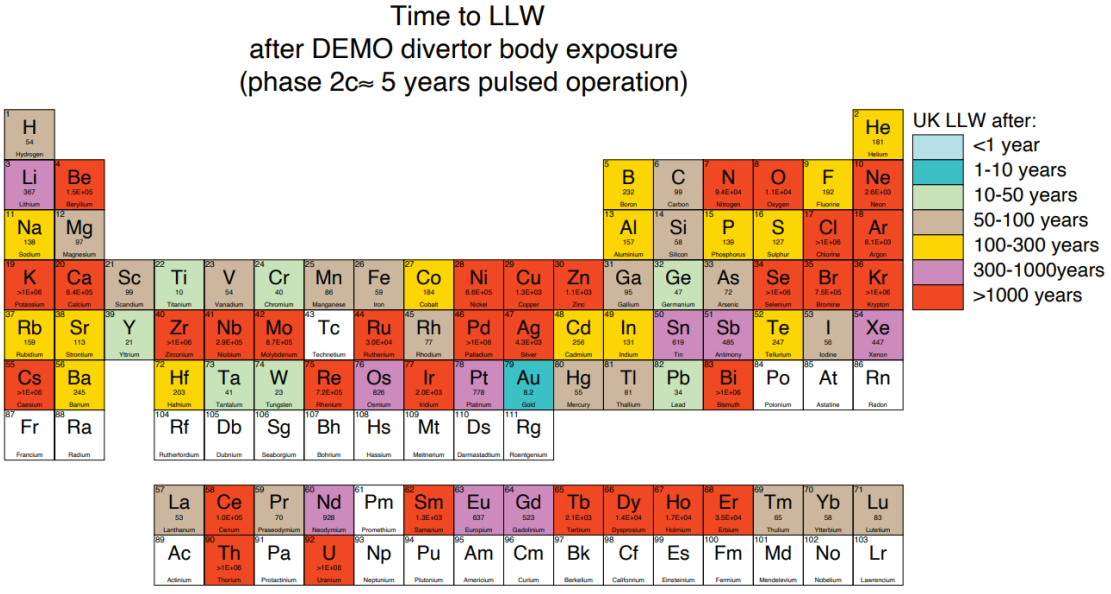

Figure 2.7: Periodic table of elements coloured to represent the amount of time it would take for the element to become low level waste (LLW) after operational exposure to the predicted neutron flux conditions in the DEMO reactor [49].

From this figure it can be determined that the transition and refractory elements with low durations until LLW (10-100 years) include Ti, V, Cr, Mn, Fe, Ta, and W. The neutron activation rates severely limit the choice of materials and so promotes the need for further novel material

research on low activation elements. Additionally, the use of high-performance reduced activation PFMs must provide enough protection to the reactor by being tolerant to damage from the extreme fusion core environment.

2.2.3 First Wall Plasma-Facing Material Candidates

From the previous section it is apparent that the development of suitable plasma-facing materials (PFMs) is a key obstacle that still needs to be resolved for fusion to be an attainable source of energy. This section evaluates some potential candidate plasma-facing materials as well as a structural material for the first wall. The following low activation materials are current candidates for PFMs due to their thermomechanical properties and their radiation damage resistance. For the first wall and divertor components, the most promising materials include the following: carbon composites, beryllium, and tungsten.

2.2.3.1. Carbon-Fibre Composites (CFCs)

Carbon, in the form of fine-grained graphite or carbon-fibre composite, is one material option considered as a potential PFM due to its low activation, low Z, good thermal conductivity, and its ability to not melt (melting point of around 3652 °C). The low Z feature of carbon means it has a negligible impact on the plasma performance. However, some negative attributes of carbon including high tritium retention and strong erosion (resulting from physical and chemical sputtering and radiation-enhanced sublimation) have been observed [51].

Tritium from the plasma is easily retained in the porous and granular structure of graphite and CFCs. High impact energies cause these atoms to be very mobile in the material's surface creating clusters of low electronic density, such as voids and dislocations. Detrimental results from tritium depth profiles reveal that a surprisingly large amount of tritium (up to 61%) had diffused deep into the bulk of the woven CFC sheets [52]. Upon irradiation graphite is known to increase in density from the bombardment of neutrons causing swelling and displacing carbon atoms into the interstitial positions within the carbon layers. The closing of some of the pores and increase of point defects within graphite causes a loss of thermal conductivity whilst the swelling leads to internal fractures and loss of strength. Additionally, the accumulation of vacancies serves as further traps for hydrogen and tritium.

Chemical sputtering, resulting in the formation of hydrocarbons from carbon and the fusion fuel, is the main mechanism responsible for material erosion of the JET main chamber wall and the outer divertor surfaces, as previously discussed in Section 2.2.2.5. For carbon components, the presence of hydrogen isotopes in the plasma can promote the formation of mobile hydrocarbons which migrate to cooler surfaces of the divertor. Here they are co-deposited to form flaky layers which can detach to produce the problematic dust. Additionally, the removal of the valuable tritium fuel from the plasma in this mechanism is also concerning for the long-term viability of the fusion reaction. Roth et al [39] concluded that for low Z elements (like carbon materials) the steady state erosion is too high when considering the required lifetime of PFCs. Furthermore, the accumulation of tritium inventory is dominated for low Z elements where the high erosion yield is co-deposition with eroded material and will be an important issue that needs to be resolved for future fusion reactors.

Graphite was initially used in the first wall of JET in 1983 and in the National Spherical Torus Experiment (NSTX) in 1999. The first wall graphite and CFC tiles were coated with evaporated beryllium layers to mitigate the chemical erosion of the carbon surfaces. Carbon tiles were also used in the 2007-2009 JET first wall [53]. Studies of the extent of tritium retention in the first wall by Tanabe et al [54] concluded that high energy tritium is implanted deeply into the first wall surface, but the long-term inventory could be decreased at higher surface temperatures. For this reason, due to the unacceptable level of tritium inventory, first wall components made from purely carbon are unlikely to be suitable for future fusion reactors.

2.2.3.2. Beryllium (Be)

Beryllium (Be) has been proposed for use as a PFM coating in ITER, as it is a low Z element that has an affinity to trap unwanted oxygen impurities present in the plasma. However, for future water-cooled reactors, due to the risk of evolution of hydrogen gas igniting an explosion, beryllium is unlikely to be used. The low melting temperature (1287 °C), high erosion rates [55], and associated toxicity has also rendered beryllium somewhat unfavourable and suggests it can only be used as a material for the first wall. Like graphite, beryllium also has a large trapping rate for tritium which impacts the D-T reaction rate.

At room temperature, beryllium is intrinsically brittle due to its hexagonal crystal structure which is resistant to slip and poor alloying properties. However, at elevated temperatures (400

°C) it becomes moderately ductile and furthermore, beryllium sheet has also shown some ductility at room temperature. This is because of texturing on anisotropy, where ingot sheet has a moderate amount of texture which has higher elongation in the two in-plane directions and more ductility in the out of plane direction than sheet made using powder metallurgy methods [56]. The anisotropy of the HCP structure also adversely affects beryllium's mechanical properties through the development of intergranular thermal strains which leads to distortion and loss of creep strength and cracking. The thermal conductivity of beryllium (and tungsten) is also comparable to that of graphite. Unlike graphite however, beryllium does not produce chemical sputtering when in contact with the plasma fuel so has an advantage over CFC materials.

Beryllium was previously used to reline the main chamber walls and divertor of JET in 2009 due to its non-reactivity with hydrogen and oxygen getter capabilities. Since then, beryllium has been shown to degrade by radiation damage due to transmutation and displacement damage [57]. The main damage mechanism of beryllium results from helium and tritium, whether it is transmuted in the material or implanted from the plasma. As with the carbon candidate, for low Z materials the build-up of tritium inventory is dominated by co-deposition. Helium gas concentrates into bubbles at the surface of beryllium where these bubbles can then agglomerate and grow until they form blisters on the surface and are exfoliated off. Studies have shown that the dust particulates could be in the range of 10 nm to 100 µm [51] where particle sizes as small as 30 µm has the potential to disrupt plasma discharges. Bubbles are also likely to form at vacancy sites – at grain boundaries and dislocations and where their size is a function of temperature. Only at higher temperatures (near the melting temperature of beryllium) can these helium bubbles be released from the material. The first wall of ITER will be mainly composed of actively cooled beryllium and the divertor tiles made from CFC. Experimental research by Brezinsek et al [58] found that the long-term deuterium retention of CFC tiles was lower than walls made from pure carbon by more than a factor of 10. This is speculated to result from the formation of the protective beryllium carbide layer which could prevent diffusion of deuterium, thus reducing retention. However, due to the higher plasma fluences of ITER, alongside beryllium's reasonably high sputtering yield can lead to elevated net erosion rates [59]. Other components of the divertor will be made from tungsten due to its low sputtering yield, discussed in Section 2.2.3.3. As previously discussed, the aim of ITER is to use materials already tested in previous tokamak devices to demonstrate breakeven. Only

future commercial fusion reactors are expected to be constructed from novel, reduced activation materials.

Irradiation of beryllium with high energy neutrons produces small dislocation loops at low temperatures [60]. The neutron irradiation damage of beryllium anneals out at elevated temperatures due to its tolerable thermal conductivity, however this is overshadowed by the deterioration caused by helium bubbles. Between 325-600 °C the helium bubbles tend to form at grain boundaries, which renders beryllium inefficient as a PFM above 800 °C [57]. Therefore, it cannot be used in areas such as the divertor due to excessive embrittlement at high temperatures. The toxicity of beryllium and its associated oxides has been well known, and special safety requirements must be fulfilled during operation in a fusion reactor [26].

2.2.3.3. Tungsten (W)

The desirable physical properties of tungsten: high melting temperature (3422 °C), high thermal conductivity, high resistance to sputtering and erosion, and low coefficient of thermal expansion make pure tungsten and tungsten alloys a premier frontrunner as a PFM both for the divertor and first wall. However, there are some concerns with irradiation-induced microstructural changes (and effects of helium, deuterium, and tritium) and resulting component performance. Additionally, tungsten is a high Z material, therefore plasma performance is impaired due to strong radiative losses.

The ASDEX Upgrade (Axially Symmetric Divertor Experiment) is a divertor tokamak that went into operation in 1991 and is currently Germany's second largest fusion experimental reactor. The installation of tungsten tiles on the inner wall of ASDEX- Upgrade tokamak (as well as being used for the divertor JET and ITER) has yielded encouraging results, yet these systems have not encompassed a cooling system [61]. Graphite tiles plasma sprayed with tungsten were used for the divertor for the ASDEX divertor. Proven to have high erosion resistance and low tritium (and deuterium) retention, the brittleness of pure tungsten at higher temperatures can be overcome by alloying with enough tantalum to retain some of the advantages. Pure tungsten has a high DBTT (of 200-400 °C), low temperature embrittlement (recrystallization temperature of around 1200 °C), and has a very high hardness – these properties limit the operational temperature of the components from 800 °C to 1200 °C. The relatively high DBTT of tungsten is expected to further increase under neutron irradiation (up to 800-1000 °C)

resulting in tungsten remaining brittle at high temperatures which can prompt premature failure in-service.

As such, it is of great importance to improve the ductility of tungsten either by employing the use of alloying pure tungsten or by nanostructuring. For the latter, Nygren [62] designed a ‘monoblock’ of pure tungsten with a segmented surface to relieve thermal stressing and reduce the brittle fracture of a tungsten divertor PFM. In terms of geometry the lining of the main chamber must be typically thin enough to limit the increase in surface temperature of the components. Additionally, it would also reduce neutron absorption and allow a high tritium breeding ratio.

There are few studies detailing neutron irradiated tungsten alloys; research has shown that hydrogen isotopes are trapped in the surface of tungsten and contained in the vacancies and voids of the material. Helium implantation into tungsten at high temperatures (above 720 °C) results in tendril-like formations which extrude from the surface of tungsten [63]. Termed ‘nano-fuzz’ this structure was first reported in 2006 by Takamura [64]. At temperatures over 1720 °C, crystallisation of tungsten occurs, and micron sized helium bubbles are observed to be connected to the surface. As discussed with erosion of carbon and beryllium, these helium structures are significantly brittle and so cause concerns regarding further erosion and dust formation. Additionally, helium bubbles in tungsten act as trapping sites for hydrogen isotopes therefore reducing the diffusion of hydrogen [65].

Comparable to tungsten, molybdenum possesses favourable properties for a PFM and has been researched as a coating for tungsten-rhenium based divertor components. Unfortunately, molybdenum is not a low activation element so would require high level waste disposal. Naturally occurring molybdenum consists of isotopes which will transmute in a neutron environment to a radioisotope (Mo-99) and this decays to Tc-99 [66]. It is possible to remove the unstable isotopes of molybdenum through isotopic tailoring; however, this process has a significant cost attached.

Tungsten has a lower erosion rate than that of lower Z materials like beryllium and CFCs. The disadvantage for using a high Z material is the lower tolerable impurity concentration within the plasma [43]. When using layers of different materials (beryllium and carbon in JET; and tungsten, beryllium, and carbon in ITER) it is unknown how the materials will interact with one another. For example, it is hypothesised that carbon ions can increase the sputtering of

tungsten which will be disadvantageous in a reactor. For tungsten and beryllium, beryllium rich tungsten alloys, which have a much lower melting temperature, may be formed.

Tungsten freely transmutes into Re and then Os, and by the end of service pure tungsten becomes 91W-6Re-3Os (at%). This alloy composition nears the highly brittle sigma phase which is unfavourable for use as an armour material. Figure 2.8 shows the transmutations of tungsten as a first wall material of a DEMO reactor [67].

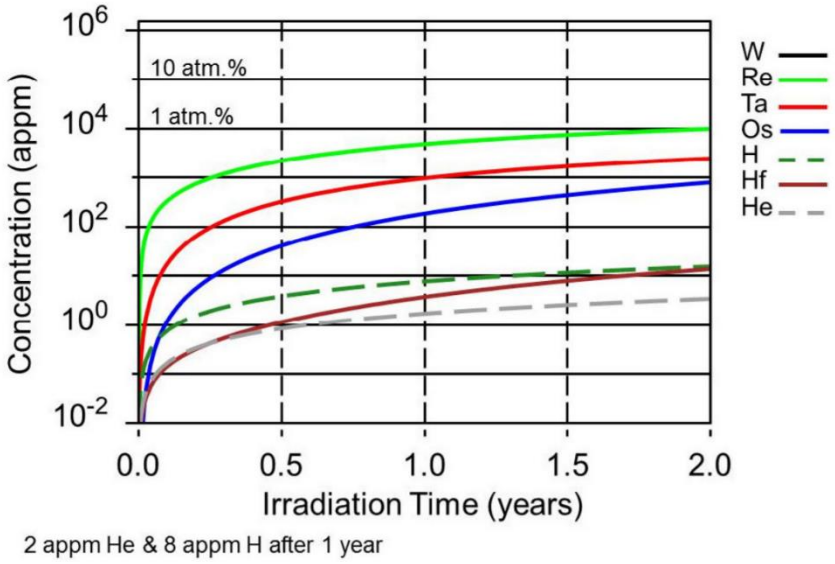

Figure 2.8: The transmutation products of tungsten as a material for the first wall of a DEMO reactor [67].

Whilst pure tungsten has a low room temperature ductility and low recrystallization temperature, alloying with rhenium can improve some of these ailments. Further, rhenium is a transmutation product of tungsten after neutron irradiation. Neutron irradiated tungsten-rhenium alloys show the formation of a platelet-like precipitation phase and rhenium clusters causing significant hardening and an increase in the DBTT of the material. Irradiation-induced defects and clusters cause hardening and brittleness which affects the mechanical properties of the material, this influences the lifetime and reliability of the PFM [68]. For tungsten rhenium alloys at temperatures above 420 °C, suppression of void formation is attributed to the binding of rhenium to self-interstitial atoms, thus decreasing their mobility [69]. For W-10%Re, the transmutation to rhenium can decrease the thermal conductivity of the material compared to pure tungsten (which possesses a favourable high thermal conductivity). This inhibits the heat exhaust properties, and this can subsequently limit the power handling capabilities of the divertor [70].

2.2.4. Summary

This section extensively outlined the effects of the harsh environment on the plasma-facing components in a magnetically confined tokamak reactor. The presence of high energy neutron (14.1 MeV) irradiation, high neutron fluxes (around 8.25 x 10^{14} n $cm^{-2}s^{-1}$ in the first 2 cm of the first wall armour) and high heat fluxes (up to 20 MWm^{-2}) are key constraints for these materials. Beryllium, carbon materials, and tungsten alloys have all been considered for use as plasma-facing materials. It is necessary to reduce the potential activation of elements in the first wall material to ensure all materials are suitable for recycling in non-active landfills (approximately 100 years after removal from the reactor). Due to this strict criterion, the available elements for use as first wall materials are severely limited; this ultimately affects the design of novel potential alloys as PFM. Finally, an assessment of the most promising material candidates was given. A general overview of the destructive processes which occur in materials upon irradiation and the resultant effects on the component performance was also assessed.

Firstly, elements with small atomic masses and neutron-absorption cross sections were considered; both carbon and beryllium have been tested in tokamak reactors. It was found that the significant erosion of carbon materials was somewhat offset by the addition of beryllium. However, excessive helium embrittlement at low temperatures and the associated toxicity of beryllium are deemed unfavourable for the performance of a PFC.

Tungsten was shown to be a promising material for use in plasma-facing components mostly owing to its high melting point, low tritium retention, and high resistance to sputtering and erosion. On the other hand, there are some associated risks with using tungsten as a divertor component which stem from its inherent brittleness and occurrence of nanostructured fuzz-type structure after irradiation in helium plasma. Under neutron irradiation, the DBTT further increases for pure tungsten which renders tungsten incredibly brittle and can induce component failure in-service. Promising studies have shown benefits of alloying tungsten with its transmutation product – rhenium, where room temperature ductility is improved. However, a reduction in thermal conductivity for tungsten-rhenium alloys subsequently limits the power handling capabilities of the divertor component.

The clear limitations of the performance of the discussed materials therefore highlight a need for enhanced materials that can withstand the high operating temperatures and extensive neutron bombardment. It is at the forefront of this research to investigate low activation

refractory alloy compositions to improve on the disadvantages of current potential plasma-facing materials and ultimately for the prospect of commercial fusion power.

Chapter 2.3: High Entropy Alloys

This chapter introduces and explores the new class of materials - High Entropy Alloys (HEAs) from their conception in 2004 to their intriguing core effects and exceptional properties. A summary of some of the design processes, including modelling approaches and empirical parameters, and notable developments of these alloys is included in this section. A review of the fabrication and thermal stability of HEAs in literature is undertaken and critically evaluated. Finally, an assessment is made for the suitability of refractory-based high entropy alloys (RHEAs) for the potential use as first-wall materials in future advanced nuclear reactors.

Related terms include compositionally complex alloys, single-phase concentrated alloys

2.3.1 Discovery and Background

From the earliest records of metalworking gold in the Paleolithic period, humankind has always strived to make better materials for the challenges of daily life. The Bronze Age defined a crucial development in materials when improved weapons and tools were fashioned from bronze – copper alloyed with a small amount of tin. The tradition of alloying has driven a technological development for better materials with enhanced mechanical performance.

After only 16 years of study, high entropy alloys (HEAs) are regarded as one of the newest areas of materials science and yet have received considerable attention. Typically, they are formed of five or more principal metallic elements where each constituent has a concentration between 5-35 at%. In comparison, conventional engineering alloys usually consist of one or two major elements. Conventional metallic alloys can also be multicomponent in nature. However, the conventional alloy strategy consists of selecting a primary component with preferred elemental properties with the small amount of alloying additions to enhance desirable secondary properties. For example, stainless steel is based primarily on iron for formability with small additions of chromium for corrosion resistance [71].

The original concept of HEAs arose in 2004 from the simultaneous investigation of multicomponent alloys by two separate research groups. Cantor et al [72] fabricated an alloy containing 20 different elements (Mn, Cr, Fe, Co, Ni, Cu, Ag, W, Mo, Nb, Al, Cd, Sn, Pb, Bi, Zn, Ge, Si, Sb, and Mg) in equal quantity (5 at%) to demonstrate that multicomponent systems can exhibit fewer phases than anticipated when using the Gibbs phase rule (defined below). A single-phase FCC solid solution was observed for an equimolar composition of FeCrMnNiCo

termed ‘Cantor’s Alloy’ and is now regarded as a widely studied HEA system, by becoming the benchmark for fundamental studies of compositionally complex alloys. Many fundamental experiments investigate additions and substitutions of various elements to Cantor’s alloy including CoCrFeMnNi-C [73], $Al_xCoCrCuFeNi$ [74], and CoCrFeNi [75].

A few months prior to this research, Yeh et al [76] evaluated the multicomponent systems $CuCoNiCrAl_xFe$ and found that for the alloys where x=0 to x=0.5 a simple FCC structure was observed in the X-ray diffraction patterns. From this work, the four ‘core effects’ of HEAs were proposed and have since been critically assessed:

1) The high configurational entropy of HEA stabilises the formation of a solid solution in relation to unfavourable intermetallic compounds due to the lower Gibbs free energy (this is discussed in more depth in the following section).
2) Anomalously slow diffusion in HEAs compared to conventional alloys is due to difficulty of atoms moving through a solid solution where the atoms in the lattice have varying sizes. Sluggish diffusion has been used to explain exceptional mechanical performance such as high temperature strength [77]. There have been many studies investigating the cause of the apparent slow diffusion. Tsai et al [78] suggested that the activation energy in HEAs is higher than conventional alloys due to the lattice sites containing varying elements. Experimental measurements of tracer diffusion coefficients of Ni in CoCrFeNi and CoCrFeMnNi by Vaidya et al [79] revealed that the diffusion rates decrease with increasing elemental components. However, conflicting results by Zhang et al [80] reveal that the diffusion kinetics of Ni in AlCrFeCoNi and CoCrMnFeNi are not particularly sluggish.
3) Lattice distortion arises in HEAs due to the many kinds of elements with differing atomic sizes. Experimental studies using high-resolution transmission electron microscopy, X-ray diffraction, and neutron scattering have investigated the true extent of lattice distortion in HEAs compared to conventional materials [81], [76], [82]. Lattice strain, proportional to the misfit parameter of the atomic size difference, is hypothesised to increase the hardness, however this resultant effect may also derive from the solid solution strengthening of the alloy. Quantitative analysis has suggested that the lattice distortion of HEAs may not be exceptional large compared to typical metallic alloys [83], [84].
4) The cocktail effect was first proposed by Ranganathan [85] and was used to describe the subsequent effect of the chemical complexity of HEAs. When designing the alloy

compositions of HEAs with material properties, the cocktail effect advises for the inclusion of elements with these inherent properties. For example, addition of refractory elements (i.e., Nb) will likely increase the high temperature capabilities of the alloy [86], due to an increase in alloy melting point, as dictated by the rule of mixtures.

It was in this seminal work that the term 'high entropy alloy' was coined. According to the first core effect, this is due to the consequential increase in the entropy of mixing of the alloy expected to occur from the rise of elements in higher proportions. This phenomenon was theorised to stabilise single-phase microstructures and inhibit the formation of intermetallic compounds despite when the Gibbs phase rule predicts more equilibrium phases to form:

$$P = C + 1 - F \qquad \textit{Equation 2.2}$$

where P is the number of phases, C is the number of components, and F is the degrees of freedom. For example, using the Gibbs phase rule, Cantor's alloy ($Fe_{0.2}Cr_{0.2}Mn_{0.2}Ni_{0.2}Co_{0.2}$) which has five components, is expected to form five phases (P=5). Whilst this alloy experimentally displayed a single FCC phase it should be noted that the Gibbs phase rule predicts the maximum number of phases which can form in a system. Therefore, under manufacturing processes where high temperature or transition phases may form and non-equilibrium cooling cannot be controlled, there is likely to be further phases that may be retained.

Yeh et al [76] stipulated that the mitigation of brittle, unwanted intermetallic compounds and the stability of solid solutions can be predicted using Boltzmann's hypothesis on the relationship between entropy and the complexity of the system:

$$\Delta S_{conf} = -k \ln w = R \ln n \qquad \textit{Equation 2.3}$$

where ΔS_{conf} is the configurational entropy change per mole during the formation of a solid solution from *n* elements of an equimolar system. *k* is Boltzmann's constant and w is the number of ways of mixing, and R is the gas constant (8.314 J/Kmole). For an equimolar alloy, the entropy of the system increases as the number of components increase (e.g., alloys with 3, 5, 6, and 9 elements are 1.1R, 1.61R, 1.79R, and 2.2R respectively).

However, solely maximising the configurational entropy is not sufficient in stabilising the formation of a simple solid solution in equiatomic multicomponent alloys. As explained further in Chapter 3: VCrMoWCo, a systematic study by Otto et al [87] of the substitution of similar

elements in Cantor's quinary alloy (Ti for Co, Mo/V for Cr, V for Fe, and Cu for Ni) resulted in multiphase microstructures. This demonstrated that by retaining the entropy of mixing for the new substitutional alloys the consequential loss of the single-phase solid solution of Cantor's alloy indicated that configurational entropy was not a dominant factor in phase stability. In this work, when considering an appropriate substituent element, the Hume-Rothery rules were taken into consideration to account for complete solubility for the replacement component. These rules state that for the formation of solid solution between a binary pair (between a solute atom and a solvent atom) both elements must have similar crystal structures, similar valence electron concentrations (VEC), low atomic radii differences (<15%), and similar electronegativities (which tend to be dissimilar in intermetallic compounds) [88].

When the Gibbs free energy of a system is minimised the likelihood of the formation of a stable solid solution is increased. The Gibbs free energy of a system, which includes the configuration of entropy term, is given by:

$$\Delta G_{mix} = \Delta H_{mix} - T\Delta S_{mix} \qquad \textit{Equation 2.4}$$

where ΔH_{mix} is the enthalpy of mixing of the components, T is the temperature of the system and ΔS_{mix} is the mixing entropy of the components in the system. Otto et al [87] stated that the minimisation of the total ΔG_{mix} (taking into consideration both the enthalpy and entropy contributions of the system) was important in predicting the stability of the solid solution of the alloy system. Making the Gibbs free energy term as negative as possible drives the system towards a solid solution by making this microstructure the most energetically preferential. For the maximisation of the negative magnitude of ΔG_{mix} (and for where T is a constant), the ΔS_{mix} term must be sufficiently large enough to outweigh the ΔH_{mix} term. The entropy of mixing can be maximised by increasing the number of components in the system and by increasing the concentration of these elements to form equimolar systems. At decreasing temperatures, the overall contribution of the entropy term for the stabilisation of a solid solution is decreased. This allows for the precipitation of intermetallic phases when HEAs are annealed at intermediate-low temperatures. Stepanov et al [89] observed the precipitation of an HCP phase (enriched with Hf and Ta) after annealing the homogenised single BCC phase refractory $Hf_{20}Nb_{20}Ta_{20}Ti_{20}Zr_{20}$ at 600 °C and 800 °C. Minimisation of the enthalpy of mixing term is discussed in the next section. These terms have been identified as parameters that can be used to assess the likelihood of an alloy composition forming a stable solid solution.

2.3.2 Empirical Parameters for the Prediction of Solid Solution Formation

Since the inception of high entropy alloys, the motivation for designing alloy compositions that stabilise single-phase microstructures has subsequently been the primary aim of the research. Rather than employing a trial-and-error approach, it was necessary to establish phase formation rules to navigate high entropy alloy design. This early literature on isolating single-phase microstructures for HEAs has incentivised the attempts to quantify parameters that drive the formation of simple solid solutions. Due to the broad definition of high entropy alloys, encompassing equimolar and near equimolar (5-35 at%) compositions for elements across the whole periodic table, the unexplored compositional space results in a vast number of possible HEAs. Therefore, much research has focussed on the prediction of stable solid solution formation for the development of high entropy alloys. As mentioned previously, the empirical Hume-Rothery rules and thermodynamic parameters in the Gibbs free energy equation were criteria used to assess the formation of a solid solution for multicomponent alloys.

Zhang et al [90] identified three empirical parameters that quantify the probability of forming a simple single-phase solid solution in a HEA: 1) the atomic size difference (derived from the Hume-Rothery rules), 2) the enthalpy of mixing, and 3) the entropy of mixing (from the Gibbs free energy equation) given by the equations below:

$$\delta = \sqrt{\sum_{i=1}^{N} c_i \left(1 - \frac{r_i}{\bar{r}}\right)^2} \qquad \textit{Equation 2.5}$$

Where δ is the atomic size difference, N is the number of components, c_i is the atomic percentage of the *i*th component and $\bar{r} = (\sum_{i=1}^{n} c_i r_i)$ where r_i is the atomic radius.

$$\Delta H_{mix} = \sum_{i=1}^{n} \Omega_{ij} c_i c_j \qquad \textit{Equation 2.6}$$

Where $\Omega_{ij} = 4\Delta H_{AB}^{mix}$.

$$\Delta S_{mix} = -R \sum_{i=1}^{N} c_i \ln c_i \qquad \textit{Equation 2.7}$$

Where R is the gas constant, 8.314 x 10^3 $Nmkmol^{-1}K^{-1}$. In order to define boundaries of values for each of these parameters within which solid solutions form, Zhang et al [90] plotted data of fabricated HEAs in terms of their empirical parameters.

Figure 2.9 shows the relationship between the atomic size difference and the enthalpy of mixing terms for a variety of reported alloys. The marked boundaries highlight alloys that exhibit specific phases, for example the areas denoted S represents the alloys that form solid solutions. The area B2 refers to Mg and Cu-based multicomponent bulk metallic glasses and the B1 zone contains the other kinds of bulk metallic glasses (e.g., Zr-based bulk metallic glasses) [90].

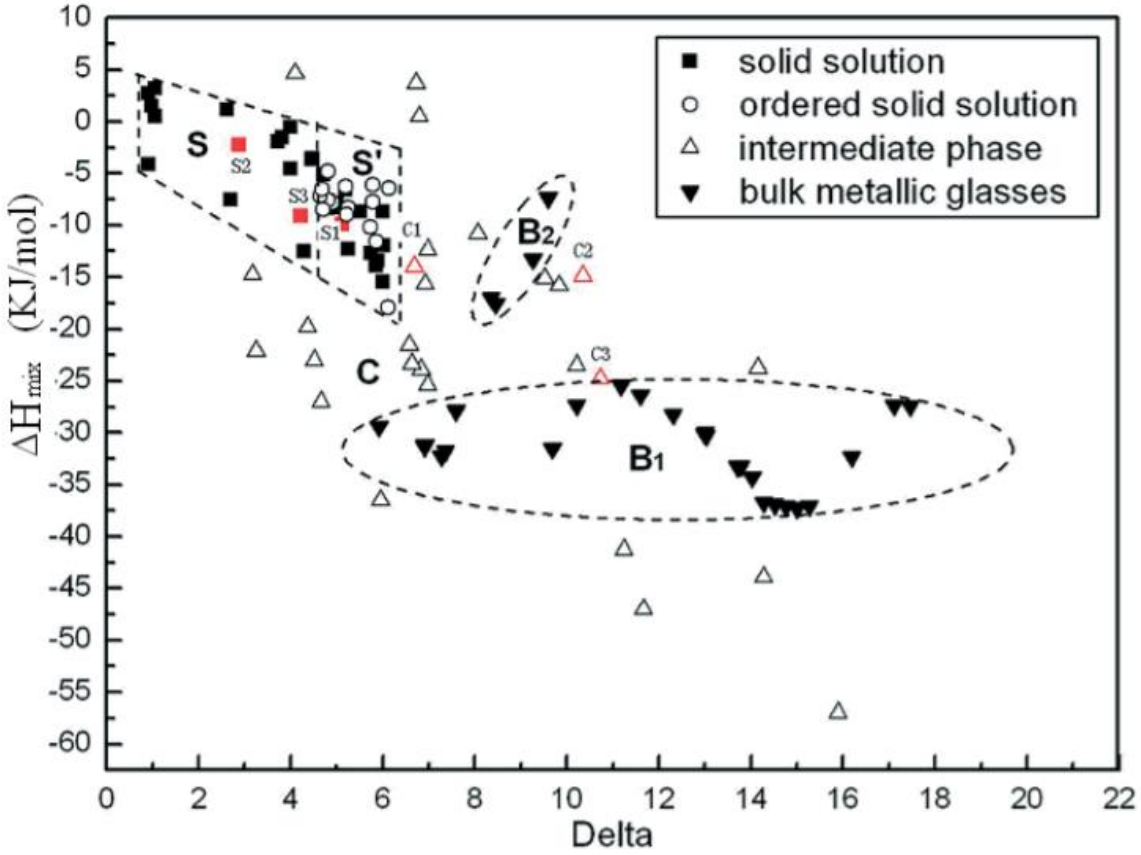

Figure 2.9: Relationship between the atomic size difference parameter and enthalpy of mixing terms for typical multicomponent alloys [90].

The regions of space where alloys were identified by experimental characterisation to have solid solutions were depicted. The areas highlighted were quantified and it was suggested for novel alloys that had an atomic size difference and enthalpy of mixing values that lie in this

boundary were also likely to form a solid solution. Zhang et al [90] suggested that for an alloy that has an atomic size difference between 0<δ<4.6 and an enthalpy of mixing defined by $-15 < \Delta H_{mix} < 5$. From this figure it can be deduced that it is favourable for an alloy to have a relatively small atomic size difference to stabilise the formation of a solid solution. And this may be due to the constituent elements being similar in size to allow for the substitution of elements in the crystal lattice without imposing increased strain. Furthermore, this rule coincides with the Hume-Rothery rules which suggest that the difference in atomic size between the solute and solvent be less than 15 %.

For an alloy with a small δ, this corresponds with a ΔH_{mix} which is small and negative for the formation of a solid solution. At greater δ, this relates to a relatively smaller and more negative value of ΔH_{mix} most likely to compensate for the increased difference in atomic size between the elements. This increases the probability of forming an ordered solid solution, as shown in Figure 2.1, due to the greater atomic size mismatch encouraging more ordering to adapt to the lattice strain and the more negative enthalpy of mixing promoting the precipitation of intermetallic compounds.

Very negative values of ΔH_{mix} relates to extremely favourable mixing of elements which is expected to encourage the formation of intermetallic compounds which is generally discouraged when designing a single-phase alloy. Overly positive values of ΔH_{mix} for a binary constituent pair results in elemental segregation and overly negative values promotes favourable mixing. Values for ΔH_{mix} can be determined using Miedema's model [91]. Whilst ΔH_{mix} gives the overall value of the tendency for the elements to form a solid solution, the ΔH_{mix} of each of the binary pairs of the constituents of the system may be more valuable in determining the stability of the solid solution. Overly negative ΔH_{mix} for some of the constituents will result in intermetallic formation for these elements, but if there are some positive ΔH_{mix} values for the residual constituents, the overall ΔH_{mix} will be near-zero, predicting the alloy to form a solid solution rather than exhibit elemental segregation and intermetallic formation. This demonstrates a flaw in the sole reliance on ΔH_{mix} and so further parameters must be taken into consideration.

Additional parameters, also modulated from the Hume-Rothery rules, were later suggested by Guo and Liu [92] included: electronegativity difference and valence electron concentration (VEC) given below:

$$\Delta\chi = \sqrt{\sum_{i=1}^{N} c_i(\chi_i - \bar{\chi})^2} \qquad \textit{Equation 2.8}$$

Where $\bar{\chi} = \sum_{i=1}^{n} c_i\chi_i$ and χ_i is the Pauling electronegativity for the *i*th component.

$$VEC = \sum_{i=1}^{n} c_i(VEC)_i \qquad \textit{Equation 2.9}$$

These findings were based on the experimental observation of around twenty multicomponent systems. It was found that for the stable formation of an FCC solid solution VEC≥8 and for a BCC solid solution VEC≤6.87. For VEC values in between these boundaries, a mixture of FCC and BCC phases exist. Several refractory high entropy alloys (RHEAs) have shown the VEC rule to be effective in predicting the appropriate crystal structure: ReMoTaW [93], MoNbHfZrTi [94], and HfNbTaTiVZr [95]. Additionally, Tsai et al [96] suggested a new boundary of the VEC rule for the formation of the sigma phase in high entropy alloys. They stipulated that for 6.88 ≤ VEC ≤ 7.84 a sigma phase would form; this range also overlaps with the range required for the formation of the duplex FCC and BCC phases proposed by Guo and Liu [97]. However, the legitimacy of the VEC rule for fabricated HEAs has been drawn into question. Due to the inherent nature of HEAs, there are various alloy systems with very differing material properties, the VEC rules are not consistent across all HEAs. Kube et al [98] used combinatorial methods to fabricate and characterise 2478 quinary alloys based on transition metals and aluminium. They utilised the phase selection rules of crystal structure of the solid solution formed for the alloys. In general, they found that the VEC thresholds would vary depending on the alloy compositions and the constituent elements; aluminium destabilises the FCC phase due to its large atomic size and 3d elements change from BCC to FCC. Kube et al [98] concluded that with increasing atomic size difference the formation of a BCC structure was preferred over an FCC structure.

Further research by Yang and Zhang [99] defined a new parameter Ω to separate the solid solution and intermetallic phase fields. They proposed Ω, which contains both ΔH_{mix} and ΔS_{mix} parameters used to estimate solid solution formation in a multicomponent alloy and is given by:

$$\Omega = \frac{T_m \Delta S_{mix}}{\Delta H_{mix}} \qquad \textit{Equation 2.10}$$

Where the melting temperature T_m can be calculated using the rule of mixtures approach using:

$$T_m = \sum_{i=1}^{n} c_i (T_m)_i \qquad \textit{Equation 2.11}$$

For values Ω≥1.1 and δ≤3.6 %, the multicomponent alloy is expected for form a stabilised solid solution. When Ω≥1 the mixing entropy has a greater influence than the mixing enthalpy at the melting temperature of the alloy. This is postulated to increase the stability of the formation of a solid solution. Most intermetallic alloys have δ≤6.6 % and 1≤Ω≤2. When Ω>10 the likelihood of intermetallic formation is reduced and only a solid solution is predicted to form.

The empirical phase selection rules detailed above (Equations 4-10) have been cited in numerous studies for HEA systems containing a wide variety of elements [100], [101], [102], [103], [104]. However, their accuracy in determining single-phase solid solutions has also been contended. Pickering and Jones [105] have considered that the basis of the suggested boundaries rely on experimental characterisation of fabricated alloys rather than being founded on fundamental principles. Furthermore, the numerous systems designed utilising some (or all) of these parameters are often characterised in their as-cast state which often represent the unstable state of the alloy due to processing conditions therefore equilibrium phases are not taken into consideration. For this reason, homogenisation treatments are necessary to assess the thermal stability of HEAs and whether the solid solution will transform into multiple phases or precipitate any intermetallic compounds.

Wang et al [106] reviewed the temperature dependence on the phase selection rules. They evaluated the criteria for the prediction of equilibrium solid solutions and intermetallic phases in homogenised and low temperature annealed HEAs; only a limited number of studies were available at the time (around 27 alloys). For lower temperature annealed solid solution HEAs the authors advocated for the reduction of criteria boundaries due to the reduced configurational entropy effect. For these alloys treated at temperatures between $0.5<T/T_m<0.9$ the formation of a sold solution shrinks to $\Delta H_{mix} \geq -7.5$ kJ/mol and $\delta<3.3$ %. This is compared to the as-cast alloys which had $\Delta H_{mix} \geq -12.5$ kJ/mol and $\delta<6.2$ %. Troparevsky et al [107] suggested a novel model which utilised the high-throughput computation of the enthalpies of formation of binary compounds. They compared solid solution and intermetallic contributions to the Gibbs free energy, where $\Delta H_{mix} = 0$ and $\Delta S_{IM} = 0$. Their results were consistent with Wang et al [106], where there was prediction of a NiAl intermetallic phase for AlCrFeCoNiCu, despite earlier predictions of a stable solid solution. However, critical analysis from Senkov and Miracle [108] highlighted the assumptions made for the Troparevsky et al [107] model

may result in accurate predictions, noting that many of the non-equiatomic HEAs containing elements deemed unfavourable were able to retain a solid solution structure after annealing.

Table 2.2 shows a summary of the reported parameter boundaries required for the formation of a solid solution. These thresholds are referred to in the alloy design section of this thesis: Chapter 5: Design of Novel Low Activation High Entropy Alloys.

Reference	**Atomic size difference** δ	**Enthalpy of mixing (KJmol^{-1})**	**Entropy of mixing (KJmol^{-1})**	**VEC**
Zhang et al (2008)	$0<\delta<4.6$	$-15< \Delta H_{mix} < 5$		
Guo and Liu (2011)	δ<8.5 %	$-22< \Delta H_{mix} < 7$	$11< \Delta S_{mix}<19.5$	VEC>8 FCC VEC<6.87 BCC
Zhang (2014)	δ<4.0 %	$-10< \Delta H_{mix} < 5$	$\Delta S_{mix}>13.38$	
Wang et al (2014)	δ<6.6 %	$-15< \Delta H_{mix} < 5$		VEC>7.84 FCC VEC<6.87 BCC

2.3.3 Thermal Stability

Many high entropy alloys, including refractory based HEAs, are produced using conventional casting processes, including vacuum arc melting and induction melting. Potential issues that may arise from fabrication of refractory based HEAs may be derived from their weak liquidity, castability, and homogeneity [109]. Thermal stability and the resultant effects on the microstructure of an alloy are of great importance for components subjected to long in service durations, particularly at elevated temperatures. Whilst many HEA investigations have deduced the effects of alloying, phase transformations, and material properties, there have been fewer reports of annealing behaviour of different HEA systems [110]. Lin et al [111]

performed serial ageing heat treatments for $Cu_{0.5}CoCrFeNi$ for the investigation of temperature on the microstructure and to qualitatively assess the extent of precipitation. The alloy was held for 24 hours at 350 °C, 500 °C, 650 °C, 800 °C, 950 °C, 1100 °C, 1250 °C, and 1350 °C. Whilst the as-cast $Cu_{0.5}CoCrFeNi$ displayed a single FCC phase, under different aging treatments a further Cr-rich phase and a Cu-rich phase precipitated. Lin et al [111] noted that the extent of the previous phases depended on the temperature of the heat treatment.

However, there are fewer reports of systematic thermal studies of RHEAs including successful homogenisation heat treatments. As detailed by Gorr et al [112], complete homogenisation can be characterised by the reduction of dendrite volume fraction and elemental microsegregation from the as-cast condition. Increasing the annealing time and annealing temperature encourages the likelihood for successful homogenisation however, this is not always viable due to the experimental facilities available (this is discussed in more depth in Chapter 6: Experimental Assessment of Novel High Entropy Alloys). On the other hand, lower and intermediate temperature annealing treatments can assist the formation of new phases [113]. In the study by Gorr et al [112], the BCC refractory HEA $W_{20}Mo_{20}Cr_{20}Ti_{20}Al_{20}$ was investigated for its microstructural evolution during heat treatment. During heat treatment at high temperatures the alloy tended to form a single BCC phase. It was concluded that the enthalpy of mixing between the binary elemental pairs was one of the driving forces propelling the elemental microsegregation observed in the dendritic arms and interdendritic regions. Secondly, thermodynamic calculations of each constituent of the alloy were calculated to demonstrate the effect of elemental concentration on the activity of the other elements. For $W_{20}Mo_{20}Cr_{20}Ti_{20}Al_{20}$, whilst Cr and W have no effect on the other constituents, increasing concentration of Mo in the dendrites decreases the W content in this region.

Ageing at lower and intermediate temperatures is greatly affected by the temperature and duration of the heat treatment. For example, the phase stability of the RHEA $Al_{0.5}NbTa_{0.8}Ti_{1.5}V_{0.2}Zr$ was investigated by Soni et al [114] from temperatures between 600-1000 °C. The initial two BCC phases transformed into a BCC matrix with dispersed B2 precipitates at 600 °C for 120 hours. An additional phase, Al,Zr-rich HCP intermetallic precipitation was formed in the BCC matrix after ageing at 800 °C and 1000 °C for 20 hours.

However, the as-cast dendritic microstructure is not necessarily always detrimental to the material's properties. Initial work by Senkov et al. [115] for the single-phase near-equiatomic alloys WNbMoTa and WNbMoTaV was the first report of an RHEAs. Both alloys in the as-cast

condition demonstrated a typical dendritic microstructure with microsegregation of elements. For the quaternary alloy, Ta was uniformly distributed with enrichment of W in the dendrite arms and depletion of Mo and Nb. In the quinternary alloy, Ta and Mo were both uniformly distributed with enrichment of W in the dendrite arms and depletion of Nb and V. Despite this, both alloys have a single-phase BCC structure and displayed exceptional microhardness (greater than any individual constituent) suggesting strengthening of a solid solution-like mechanism.

RHEAs have garnered considerable interest primarily due to the retention of strength at higher temperatures beyond 1000 °C and up to 1600 °C [116]. Metallic alloys are known to suffer from a decrease in strength from temperatures between $0.6T_m$-T_m (where T_m is the melting point of the alloy). Increasing the T_m of an alloy will therefore increase the operating temperature; this is increasingly important for alloys with nuclear applications. Refractory metals typically have higher melting points and so can be considered for applications where high activation Ni-based superalloys are deemed unsuitable. Furthermore, many of the reported RHEAs are single-phase BCC due to the high solubility among refractory elements. Several studies have demonstrated several RHEAs which have good yield strength at elevated temperatures including: CrTaVW [117], HfMoNbTiZr [92], and MoNbTaTiVW [118]. However, it is difficult to obtain a high temperature strength whilst maintaining low temperature ductility [104]. Precipitation strengthening is an important strengthening mechanism at increasing temperatures due to the loss of strength from the solid solution. The Laves phase is observed frequently in fabricated HEAs, this is discussed in more depth in Chapter 5: Design of Novel Low Activation High Entropy Alloys. The Laves phase can both enhance strength, as it is often a hard intermetallic, but can also reduce ductility. For example, for the alloy $HfMo_{0.5}NbTiV_{0.5}Si_x$ (where x=0-0.7) the formation of a $(Hf, Nb, Ti)_5Si_3$ silicide, resulted in an increase in the strength of the alloy increased at 1200 °C, however, this was at the cost of a certain degree of ductility [119].

2.3.4. CALPHAD Approach

The novel high entropy alloy approach has revived the alloy development process and garnered interest in the tailoring of alloy compositions for obtaining enhanced material properties. The immense number of possible HEA compositions (taking into consideration the large number of elements in the periodic table) not only provides an opportunity to develop a number of interesting systems but also proves to be a formidable challenge [120]. From the

previous section discussing the thermal stability of HEAs, it has proven vital to establish reliable thermodynamic data, including phase transformations and phase stability at higher temperatures, for these novel complex systems. The HEA empirical parameters for the assessment of the formation of a stable solid solution, discussed in Section 2.3.2, suffers from some limitations, especially when considering thermal effects. This has provided motivation to explore computational modelling methods for the screening of potential HEA systems.

The CALPHAD approach (CALCulation of PHAse Diagrams) has been widely used for a variety of conventional and novel alloys for the prediction of equilibrium phases as a function of temperature [121]. The CALPHAD method approximates the Gibbs energy function of each phase as a function of temperature, derived mainly from experimentally known binary and ternary systems, to determine the likely stable phases. The effects of both enthalpy and entropy are taken into consideration as well as thermodynamic physical contributions. A full description of CALPHAD and the computational tool which employs this method – Thermo-Calc, is given in Chapter 3: Experimental Methods.

The validity of the Thermo-Calc predictions rely on the suitability of the thermodynamic database used for the calculation. Most of the available databases were designed for conventional alloys therefore their extrapolation into multicomponent space may be somewhat unreliable in some respects. For example, the thermodynamic databases are often based around one element (i.e., the nickel-based database is TCNI8) and so the corresponding assessed binary and ternary phase diagrams are mainly for the systems based around the major component and may not be complete across the whole system for all of the constituents in the alloy. Additionally, some phases which may be seen as irrelevant to the targeted type of alloys are deliberately excluded [122]. Despite this there have been many reported cases where the experimental identification of phases observed in fabricated high entropy alloys demonstrated good agreement with the Thermo-Calc predictions [123], [124], [125]. All of these considerations are addressed in further detail in Chapter 5: Design of Novel High Entropy Alloys where justifications for the use of the SSOL4 and TCHEA4 databases are made.

2.3.5. Summary

In this section, the recent conception of high entropy alloys was introduced and their properties and possible compositions with low activation elements was discussed. A review of the design processes was undertaken to underpin important empirical parameters for the prediction of a single BCC structure solid solution. Defining the thresholds for these parameters is important in the assessment of a stable solid solution for a given alloy composition.

An assessment of the literature of the investigation of the thermal stability of high entropy systems was also given in this section. Few studies have systematically investigated compositions over a wider range of temperatures to determine the extent of precipitation at lower temperatures and the effect of high temperature homogenisation on elemental microsegregation. This is especially important for components used in high temperature and demanding environments, like those used for plasma-facing components; microstructural changes in-service can have detrimental effects on the mechanical performance of the alloy resulting in failure.

The accurate prediction of the equilibrium phases of HEAs using the CALPHAD approach was also given. Thermo-Calc simulations for conventional alloys are the default for the thermodynamic databases, however, the recent interest in compositionally complex alloys, that veer away from currently assessed compositional space, has prompted the development of better CALPHAD predictions.

The design of HEA systems with favourable elements that encourage high temperature capabilities, and the assessment of these two alloy design strategies for the prediction of a stable BCC solid with minimisation of intermetallic formation is undertaken in this work. The development of low activation refractory high entropy alloys for potential as plasma-facing materials is therefore at the forefront of this research.

2.4. High Entropy Alloys: Irradiation

Conventionally, HEAs have been proposed for use as structural applications due to their superior mechanical properties including high strength and ductility, high temperature and corrosion resistance; it is these properties which make HEAs attractive for applications within extreme environments. Recent research has focused on their functional properties, namely the microstructural response of HEAs to radiation damage. The potential of adopting these alloys as first wall materials in a fusion reactor is currently unknown and will depend on the material's irradiation performance. Experimental examination of phase stability, void swelling, irradiation-induced defect formation, and changes in mechanical properties all contribute toward the understanding of the irradiation response of HEAs.

The ability of varying alloying elements and composition in a wide compositional space allows for tailoring of mechanical and alloy properties. Design of radiation tolerant materials has often been achieved by the inclusion of high-density defect sinks in the form of secondary phases or grain boundaries to reduce residual defects brought on by irradiation. This approach has been successfully shown by oxide-dispersion strengthened (ODS) steels [126] and nano-crystalline alloys [127]. Yet, stability of these structures at elevated temperatures in an extreme radiation environment has shown to be problematic. Application of these mechanisms, especially under high-dose irradiation at high temperatures, in multicomponent alloys is of strong scientific interest in determining the radiation damage tolerance of materials for nuclear components.

Single-phase concentrated solid-solution alloys (SP-CSAs), including HEAs, are composed of multiple elements at high concentrations. They form solid solution alloys with simple crystal structures of either face-centered cubic (FCC), body-centered cubic (BCC), or hexagonal close-packed (HCP). Solid solutions with multicomponent elements have been found to be more stable at elevated temperatures than intermetallic compounds due to their large entropies of mixing. This implies that high-entropy materials may have better phase stability against irradiation damage than intermetallic compounds [128]. Much of the research that has investigated the irradiation properties of HEAs has focussed on alloy compositions based around the well-known Cantor's alloy (CrMnFeCoNi). As such there are only a few studies which review low activation alloys relevant for nuclear fusion applications.

2.4.1. Chemical Disorder - Defect and Void Behaviour

As previously discussed, lattice disorder is one of the four core effects and is primarily responsible for the mechanical behaviours of HEAs [129]. The high degree of disorder arises from the random arrangement of different elements in high concentrations with greater atomic size difference resulting in high atomic-level distortion. The chemical disorder is proposed to affect the defect properties of multicomponent alloys causing them to behave differently to pure metals. Upon irradiation HEAs have exhibited enhanced defect recombination, in comparison to pure metals (for example nickel) due to the mobility of point defects and mutual interaction between vacancies and interstitials [130]. Bonny et al [131] have demonstrated that defect migration is hindered by the increased likelihood of being trapped in the deeper energy valleys of multicomponent alloys from the random arrangement of atoms.

The intrinsic energy transport properties are an important factor when considering the irradiation damage resistance of alloys. For multicomponent alloys, on the electronic level, the *disordered state and compositional complexities result in strong electron scattering which decreases the mean free path of electrons, phonons, and magnons. In the early stages of irradiation this may affect the defect formation, defect interaction, and interstitial-vacancy recombination. Reducing the electron mean free path can also provoke a prolonged thermal spike which promotes recovery in the very early stages of irradiation [132]. This effect is amplified with an increasing number of components in the alloy. *Ab initio* calculations, of both NiCo and NiFe, have demonstrated that the low electronic and thermal conductivity of CSAs, when exposed to energetic ion bombardment, will cause extended localised melting resulting in defect recombination. This contrasts with pure Ni which showed no melting or discernible damage. Thermal spikes caused by particle irradiation prompt local melting and recrystallization which also reduces defects.

Elemental species themselves have distinctive defect formation and migration energies and preferential binding of binaries has the ability of impacting defects. For example, Ni-Ni and Ni-Fe interstitial dumbbells have lower formation energies than Fe-Fe dumbbells in Ni-Fe alloys [133]. The consequence of uneven energy distribution is that elements with lower vacancy migration energies (i.e., chromium and iron) are more likely to exchange positions with vacancies thus creating radiation-induced segregation (RIS) where depletion of the element will occur around defect sinks such as grain boundaries, secondary phases, dislocations, and voids. Advanced transmission electron microscopy (TEM) with electron energy loss

spectroscopy (EELS) has detailed the suppression of RIS in more compositionally complex alloys and attributed this behaviour to sluggish atomic diffusion [134]. SP-CSAs including NiFe, NiCoFe, NiCoFeCr, and NiCoFeCrMn underwent irradiation with 3 MeV Ni^{2+} ions at 773 K and with distribution of the segregated elements (Cr, Fe, Mn) forming in a 'disk' around the entire defect clusters. The small scale of the clusters and limited amount of RIS may make characterisation more difficult. However, these studies are important as elemental segregation around defect clusters will affect the deformity upon continued irradiation and can result in degradation of mechanical properties of the material (i.e., radiation-induced hardening and embrittlement).

It is important to note that the elements included in these studies (nickel, cobalt, iron) are classed as high activation elements and primarily form single phase FCC alloys which are unsuitable for fusion applications. Additionally, defect density and size strongly depend on each elemental species of the alloy as well as the number of elements in the alloy [135]. This highlights the need for further research on the irradiation effects of low activation alloys. Selecting elements which can inhibit defect motion will reduce the amount of defect clusters within the material; this effect can be beneficial when engineering alloys for radiation resistant components.

Density functional theory (DFT) simulations of the predictions for the defect energies in different multicomponent alloys have been reported and compared to pure metals (most notably nickel). Lower formation energies of interstitials in CSAs suggests higher stability compared to pure nickel. Additionally, the higher energy barriers of interstitials results in suppression of interstitial diffusion and the lower energy barriers of vacancies means vacancy diffusion is increased and so is the dominant defect mechanism. This has been proven experimentally in CSAs, by high resolution TEM characterization and molecular dynamic (MD) simulations, where the kinetics of formation is greatly reduced and so promotes the formation of smaller and more frequent clusters compared to pure nickel where larger defect clusters have been observed [136]. MD simulations have reported that smaller vacancy clusters diffuse faster whilst larger clusters are more immobile and the diffusion modes in multicomponent alloys differ from pure nickel, thus clarifying the void swelling resistance of CSAs [137]. Results from MD simulations have shown that the reduction of dislocation mobility is the main reason for smaller defect clusters.

Another mechanism shown to degrade materials upon irradiation is void swelling. Suppression of void formation and swelling in the same suite of SP-CSAs mentioned previously [137] has been credited to the sessile interstitial loops acting as stable sinks which absorb vacancies, thus decreasing the overall vacancy concentration in the matrix. Defect mobility by thermal activation also plays an integral role in void formation. Vacancies that escape the cascade formation range are able to agglomerate into voids in the deeper region of the material; in the near-surface region they are likely to be annihilated by interstitials. In pure nickel, interstitials have a faster migration than vacancies and so more vacancies form larger and more considerable voids at elevated temperatures. In the more compositionally complex alloys much smaller voids were observed in the extended regions due to the lower concentration of surviving vacancies which can migrate from the surface.

Much like the defect formation and migration energies, the amount of void swelling in an alloy has been shown to be dependent on the alloying element (as well as compositional complexity). Jin et al [138] has reported the irradiation-induced swelling and hardening of pure nickel and nickel-containing CSAs at 773 K. Previous void swelling studies have failed to account for complicated phase evolutions and microstructural changes between the studied alloys that could also affect density changes within the material. The alloys investigated in this study all have simple FCC structures and so any material properties can be correlated to compositional effects. All the equiatomic FCC CSAs have lower swelling than pure nickel and irradiation resistance was improved by alloying elements iron and manganese, whereas cobalt and chromium slightly increase swelling. The most compositionally complex alloy, FeCoCrMnNi, was shown to have volume swelling 30 times lower than that of pure nickel from 5 MeV Ni^{2+} ion implantation.

Whilst previous studies have focused on the void swelling resistance of HEAs due to defect recombination, few have demonstrated the role of dislocations on irradiation-induced void formation. Lu et al [139] have systematically investigated the single-phase FCC HEA NiCoFeCrPd with and without high density dislocations and then irradiated with 3 MeV Ni^{2+} ions at 853 K. Most CSAs studied for their radiation damage have been annealed prior to ion implantation so that they possess a single phase with coarse grains and low density of dislocations. This means effects of defects prior to ion implantation, including dislocations, precipitations, etc., are not normally considered in these studies, even though they may be introduced during the fabrication and processing of components. Lu et al [139] concluded that having a high irradiation temperature, introducing enough dislocations into a material prior to

irradiation, and a smooth dose rate were all conditions which would encourage a 'sink-dominated regime'. This means that there is a lack of interstitials available for recombination which results in void nucleation and growth, ergo void swelling may be amplified by an increase in dislocation density.

Diffusion of defect clusters has a direct impact on the microstructural evolution of multicomponent alloys; aggregation of interstitials form dislocation loops whilst vacancies form stacking fault tetrahedra (SFT). Irradiation studies of a single-phase FCC multicomponent alloy, FeNiMnCr, with 3 or 5.8 Ni ions at temperatures up to 973 K (0.03 to 10 dpa) revealed that the main microstructural feature at all temperatures was high density small dislocation loops [140]. No voids were observed, and this alloy showed superior radiation resistance compared to conventional single phase FeCrNi austenitic alloys. With increasing dosage, the dislocation loops increased in density until saturation at 0.1 dpa. At room temperature, the hardness of FeNiMnCr increased rapidly with increasing dpa; irradiation-induced dislocation loops are important components for irradiation hardening and embrittlement and can be one of the hardening sources for both HEAs and conventional materials [141]. Consistent with these results, El-Atwani et al [142] reported for the BCC refractory HEA (RHEA) W-Cr-V-Ta that even after 3 MeV Cu ions at 773 K after 8 dpa there were no observable radiation-induced dislocation loops and this suppression of defect production resulted in negligible irradiation hardening at these high temperatures.

It is widely accepted that for conventional materials, irradiation at higher temperatures will cause dislocation loop size to increase and density to decrease due to loop growth and coalescence. Lu et al [139] reported that ion implantation of multicomponent alloys at higher temperatures caused loop density increases whilst loop growth is delayed with increasing composition complexity. Surprisingly, for NiCoFeCrPd irradiated at 873 K, the loop density size is much smaller and density much higher than NiCoFeCrMn at 773 K. This has been attributed to a stronger local lattice distortion pinning irradiation-induced defects [139].

Defect recombination is an integral process in the suppression of defect evolution in multicomponent alloys, as mentioned previously. MD calculations have tracked the damage process in CSAs using the accumulated cascade simulations. In the case of NiFe and NiCoCr, the amount of defect build-up in these CSAs is considerably lower than pure nickel, however the initial amount of defect accumulation is much greater at the beginning of irradiation [143]. This can be attributed to the slowing of point defect motion which reduces defect

recombination. Also, dislocation mobility is lower and onset stress is higher in the more complex alloys. As the initial ballistic stage is similar for pure metals and complex alloys, this shows that one of the factors limiting the damage accumulation is in the long-range diffusion process and defect recombination mechanisms [133].

It is postulated that the suppressed defect production in BCC multicomponent alloys, as mentioned previously [142], is resulting from increased defect recombination for the larger lattice distortion from the bcc structure. Negligible hardening post helium ion irradiation is further confirmed in another single-phase bcc CSA, $Ti_2ZrHfV_{0.5}Mo_{0.2}$ at 873 K [144], which proves promising for future nuclear components. Irradiation-induced embrittlement is a major failure mode of structural nuclear components, so minimal hardening of the material after irradiation shows great promise to the lifetime of the material. Interestingly, this was also the first reported case of irradiation-induced shrinking of the lattice parameter, where conventional materials undergo expansion of lattice parameter post-irradiation. Irradiation is speculated to relax the extreme lattice distortion, thus resulting in shrinking of the lattice parameter. The irradiation behaviour of single-phase BCC HEAs is limited and further insight in the defect energy landscape is needed to determine the mechanisms behind the excellent mechanical performance of these alloys [133].

2.4.2 Phase Stability

At elevated temperatures, phase degradation is a common phenomenon which can severely impact the mechanical properties and the change in volume of an irradiated material. Formation of undesirable intermetallic phases during service, induced by the displacement cascade from radiation, can result in a loss of both ductility and corrosion resistance. For example, exposure of pure tungsten to fusion neutrons causes the radiation-induced precipitation (RIP) of transmutation elements (TE - i.e., rhenium and osmium). Whilst a small addition of rhenium can reduce the ductile to brittle transition temperature and void size and density compared to pure tungsten, agglomeration of TEs causes the formation of sigma and chi phase precipitations [145]. This adversely affects the mechanical properties of tungsten by increasing hardening and embrittlement of the material. However, TEs may have other benefits - exposure of deuterium to irradiated W-3%Re reportedly has lower amounts of deuterium trapped at defects than pure tungsten (explained further in plasma-facing components section). Another example is shown by the self-ion implantation (to 16.6 dpa at 705 K) of HT9 steel, a 12 wt% Cr Ferritic/Martensitic (F/M) steel which is a promising candidate

for core materials used in advanced nuclear reactors and structural applications in the first wall of fusion reactors. The radiation-induced Ni/Si/Mn-rich precipitates (MSNPs) heterogeneously nucleated at dislocation sites is not observed in pristine alloy HT9. Defect sinks are known to be favourable nucleation sites due to the precipitation process releasing excess free energy. Ni and Si are known to segregate at defect sinks upon irradiation and this generates more second-phase precipitation with these solutes [146]. A follow-up study [147] to investigate the precipitation kinetics of self-ion implanted HT9 revealed discrepancies between in-situ and ex-situ experiments (while keeping temperature the same) for the same alloy. In part, suppression of formation of MSNPs in the in-situ experiments is associated with the thinness of the TEM samples acting as sinks of point defects which reduces the motion of solutes towards grain boundaries and dislocations. This has an overall effect of diminishing precipitation formation at defect sinks. In ex-situ experiments, bulk materials are irradiated and then subsequently examined in a laboratory; this only allows for the observation of a snapshot of the microstructure at a certain dose. Ion irradiation with in-situ TEM provides a powerful method to track the radiation-induced damage and thus to characterise the precipitation kinetics. This highlights that care must be taken when drawing conclusions from irradiation damage regarding different experimental methods and sample preparations, even under the same temperatures and dosages.

An in-situ TEM under high voltage electron microscopy (HVEM) observational study, of the nano-crystalline HEA CoCrCuFeNi, has documented the impact of fast electron irradiation on phase stability over a wide temperature range from 298 to 773 K for up to 40 dpa [148]. The alloy demonstrated excellent phase stability where the FCC solid solution remained as the main constituent phase, with a small amount of bcc phase forming from the FCC to BCC transition, additionally there was no further grain coarsening.

AlxCoCrFeNi (x=0.1, 0.75, and 1.5 M ratios) is another widely studied series of HEAs which have been examined for their irradiation resistance, for their phase stability upon thermal exposure. Xia et al [149], [150] and Yang et al [151] have both extensively demonstrated the phase stability of these alloys; all alloys upon irradiation have maintained their pristine phase(s): single FCC, FCC and ordered BCC (B2 phase), and B2 and disordered BCC (A2) respectively.

The alloying effect of aluminium has been shown to result in structural and mechanical evolution; increasing amounts of aluminium on $(FeCoNiCrMn)_{100-x}Al_{x(0\text{-}20\ at\%)}$ results in a phase

change from single phase FCC to a duplex FCC and BCC and then to a single phase bcc at the highest Al concentration [152]. The changes in structure correspond directly to variations in tensile properties. The single-phase FCC alloy, with the lowest aluminium amount, has the lowest strength but extended ductility due to its solid solution. The duplex alloy had a sharper increase in strength, but reduced strength, and the single-phase BCC alloy demonstrated extreme brittleness.

In response to radiation damage, the single-phase FCC $Al_{0.1}$CoCrFeNi, showed exceptional structural phase stability upon 3MeV Au ion implantation, with no precipitation being observed. Contrastingly, the other two alloys ($Al_{0.75}$, $Al_{1.5}$) displayed uniformly distributed nano-sized precipitates, but with different densities and sizes in different phases, implying a homogeneous nucleation mechanism [153]. Even at higher temperatures and dosage, 523 K to 923 K up to 43 dpa, $Al_{0.1}$CoCrFeNi exhibited excellent phase stability with no apparent phase transformation or decomposition. More in-depth analysis using atom probe tomography (APT) characterisation has detailed irradiation-induced compositional fluctuations [154]. It was revealed that an enrichment of nickel and cobalt and depletion of iron and chromium at defect clusters, including dislocation loops and long dislocations post-irradiation. The remarkable phase stability of $Al_{0.1}$CoCrFeNi HEA has been credited to its high configurational entropy and suppression of atomic diffusion, which overall reduces the thermodynamic driving force and kinetically hinders precipitation formation.

However, a study of the equiatomic HEAs CrFeCoNi, CrFeCoNiMn, and CrFeCoNiPd revealed depletion of Cr/Fe/Mn/Pd and accumulation of Co/Ni at dislocation loops post-electron irradiation to 1250 kV at 673 K [155]. For the alloys CrFeCoNiMn, and CrFeCoNiPd L10 (NiMn)-type ordering decomposition and spinodal decomposition occurred between Co/Ni and Pd driven by the positive enthalpy of mixing between the elements.

2.4.3. Summary

Understanding the importance between intrinsic properties and defect dynamics is a priority when phase engineering alloys for nuclear applications. HEAs have demonstrated exceptional tolerance to radiation damage, including void swelling resistance, delayed defect formation and increased recombination of radiation-induced vacancies and interstitials, these effects are in part credited by their intrinsic chemical disorder and lower thermal and electrical conductivities.

Some CSAs have even demonstrated exemplary phase stability and suppression of precipitation and elemental segregation around defect sinks at elevated temperatures. These promising features reveal great potential for these materials for use within extreme environments to extend the lifetime of these reactor components. There is a critical need for more advanced materials for future nuclear reactors which operate at higher temperatures and high irradiation dose environments. However, many of the systematic irradiation studies focus on suites of alloys with similar elements including nickel, cobalt, aluminium, etc. These elements are not suitable for use within the fusion reactor environment as exposure to high energy neutrons can transmute them to problematic elements which would need specialised waste management during disposal of these components. Further insight into the relationship between elemental species and the defect energy landscape is required for the successful design of low activation bcc nuclear materials.

Caution is needed when comparing radiation tolerance in different alloys as the variance in irradiation conditions and experimental methods can directly impact results. Also, the drive to obtain single phase HEAs has meant that many of the implantation studies focus on the radiation damage response of single phase (mostly FCC) alloys with very little defects from alloy processing. This does not mean though that only single-phase alloys can exhibit phase stability upon irradiation and further exploration of the intentional introduction of precipitates or strengthening second phases is required.

From the discussion above, an integral stage in the design of radiation tolerant multicomponent alloys can in part be attained by careful selection of alloying elements to promote the formation of the bcc phase. Alongside HEA thermodynamic parameter rules, and CALPHAD calculations, refinement of alloy composition can be achieved for the purpose of designing complex alloys which can mitigate the ramifications of irradiation damage.

2.5. References

[1] Was, G.S., 2016. Fundamentals of radiation materials science: metals and alloys. springer.

[2] Gilbert, M.R. and Sublet, J.C., 2011. Neutron-induced transmutation effects in W and W-alloys in a fusion environment. Nuclear Fusion, 51(4), p.043005.

[3] Rest, J., 2008. A generalized hard-sphere model for the irradiation induced viscosity of amorphous binary alloys. Computational materials science, 44(2), pp.207-217.

[4] Sekimura, N., 1996. Primary knock-on atom energy dependence of cascade damage formation and interaction. Journal of nuclear materials, 233, pp.1080-1084.

[5] Andrianova, N.N., Borisov, A.M., Kazakov, V.A., Makunin, A.V., Mashkova, E.S. and Ovchinnikov, M.A., 2020. Dynamic annealing effects under high-fluence ion irradiation of glassy carbon. Vacuum, 179, p.109469.

[6] Nordlund, K., Sand, A., Granberg, F., Zinkle, S., Stoller, R., Averback, R., Suzudo, T., Malerba, L., Banhart, F., Weber, W. and Willaime, F., 2015. Primary radiation damage in materials (Vol. 9). Report NEA/NSC/DOC.

[7] Chang, J., Cho, J.Y., Gil, C.S. and Lee, W.J., 2014. A simple method to calculate the displacement damage cross section of silicon carbide. Nuclear Engineering and Technology, 46(4), pp.475-480.

[8] Zinkle, S.J. and Busby, J.T., 2009. Structural materials for fission & fusion energy. Materials today, 12(11), pp.12-19.

[9] Braislford, A.D. and Bullough, R., 1978. Void growth and its relation to intrinsic point defect properties. Journal of Nuclear Materials, 69, pp.434-450.

[10] Was, G.S., Wharry, J.P., Frisbie, B., Wirth, B.D., Morgan, D., Tucker, J.D. and Allen, T.R., 2011. Assessment of radiation-induced segregation mechanisms in austenitic and ferritic–martensitic alloys. Journal of Nuclear Materials, 411(1-3), pp.41-50.

[11] Jiao, Z. and Was, G.S., 2011. Novel features of radiation-induced segregation and radiation-induced precipitation in austenitic stainless steels. Acta Materialia, 59(3), pp.1220-1238.

[12] Kenik, E.A. and Nastasi, M., 1989. Disordering and phase decomposition of Ni2Al3 under low-temperature electron irradiation. Ultramicroscopy, 30(1-2), pp.181-187.

[13] Zhang, Y., Zhao, S., Weber, W.J., Nordlund, K., Granberg, F. and Djurabekova, F., 2017. Atomic-level heterogeneity and defect dynamics in concentrated solid-solution alloys. Current Opinion in Solid State and Materials Science, 21(5), pp.221-237.

[14] Wharry, J.P. and Was, G.S., 2013. A systematic study of radiation-induced segregation in ferritic–martensitic alloys. Journal of nuclear materials, 442(1-3), pp.7-16.

[15] Wiedersich, H., Okamoto, P.R. and Lam, N.Q., 1979. A theory of radiation-induced segregation in concentrated alloys. Journal of Nuclear Materials, 83(1), pp.98-108.

[16] Bruemmer, S.M., Simonen, E.P., Scott, P.M., Andresen, P.L., Was, G.S. and Nelson, J.L., 1999. Radiation-induced material changes and susceptibility to intergranular failure of light-water-reactor core internals. Journal of Nuclear Materials, 274(3), pp.299-314.

[17] Was, G.S., Busby, J. and Andresen, P.L., 2006. Effect of irradiation on stress-corrosion cracking and corrosion in light water reactors. ASM Handbook, 13, pp.386-414.

[18] Lee, E.H., Maziasz, P.J. and Rowcliffe, A.F., 1980. Structure and composition of phases occurring in austenitic stainless steels in thermal and irradiation environments (No. CONF-801072--11). Oak Ridge National Lab.

[19] Server, W.L., Griesbach, T.J., Dragunov, Y. and Amaev, A., 1998. Effects of irradiation on mechanical properties (No. IWG-LMNPP--98/3).

[20] Byun, T.S., Farrell, K. and Li, M., 2008. Deformation in metals after low-temperature irradiation: Part II–Irradiation hardening, strain hardening, and stress ratios. Acta materialia, 56(5), pp.1056-1064.

[21] Matsui, H., 1999. Microstructural evolution in BCC metals and alloys under irradiation. Radiation effects and defects in solids, 148(1-4), pp.515-516.

[22] Wiffen, F.W., 1984, January. Effects of irradiation on properties of refractory alloys with emphasis on space power reactor applications. In Proc. Symp. on Refractory Alloy Technology for Space Nuclear Power Applications, CONF-8308130, Oak Ridge National Lab (pp. 252-277).

[23] Scibetta, M., Chaouadi, R. and Puzzolante, J.L., 2000. Analysis of tensile and fracture toughness results on irradiated molybdenum alloys, TZM and Mo–5% Re. Journal of nuclear materials, 283, pp.455-460.

[24] Zinkle, S.J. and Wiffen, F.W., 2004, February. Radiation effects in refractory alloys. In AIP Conference Proceedings (Vol. 699, No. 1, pp. 733-740). American Institute of Physics.

[25] Fluss, M.J., Hosemann, P. and Marian, J., 2002. Charged-Particle Irradiation for Neutron Radiation Damage Studies. Characterization of Materials, pp.1-17.

[26] Linsmeier, C., Unterberg, B., Coenen, J.W., Doerner, R.P., Greuner, H., Kreter, A., Linke, J. and Maier, H., 2017. Material testing facilities and programs for plasma-facing component testing. Nuclear Fusion, 57(9), p.092012.

[27] Knaster, J., Moeslang, A. and Muroga, T., 2016. Materials research for fusion. Nature Physics, 12(5), pp.424-434.

[28] De Vicente, S.G., Boutard, J.L., Zinkle, S.J. and Tanigawa, H., 2017. Materials testing facilities and programmes for fission and ion implantation damage. Nuclear Fusion, 57(9), p.092011.

[29] Mazey, D.J., 1990. Fundamental aspects of high-energy ion-beam simulation techniques and their relevance to fusion materials studies. Journal of nuclear materials, 174(2-3), pp.196-209.

[30] Gupta, J., Hure, J., Tanguy, B., Laffont, L., Lafont, M.C. and Andrieu, E., 2018. Characterization of ion irradiation effects on the microstructure, hardness, deformation and crack initiation behavior of austenitic stainless steel: Heavy ions vs protons. Journal of Nuclear Materials, 501, pp.45-58.

[31] Ziegler, J.F. and Biersack, J.P., 1985. The stopping and range of ions in matter. In Treatise on heavy-ion science (pp. 93-129). Springer, Boston, MA.

[32] Navinšek, B., 1976. Sputtering—Surface changes induced by ion bombardment. Progress in Surface Science, 7(2), pp.49-70.

[33] Romanelli, F., Barabaschi, P., Borba, D., Federici, G., Horton, L., Neu, R., Stork, D. and Zohm, H., 2013, June. A roadmap to the realization of fusion energy. In Proc. IEEE 25th Symp. Fusion Eng (pp. 1-4).

[34] Janeschitz, G., Boccaccini, L., Fietz, W.H., Goldacker, W., Ihli, T., Meyder, R., Moeslang, A. and Norajitra, P., 2006. Development of fusion technology for DEMO in Forschungszentrum Karlsruhe. Fusion engineering and design, 81(23-24), pp.2661-2671.

[35] Gilbert, M.R., Dudarev, S.L., Nguyen-Manh, D., Zheng, S., Packer, L.W. and Sublet, J.C., 2013. Neutron-induced dpa, transmutations, gas production, and helium embrittlement of fusion materials. Journal of Nuclear Materials, 442(1-3), pp.S755-S760.

[36] Huang, C.H., Gilbert, M.R. and Marian, J., 2018. Simulating irradiation hardening in tungsten under fast neutron irradiation including Re production by transmutation. Journal of Nuclear Materials, 499, pp.204-215.

[37] Zinkle, S.J., 2005. Fusion materials science: Overview of challenges and recent progress. Physics of Plasmas, 12(5), p.058101.

[38] Wakai, E., Jitsukawa, S., Tomita, H., Furuya, K., Sato, M., Oka, K., Tanaka, T., Takada, F., Yamamoto, T., Kato, Y. and Tayama, Y., 2005. Radiation hardening and-embrittlement due to He production in F82H steel irradiated at 250° C in JMTR. Journal of nuclear materials, 343(1-3), pp.285-296.

[39] Roth, J., Tsitrone, E., Loarte, A., Loarer, T., Counsell, G., Neu, R., Philipps, V., Brezinsek, S., Lehnen, M., Coad, P. and Grisolia, C., 2009. Recent analysis of key plasma wall interactions issues for ITER. Journal of Nuclear Materials, 390, pp.1-9.

[40] Wang, Z., Wang, J., Yuan, Y., Cheng, L., Qin, S.Y., Kreter, A. and Lu, G.H., 2019. Effects of tantalum alloying on surface morphology and deuterium retention in tungsten exposed to deuterium plasma. Journal of Nuclear Materials, 522, pp.80-85.

[41] Brooks, J.N., El-Guebaly, L., Hassanein, A. and Sizyuk, T., 2015. Plasma-facing material alternatives to tungsten. Nuclear Fusion, 55(4), p.043002.

[42] Cottrell, G.A., 2006. A survey of plasma facing materials for fusion power plants. Materials science and technology, 22(8), pp.869-880.

[43] Bolt, H., Barabash, V., Krauss, W., Linke, J., Neu, R., Suzuki, S., Yoshida, N. and Team, A.U., 2004. Materials for the plasma-facing components of fusion reactors. Journal of nuclear materials, 329, pp.66-73.

[44] Sizyuk, T. and Hassanein, A., 2010. Dynamic analysis and evolution of mixed materials bombarded with multiple ions beams. Journal of nuclear materials, 404(1), pp.60-67.

[45] Brooks, J.N., Allain, J.P. and Rognlien, T.D., 2006. Erosion/redeposition analysis of the ITER first wall with convective and non-convective plasma transport. Physics of Plasmas, 13(12), p.122502.

[46] Gorley, M.J., 2015. Critical Assessment 12: Prospects for reduced activation steel for fusion plant. Materials Science and Technology, 31(8), pp.975-980.

[47] Rubel, M., 2019. Fusion neutrons: tritium breeding and impact on wall materials and components of diagnostic systems. Journal of Fusion Energy, 38(3), pp.315-329.

[48] Klueh, R.L. and Bloom, E.E., 1985. The development of ferritic steels for fast induced-radioactivity decay for fusion reactor applications. Nuclear engineering and design. Fusion, 2(3), pp.383-389.

[49] Gilbert, M.R., Eade, T., Rey, T., Vale, R., Bachmann, C., Fischer, U. and Taylor, N.P., 2019. Waste implications from minor impurities in European DEMO materials. Nuclear Fusion, 59(7), p.076015.

[51] Federici, G., Skinner, C.H., Brooks, J.N., Coad, J.P., Grisolia, C., Haasz, A.A., Hassanein, A., Philipps, V., Pitcher, C.S., Roth, J. and Wampler, W.R., 2001. Plasma-material interactions in current tokamaks and their implications for next step fusion reactors. Nuclear Fusion, 41(12), p.1967.

[52] Bekris, N., Skinner, C.H., Berndt, U., Gentile, C.A., Glugla, M. and Schweigel, B., 2003. Tritium depth profiles in 2D and 4D CFC tiles from JET and TFTR. Journal of nuclear materials, 313, pp.501-506.

[53] Hatano, Y., Yumizuru, K., Likonen, J., Koivuranta, S., Ikonen, J. and Contributors, J.E.T., 2016. Tritium distributions on tungsten and carbon tiles used in the JET divertor. Physica Scripta, 2016(T167), p.014009.

[54] Tanabe, T., Bekris, N., Coad, P., Skinner, C.H., Glugla, M. and Miya, N., 2003. Tritium retention of plasma facing components in tokamaks. Journal of nuclear materials, 313, pp.478-490.

[55] Causey, R.A., 2002. Hydrogen isotope retention and recycling in fusion reactor plasma-facing components. Journal of Nuclear Materials, 300(2-3), pp.91-117.

[56] Dombrowski, D.E., 1997. Manufacture of beryllium for fusion energy applications. Fusion engineering and design, 37(2), pp.229-242.

[57] Gelles, D.S., Sernyaev, G.A., Dalle Donne, M. and Kawamura, H., 1994. Radiation effects in beryllium used for plasma protection. Journal of Nuclear Materials, 212, pp.29-38.

[58] Brezinsek, S., Loarer, T., Philipps, V., Esser, H.G., Grünhagen, S., Smith, R., Felton, R., Banks, J., Belo, P., Boboc, A. and Bucalossi, J., 2013. Fuel retention studies with the ITER-like wall in JET. Nuclear Fusion, 53(8), p.083023.

[59] Ding, R., Pitts, R.A., Borodin, D., Carpentier, S., Ding, F., Gong, X.Z., Guo, H.Y., Kirschner, A., Kocan, M., Li, J.G. and Luo, G.N., 2015. Material migration studies with an ITER first wall panel proxy on EAST. Nuclear Fusion, 55(2), p.023013.

[60] Snead, L.L., 2004. Low-temperature low-dose neutron irradiation effects on beryllium. Journal of nuclear materials, 326(2-3), pp.114-124.

[61] Neu, R., Rohde, V., Geier, A., Krieger, K., Maier, H., Bolshukhin, D., Kallenbach, A., Pugno, R., Schmidtmann, K., Zarrabian, M. and Team, A.U., 2001. Plasma operation with tungsten tiles at the central column of ASDEX Upgrade. Journal of nuclear materials, 290, pp.206-210.

[62] Nygren, R.E., 2002. Actively cooled plasma facing components for long pulse high power operation. Fusion engineering and design, 60(4), pp.547-564.

[63] Ueda, Y., Peng, H.Y., Lee, H.T., Ohno, N., Kajita, S., Yoshida, N., Doerner, R., De Temmerman, G., Alimov, V. and Wright, G., 2013. Helium effects on tungsten surface morphology and deuterium retention. Journal of Nuclear Materials, 442(1-3), pp.S267-S272.

[64] Takamura, S., Ohno, N., Nishijima, D. and Kajita, S., 2006. Formation of nanostructured tungsten with arborescent shape due to helium plasma irradiation. Plasma and fusion research, 1, pp.051-051.

[65] Lee, H.T., Tanaka, H., Ohtsuka, Y. and Ueda, Y., 2011. Ion-driven permeation of deuterium through tungsten under simultaneous helium and deuterium irradiation. Journal of nuclear materials, 415(1), pp.S696-S700.

[66] Jaber, A., El-Guebaly, L., Robinson, A., Henderson, D. and Renk, T., 2012. Rhenium and molybdenum coatings for dendritic tungsten armors of plasma facing components: Concept, problems, and solutions. Fusion Engineering and Design, 87(5-6), pp.641-645.

[67] Gilbert, M.R., Marian, J. and Sublet, J.C., 2015. Energy spectra of primary knock-on atoms under neutron irradiation. Journal of nuclear materials, 467, pp.121-134.

[68] Hwang, T., Hasegawa, A., Tomura, K., Ebisawa, N., Toyama, T., Nagai, Y., Fukuda, M., Miyazawa, T., Tanaka, T. and Nogami, S., 2018. Effect of neutron irradiation on rhenium cluster formation in tungsten and tungsten-rhenium alloys. Journal of Nuclear Materials, 507, pp.78-86.

[69] Tyburska-Püschel, B. and Alimov, V.K., 2013. On the reduction of deuterium retention in damaged Re-doped W. Nuclear Fusion, 53(12), p.123021.

[70] Fujitsuka, M., Tsuchiya, B., Mutoh, I., Tanabe, T. and Shikama, T., 2000. Effect of neutron irradiation on thermal diffusivity of tungsten–rhenium alloys. Journal of nuclear materials, 283, pp.1148-1151.

[71] Cantor, B., 2020. Multicomponent high-entropy cantor alloys. Progress in Materials Science, p.100754.

[72] Cantor, B., Chang, I.T.H., Knight, P. and Vincent, A.J.B., 2004. Microstructural development in equiatomic multicomponent alloys. Materials Science and Engineering: A, 375, pp.213-218.

[73] Ko, J.Y. and Hong, S.I., 2018. Microstructural evolution and mechanical performance of carbon-containing CoCrFeMnNi-C high entropy alloys. Journal of Alloys and Compounds, 743, pp.115-125.

[74] Tong, C.J., Chen, Y.L., Yeh, J.W., Lin, S.J., Chen, S.K., Shun, T.T., Tsau, C.H. and Chang, S.Y., 2005. Microstructure characterization of Al x CoCrCuFeNi high-entropy alloy system with multiprincipal elements. Metallurgical and Materials Transactions A, 36(4), pp.881-893.

[75] Rahul, M.R., Samal, S., Venugopal, S. and Phanikumar, G., 2018. Experimental and finite element simulation studies on hot deformation behaviour of AlCoCrFeNi2. 1 eutectic high entropy alloy. Journal of Alloys and Compounds, 749, pp.1115-1127.

[76] Yeh, J.W., Chen, S.K., Lin, S.J., Gan, J.Y., Chin, T.S., Shun, T.T., Tsau, C.H. and Chang, S.Y., 2004. Nanostructured high-entropy alloys with multiple principal elements: novel alloy design concepts and outcomes. Advanced Engineering Materials, 6(5), pp.299-303.

[77] Senkov, O.N., Wilks, G.B., Scott, J.M. and Miracle, D.B., 2011. Mechanical properties of Nb25Mo25Ta25W25 and V20Nb20Mo20Ta20W20 refractory high entropy alloys. Intermetallics, 19(5), pp.698-706.

[78] Tsai, K.Y., Tsai, M.H. and Yeh, J.W., 2013. Sluggish diffusion in Co–Cr–Fe–Mn–Ni high-entropy alloys. Acta Materialia, 61(13), pp.4887-4897.

[79] Vaidya, M., Pradeep, K.G., Murty, B.S., Wilde, G. and Divinski, S.V., 2017. Radioactive isotopes reveal a non-sluggish kinetics of grain boundary diffusion in high entropy alloys. Scientific reports, 7(1), pp.1-11.

[80] Zhang, F., Zhang, C., Chen, S.L., Zhu, J., Cao, W.S. and Kattner, U.R., 2014. An understanding of high entropy alloys from phase diagram calculations. Calphad, 45, pp.1-10.

[81] Zou, Y., Maiti, S., Steurer, W. and Spolenak, R., 2014. Size-dependent plasticity in an Nb25Mo25Ta25W25 refractory high-entropy alloy. Acta Materialia, 65, pp.85-97.

[82] Wang, F.J., Zhang, Y. and Chen, G.L., 2009. Atomic packing efficiency and phase transition in a high entropy alloy. Journal of Alloys and Compounds, 478(1-2), pp.321-324.

[83] Toda-Caraballo, I., Wróbel, J.S., Dudarev, S.L., Nguyen-Manh, D. and Rivera-Díaz-del-Castillo, P.E.J., 2015. Interatomic spacing distribution in multicomponent alloys. Acta Materialia, 97, pp.156-169.

[84] Owen, L.R., Pickering, E.J., Playford, H.Y., Stone, H.J., Tucker, M.G. and Jones, N.G., 2017. An assessment of the lattice strain in the CrMnFeCoNi high-entropy alloy. Acta Materialia, 122, pp.11-18.

[85] Ranganathan, S., 2003. Alloyed pleasures: multimetallic cocktails. Current science, 85(10), pp.1404-1406.

[86] Yurchenko, N.Y., Stepanov, N.D., Shaysultanov, D.G., Tikhonovsky, M.A. and Salishchev, G.A., 2016. Effect of Al content on structure and mechanical properties of the AlxCrNbTiVZr (x= 0; 0.25; 0.5; 1) high-entropy alloys. Materials Characterization, 121, pp.125-134.

[87] Otto, F., Yang, Y., Bei, H. and George, E.P., 2013. Relative effects of enthalpy and entropy on the

phase stability of equiatomic high-entropy alloys. Acta Materialia, 61(7), pp.2628-2638.

[88] Hume-Rothery, W., 1969. The structure of metals and alloys. Indian Journal of Physics, 11, pp.74-74.

[89] Stepanov, N.D., Yurchenko, N.Y., Zherebtsov, S.V., Tikhonovsky, M.A. and Salishchev, G.A., 2018. Aging behavior of the HfNbTaTiZr high entropy alloy. Materials Letters, 211, pp.87-90.

[90] Zhang, Y., Zhou, Y.J., Lin, J.P., Chen, G.L. and Liaw, P.K., 2008. Solid-solution phase formation rules for multi-component alloys. Advanced Engineering Materials, 10(6), pp.534-538.

[91] Takeuchi, A. and Inoue, A., 2005. Classification of bulk metallic glasses by atomic size difference, heat of mixing and period of constituent elements and its application to characterization of the main alloying element. Materials Transactions, 46(12), pp.2817-2829.

[92] Guo, N.N., Wang, L., Luo, L.S., Li, X.Z., Su, Y.Q., Guo, J.J. and Fu, H.Z., 2015. Microstructure and mechanical properties of refractory MoNbHfZrTi high-entropy alloy. Materials & Design, 81, pp.87-94.

[93] Wei, Q., Shen, Q., Zhang, J., Chen, B., Luo, G. and Zhang, L., 2018. Microstructure and mechanical property of a novel ReMoTaW high-entropy alloy with high density. International Journal of Refractory Metals and Hard Materials, 77, pp.8-11.

[94] Juan, C.C., Tsai, M.H., Tsai, C.W., Lin, C.M., Wang, W.R., Yang, C.C., Chen, S.K., Lin, S.J. and Yeh, J.W., 2015. Enhanced mechanical properties of HfMoTaTiZr and HfMoNbTaTiZr refractory high-entropy alloys. Intermetallics, 62, pp.76-83.

[95] Gao, M.C., Zhang, B., Yang, S. and Guo, S.M., 2016. Senary refractory high-entropy alloy HfNbTaTiVZr. Metallurgical and Materials Transactions A, 47(7), pp.3333-3345.

[96] Tsai, M.H., Chang, K.C., Li, J.H., Tsai, R.C. and Cheng, A.H., 2016. A second criterion for sigma phase formation in high-entropy alloys. Materials Research Letters, 4(2), pp.90-95.

[97] Sheng Guo, C.T. Liu, Phase stability in high entropy alloys: formation of solid- solution phase or amorphous phase, Prog. Nat. Sci.: Mater. Int. 21 (6) (2011) 433e446.

[98] Kube, S.A., Sohn, S., Uhl, D., Datye, A., Mehta, A. and Schroers, J., 2019. Phase selection motifs in High Entropy Alloys revealed through combinatorial methods: Large atomic size difference favors BCC over FCC. Acta Materialia, 166, pp.677-686.

[99] Yang, X. and Zhang, Y., 2012. Prediction of high-entropy stabilized solid-solution in multi-component alloys. Materials Chemistry and Physics, 132(2-3), pp.233-238.

[100] Gao, M.C., Carney, C.S., Doğan, Ö.N., Jablonksi, P.D., Hawk, J.A. and Alman, D.E., 2015. Design of refractory high-entropy alloys. Jom, 67(11), pp.2653-2669.

[101] Feng, R., Gao, M.C., Lee, C., Mathes, M., Zuo, T., Chen, S., Hawk, J.A., Zhang, Y. and Liaw, P.K., 2016. Design of light-weight high-entropy alloys. Entropy, 18(9), p.333.

[102] Tian, F., Varga, L.K., Chen, N., Shen, J. and Vitos, L., 2015. Empirical design of single phase high-entropy alloys with high hardness. Intermetallics, 58, pp.1-6.

[103] Gao, M.C., 2016. Design of high-entropy alloys. In High-Entropy Alloys (pp. 369-398). Springer, Cham.

[104] Tan, Y., Li, J., Tang, Z., Wang, J. and Kou, H., 2018. Design of high-entropy alloys with a single solid-solution phase: average properties vs. their variances. Journal of Alloys and Compounds, 742, pp.430-441.

[105] Pickering, E.J. and Jones, N.G., 2016. High-entropy alloys: a critical assessment of their founding principles and future prospects. International Materials Reviews, 61(3), pp.183-202.

[106] Wang, Z., Guo, S. and Liu, C.T., 2014. Phase selection in high-entropy alloys: from nonequilibrium to equilibrium. Jom, 66(10), pp.1966-1972.

[107] Troparevsky, M.C., Morris, J.R., Kent, P.R., Lupini, A.R. and Stocks, G.M., 2015. Criteria for predicting the formation of single-phase high-entropy alloys. Physical Review X, 5(1), p.011041.

[108] Senkov, O.N. and Miracle, D.B., 2016. A new thermodynamic parameter to predict formation of solid solution or intermetallic phases in high entropy alloys. Journal of Alloys and Compounds, 658, pp.603-607.

[109] Shi, T., Lei, PH., Yan, X. et al. Current development of body-centered cubic high-entropy alloys for nuclear applications. Tungsten (2021).

[110] Bhattacharjee, P.P., Sathiaraj, G.D., Zaid, M., Gatti, J.R., Lee, C., Tsai, C.W. and Yeh, J.W., 2014. Microstructure and texture evolution during annealing of equiatomic CoCrFeMnNi high-entropy alloy. Journal of Alloys and Compounds, 587, pp.544-552.

[111] Lin, C.M., Tsai, H.L. and Bor, H.Y., 2010. Effect of aging treatment on microstructure and properties of high-entropy Cu0. 5CoCrFeNi alloy. Intermetallics, 18(6), pp.1244-1250.

[112] Gorr, B., Azim, M., Christ, H.J., Chen, H., Szabo, D.V., Kauffmann, A. and Heilmaier, M., 2016. Microstructure evolution in a new refractory high-entropy alloy W-Mo-Cr-Ti-Al. Metallurgical and Materials Transactions A, 47(2), pp.961-970.

[113] Stepanov, N.D., Yurchenko, N.Y., Panina, E.S., Tikhonovsky, M.A. and Zherebtsov, S.V., 2017. Precipitation-strengthened refractory Al0. 5CrNbTi2V0. 5 high entropy alloy. Materials Letters, 188, pp.162-164.

[114] Soni, V., Gwalani, B., Senkov, O.N., Viswanathan, B., Alam, T., Miracle, D.B. and Banerjee, R., 2018. Phase stability as a function of temperature in a refractory high-entropy alloy. Journal of Materials Research, 33(19), pp.3235-3246.

[115] Senkov, O.N., Wilks, G.B., Miracle, D.B., Chuang, C.P. and Liaw, P.K., 2010. Refractory high-entropy alloys. Intermetallics, 18(9), pp.1758-1765.

[116] Senkov, O.N., Miracle, D.B., Chaput, K.J. and Couzinie, J.P., 2018. Development and exploration of refractory high entropy alloys—A review. Journal of materials research, 33(19), pp.3092-3128.

[117] Waseem, O.A., Lee, J., Lee, H.M. and Ryu, H.J., 2018. The effect of Ti on the sintering and mechanical properties of refractory high-entropy alloy TixWTaVCr fabricated via spark plasma sintering for fusion plasma-facing materials. Materials Chemistry and Physics, 210, pp.87-94.

[118] Han, Z.D., Chen, N., Zhao, S.F., Fan, L.W., Yang, G.N., Shao, Y. and Yao, K.F., 2017. Effect of Ti additions on mechanical properties of NbMoTaW and VNbMoTaW refractory high entropy alloys. Intermetallics, 84, pp.153-157.

[119] Liu, Y., Zhang, Y., Zhang, H., Wang, N., Chen, X., Zhang, H. and Li, Y., 2017. Microstructure and mechanical properties of refractory HfMo0. 5NbTiV0. 5Six high-entropy composites. Journal of Alloys and Compounds, 694, pp.869-876.

[120] Miracle, D.B., 2019. High entropy alloys as a bold step forward in alloy development. Nature communications, 10(1), pp.1-3.

[121] Lukas, H., Fries, S.G. and Sundman, B., 2007. Computational thermodynamics: the Calphad method. Cambridge university press.

[122] Chen, H.L., Mao, H. and Chen, Q., 2018. Database development and Calphad calculations for high entropy alloys: Challenges, strategies, and tips. Materials Chemistry and Physics, 210, pp.279-290.

[123] Sanchez, J.M., Vicario, I., Albizuri, J., Guraya, T. and Garcia, J.C., 2019. Phase prediction, microstructure and high hardness of novel light-weight high entropy alloys. Journal of Materials Research and Technology, 8(1), pp.795-803.

[124] Detrois, M., Antonov, S. and Tin, S., 2019. Phase stability and thermodynamic database validation in a set of non-equiatomic Al-Co-Cr-Fe-Nb-Ni high-entropy alloys. Intermetallics, 104, pp.103-112.

[125] Patel, D., Richardson, M.D., Jim, B., Akhmadaliev, S., Goodall, R. and Gandy, A.S., 2020. Radiation damage tolerance of a novel metastable refractory high entropy alloy V2. 5Cr1. 2WMoCo0. 04. Journal of Nuclear Materials, 531, p.152005.

[126] Odette, G.R., Alinger, M.J. and Wirth, B.D., 2008. Recent developments in irradiation-resistant steels. Annu. Rev. Mater. Res., 38, pp.471-503.

[127] Ackland, G., 2010. Controlling radiation damage. Science, 327(5973), pp.1587-1588.

[128] Nagase, T., Anada, S., Rack, P.D., Noh, J.H., Yasuda, H., Mori, H. and Egami, T., 2012. Electron-irradiation-induced structural change in Zr–Hf–Nb alloy. Intermetallics, 26, pp.122-130.

[129] Miracle, D.B. and Senkov, O.N., 2017. A critical review of high entropy alloys and related concepts. Acta Materialia, 122, pp.448-511.

[130] Zhao, S., Osetsky, Y., Barashev, A.V. and Zhang, Y., 2019. Frenkel defect recombination in Ni and Ni–containing concentrated solid–solution alloys. Acta Materialia, 173, pp.184-194.

[131] Bonny, G., Terentyev, D., Pasianot, R.C., Poncé, S. and Bakaev, A., 2011. Interatomic potential to study plasticity in stainless steels: the FeNiCr model alloy. Modelling and simulation in materials science and engineering, 19(8), p.085008.

[132] Yan, X. and Zhang, Y., 2020. Functional properties and promising applications of high entropy alloys. Scripta Materialia, 187, pp.188-193.

[133] Zhao, S., Zhang, Y. and Weber, W.J., 2020. High Entropy Alloys: Irradiation.

[134] Lu, C., Yang, T., Jin, K., Gao, N., Xiu, P., Zhang, Y., Gao, F., Bei, H., Weber, W.J., Sun, K. and Dong, Y., 2017. Radiation-induced segregation on defect clusters in single-phase concentrated solid-solution alloys. Acta Materialia, 127, pp.98-107.

[135] Shi, S., He, M.R., Jin, K., Bei, H. and Robertson, I.M., 2018. Evolution of ion damage at 773K in Ni-containing concentrated solid-solution alloys. Journal of Nuclear Materials, 501, pp.132-142.

[136] Aidhy, D.S., Lu, C., Jin, K., Bei, H., Zhang, Y., Wang, L. and Weber, W.J., 2015. Point defect evolution in Ni, NiFe and NiCr alloys from atomistic simulations and irradiation experiments. Acta Materialia, 99, pp.69-76.

[137] Lu, C., Niu, L., Chen, N., Jin, K., Yang, T., Xiu, P., Zhang, Y., Gao, F., Bei, H., Shi, S. and He, M.R., 2016. Enhancing radiation tolerance by controlling defect mobility and migration pathways in multicomponent single-phase alloys. Nature communications, 7(1), pp.1-8.

[138] Jin, K., Bei, H. and Zhang, Y., 2016. Ion irradiation induced defect evolution in Ni and Ni-based FCC equiatomic binary alloys. Journal of Nuclear Materials, 471, pp.193-199.

[139] Lu, C., Yang, T., Jin, K., Velisa, G., Xiu, P., Song, M., Peng, Q., Gao, F., Zhang, Y., Bei, H. and Weber, W.J., 2018. Enhanced void swelling in NiCoFeCrPd high-entropy alloy by indentation-induced dislocations. Materials Research Letters, 6(10), pp.584-591.

[140] Kumar, N.K., Li, C., Leonard, K.J., Bei, H. and Zinkle, S.J., 2016. Microstructural stability and mechanical behavior of FeNiMnCr high entropy alloy under ion irradiation. Acta Materialia, 113, pp.230-244.

[141] Chen, W.Y., Liu, X., Chen, Y., Yeh, J.W., Tseng, K.K. and Natesan, K., 2018. Irradiation effects in high entropy alloys and 316H stainless steel at 300° C. Journal of Nuclear Materials, 510, pp.421-430.

[142] El-Atwani, O., Li, N., Li, M., Devaraj, A., Baldwin, J.K.S., Schneider, M.M., Sobieraj, D., Wróbel, J.S., Nguyen-Manh, D., Maloy, S.A. and Martinez, E., 2019. Outstanding radiation resistance of tungsten-based high-entropy alloys. Science advances, 5(3), p.eaav2002.

[143] Granberg, F., Djurabekova, F., Levo, E. and Nordlund, K., 2017. Damage buildup and edge dislocation mobility in equiatomic multicomponent alloys. Nuclear Instruments and Methods in Physics Research Section B: Beam Interactions with Materials and Atoms, 393, pp.114-117.

[144] Lu, Y., Huang, H., Gao, X., Ren, C., Gao, J., Zhang, H., Zheng, S., Jin, Q., Zhao, Y., Lu, C. and Wang, T., 2019. A promising new class of irradiation tolerant materials: Ti2ZrHfV0. 5Mo0. 2 high-entropy alloy. Journal of materials science & technology, 35(3), pp.369-373.

[145] Li, Y., Ma, F., Yue, F., Ren, Q., Zhou, H. and Lu, G., 2019. Radiation-induced precipitation of transmutation elements rhenium/osmium and their effects on hydrogen behavior in tungsten. Progress in Natural Science: Materials International, 29(3), pp.285-294.

[146] Zheng, C. and Kaoumi, D., 2017. Radiation-induced swelling and radiation-induced segregation & precipitation in dual beam irradiated Ferritic/Martensitic HT9 steel. Materials Characterization, 134, pp.152-162.

[147] Zheng, C., Ke, J.H., Maloy, S.A. and Kaoumi, D., 2019. Correlation of in-situ transmission electron microscopy and microchemistry analysis of radiation-induced precipitation and segregation in ion irradiated advanced ferritic/martensitic steels. Scripta Materialia, 162, pp.460-464.

[148] Nagase, T., Rack, P.D., Noh, J.H. and Egami, T., 2015. In-situ TEM observation of structural changes in nano-crystalline CoCrCuFeNi multicomponent high-entropy alloy (HEA) under fast electron irradiation by high voltage electron microscopy (HVEM). Intermetallics, 59, pp.32-42.

[149] Xia, S.Q., Zhen, W.A.N.G., Yang, T.F. and Zhang, Y., 2015. Irradiation behavior in high entropy alloys. Journal of Iron and Steel Research, International, 22(10), pp.879-884.

[150] Xia, S.Q., Gao, M.C. and Zhang, Y., 2018. Abnormal temperature dependence of impact toughness in AlxCoCrFeNi system high entropy alloys. Materials Chemistry and Physics, 210, pp.213-221.

[151] Yang, T., Xia, S., Liu, S., Wang, C., Liu, S., Zhang, Y., Xue, J., Yan, S. and Wang, Y., 2015. Effects of Al addition on microstructure and mechanical properties of AlxCoCrFeNi High-entropy alloy. Materials Science and Engineering: A, 648, pp.15-22.

[152] He, J.Y., Liu, W.H., Wang, H., Wu, Y., Liu, X.J., Nieh, T.G. and Lu, Z.P., 2014. Effects of Al addition on structural evolution and tensile properties of the FeCoNiCrMn high-entropy alloy system. Acta Materialia, 62, pp.105-113.

[153] Yang, T., Xia, S., Liu, S., Wang, C., Liu, S., Fang, Y., Zhang, Y., Xue, J., Yan, S. and Wang, Y., 2016. Precipitation behavior of Al x CoCrFeNi high entropy alloys under ion irradiation. Scientific reports, 6(1), pp.1-8.

[154] Yang, T., Xia, S., Guo, W., Hu, R., Poplawsky, J.D., Sha, G., Fang, Y., Yan, Z., Wang, C., Li, C. and Zhang, Y., 2018. Effects of temperature on the irradiation responses of Al0. 1CoCrFeNi high entropy alloy. Scripta Materialia, 144, pp.31-35.

[155] He, M.R., Wang, S., Shi, S., Jin, K., Bei, H., Yasuda, K., Matsumura, S., Higashida, K. and Robertson, I.M., 2017. Mechanisms of radiation-induced segregation in CrFeCoNi-based single-phase concentrated solid solution alloys. Acta Materialia, 126, pp.182-193.

Chapter 3: Experimental Methodology

In this chapter, the theoretical and practical application of the experimental techniques used to fabricate and characterise the novel alloys in this work is discussed. Firstly, a detailed discussion of the fabrication method used to manufacture the novel refractory high entropy alloys is considered, together with some limitations and considerations that need to be considered. The sample preparation procedures and the main principles of the experimental characterisation techniques applied to analyse the novel samples follows this discussion.

3.1. Cold Crucible Vacuum Arc Melting

Cold crucible vacuum arc melting (VAM) is a well-established method of fabricating small amounts of novel alloys. An electron plasma arc is created to melt elemental metals to form small-scale ingots up to 250 g in size. Often used for low level Technology Readiness Level (TRL) research, VAM is an inexpensive, relatively quick process which can melt a wide range of elements to produce alloys for characterisation and mechanical testing. This section goes into detail about the process of making small samples (approximately 20 g) for further analysis and highlights precautions and considerations that need to be considered especially for the refractory alloys produced during this project.

Figure 3.1 shows a detailed schematic of the Vacuum Arc Melting equipment. In this work, the Arcast200 was used to fabricate the alloys. We wish to acknowledge the Henry Royce Institute for Advanced Materials, funded through EPSRC grants EP/R00661X/1, EP/S019367/1, EP/P02470X/1, and EP/P025285/1, for Arcast200 access at Royce at the University of Sheffield.

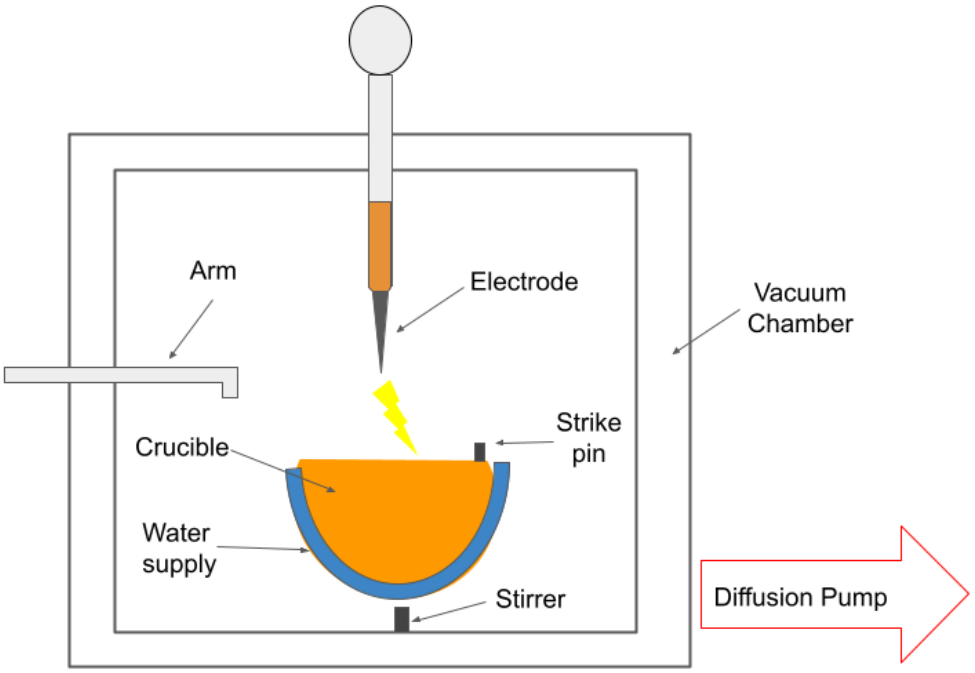

Figure 3.1: Schematic of Arcast 200 equipment set-up

3.1.1. The Arcast200, Arcast Inc.

3.1.1.1. *Crucible Hearth*

Metals are placed inside a water-cooled copper crucible inside a steel chamber which is evacuated to 4.1 x10^{-1} mbar to remove any impurities from the air inside the chamber. The chamber is then backfilled with high purity argon gas (other inert gases may also be used). This purging process is repeated three times to minimise any contaminants inside the chamber prior to melting.

3.1.1.2. *Arc Electrode*

The plasma used to melt the alloy is created from the tungsten electrode which is connected to a direct current power source. The magnitude of the current, the geometry of the electrode tip, and the pressure of the chamber are all factors which can affect the power of the plasma, this in turn affects how much melting power is achieved. As such we cannot measure the temperature of the plasma arc and so the temperature and cooling rates of the melt cannot be directly determined. For safety and to ensure sufficient melting of the refractory metals the

voltage of the current was set between 400 V and 500 V (depending on which elements were being melted).

3.1.1.3. *Strike Pin*

To ‘activate’ the plasma to melt the metals, the tungsten electrode will need to have a contact point with a ‘sacrificial’ piece of conductive metal to start the melting process. In the case of the Arcast 200, this is the tungsten strike pin. As soon as melting starts and the plasma can be seen (behind brazing windows to protect the eyes of the user) the electrode is moved across to the metals to be melted in the crucible. The argon atoms provide a pathway for the plasma to travel and ensures a medium for the current to travel through and thus creates the electron plasma.

3.1.1.4. *Vacuum Equipment - Rotary and Diffusion Pump*

The rotary pump is used to achieve a vacuum of 4.1 $x10^{-1}$ mbar within the chamber. Whilst this magnitude of vacuum is sufficient to remove the majority of air impurities, higher levels of vacuum can ensure an even cleaner vacuum chamber and thus reduce the number of impurities which can enter the alloy during melting. Impurities which can be present in the air of the chamber include lighter elements such as nitrogen, oxygen, carbon etc. The diffusion pump is an external device with oil in the bottom which is heated once activated. The hot oil rises, due to evaporation, and traps any extra impurities in the chamber before cooling and collecting in the bottom of the pump again. This results in vacuum pressures of $2x10^{-5}$ mbar being achieved. This is important when alloying refractory elements as any impurities dissolved into the alloy during melting can introduce unwanted phases which will affect the overall crystal structure of the material and thus could impair the overall radiation damage resistance.

3.1.1.5. *Electromagnetic Stirring*

The Arcast 200 has the additional function of electromagnetic stirring. Underneath the crucible is a coil which induces a small magnetic field, where the intensity can be controlled during a melt. Once a mixture is fully molten, this function can be applied to stir the alloy to ensure pieces of metal within the alloy are fully melted and also to encourage maximum elemental homogeneity. For an alloy whose composition has good fluidity, electromagnetic stirring can be applied. Unfortunately for some of the alloys in this thesis, poor fluidity of the alloys meant that neither casting of the alloy (into a more functional shape for experimental work, i.e.

cylinders) or electromagnetic stirring could be applied. This is explained further in Chapter 6: Experimental Assessment of Novel High Entropy Alloys. Flipping the ingot in between melts is an alternative method that further increases the chemical homogeneity of the alloy. All samples prepared in this work were flipped and remelted between 5-10 times.

3.2. Experimental Methods

Raw elemental metals supplied by Alfa Aesar, in various forms detailed below in Table 3.1, were weighed out to the nearest 0.01 g, cleaned thoroughly in acetone, and dried before being placed in the copper crucible of the Arcast 200. The important issues to consider when using VAM to fabricate novel alloys are impurities within the melt and heating and cooling rates of the alloy.

Table 3.1: Purities of the elements used for alloying as displayed on the suppliers' website.

Element	Purity (wt%)	Form	Dimensions
Vanadium	99.9	Rod	12.7 x 25 mm
Chromium	99.99	Lumps	Irregular
Manganese	99.95	Broken plate	Irregular
Iron	99.97	Lumps	2.5 - 25 mm
Tantalum	99.95	Sheet	0.5 x 100 x 100 mm
Tungsten	99.95	Sheet	0.5 x 100 x 100 mm

3.2.1. Impurities Within the Melt

The suppliers of the pure metals may supply a list of impurities, however, is it important to note that this list is not exhaustive and so the pure metals themselves may be a source of contamination within the alloy. Some pure elements, like manganese, readily oxidise when

exposed to air and so some grinding of the material prior to melting is necessary to remove this small oxide layer prior to melting. Argon purging of the chamber will not reduce this source of contamination, so it is of great importance to source high purity metals.

3.2.2. Melting Strategies (Heating and Cooling Rates of the Alloy)

Difficulties in melting can occur when elements have vastly different melting temperatures. The form and dimensions of the metal can also impact ease of melting. For example, when considering the high melting temperature of tungsten (3422 °C) in sheet form, a smaller surface area will allow for less excessive heat loads from the plasma to melt the sheet. For this reason, the tungsten sheet was sectioned into smaller pieces prior to melting. There is some evidence that the form and dimensions of the elements can also influence the phases formed upon solidification, this is discussed further in Chapter 6: Experimental Assessment of High Entropy Alloys. Figure 3.2 shows the schematic of the inside of the Arcast crucible.

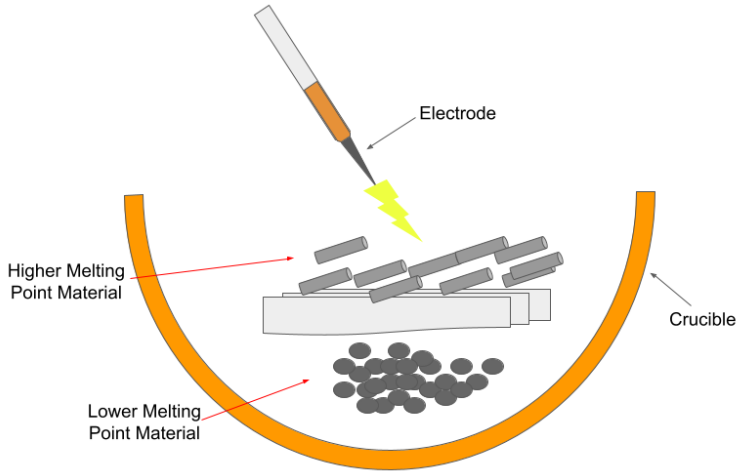

Figure 3.2: Schematic of the contents of the water-cooled copper crucible

The raw elemental metals are placed inside the crucible with the higher melting elements layered at the top and lower vapour pressure/melting elements are underneath. If there are any small granules or pieces of elements with lower melting temperature, then these can be wrapped into the foils of higher melting metals to protect them from direct exposure of the high energy electron plasma arc. The high temperatures of the plasma required to melt high melting temperature elements (i.e., tantalum, tungsten) can be high enough to evaporate elements with low vapour pressure (i.e., manganese). Figure 3.3 shows the vapour pressures exerted

by a range of metals and compounds as a function of temperature. The area to the left-hand side of each curve is the temperature at which the material is a solid and to the right of the curve the material exists as a gas [1].

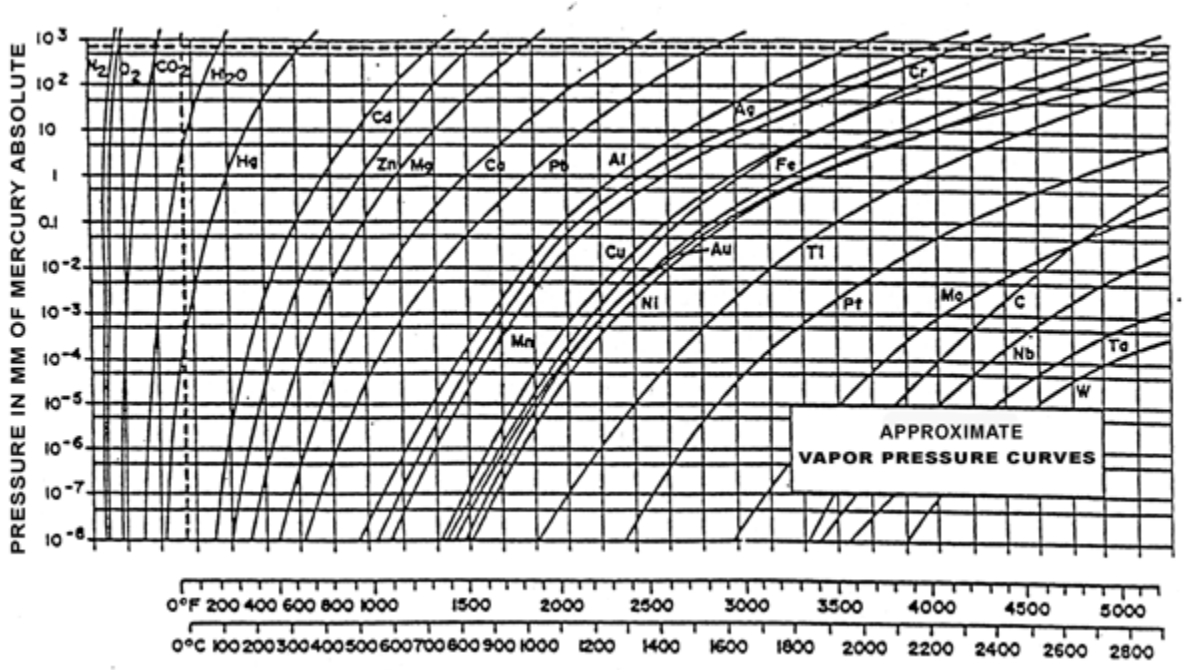

Figure 3.3: Vapour pressure curves for various metals and compounds, including manganese, tungsten, tantalum, iron and chromium [1]

From this figure it can be observed that heating manganese, relative to iron, chromium, tungsten, and tantalum, will result in vaporisation at much lower temperatures. This can be avoided by pre-alloying tungsten with similar melting temperature elements to lower the overall melting temperature of the alloy before incorporating the more volatile elements (like manganese). Slightly increasing the pressure of the chamber, in this final melting stage, can also aid in preventing evaporation of manganese.

The complex factors involved in measuring the direct temperature of the plasma result in inconsistencies when reproducing ingots of the same alloy composition. The time the alloy spends in the molten state, the number of times the alloy has been flipped, and the pressure within the chamber are all factors which impact the resultant phases and microstructure of the as-cast alloy. Ensuring the plasma is hot enough to melt the highest melting temperature element is crucial to reduce any unwanted unmelted inclusions or elemental segregation. For these reasons, each ingot was flipped and remelted at least 7 times with each melt lasting

approximately 30 seconds. For higher melting point elements, the voltage controlling the power of the plasma was increased to ~500 V and for volatile elements (manganese, chromium) was reduced to ~300 V. In the final stages of melting, once all of the constituent elements had been incorporated into the ingot, the voltage was decreased to 300 V and the pressure of the chamber was increased to impede the evaporation of manganese.

Additionally, the cooling rate of the alloy is also not able to be controlled. The copper crucible is cooled with water pumped from a water chiller at a temperature of around 13 °C, but the actual temperature of the water inside the chamber is not able to be directly measured. This means the surface temperature of the alloys underside as it cools cannot be known. But the high cooling rate is high enough to quench and thermally freeze metastable high temperature phases and microstructures that form on solidification [2]. An example of this can be observed by the work of Chen et al [3] who reported the additional formation of an FCC A1 phase for the alloy $CoCrFeNiAl_{1.1}$ due to the solidification deviation from the equilibrium state. In this case, it was the relatively high cooling rates that was suggested to be responsible for the extra phase formed at the later stage of the Scheil solidification simulation. For this reason, heat treating the alloy post-fabrication is needed to establish thermodynamically stable phases. Therefore, alloys fabricated using VAM are not necessarily representative of larger industrially produced components, but this method is a relatively clean, economic practice useful for producing small amounts of material for characterisation.

3.2.3. Heat Treatments

Alloys were placed in alumina crucibles in a box furnace and heat treated under flowing argon gas. Each alloy composition underwent a high temperature short homogenisation heat treatment and a lower temperature long heat treatment. The duration and temperatures of the heat treatments were determined from the predicted melting points of the alloys using Thermo-Calc simulations. A detailed explanation of these thermal treatments is in Chapter 6: Experimental Assessment of Novel High Entropy Alloys. Due to the high propensity of oxidation of some of the elements in the alloys (i.e., vanadium readily oxidises to vanadium pentoxide, which is hazardous if inhaled) the samples were wrapped in tantalum foil to further prevent oxidation of the alloys. At the end of the heat treatment, the samples were taken out of the furnace and quenched in room temperature water.

3.2.4. Sample Preparation

The ingots were measured for their density (gcm^{-3}) using the Archimedes principle on a Mettler Toledo NewClassic MF balance. The measured displacement of water can give the density of an ingot and when compared to the theoretical density, can give insight to the amount of porosity within the sample. Three scales are available for measuring the ingot, a total of 5 repeat measurements were taken using at least one of the scales once each time.

The samples were then cut cross-sectionally using a Struers Secotom 50, to observe any elemental inhomogeneities or porosity and to ensure a representative section.

For Scanning Electron Microscopy, sections of each alloy were prepared by hand using standard metallographic methods. Samples with flat parallel sides were mounted on to an aluminium stub using an adhesive crystal bond. The samples were ground using grit papers p1200, p2500 with the sample face down on the grit paper and using the aluminium 'doughnut' to ensure the sample was flat and not bevelled. In between papers the sample was rotated 90 degrees so subsequent scratches were removed. After grinding, the following diamond suspension polishing steps (with the appropriate cloths) were used: 6 µm, 1 µm, and finally colloidal silica. After all the scratches had been removed, the sample was then placed in an ultrasonic bath filled with water and cleaned for 15 minutes to remove residual colloidal silica.

Samples prepared for microhardness testing are required to be hot mounted in bakelite prior to indentation. These samples were prepared automatically using a Beuhler Automet 250, using the same metallographic steps as the manually prepared samples.

3.2.5. Computational Modelling

Computational tools were used in the alloy design process to assess candidate low activation high entropy alloys. Elements and compositions which promote the formation of single-phase BCC solid solutions were targeted using two approaches: High entropy alloy thermodynamic parameters (described in Chapter 5: Alloy design) incorporated into a Python Script, and the use of the Thermo-Calc software [4].

3.2.5.1 Python Script

High entropy alloy thermodynamic parameters were calculated for the alloys in this work and explained in detail in Chapter 5: Alloy Design. The equations for these parameters were written into a script using Python (version 2.7.18). This code was then used in Pycharm (community

edition version 2017.3.4) to run the script iteratively for a range of alloy compositions from 5-35 at%. The output of these results was saved as an excel file.

3.2.5.2. Thermo-Calc Software

Thermo-Calc is a global computational tool widely used by material scientists to predict and understand material properties.

The CALCulation of PHAse Diagrams (CALPHAD) method is a validated means of predicting the kinetic and thermodynamic properties of a system. This approach is implemented by Thermo-Calc in the advancement of their databases, which are based on available experimental data. These databases can then be used for the prediction of phase equilibria and thermodynamic properties of a novel system.

Known experimental data on phase equilibria, crystal structures, enthalpies of mixing, and formation energies of materials are firstly collected for critical assessment - known as 'Model Selection'. For a binary alloy, for each distinct region of a phase diagram for elements A and B, a model for the Gibbs energy, which is the thermodynamic potential used as a measure of the maximum available work that can be derived from a system under constant temperature and pressure [5], is assigned depending on the crystal structure. The Gibbs energy is used as it describes all the thermodynamic properties of a material. The parameters of the model are then fitted to the input data and are optimised; this process is repeated for all the phases in the phase diagram. The models, with their fitted parameters, are known as thermodynamic databases and are typically based on binary and ternary systems. The user can elect the most optimal database depending on their system of interest.

Whilst not explored in this work, Thermo-Calc is also able to simulate solidification curves, namely the calculation of Scheil curves for novel materials. The Scheil equation describes the redistribution of solutes during the solidification of an alloy based on non-equilibrium transformations. During the solidification process, cooling rates are too high to allow for the redistribution of elements in the alloy and diffusion in the solid state is restricted. Therefore, typical equilibrium calculations to determine compositions of the last liquid to solidify and composition gradients are not always representative of a material's condition following solidification.

In this work, the software Thermo-Calc (version 2021a) was used to calculate the property diagram of equilibrium phases as a function of temperature [6]. For this work, the property diagrams calculated for the high entropy alloys display the change in the amount of predicted equilibrium phases as a function of temperature. Two thermodynamic databases were used for comparison of the same alloys: SSOL4 (SGTE Alloy Solutions Database v4.9g) and TCHEA4 (v4.2). Compositions of the fabricated alloys, as determined by X-ray fluorescence (XRF), instead of the compositions generated by the Python script, were inputted into the software to aid in the prediction of phases likely to be formed in the fabricated alloys.

3.2.6. X-ray Diffraction

X-ray powder diffraction (XRD) is a powerful non-destructive technique used to gain insight into the crystallographic structure of materials including crystal structure, average grain size, lattice strain, crystallinity, and crystal defects. For all the XRD analysis carried out for this project, a PANalytical X'Pert^3 Powder diffractometer with Cu Kα radiation operated at 45 kV and 40 mA was used. Compared to similar machines, the higher resolution of the X'Pert is useful to observe small amounts of precipitation. Instrument conditions specific to each analysis are given within the relevant results chapters.

Inside the diffractometer, the flat polished surface of a material is probed with incident monochromatic X-rays generated by a cathode ray tube with a copper target material. The sample and detector are rotated, and the regular array of the material's atoms causes the X-ray beam to elastically scatter - the intensity and angles diffracted from the sample are recorded. This occurs due to the wavelength of X-rays being comparable to the interatomic distances in solid materials. For a crystalline material the incoming beam is scattered by lattice planes separated with a spacing, d(hkl). Bragg's law (Equation 1) describes the conditions for constructive interference [7]:

$$2d_{(hkl)} \sin \theta = n \lambda \qquad \text{Equation 3.1}$$

Where θ is the glancing angle, n is a positive integer, and λ is the wavelength of the incident X-ray. When the incoming X-rays satisfy the Bragg equation then constructive interference occurs and this is represented by a peak in the diffraction pattern.

3.2.6.1. Grazing Incidence X-ray Diffraction

X-ray diffraction can also be applied to study just the near surface of a sample (from a few hundred nanometers to several micrometres below the surface). Some of the alloys produced during this project were subjected to energetic particle bombardment, by a process called ion implantation (described in Chapter 2.2 Radiation Damage in Materials) which resulted in ion implantation induced damage being produced in the samples from the surface up to a depth of about a micron. To determine whether this radiation damage had induced any modifications to the alloys' crystal structure, XRD in grazing incidence mode was used to probe only this damaged region. To ensure that only the implanted region is penetrated by the X-rays, Grazing (sometimes referred to as Glancing) Incidence XRD (GI-XRD) is used. The depth of required X-ray penetration (theta) will vary depending on the depth of damage (this will vary according to the ion implantation conditions, such as ion species and ion energy, as well as alloy composition). Using the linear attenuation theory (Equation 2) the required incident angle can be calculated to probe the near-surface of the implantation-induced damage region [8]:

$$Z_p = \frac{1}{\mu(E)\theta} \qquad \textit{Equation 3.2}$$

Where the incident X-ray beam, θ, can be calculated from the μ(E), the absorption coefficient which depends on the sample's density, atomic number and mass of the elements comprising the alloy, and X-ray energy, E. The X-ray penetration depth required, Z_p (i.e., the depth of damage to be probed) can be determined using SRIM calculations, which are described in Section 3.2.10. Heavy Ion Implantation.

3.2.4.2. High Temperature X-ray Diffraction

When designing new alloys for high temperature applications, it is important to reveal any temperature induced phase transitions, as well as determining any changes in crystal structure in an as-cast alloy as it moves towards thermal equilibrium. One method used to investigate thermal stability of the produced alloys during this project was high temperature XRD; an in-situ method that enables accurate phase transition temperatures to be determined. To undertake HT-XRD using the PANalytical X'Pert^3 Powder diffractometer, samples must either be processed into a very thin film or be in the form of a fine powder. For the HT-XRD carried out during this project, selected samples were ground using a pestle and mortar. The fine powder sample was then placed into a thin 1 mm diameter silica capillary tube and placed inside the diffractometer, into a furnace under vacuum. The as-cast powder sample was

heated from room temperature (25 °C) to 1000 °C and the sample was isothermally held at every 100 °C increments and XRD data were collected at these temperatures. Once the maximum operating temperature (1000 °C) was reached, the sample was cooled to room temperature with XRD data being collected again at every 100 °C increments until the furnace reached 100 °C.

3.2.4.3. XRD Software

For phase analysis the International Centre for Diffraction Data ICDD SIeve+ was used to search the PDF -4+ database for matching Powder Diffraction Files (PDF). Data analysis begins with indexing the reflections to determine the dimensions of the unit cell. Due to the novel nature of these alloys, the exact crystal structures are unknown and so for phase identification the diffraction peaks are instead best matched to an experimentally known diffraction pattern for analogous matching. In this work, PDF cards are matched to the experimental XRD pattern where most of the PDF cards fit the same peak positions as those experimentally obtained for the fabricated alloy. The PDF card is used to gather the crystallographic information of the peaks including the analogous structure, space group, crystal structure, Pearson symbol, and lattice parameters.

The STOE WinX^{POW} software was used for the least squares refinement of the lattice parameters for the crystal structures.

3.2.5. X-ray Fluorescence

Due to the inconsistencies of the melting process as described in Section 3.1. Cold Crucible Vacuum Arc Melting, the composition of the fabricated alloys may differ to the designed composition. To accurately determine the solid elemental atomic percentages in the alloys fabricated during this project, X-ray fluorescence (XRF) was used on the bulk samples. This non-destructive technique works by directing an incident beam of X-rays onto the sample. Energy is transferred from the X-rays to electrons, bound to atoms in the material. The transferred energy allows the excitation and ionisation of core shell electrons, resulting in an electron hole being formed. An electron from an outer shell will drop down to fill the core shell electron hole, releasing electromagnetic energy, in the form of an X-ray, in the process. Because the energies associated with each shell are unique to a particular atom, the energy of the emitted X-ray is characteristic of a specific element, thereby allowing identification of elements comprising a material.

Some elements are unable to be detected using this method, most notably lighter elements (Na, Mg, Al, Si) as they have very low energy X-rays which are difficult to detect even at relatively small sample depths. However, these elements are not used in the alloys fabricated in this work and so this is not of concern.

XRF data was collected using a PANalytical Zetium spectrometer under vacuum at room temperature with a spot size of 6 mm and analysed using the PANalytical Omnian software.

3.2.6. Scanning Electron Microscopy

Scanning electron microscopy (SEM) is a high-resolution imaging tool and is used to observe the surface microstructural features of prepared samples. The electron microscope produces a focused beam of electrons which scans across the surface of the material. This beam is emitted from an electron gun and focussed to a nanometer wide spot. The beam then passes through some scanning coils and in the final lens the beam is deflected so it can raster over a rectangular surface area. There are three modes of interest which are commonly used in this work: secondary electrons, back-scattered electrons, and electron-dispersive X-ray analysis (discussed in more detail in the next section).

The most common imaging mode uses secondary electrons (SE) where the electrons typically interact with the sample by inelastic scattering and the emission of electromagnetic radiation is collected by the detectors. This is sensitive to the incident electron angle and so this mode illustrates topographical contrast of the surface of the material.

Back-scattered electrons (BSE) are reflected from the nuclei of the sample due to elastic scattering. This means that whilst the resolution of the BSEs is less than SEs the intensity of the signal is much greater. This factor is strongly related to the atomic number (Z) of the sample, therefore the contrast observed in BSE images is representative of the distribution of elements within the sample near surface volume. Areas of lighter contrast are composed of atoms with a greater mass (Z) as they backscatter electrons more strongly than lighter atoms and thus reflect more brightly. Similarly, darker areas have atoms that are lighter in mass and so have a lower atomic number.

3.2.7. Energy Dispersive X-ray Spectroscopy

X-rays can be emitted when the electron beam gives enough energy to emit inner shell electrons from the sample. This causes a higher energy electron to fall into the lower energy state, subsequently emitting X-rays due to the difference in energy of these states. Much like

the method in XRF, each element has a unique X-ray energy it will emit and so energy dispersive X-ray spectroscopy (EDX) is a useful technique for the assessment of elemental composition for different phases in each point or area. The difference between XRF and EDX is the type of radiation encountering the sample. EDX uses an electron beam whereas XRF uses an X-ray beam. Electrons have a smaller beam size and so analysis can be obtained for volumes as small as 1 µm in diameter. In this method emitted X-rays are collected by a silicon-drift detector, however a drawback to EDX is that low atomic number elements can only emit low energy X-rays which are unable to be measured sufficiently by the detector.

Compared to XRF, this method is quicker at collecting data, but is less accurate at quantifying elemental composition. Qualitative analysis is also possible by mapping the elemental distribution of an area.

The resolution of SEM and EDX are limited by the experimental technique. The types of scattering electrons and X-rays and their interaction volumes are summarised in Figure 3.4

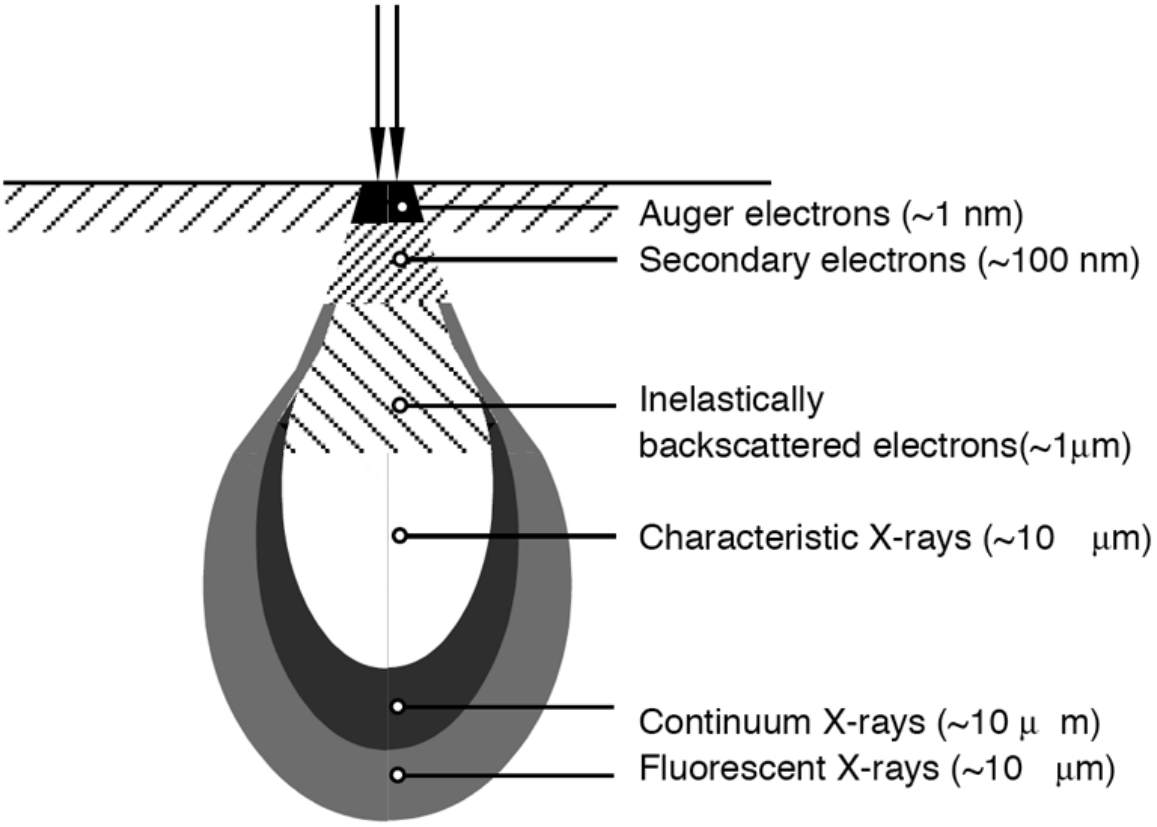

Figure 3.4: The interaction volume of the material probed by different types of scattered electrons and X-rays. The imaging resolution is dependent on the volume generated by the emission type.

From this figure, BSE electrons have a much larger interaction volume than SE electrons which results in the BSE mode (~ 1µm) has a lower resolution than SE mode (~10 nm). For the quantitative analysis of elements in the alloy sample, the EDX detector collects characteristic X-rays emitted from excited atoms. Depth resolution for EDX is around 2-5 µm, whereas spatial resolution for EDX in SEM is ~2 µm. Additionally, areas of interest should be greater than this spatial resolution to allow for proper quantification without overlap from other areas in its interaction volume.

For SEM analysis, samples need to be prepared to a mirror-finished scratch-free surface and are placed in the instrument under a high vacuum (5×10^{-5} mbar). The instrument used to collect images of all the alloys in this work was the Inspect F50 operating at an accelerating voltage of 20 keV with a spot size of 5. An EDX detector attachment was used for SEM-EDX point scans and elemental maps and analysis was conducted using the Oxford Instruments Aztec software. For SEM-EDX elemental maps, the energy window (keV) was set appropriately to ensure that all the relevant elements are detected and measured. For the SEM-EDX point scans, 5 separate point scans in different areas of the contrast region were averaged.

3.2.10. High Temperature Differential Scanning Calorimetry

Differential Scanning Calorimetry (DSC) is a thermal analytical technique, used to determine any microstructural changes and phase transformations, where a sample and a reference pan are both heated to the same temperature for the same amount of time. The difference in the heat required to increase the temperature of the sample is measured as a function of temperature. The main principle for using DSC is to record the phase transitions at different temperatures. This is represented by a sudden increase or decrease in the heat required to maintain both the reference pan and sample pan. A peak in the produced data is representative of an exothermic reaction as less heat is required to keep the sample at the same temperature. The analysis of the DSC data can give us insight into material behaviour such as: precipitation, crystallisation, oxidation, phase transformation and loss of dendrites.

However, it is worth noting that normally DSC can show the melting temperature of an alloy, represented by a sharp endothermic peak in the DSC curve. Unfortunately, due to the very high melting temperatures of the refractory alloys produced during this project, (< 2000 °C), this could not be measured even by the specialist High Temperature Differential Scanning Calorimetry (HT-DSC) equipment used in this work, where the maximum operating

temperature is approximately 1600 °C. The DSC instrument was a Netzsch 404F1 HT-DSC accessed through the Royce Institute. This work was supported by the Henry Royce Institute for advanced materials, funded through EPSRC grants EP/R00661X/1 and EP/P025021/1.

Alumina crucibles were used as the reference pan and to contain the sample to minimise any interaction with the reference pan and the alloy upon heating. This reduces the risk of possible contamination of the DSC instrument. Additionally, volatile compounds may evaporate from the alloy at higher temperatures - for example vanadium pentoxide readily forms from vanadium alloys in the presence of heat and oxygen. As all the alloys in this work contain vanadium, samples were never processed in air and were only run under a vacuum.

A small amount of the sample (~20 mg) was placed into a pan and positioned into the DSC chamber along with an empty reference pan. The chamber was evacuated and backfilled with argon to reduce any contamination. This purging cycle was repeated three times. The sample and reference pan were heated at a rate of 5 $Kmin^{-1}$ to 1600 °C, held for 15 minutes, and cooled back down to room temperature at the same rate.

3.2.11. Hardness Testing

Hardness testing is a relatively quick and easy way to investigate the mechanical properties of a material. Specifically, the hardness of a material can be determined, and used to infer other mechanical properties such as Young's modulus (the elastic modulus). There are several standard methods that can be used for hardness testing, all based on the application of a measured load on the surface of a sample, and the inspection of the resultant indent. In this project, Vickers microindentation and nanoindentation were used.

3.2.11.1 Vickers Microhardness

Vickers microhardness is typically used for smaller samples with loads under 10 N. Microhardness testing uses a square-based pyramidal diamond tip to indent the alloy. The force of the indent is known and set by the user. The hardness is calculated by first measuring the dimension of the indentation, diagonally - corner to corner, using an optical microscope, then calculating the average diameter of the indent (d). This value is then inputted into Equation 3 to calculate the Vickers hardness (HV).

$$HV = 0.1891 \frac{F}{d^2} \qquad \textit{Equation 3.3}$$

Vickers Hardness (HV) is measured in MPa, the applied load (F) is measured in N, and the average diameter (d) of the indentation is measured in mm.

In this project, test samples were prepared and measured in accordance with ASTM E384 methodology [9]. Samples were mounted in bakelite and automatically prepared using the grinding and polishing steps described in Section 3.2.2: Sample Preparation. Microindentation was carried out on a Durascan 70 (Struers) with an average of 5 indents taken in each localised region of each sample. The dwell time was set to 15 s, magnification x 40, with a load of 1 kg. Optical images of the samples were taken before and after each indent to qualitatively examine the brittle/ductile nature of the alloy.

3.2.11.2. Nanoindentation

Nanoindentation testing allows for hardness testing on a smaller scale than microhardness; typically, on the scale of nanometers. Hardness testing of specific grains, secondary phases, and dendritic arms and interdendritic regions is possible. Nanoindentation is a robust technique which allows the assessment of the elastic modulus and hardness of a material.

Similar to the Vickers microhardness procedure, a diamond tip is lowered on the sample's surface. In this case the diamond tip is called a Berkovich tip and is shaped as a triangular-based pyramid. In this work, the Continuous Stiffness Measurement (CSM) method is applied, where a dynamic load is applied on top of the static load when loading. The dynamic load is used to measure the stiffness which is further used to calculate the modulus and hardness of the material. The accurate measurement of the initial surface contact as well as the continuous measurement of the contact stiffness means that the unloading data is not required.

The Oliver-Pharr polynomial curve fit methodology is applied and includes the following equations (Equations 4-6) for the calculation of modulus and hardness as a function of depth [10]:

$$H = \frac{P_{max}}{A} \qquad \textit{Equation 3.4}$$

$$\frac{1}{E_{meas}} = \frac{1-\mathrm{v}2}{E_{real}} + \frac{1-v^2}{E_i} \qquad \textit{Equation 3.5}$$

$$S_{unload} = \beta \frac{2}{\sqrt{\pi}} E_{meas} \sqrt{A} \qquad \textit{Equation 3.6}$$

Where H is the hardness (Pa), P_{max} is the load (N), and A is the contact area (m^2). And E is the Young's modulus of either the material's real value (real), measured value (meas), or the indenter (i) (Pa). v is Poisson's ratio, β is a correction coefficient, and S_{unload} is the elastic unloading stiffness (Pa).

The Hysitron Triboscope NanoIndenter (Bruker) was used for the nanoindentation testing. A matrix of indents is used across the sample for representative values to be taken into account. Where multi phases are present, each phase can be indented separately. In this work a 5 x 5 matrix was applied with a 5 s load, 5 s hold, and 5 s unload profile. This load-displacement data is then converted into mechanical data for the sample.

3.2.10. Heavy Ion Implantation

Heavy ion implantation is a process where ions of a selected element are accelerated and made to penetrate a solid target. In this work ion implantation is used to emulate a nuclear fusion environment as current neutron sources with an energy spectrum typical of the conditions within a fusion reactor (14 MeV neutrons) do not reach a sufficient fluence. The atoms of choice are converted into ions by electron collisions in a plasma and then focused into a beam using magnets. They are then accelerated by a voltage gradient towards the solid target. The high energy ion beam is directed onto the alloy's surface. A resulting consequence of this process is the damage induced in the near surface region of the material. This technique is described in detail in Chapter 2.2: Radiation Damage in Materials.

The polished side of the as-cast VCrWMoCo alloy was implanted at room temperature with 5 MeV Au^{2+} ions to a fluence of 5×10^{15} Au^{2+} ions per cm^2 at the Ion Beam Centre in Helmholtz-Zentrum Dresden-Rossendorf, Germany. The implantation was carried out using a scanning beam. The beam spot size was approximately 3–5 mm on the sample and the irradiated area was 50 mm in diameter. The ion flux was around 1.6×10^{11} Au^{2+} ions per second per cm^2. The ion beam current density was about 50 nA/cm^2.

To calculate the implantation-induced damage depth an irradiation damage predictive simulation is required. In this work, the Monte Carlo code SRIM was used [11]. The detailed calculation with full damage cascade was employed with a displacement energy, Ed, of 50 eV for each element, and the experimentally determined density was used.

3.2.11. Conclusion

These methods were employed to design and fabricate a range of novel refractory high entropy alloy. The design tools, the empirical HEA parameters and Thermo-Calc were used to determine the optimised alloy compositions which were then fabricated using Vacuum Arc Melting. Characterisation of the alloys in the as-cast and heat-treated conditions was undertaken using the techniques discussed in this chapter. In this work, the determination of the microstructure, identification of the phases present, and an assessment of the hardness of the fabricated alloys was evaluated using the methods described here. The results of from these techniques are presented and discussed in Chapters 4, 5, 6, and 7 for the evaluation of these alloy for fusion applications.

3.2.12. References

[1] Jeff Pritchard, ‘When to use a partial pressure in a vacuum furnace’, May 26, 2014 [online] Available https://vacaero.com/information-resources/vac-aero-training/674-when-to-use-a-partial-pressure-in-a-vacuum-furnace.html

[2] Kube, S.A. and Schroers, J., 2020. Metastability in high entropy alloys. Scripta Materialia, 186, pp.392-400.

[3] Chen, H.L., Mao, H. and Chen, Q., 2018. Database development and Calphad calculations for high entropy alloys: Challenges, strategies, and tips. Materials Chemistry and Physics, 210, pp.279-290.

[4] Kaufman, L. and Bernstein, H., 1970. Computer calculation of phase diagrams. With special reference to refractory metals.

[5] Baker, L.E., Pierce, A.C. and Luks, K.D., 1982. Gibbs energy analysis of phase equilibria. Society of Petroleum Engineers Journal, 22(05), pp.731-742.

[6] Andersson J.O., Helander T., Höglund L., Shi P.F., and Sundman B., (2002). Thermo-Calc and DICTRA, Computational tools for materials science. Calphad, 26, 273-312.

[7] Jauncey, G.E.M., 1924. The scattering of x-rays and Bragg's law. Proceedings of the National Academy of Sciences of the United States of America, 10(2), p.57.

[8] Huda, W. and Slone, R.M., 2003. Review of radiologic physics. Lippincott Williams & Wilkins.

[9] ASTM International, 2016. ASTM E384-16-Standard Test Method for Microindentation Hardness of Materials.

[10] Oliver, W.C. and Pharr, G.M., 2004. Measurement of hardness and elastic modulus by instrumented indentation: Advances in understanding and refinements to methodology. Journal of materials research, 19(1), pp.3-20.

[11] Zeigler, J.F., Biersack, J.P. and Littmark, U.N.D.U., 1985. The stopping and range of ions in solids. The Stopping and Range of Ions in Matter, 1.

Chapter 4: Radiation Damage Tolerance of a Novel Metastable Refractory High Entropy Alloy $V_{2.5}Cr_{1.2}WMoCo_{0.04}$

4.1. Context Within Thesis

This paper provides the preliminary investigations of a promising novel refractory high entropy alloy, VCrWMo with a small amount of cobalt contamination. Whilst this alloy composition is not specifically classified as a low activation alloy (it would not be suitable for use as a plasma-facing alloy) each constituent comprises a BCC element, and so it can be ascertained that the overall alloy should form a favourable BCC solid solution. The study of the thermal stability of the phases formed, and the irradiation response of the as-cast alloy is discussed in the following paper. The following experimental procedures can then be used to determine a range of suitable low activation alloys for use as plasma-facing materials – this is discussed in Chapter 5-7.

4.2. Lead Author Contributions

- Consolidation of resources for literature review and addition of all references
- Experimental data selection and validation, formal analysis, and presentation
- Writing of original draft, review, and editing

4.3. Publication Status

This paper was published in 'Journal of Nuclear Materials' vol. 531, p. 152005, available online January 2020.

https://doi.org/10.1016/j.jnucmat.2020.152005

4.4. Approval Status

Co-authors and supervisors:	Internal (REVIEWED)	External (REVIEWED)
EUROfusion:	Kinga Gal (ENDORSED)	Tony Donne (CLEARED)

Journal of Nuclear Materials 531 (2020) 152005

Contents lists available at ScienceDirect

Journal of Nuclear Materials

Radiation damage tolerance of a novel metastable refractory highentropy alloy $V_{2.5}Cr_{1.2}WMoCo_{0.04}$

Dhinisa Patel [a, *], Mark D. Richardson [b], Bethany Jim [a, c], Shavkat Akhmadaliev [d], Russell Goodall [a], Amy S. Gandy [a]

[a] Department of Materials Science and Engineering, University of Sheffield, S1 3JD, UK
[b] UKAEA, Culham Centre for Fusion Energy, Culham Science Centre, Abingdon, Oxfordshire, OX14 3EB, UK
[c] Department of Materials, University of Oxford, Parks Road, Oxford, OX1 3PH, UK
[d] Institute of Ion Beam Physics and Materials Research, Helmholtz-Zentrum Dresden-Rossendorf, Dresden, 01328, Germany

a r t i c l e i n f o

Article history:
Received 24 September 2019
Received in revised form
20 December 2019
Accepted 14 January 2020
Available online 18 January 2020

Keywords:
High entropy alloy (HEA)
Structural materials
Ion implantation
Radiation damage
Metastability

a b s t r a c t

A novel multicomponent alloy, $V_{2.5}Cr_{1.2}WMoCo_{0.04}$, produced from elements expected to favour a BCC crystal structure, and to be suitable for high temperature environments, was fabricated by arc melting and found to exhibit a multiphase dendritic microstructure with W-rich dendrites and V-Cr segregated to the inter-dendritic cores. The as-cast alloy displayed an apparent single-phase XRD pattern. Following heat treatment at 1187 °C for 500 h the alloy transformed into three different distinct phases - BCC, orthorhombic, and tetragonal in crystal structure. This attests to the BCC crystal structure observed in the as-cast state being metastable. The radiation damage response was investigated through room temperature 5 MeV Au^+ ion irradiation studies. Metastable as-cast $V_{2.5}Cr_{1.2}WMoCo_{0.04}$ shows good resistanceto radiation induced damage up to 40 displacements per atom (dpa). 96 wt% of the as-cast single-phase BCC crystal structure remained intact, as exhibited by grazing incidence X-ray diffraction (GI-XRD) patterns, whilst the remainder of the alloy transformed into an additional BCC crystal structure with a similar lattice parameter. The exceptional phase stability seen here is attributed to a combination of self-healing processes and the BCC structure, rather than a high configurational entropy, as has been suggested for some of these multicomponent "High Entropy Alloy" types. The importance of the stability of metastable high entropy alloy phases for behaviour under irradiation is for the first time highlighted andthe findings thus challenge the current understanding of phase stability after irradiation of systems like the HEAs.

1. Introduction

Initially detailed by Yeh et al. (2004) [1] and Cantor et al. (2004) [2], high entropy alloys (HEAs) are described as multi-component metallic systems with no principal element. Sometimes termed multicomponent concentrated solid-solution alloys (CSAs) they are defined as alloys with five or more alloying elements present either equiatomically, or in the range of 5-35 at %, offering a wide range of possible HEAs. Typically, HEAs have been proposed for use as structural applications due to their superior mechanical properties, including high hardness and wear resistance (Huang et al., 2004 and Chuang et al., 2011) [3,4], high temperature strength (Senkov et al., 2014) [5] and corrosion resistance; it is these properties which make HEAs attractive for applications in extreme environments. The high configurational entropy of these alloys has beenproposed to encourage the formation of solid solutions consistingof simple body-centered cubic (BCC) or face-centered cubic (FCC)crystal structures rather than the more highly ordered intermetallic phases. For extreme environments, including high temperature and neutron bombardment, the formation of undesirable phases during exposure to operational temperatures would likely result in a decline of mechanical performance potentially to an inoperable level. At elevated temperatures the high mixing entropy decreases the Gibbs free energy of the system and so greatly contributes tothe stability of single-phase HEAs, but this effect bears less significance at lower temperatures. Additionally, enthalpy can also lead to phase separation even at high mixing entropy states (Wei et al.,

* Corresponding author.
E-mail address: ddpatel1@sheffield.ac.uk (D. Patel).

2018) [6]. Exploration of the temperature-dependent metastability of HEAs has shown to sometimes result in enhanced toughness, ductility, and strength. For example, upon quenching, non-equiatomic $Fe_{50}Mn_{30}Co_{10}Cr_{10}$ undergoes a partial martensitic transformation to HCP from room temperature stable FCC, resulting in an increase of ductility and strength (Li et al., 2016) [7].

HEAs have been reported to exhibit a self-healing process (Egami et al., 2014) [8] during energetic ion implantation, proposed to be due to high formation energies of vacancies and interstitials in HEAs induced by local atomic-level stresses. It has often been re- ported that HEAs possess high atomic stresses, in comparison to conventional alloys, due to the large differences in atomic sizes of the elements incorporated in the lattice (He and Yang, 2018) [9]. However, the difficulty of directly quantifying lattice strain by experimental methods has led to uncertainty in attributing the exceptional properties observed in HEAs to lattice distortion. For example, recent work by Owen et al. (2017) [10] examined the local lattice distortion of CrMnFeCoNi, 'Cantor's alloy', using total scattering data from neutron diffraction studies. They reported that the lattice strain was not significantly large and was similar to the lattice strain in CrNi and CoCrNi. It should be noted that in this work, the atomic level stresses in the alloys are not assessed in this manner, and so the effect on the radiation damage tolerance cannot be assessed. Upon ion implantation, particle bombardment can initiate atomic displacements leading to thermal spikes, which may result in the recovery of Frenkel pairs. For high entropy alloys, this can result in high recombination of defects, decreasing local strain, leaving the alloy with significantly fewer defects than conventional materials, and thus restrains the formation of dislocation loops and voids (Xia et al., 2015) [11]. Irradiation-induced defects lead to structural damage in materials and so the self-healing effect is another feature making HEAs an attractive candidate for fission and fusion-based nuclear reactors (Liaw et al., 2015) [12].

Recent studies have reported the radiation response of some HEAs (Kombaiah et al., 2018; Kumar et al., 2016; Xia et al., 2015) [11,13,14] where many of these studies have been for homogenised single-phase alloys. Studies regarding the phase stability of HEAs after irradiation mostly focus on single-phase FCC crystalline structures with many revolving around relatively minor variations to the content and composition of CrMnFeCoNi (Lu et al., 2018; He et al., 2017; Xia et al., 2015) [11,15,16] and therefore concentrating on the 3d transition metals. For materials exposed to irradiation by heavy, energetic particles, BCC-structured materials are generally preferred over those with an FCC crystal structure as they are more radiation damage-tolerant. This is likely due to the enhanced formation of small defect clusters and finely dispersed point defects in non-close-packed BCC materials as opposed to the larger, less mobile defect clusters seen in FCC materials. Smaller defect clusters enhance the probability of vacancy-interstitial recombination upon ion implantation, thus reducing irradiation-induced structural changes in materials (Zinkle, 2005) [17]. When considering materials for radiation damage resistance, phase changes during service are of concern as they are likely to alter the microstructure of the alloy, thus affecting the in-service mechanical performance.

Conventional multiphase alloys subjected to ion implantation have been studied to determine their response in extreme environments. It is known for multiphase alloys that upon ion implantation the second-phase precipitates undergo a series of complex processes simultaneously including: disordering or amorphisation, radiation enhanced diffusion, and irradiation-induced solute segregation (Li et al., 2015) [18]. Alternatively, in nano-structured alloys irradiation generally leads to the formation of precipitates. Nano-structured Cu-based alloys, $Cu_{93.5}W_{6.5}$ and $Cu_{99}W_1$, upon 1.8 MeV Kr irradiation resulted in the uniform distribution of W-rich nano-precipitates. The absence of nano-precipitates after thermal annealing implies the formation of nano-precipitates occurred during the thermal spike phase of the cascade evolution (Tai et al., 2012 and 2014) [19,20]. It has been shown that nanoscale precipitates serve as point defect recombination sites and so are an effective way of minimising remaining defects at high temperatures (Zinkle, 2005) [17].

There is a clear need therefore to explore the effectiveness of multiphase HEAs against radiation damage. This sentiment is echoed by both Miracle et al. (2014) [21] and Liaw et al. (2015) [12] who advise against the sole pursuit of single-phase solid solution alloys and instead suggest intentionally adding secondary phases to examine the efficacy of particle strengthening of HEAs which can be more effective at higher temperatures than other classical strengthening mechanisms (work-hardening, solid solution strengthening, grain boundary strengthening).

The Single-Phase High Entropy Alloy (SP-HEA) 31.3Cr-23.6Mo-26.4V-18.7W (termed CrMoVW) was recently fabricated and characterised in the as-cast state for application in high temperature, oxidising environments (Ikeuchi et al., 2019) [22]. The composition was determined through Density Functional Theory (DFT) studies and the Alloy Search and Predict (ASAP) method to maximise the alloy melting temperature whilst also maintaining a single phase below the solidus. Refractory elements were chosen for their high melting temperatures (and then ranked by low cost) as well as an addition of Cr to prevent oxide scale formation. The binary phase diagrams of the elements all indicate formation of a BCC solid solution over a wide temperature range and across a variety of compositions with no apparent binary intermetallic compounds. All the elemental crystal structures are BCC-structured over a wide range of temperatures which further promotes the stability of a BCC solid solution. In the current work, to reduce the elemental segregation displayed by the alloys fabricated by Ikeuchi et al. [22] (formed by large differences in the melting temperatures of the components), refinement of the alloy composition and amendment of the arc-melting process were undertaken. The alloy design process was achieved by utilising a combination of the CALPHAD method and the thermodynamic parameters used for prediction of solid solution for high entropy alloys (Gandy et al., 2019) [23] resulting in the prediction of a novel alloy of nominal composition $V_{2.5}Cr_{1.2}WMo$. To avoid the only partial melting of the MoVW phase observed in the CrMoVW alloy, all constituents were melted together with the highest melting temperature elements covering the lowest melting temperature elements. Additional Cr was added to the elemental mix to account for its low boiling point and subsequent partial evaporation during fabrication. To explore the microstructural and elemental distribution changes after irradiation this alloy was characterised in the as-cast state and after room temperature Au^+ ion implantation, and to assess thermal stability the alloy was annealed at intermediate temperature (1187 °C) for 500 h.

The key aim of this study is to evaluate whether a multiphase HEA, in this case VCrMoWCo, may possess the same phase stability as found for some single-phase HEAs. Many alloys described as HEAs do not have a single-phase structure, and this is particularly true of those based on the refractory elements (Huang et al., 2017; Fazakaz et al., 2014; Guo et al., 2016) [24,26]. This could be significant for radiation damage resistance as, on the atomic scale where incident particles are interacting with the material, potentially inducing damage, the local environment of the atoms in a multiphase structure will be significantly different and potentially much less disordered and therefore less likely to benefit from some of the suggested inherent advantages to HEAs. However, in contrast to recent research, we find that the multiphase nature does not negatively impact the radiation damage response, therefore suggesting an alternative mechanism to configurational entropy stability underlying the behaviour on irradiation.

2. Materials and methods

2.1. Alloy design

Efforts have been made to quantitatively predict alloy compositions with a single-phase solid solution (Takeuchi and Inoue, 2000 and 2005; Zhang et al., 2008) [27e29]. Thermodynamic parameters derived and extrapolated from the Hume-Rothery rulesinclude atomic size difference and heat of mixing of binary pairs which were proposed by Takeuchi and Inoue (2000) [27] for the formation of bulk metallic glasses (BMGs). This advancement of the understanding of formation of BMGs (Takeuchi and Inoue, 2005)
[28] has also helped high entropy alloy design. In the first instance, the following design process was implemented to approximate an alloy composition from chosen elements to form a single-phase BCC structure. To identify the possibility of the formation of any intermetallic compounds at lower temperatures, this approach was then coupled with the use of the CALPHAD approach to predict a phase diagram for the identified alloy composition over a range of temperatures.

2.2. Thermodynamic parameters approach

Zhang et al. (2008) [29] identified atomic and thermodynamic parameters which could give the likelihood of the formation of solid solution systems, specifically for multicomponent alloys based on the behaviour of its constituent elements. The terms include entropy of mixing (ΔS_{mix}), atomic size difference (δ), and mixing enthalpy of a solid solution (ΔH_{mix}), and can be expressed by their respective equations:

$$\Delta S_{mix} = -R \Sigma c_i \ln c_i \quad (1)$$

where c_i is the atomic percentage of each component and R is the gas constant. The high entropy of mixing resulting from the presence of a large (>5) number of components in an alloy was initially thought to encourage the formation of a disordered solid solution.However, Otto et al. (2003) [30] systematically studied the effect of the ΔS_{mix} term on single-phase formation. The substitution of one element at a time from the well-established single-phase solid solution Cantor's alloy, CoCrFeMnNi, would keep the ΔS_{mix} termconstant in the altered alloys. Instead of retaining the single phase of the Cantor's alloy, the substituted alloys contained multiple solidsolution phases and intermetallic compounds. This highlights thedeficiency of use of the ΔS_{mix} term in isolation to predict a single-phase solid solution.

Additional terms which have shown importance in the prediction of stable solid solution include:

$$\delta = 100 (\Sigma c_i (1-r_i/r)^2)^{1/2} \quad (2)$$

where $r = \Sigma r_i c_i$ and is the average atomic radius of all components, and r_i is the atomic radius of each component. And:

$$\Delta H_{mix} = \Sigma 4 H_{ij} c_i c_j \quad (3)$$

where the H is the enthalpy of mixing values for each binary pair of atoms (i and j) and can be calculated from the Miedema model (Takeuchi and Inoue, 2005) [28]. This approach has been used by many to determine the enthalpy of formation of multicomponent alloys and for the prediction of solid solution formation. The Miedema model was initially used for the binary pairs of elements and its extrapolation for multicomponent alloys has received criticism by some. Troparevsky (2015) [31] states that the sum of the en thalpies of pairs of elements can disguise the extreme values of individual pairs if they average to a near zero value. Particularly negative values of ΔH_{mix} for a pair of elements will result in the precipitation of this compound from the alloy, yet this is not always apparent from the sum of the values from all the pairs of elements. Whilst this method for determining ΔH_{mix} can be insufficient for some alloys, including CoCrFeMnNi, the pairs of elements used in this study all have near zero ΔH_{mix} values (Table 2) and so the approach is deemed satisfactory for this alloy as precipitation of compounds is unlikely.

Guo and Liu (2011) [32] compiled existing experimental data from as-cast high entropy alloys to determine the likelihood of solid solution phase formation. From the analysis of these findings, they stated that for the formation of a solid solution in a high entropy system the previously stated terms must be within certain limits (Table 1). As discussed above for this particular alloy, the compositionally weighted averaged ΔH_{mix} term cannot be used for the prediction of intermetallic compounds in a chosen alloy, for this ΔH_{IM} for the intermetallic-forming elements must be calculated. This highlights the need to identify the elements in the alloy which have the potential to form intermetallic compounds; it is for this reason the binary, ternary, and quaternary phase diagrams are used to establish all the potential phases that may form (Table 3). Across all combinations of elements, only a solid solution BCC phase is formed and for this reason the thermodynamic parameters calculated here for $V_{2.5}Cr_{1.2}WMo$ are deemed reasonable for design of the alloy composition.

Further expansion of these terms also includes utilising the Hume-Rothery rule for valence electron concentration (VEC); a critical parameter which determines whether an FCC (> 8) and BCC phase (< 6.87) will form. From Table 1 we can see that theaveraged VEC for $V_{2.5}Cr_{1.2}MoW$ predicts a BCC solid solution to form.

Yang and Zhang, (2012) [33] later defined a new parameter, Ω, to predict the formation of a solid solution when $\Omega > 1.1$ and $\delta < 6.6\%$:

$$\Omega = (T_m \Delta S_{mix})/\Delta H_{mix} \quad (4)$$

where T_m is the melting temperature of the alloy using the rule of mixtures approach.

For the BCC-structured elements V, Cr, Mo, and W each parameter was calculated for a range of compositions for each element from 5 to 35 at%. The most desirable alloy composition minimises the atomic size mismatch whilst ensuring the VEC is below 6.87 and the enthalpy of mixing is between 0 and -5 kJ/mol. It was determined that the composition $V_{2.5}Cr_{1.2}WMo$ met the criteria of these parameters (Table 1).

2.3. Thermo-Calc

The software Thermo-Calc version 2018b, based on the CALPHAD method, was used to calculate the property diagram of equilibrium phases as a function of temperature. The SSOL4 (SGTE Alloy Solutions Database v4.9g) thermodynamic database was utilised to ensure the binary phase diagrams of the all the elements were taken into consideration. To verify the predictions from the thermodynamic parameters approach, the equilibrium phases of

Table 1
The calculated thermodynamic parameters for $V_{2.5}Cr_{1.2}WMo$ in addition to the boundary conditions stated in literature for the formation of a solid solution.

	U	d	DS_{mix}	DH_{mix}	VEC
Literature	>1.1	0-8.5	11-19.5	−22-7	<6.87 for BCC
V2.5Cr1.2WMo	24.7	3.2	10.8	−0.92	5.6

Table 2
Calculated ΔH_{mix} values for the binary pairs of VCrMoW using Miedema's model.

	V	Cr	Mo	W
V	x	−2	0	−1
Cr	-	x	0	1
Mo	-	-	x	0
W	-	-	-	x

Table 3
Crystal Structures identified for the binary and ternary phases (at several isotherms) of V2.5Cr1.2WMo.

System	Solid Solution Phase	Intermetallic compounds
V-Cr	BCC	-
V-Mo	BCC	-
V-W	BCC	-
Cr-Mo	BCC	-
Cr-W	BCC	-
Mo-W	BCC	-
V-Cr-Mo	BCC	-
V-Cr-W	BCC	-
Cr-Mo-W	BCC	-

the nominal alloy $V_{2.5}Cr_{1.2}WMo$ were calculated. To accurately determine the phases in the as-cast alloy the experimentally obtained elemental composition from XRF data was used to calculate the equilibrium phase diagram of the $V_{2.5}Cr_{1.2}WMoCo_{0.04}$ alloy fabricated.

2.4. Alloy preparation

The mass of each elemental metal was weighed out for the required composition of a 5g alloy of VCrWMo (all elemental metals sourced from Alfa Aesar with a purity >99.5%). Using a vacuum arc melter (MAM1 Buehler) under a high-purity argon atmosphere with a water-cooled copper hearth and a Ti-getter, a button-shaped ingot was fabricated. Flipping and remelting of the ingot at least five times ensured greater chemical homogeneity.

The alloy was then prepared for irradiation and characterisation using SiC grit papers up to P2500 followed by polishing solutions and finishing with colloidal silica to ensure a mirror-like finish.

2.5. Irradiation

The polished side of the as-cast alloy was implanted at room temperature with 5 MeV Au^+ ions to a fluence of 5x 10^{15} Au^+ ions per cm^2 at the Ion Beam Centre in Helmholtz-Zentrum Dresden-Rossendorf, Germany. Using the experimental density measurement, results calculated from the Monte Carlo code SRIM (Zeigler et al., 1985) [34] indicated this implantation condition would produce ballistic damage in a region from the surface to a depth of approximately 800 nm, with a peak damage of about 40 dpa 300 nm below the surface, shown in Fig. 1.

2.6. Heat treatment

The as-cast alloy underwent an ageing heat treatment at 1187 °C. This is approximately 0.5 T_m, estimated from the experimentally determined elemental compositions from XRF data using the rule of mixtures methodology to provide an estimate of the melting point (Table 4). The alloy was encapsulated in an evacuated silica quartz ampoule to minimise oxidation, heat treated in a boxfurnace for 500 h and then quenched in water to preserve the equilibrium phases at the chosen intermediate temperature.

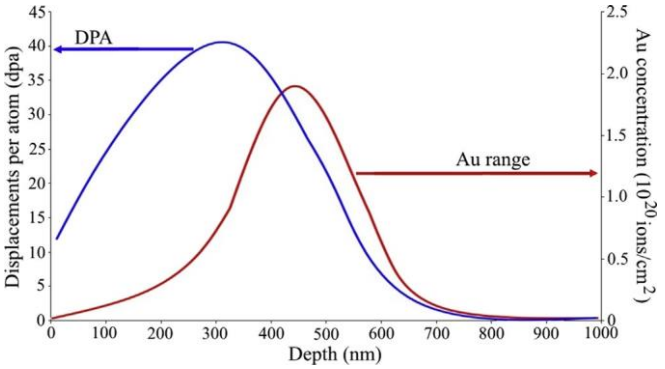

Fig. 1. Damage profile calculated using the SRIM code.

2.7. Alloy characterisation

To determine the crystal structure of the alloy after Au^+ ion implantation, Grazing-incidence X-ray diffraction (GI-XRD) was carried out using a PANalytical X'pert³ Powder diffractometer with Cu Ka radiation operated at 45 kV and 40 mA. For irradiated samples, the X-ray penetration depth was calculated using linear attenuation theory. An incident angle of 1.947° was calculated to probe a depth of 500 nm below the surface, in accordance with SRIM results, so only the near-surface implantation-induced damage region would be probed. To perform phase analysis, the International Centre for Diffraction Data's (ICDD) SIeve software wasused to search the PDF -4 database. Refined lattice parameters forthe crystal structures were determined using the least squares refinement method from the STOE WinX^{POW} software. X-ray fluorescence (XRF) using a PANalytical Zetium spectrometer under vacuum at room temperature with a spot size of 6 mm was used to establish the relative elemental composition of the alloy (in the heat-treated condition) using the PANalytical Omnian analysis software. The microstructure of the alloy was investigated by scanning electron microscopy (SEM), using a Hitachi TM3030 Tabletop SEM, operating at 15 keV, and an FEI Inspect F50 SEM, operating at 20 kV with energy dispersive X-ray (EDX) spectroscopyto detect the elemental distribution within the phases. Vickers microhardness testing was performed on a Bakelite mounted sample in five random locations of the button-shaped alloy. The dwell time was set to 10s, magnification 40, with a load of 1 kgusing a Struers DuraScan-70 system. The density of the as-cast alloywas determined using the Archimedes method using a Mettler Toledo NewClassic MF balance.

3. Results and discussion

3.1. As-cast $V_{2.5}Cr_{1.2}WMoCo_{0.04}$

There was a small contamination of Co in the water-cooled copper crucible in the vacuum chamber during the melting process, with the quantitative analysis of the heat-treated alloy by XRF characterisation calculating the composition to be 43.4V-21.75Cr- 17.11W-17.11Mo-0.635Co. Although small and unintentional, recognising the potential for this content to impact on properties wetherefore refer to the alloy throughout the rest of this work as $V_{2.5}Cr_{1.2}WMoCo_{0.04}$.

For the as-cast alloy, SEM and EDX mapping clearly show a multiphase, mostly dendritic, microstructure (Fig. 2a and c); this can be attributed to elemental segregation on a microscale. During the melting process, the highest melting element (W) solidifies preferentially into the growing dendrites, whilst V and Cr segregate

Table 4
Measured elemental composition (in atomic percentage) of the alloy using XRF data. The melting temperature, T_m, lattice constant, a, for each pure element in the alloy, as well as calculated and experimental alloy averages. The density of each pure element and calculated density, ρ, for the alloy is also displayed.

	V (at%)	W (at%)	Mo (at%)	Cr (at%)	Co (at%)	Alloy calc.	Alloy exp.
Elemental composition (at%)	43.4	17.11	17.11	21.75	0.635	-	-
T_m (°C)	1910	3422	2623	1907	1495	2277	-
a (pm)	303	316.5	314.7	291	250	302.65	-
ρ (gcm^{-3})	6.11	19.25	10.28	7.19	8.9	9.647	10.94

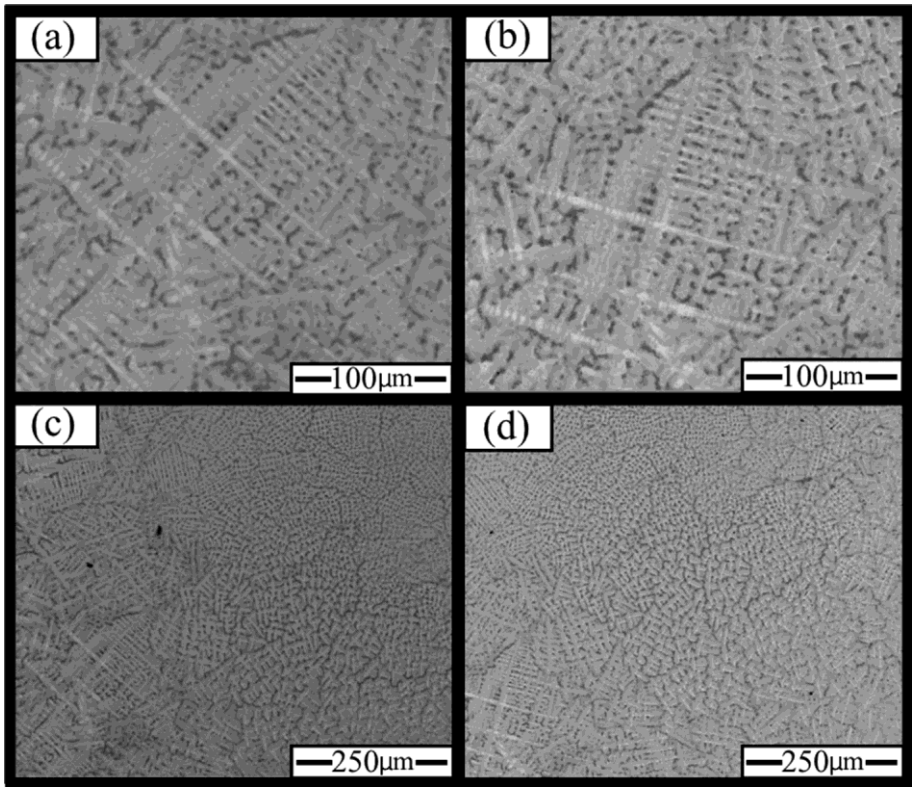

Fig. 2. (a, c) Backscattered electron images of different regions in as-cast $V_{2.5}Cr_{1.2}WMoCo_{0.04}$, (b, d) showing the same regions after 5 MeV Au^+ ion irradiation depicting that no microstructural changes have taken place. The post-irradiation alloy still displays the same dendritic microstructure, indicating stability of the elemental segregation of the as-cast state.

into the inter-dendritic regions. Mo is more homogeneously distributed, with slight preferential distribution to the inter-dendritic regions (Fig. 3a). As suggested by Ikeuchi et al. (2019) [22] the preferential segregation of V and Cr is likely to be due to the negative enthalpy of mixing of V-Cr in comparison to the slightly positive enthalpy of mixing between W-Cr and Mo-Cr. The small content of cobalt is clearly segregated from the rest of the melt and precipitates by itself in the inter-dendritic region. For the elements V, Cr, Mo, and W when assessing the binary phase diagrams (Brandes and Brook, 2013) [35] there is a continuous solidsolution formation across the entire temperature range with very little formation of intermetallic compounds (only CrW_3 is suggested as potentially forming at 91 wt% of W). The binary phasediagrams for the elements including Co are more complex and suggest the formation of a variety of intermetallic compounds overa range of temperatures and compositions with all the other elements present. This suggests that the removal of cobalt from the alloy would produce very similar results with respect to morphology and crystal structures. The small atomic percentage of cobalt present in the alloy does not appear to play a significant role in the microstructure or have a substantial effect on phase stability and thus is established as a contaminant within the alloy.

As-cast $V_{2.5}Cr_{1.2}WMoCo_{0.04}$ displayed a single BCC phase XRD pattern (Fig. 4) where indexes of the crystal planes of the experimental diffraction peaks corresponds to an Im-3m space group with a lattice parameter a=3.0348 Å (Table 6). This is in good agreement with the ROM (Vegard's law - Vegard, 1921) [36] calculated lattice parameter a=3.0265 Å (Table 4). This match is consistent with a random distribution of the elements in a single-phase structure, i.e., the BCC solid solution. Additionally, both density measurements, experimental and theoretically predicted, support that the alloy is likely in a random disordered solid solution state. The small resultantincrease in percentage volume, 13.41%, is attributed to the porosity observed in the as-cast alloy, directly formed from the rapid cooling rates induced by the process of arc-melting.

The detection of a single-phase from XRD data (Fig. 4), but observation of a multiphase microstructure from SEM (Fig. 2), may result from the crystal structures of the two (or more) observed phases being of the same type and very similar in lattice parameter; this is expected as all the pure elements are BCC metals (Table 4) and have similar lattice constants (aside from Co which has an FCC and HCP phase at room temperature) resulting in a less distorted

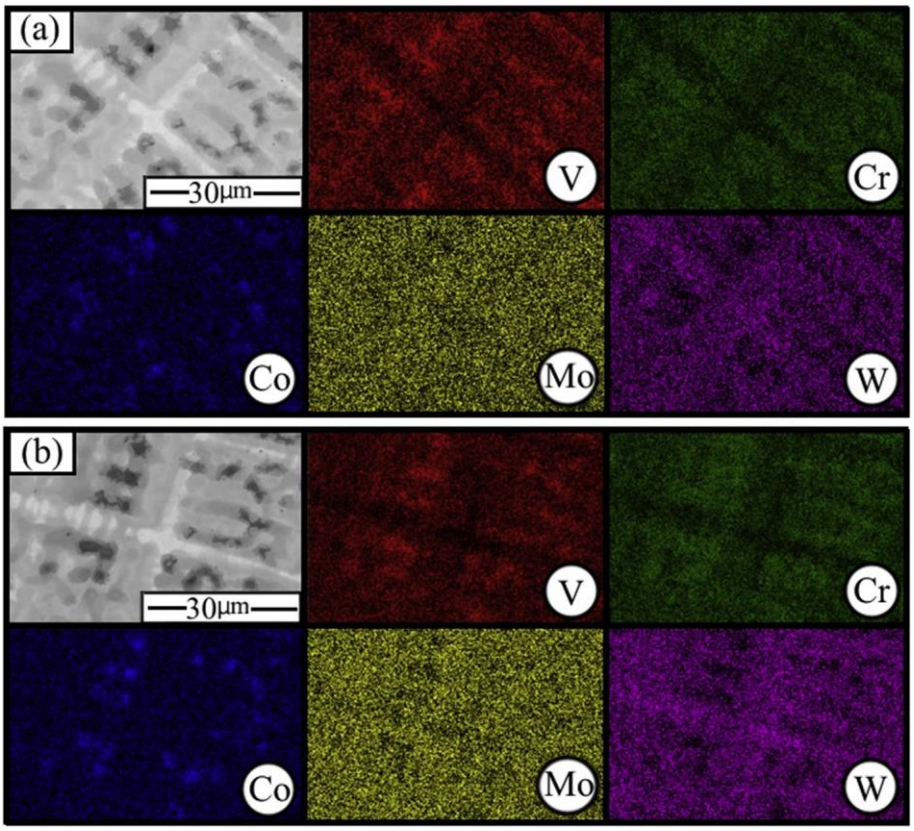

Fig. 3. BSE image and EDX maps of the same region in (a) as-cast and (b) irradiated $V_{2.5}Cr_{1.2}WMoCo_{0.04}$.

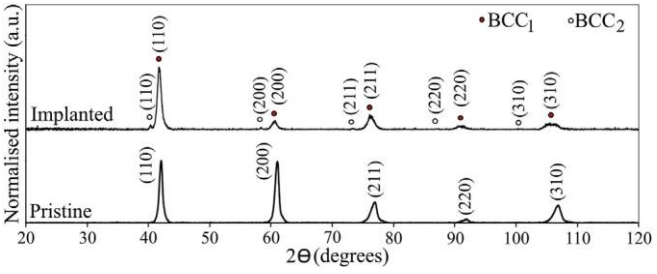

Fig. 4. XRD patterns of as-cast $V_{2.5}Cr_{1.2}WMoCo_{0.04}$ and 5 MeV Au+ ion irradiated $V_{2.5}Cr_{1.2}WMoCo_{0.04}$. The filled and unfilled circles denote the two BCC phases present in irradiated $V_{2.5}Cr_{1.2}WMoCo_{0.04}$, where the red filled circle denotes the as-cast BCC phase mostly retained post-irradiation. (For interpretation of the references to colour in this figure legend, the reader is referred to the Web version of this article.)

lattice and stable crystal structure. The as-cast XRD pattern displayed narrow peaks but with a slight shoulder on the right-hand side of the peaks at a higher angle indicating a possible overlap of two or more very similar disordered BCC phases. This coincides with SEM observations and will be further resolved using the sensitivity of neutron diffraction and transmission electron microscopy at a later date.

Confirmation that the BCC phase would be expected can be seen from the Thermo-Calc predictions which show a single ordered BCC phase over a wide temperature range from 750 °C to 2400 °C. Additionally, the presence of two ordered BCC_A2 phases is predicted up to 700 °C (Fig. 5). The Rule of Mixtures (ROM) melting temperature (Table 4) also accurately matches the Thermo-Calc calculation, mostlikely due to the absence of predicted intermediate phases resulting ina less significant temperature deviation from the ROM value.

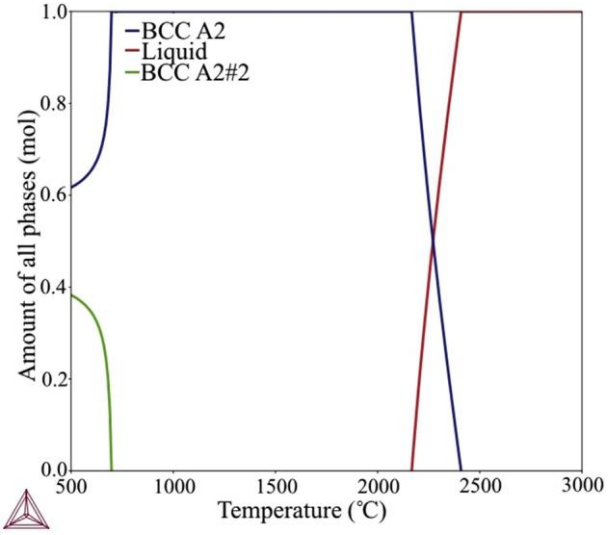

Fig. 5. Predicted Thermo-Calc property diagram, indicating the formation of two ordered BCC_A2 phases to be present in $V_{2.5}Cr_{1.2}WMoCo_{0.04}$. The first BCC_A2 phase to be formed is stable over a wide range of temperatures, indicating a single-phase is likely to be present in the alloy.

3.2. Irradiated $V_{2.5}Cr_{1.2}WMoCo_{0.04}$

GI-XRD examination of the post-irradiated $V_{2.5}Cr_{1.2}WMoCo_{0.04}$ revealed a retention of ~96 wt % of the as-cast BCC crystal structure (Fig. 4) despite some broadening of the peaks at higher angles. This predominant phase has a refined lattice parameter of a = 3.0594 Å.

The additional 4 wt% is attributed to the transformation of a second BCC structure, with an Im-3m unit cell, and an expansion of the lattice parameter a≈3.1603 Å. The retainment of the as-cast crystal structure is somewhat surprising as in conventional alloys ion implantation can promote a change in crystal structure and/or phase segregation. An example of these radiation-induced effects can be shown by the self-ion irradiation of Ferritic/Martensitic HT9steel. After irradiating at 1, 10, and 2 dpa using 5 MeV Fe^{2+} ions, Ni and Si segregation at defect sinks along with precipitation of a Ni, Si, Mn rich G-phase was reported [37]. Radiation-enhanced diffusion increases atomic diffusion during irradiation due to the enhanced number of defects and the continual creation of newdefects. Under irradiation, the concentration of interstitials and vacancies within a material are increased when compared to those produced thermally, which results in diffusion coefficients several orders of magnitude larger than thermal diffusion coefficients. For example, enhanced chromium diffusion in austenitic steel alloys is typically observed after ion irradiation, ~4 orders of magnitude higher than that of the thermally annealed sample (Chen et al., 2018) [38], however it is predicted for HEAs that sluggish atomic diffusion may suppress this effect, and this is addressed later in thediscussion.

There is no apparent elemental rearrangement or variation in composition in the dendritic and interdendritic regions following ion implantation; EDX maps (Fig. 3b) of the alloy after irradiation are in good agreement with the as-cast sample further underlining the exceptional phase stability. No radiation-induced segregation (RIS) has taken place due to the ion implantation taking place at room temperature. Normally at elevated temperatures, a redistribution of solute and impurity elements leads to enrichment or depletion of alloying elements near the implantation surface, dislocations, voids, and grain boundaries. Such radical changes can lead to localised property differences and an overall loss in integrity of the component. The stability of $V_{2.5}Cr_{1.2}WMoCo_{0.04}$ could be attributed to the chemical heterogeneity of the single-phase structure in HEAs, which results in the pinning of dislocations (Wu et al., 2016) [39] and reduced thermal conductivity, due to the lattice distortion effect (Xia et al., 2016 and Gao et al., 2016) [40,41].

Some studies have shown structural stability on irradiation of single phase HEAs and attributed the irradiation tolerance to high configurational entropy (Murty et al., 2014) [42]. Reports so far have stated that multiphase alloys exhibit phase separation and thus are not stabilised against radiation damage by the high entropy effect. In this case, the similarity between the two dendritic BCC phase lattice parameters may indicate a two-phase structure that is not detrimental to phase stability. Comparable HEA studies displaying results from similar implantation fluences include Xia et al. (2015) [11] and Yang et al. (2016) [43]. $V_{2.5}Cr_{1.2}WMoCo_{0.04}$ can be likened to the HEAs in these reports, $Al_xCoCrFeNi$, which similarly displayed structural stability up to 50 dpa from Au ions at room temperature. With regards to phase stability, the as-cast single FCC phase $Al_{0.1}CoCrFeNi$ HEA demonstrated excellent phase preservation, whereas the as-cast multiphase alloys displayed irradiation- induced defect clusters and precipitation, as observed by TEM studies, upon ion irradiation. This instability upon implantation was credited to the initial phase separation and ordered nature of the multiple phases, causing them to behave like conventional bi- nary and ternary alloys. In the same study, the single-phase as-castalloys demonstrated no precipitation for doses of 43 dpa. The atomic scale rearrangement in the ion-implanted $V_{2.5}Cr_{1.2}WMoCo_{0.04}$ cannot be observed due to the resolution of SEM. Future TEM studies will reveal if any fine scale precipitation oratomic rearrangement has occurred.

Despite having a multiphase microstructure, the structural phase stability of $V_{2.5}Cr_{1.2}WMoCo_{0.04}$ after irradiation at doses of up to 42 dpa is evident as shown by the SEM micrographs (Fig. 2 b, d) and the GI-XRD pattern (Fig. 4). In this report, results gathered from the SRIM simulation (Fig. 1) indicate that the maximum radiation damage depth would be at 800 nm below the implantation surface with peak damage of 40 dpa occurring at 300 nm, and a damage level of 10 dpa at the surface. However, there is little difference in the morphology post-irradiation, with structural features also being retained. The average ion penetration of the $Al_{0.1}CoCrFeNi$ alloywas less than 100 nm which was enough to observe by SEM irradiation-induced structural changes. Some HEAs have been found to exhibit structural changes with as little as 1 dpa; equiatomic CrFeCoNiMn and CrFeCoNiPd alloys produced a further L10 phase and spinodal decomposition after 1250 eV electron irradiation (He et al., 2017) [16]. Whilst GI-XRD allows for investigation ofany implantation-induced structural modifications below the sur-face, only surface modifications can be detected by the SEM used in this study. SRIM typically overestimates the amount of damage produced, as the simulation assumes the sample to be amorphous, and at absolute zero. Therefore, in reality the level of damage produced at surface may not have been sufficient to cause micro-structural changes.

Unlike the single-phase HEAs, where their phase stability has been attributed to their high configurational entropy, as-cast $V_{2.5}Cr_{1.2}WMoCo_{0.04}$ exhibits clear elemental separation yet has still shown excellent phase stability at similar doses to the Al_x- CoCrFeNi irradiation studies. The results from this study thereforediffers from previous reports that suggest only single phase HEAs can demonstrate superior irradiation resistance (Kumar et al., 2016and Xia et al., 2015) [11,14] and instead indicates that the stability ofthe alloy studied here is partly dependent on the particular phases which are present and which phase transformations are likely to occur. As mentioned previously, suppressed atomic diffusion due to lower diffusion kinetics in HEAs has been previously reported in numerous different alloys (Zhang et al., 2014) [44] and this sluggish solute diffusion could be contributing to the suppression of phase transformations. However, as highlighted by reviews on the topic, Pickering and Jones (2016) [45] and Miracle and Senkov (2016) [46], there is not yet enough evidence to clearly demonstrate that atomic diffusion within HEAs is particularly sluggish in comparison to conventional alloys, and it may even be faster. It is unknown whether sluggish diffusion has played a role in the stability, as suggested by Kumar et al. (2016) [14] and Yang et al. (2016) [43], as the ion irradiation study in this report was not conducted at elevated temperatures. In this case, it is proposed that the self- healing effect of HEAs is responsible for the stability of the multi- phase alloy.

3.3. Annealed $V_{2.5}Cr_{1.2}WMoCo_{0.04}$

Whilst the as-cast state is mostly stable against phase changes following ion irradiation, upon heat treatment at 1187 C for 500 h, a phase transformation occurred with a further three phases being present in the XRD patterns (composed of a tetragonal, an orthorhombic phase, and a BCC phase) indicating the alloy did not consist of equilibrium phases in the as-cast state (Fig. 6). The heat- treated BCC phase has a slightly larger refined lattice parameter (a= 3.11¼ Å) than the phase present in the as-cast alloy (a =3.348 Å) ¼and accounts for 25 wt% of the microstructure. The tetragonal phase accounts for 24 wt% of the structure, is iso- structural to $V_{0.72}N_{0.28}$ and the Bragg peaks could be well-indexed using a P42/mnm unit cell with a lattice parameter of a = 9.111 Å and c = 4.8650 Å. The predominant phase with 51 wt% is an orthorhombic phase comparable to $Mn_{0.67}N_{0.33}$, Pbna unit cell, with most of the Bragg reflections indexed to refined lattice parameters of a = 6.061 Å, b = 3.996 Å, and c =4.898 Å. This unexpected phase

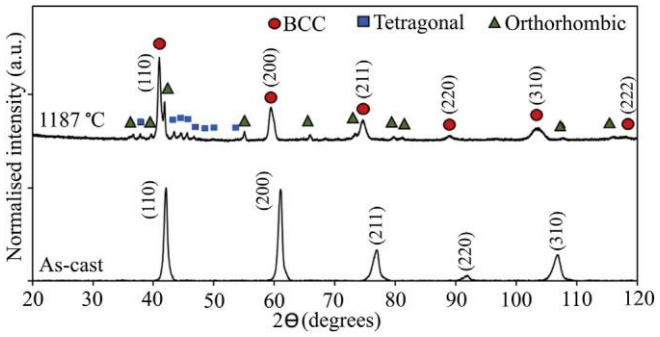

Fig. 6. XRD patterns of as-cast $V_{2.5}Cr_{1.2}WMoCo_{0.04}$ and heat-treated$V_{2.5}Cr_{1.2}WMoCo_{0.04}$ (1187 C for 500 h). The circles, squares and triangles above heat-treated $V_{2.5}Cr_{1.2}WMoCo_{0.04}$ correspond to the BCC, tetragonal, and orthorhombic structures of the phases present.

transformation, not predicted by the CALPHAD method, is evidence that the as-cast disordered BCC phases were metastable (and therefore their exceptional stability on irradiation cannot be attributed to them being in an inherently stable state). The validity of the predictive methods employed by Thermo-Calc have been examined for high entropy multicomponent systems. The thermodynamic database selected for the calculation of equilibrium phases is of great importance as this will determine which binary and ternary phase diagrams are used for the Gibbs free energy component of the phase diagram calculation. In this case the SSOL4 (Solid Solutions v4.9) thermodynamic database was chosen for this alloy as it includes all of the relevant elements. Other available thermodynamic databases: TCFE8 or TCNI8, are more suitable for steels/Fe-based alloys or Ni-alloys as the experimental data evaluated would be based on the respective elements. Another factor that needs to be considered is the relevance of the phases included in each database. For example, the TCNI8 (v8.2) Ni-alloys databasedoes not include the BCC_A2 disordered phase, whilst the SSOL4 database does. Nevertheless, the limited accuracy of the SSOL4 database may be demonstrated by the absence of some experimental data (including quaternary phase diagrams). Nonetheless the predicted phase diagram can be a good starting point for the alloy design of high entropy alloys. Contrary to this, Tancret et al. (2017) [47] reviewed a range of databases and their accuracy in predicting stable phases in concentrated alloy space but found there were small discrepancies.

Especially at lower temperatures and of the prediction of smaller concentrations of phases, Thermo-Calc has been shown to not accurately predict phases present experimentally in as-cast alloys, most likely due to the kinetic restraints of the computational method (Manzoni et al., 2015) [48]. This demonstrates that, whilst the CALPHAD method can be a useful tool in the high-throughput approach for the exploration of HEAs, care must be taken in accepting the prediction of equilibrium phases.

$V_{2.5}Cr_{1.2}WMoCo_{0.04}$ also exhibited microstructural changes after heat treatment. From the EDX maps (Fig. 7) Co is still segregated from the other elements post-heat treatment like both the as-cast state and upon irradiation. Whilst the W-rich dendritic cores remain unchanged, V has diffused out and precipitated in between the dendrites (Fig. 8). These V precipitates are attributed to the tetragonal phase detected in the XRD pattern as this structure was analogous to the $V_{0.72}Ni_{0.28}$ phase. Areas of the dendrites which appear to be retained likely consist of Cr-Mo-W according to the EDX maps, and this is expected to be isostructural to the BCC structure $Cr_{0.33}W_{0.33}Mo_{0.34}$ reported from the XRD data. This leaves the remaining inter-dendritic phase, Cr-Mo-Co to be associated with the majority orthorhombic phase. The tetragonal and orthorhombic phases were kinetically restricted during fabrication due to high cooling rates of arc-melting. Furthermore, the proposed slow diffusivity of elements in the multicomponent alloy may have contributed to the suppression of these additional phases. Due to homogenisation of the alloy, the dendritic structure is much less defined and has become globular and more rounded due to the reduction of interface area as seen in the back-scattered micrographs (Fig. 8).

The water-cooled copper crucible containing the ingot during fabrication induced rapid cooling which most likely would have suppressed the formation of equilibrium phases, resulting instead in quenched metastable BCC phases forming in the as cast state. This is also supported by the metastable dendritic microstructureas the formation of dendrites commonly occurs from the large undercooling where the melt is in contact with the cooled-copper crucible (although in such complex alloys constitutional supercooling cannot be discounted). For this reason, arc-melted HEAs frequently display dendritic microstructures in their as-cast state (Licavoli et al., 2015) [49].

Precipitation of V at 0.5 T_m was not wholly unexpected as it has been previously proposed that HEAs will decompose into more than one phase upon heat treatment above the solvus temperature (Tsai and Yeh, 2014) [50]. Precipitation of further phases at 1187 Cmay not be detrimental to its irradiation resistance at application temperatures (for example, claddings of a reactor core do not exceed a peak temperature of 700 °C) but indicates ion irradiation at elevated temperatures is needed if the application temperature is higher. Furthermore, as reported by Pickering et al. (2016) [51], there are several examples of HEAs which form precipitates at intermediate temperatures but demonstrate excellent phase stability at higher temperatures. To assess whether the as-cast phases are either metastable or if further phases are being kinetically restricted, additional prolonged annealing at intermediate temperatures is required. Even though at the intermediate temperatureof 1187 °C the alloy underwent a phase transformation, the meta- stable state of the alloy has shown stability against ion irradiation atroom temperature.

3.4. Vickers Microhardness

Table 5 shows the hardness values as determined using Vickers Microhardness testing. The exceptionally high hardness demonstrated by the as-cast alloy is comparable to many reported HEAs (Dang et al., 2018; Long et al., 2019) [52,53]. In HEAs the atoms areregarded as solute atoms and therefore form saturated solid solutions. This solid solution strengthening effect enhances the strength of these alloys, in comparison to similar conventional alloys, by impeding the motion of dislocations. The multi-phase nature of the alloy would also be expected to contribute to an increase in hardness.

The unexpected decrease in hardness post-irradiation (from 9.47 GPa ± 1.08 -7.55 GPa ± 0.18 see Table 5) may be further confirmation of the self-healing of radiation-induced defects and intrinsic material defects. Irradiating at low temperatures increases the likelihood of both radiation hardening and embrittlement in high entropy alloys and conventional alloys alike, thus causing a degradation of fracture toughness and increasing the ductile to brittle transition temperature (Victoria et al., 2001) [54]. This is a direct result of the defect-damaged microstructure that develops upon irradiation. At low irradiation temperatures (<$0.3T_m$) considerable hardening is predicted to occur due to the increase in irradiation defect clusters including dislocation loops which operate as obstacles to the glide of dislocations (Kumar et al., 2016) [14]. And so, a predicted increase in Vickers microhardness is expected to be observed post-irradiation as seen by many irradiated HEAs(Kumar et al., 2016; Yeh et al., 2004; El-Atwani et al., 2019) [1,14,55],

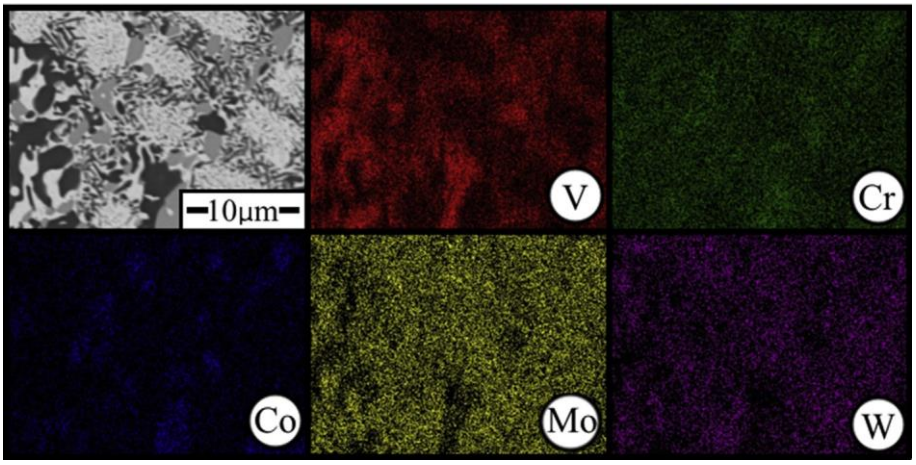

Fig. 7. BSE image and EDX map of the heat treated $V_{2.5}Cr_{1.2}WMoCo_{0.04}$.

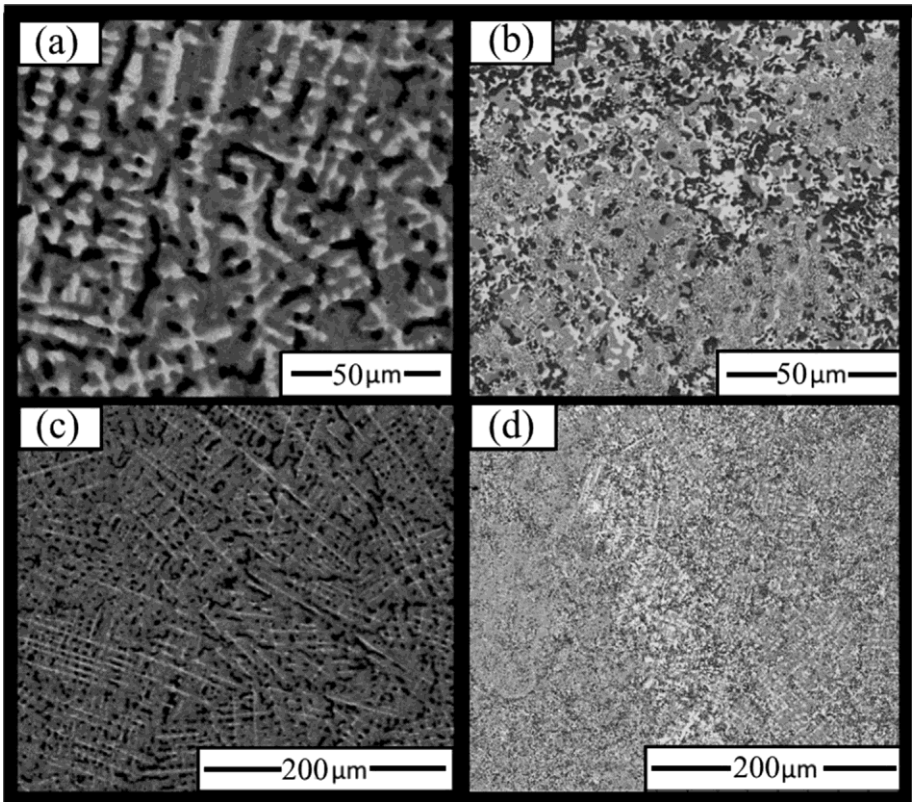

Fig. 8. BSE images of different regions in pristine $V_{2.5}Cr_{1.2}WMoCo_{0.04}$, (a, c) comparable regions to those in (b, d) respectively after heat treatment for 500 h at 1187 C.

yet the softening of the alloy can be further evidence of defect recombination, without these other hardening and embrittling effects. According to Egami et al. [8], the recrystallisation of the radiation-induced melt unexpectedly causes a reduction in hardness due to defect recombination 'healing' any intrinsic defects, leading to less mobile dislocations. The phase stability of the alloy suggests that this is not entirely the case for $V_{2.5}Cr_{1.2}WMoCo_{0.04}$. The decrease in hardness is more favourable than embrittlement for structural materials, however the long-term effect of a decrease in hardness is unknown as it is only theorised that self-healing is the responsible mechanism.

A recent study has attributed the decrease of hardness post irradiation at a dose of 1.0×10^{18} He^+ ions per cm^2 to an exfoliation of the surface of CoCrFeCuNi in addition to recovery induced by a long-term thermal spike (Wang et al., 2018) [56]. This is consistent with helium ion implantation, where regions of the implantation surface completely detach from the alloy due to the deformation caused by the intersection and agglomeration of helium ions at the surface. As expected, there is no evidence of exfoliation of the implanted layer in $V_{2.5}Cr_{1.2}WMoCo_{0.04}$ upon Au^+ irradiation. Instead, the annealing of any defects is most likely responsible for the decrease in hardness post-irradiation.

After heat treatment there was an increase in overall hardness (from 9.47 GPa ± 1.08e10.41 GPa ± 0.20) which can be attributed to the precipitation hardening seen from SEM micrographs due to the formation of V precipitates.

Table 5
Measured Vickers microhardness values (GPa) of $V_{2.5}Cr_{1.2}WMoCo_{0.04}$ in the as-cast, irradiated, and heat-treated state.

	Vickers Microhardness (GPa)
As-cast	9.47 ± 1.08
Irradiated	7.55 ± 0.18
Heat-treated	10.41 ± 1.20

Table 6
Refined lattice parameters and space groups of crystal structures acquired from least squares refinement.

	Crystal Structure	Space Group	Refined lattice parameter (Å)
As-cast	BCC	Im-3m	a = 3.0348 (7)
Irradiated	BCC 1	Im-3m	a = 3.0594 (14)
	BCC 2	Im-3m	a = 3.1603 (7)
Heat-treated	BCC	Im-3m	a = 3.1105 (10)
	Orthorhombic	Pbna	a = 6.0610 (5) b = 3.9960 (4) c = 4.8980 (3)
	Tetragonal	P42/mnm	a = 9.1110 (23) c = 4.8650 (17)

4. Conclusion

The metastable as-cast state of the alloy has shown excellent phase stability against 5 MeV Au^+ ion irradiation of doses up to 42 dpa. SEM micrographs highlight no change in microstructure post-irradiation and EDX maps show no further elemental segregation. In the as-cast state a single BCC crystal structure detected by XRD is speculated to consist of two similar microsegregated disordered BCC phases. GI-XRD has shown that post-irradiation, 96 wt % of this original BCC structure is preserved with the remaining 4 wt% phase transforming into a similar BCC phase with a slightly larger lattice parameter. This preservation has been attributed to the self-healing effect due to the multiphase nature of the alloy. Following ion implantation, $V_{2.5}Cr_{1.2}WMoCo_{0.04}$ demonstrated exceptional resistance against radiation hardening and embrittlement which may be due to self-healing and recombination of radiation-induced defects. The formation of three phases, BCC, tetragonal, and orthorhombic in crystal structure, post-heat treatment indicate that the alloy was only metastable in the as-cast state. However, this metastable state has shown to possess superior irradiation resistance.

The exceptional phase stability of the $V_{2.5}Cr_{1.2}WMoCo_{0.04}$ demonstrates the need for further research into multiphase HEAs andother multicomponent systems due to the uncertainty it raises over previous theories that only single-phase microstructures are desirable for radiation damage tolerant structural components. $V_{2.5}Cr_{1.2}WMoCo_{0.04}$ proves to be a very promising alloy as shown by the resistance to radiation damage and phase stability against ion irradiation.

Data availability

The raw/processed data required to reproduce these findings cannot be shared at this time due to technical or time limitations.

Declaration of competing interest

The authors declare that they have no known competing financial interests or personal relationships that could have appeared to influence the work reported in this paper.

CRediT authorship contribution statement

Dhinisa Patel: Writing - original draft, Writing - review & editing. Mark D. Richardson: Supervision, Funding acquisition. Bethany Jim: Data curation, Investigation. Shavkat Akhmadaliev: Investigation. Russell Goodall: Supervision, Writing - original draft, Writing - review & editing, Conceptualization. Amy S. Gandy: Supervision, Writing - original draft, Writing - review & editing, Conceptualization.

Acknowledgements

DP would like to acknowledge the financial support of Culham Centre for Fusion Energy and EPSRC grant EP/L016273 Centre for Doctoral Training in Advanced Metallic Systems for supporting this research. This work has been carried out within the framework of the EUROfusion Consortium and has received funding from the Euratom research and training programme 2014e2018 and

2019e2020 under grant agreement No 633053 and from RCUK [grant number EP/P012450/1]. The views and opinions expressed herein do not necessarily reflect those of the European Commission. RG would like to acknowledge a Fellowship supported by the Royal Academy of Engineering under the RAEng/Leverhulme TrustSenior Research Fellowships scheme. AG would like to acknowledge funding from EPSRC grant EP/R021864/1. The authors would also like to give special thanks to Dr Zhaoyuan Leong for fabricationof the alloy. This work was performed in the MIDAS Facility at The University of Sheffield, which was established with support from the Department for Energy and Climate Change, now incorporated within the Department for Business, Energy & Industrial Strategy.

Appendix A. Supplementary data

Supplementary data to this article can be found online at https://doi.org/10.1016/j.jnucmat.2020.152005.

References

[1] J.W. Yeh, S.K. Chen, S.J. Lin, J.Y. Gan, T.S. Chin, T.T. Shun, C.H. Tsau, S.Y. Chang, Nanostructured high-entropy alloys with multiple principal elements: novel alloy design concepts and outcomes, Adv. Eng. Mater. 6 (5) (2004) 299e303.
[2] B. Cantor, I.T.H. Chang, P. Knight, A.J.B. Vincent, Microstructural development in equiatomic multicomponent alloys, Mater. Sci. Eng. A 375e377 (2004) 213e218.
[3] P.K. Huang, J.W. Yeh, T.T. Shun, S.K. Chen, Multi-principal-element alloys with improved oxidation and wear resistance for thermal spray coating, Adv. Eng. Mater. 6 (2004) 74e78.
[4] M.-H. Chuang, M.-H. Tsai, W.-R. Wang, S.-J. Lin, J.-W. Yeh, Microstructure and wear behavior of AlxCo1.5CrFeNi1.5Tiy high-entropy alloys, Acta Mater. 59 (2011) 6308e6317.
[5] O. Senkov, S. Senkova, C. Woodward, Effect of aluminum on the microstructure and properties of two refractory high-entropy alloys, Acta Mater. 68 (2014) 214e228.
[6] S. Wei, F. He, C.C. Tasan, Metastability in high-entropy alloys: a review,J. Mater. Res. 33 (19) (2018) 2924e2937.
[7] Z. Li, K.G. Pradeep, Y. Deng, D. Raabe, C.C. Tasan, Metastable high-entropy dual-phase alloys overcome the strengtheductility trade-off, Nature 534(7606) (2016) 227.
[8] T. Egami, W. Guo, P.D. Rack, T. Nagase, Irradiation resistance of multicomponent alloys, Metall. Mater. Trans. A 45 (1) (2014) 180e183.
[9] Q. He, Y. Yang, On lattice distortion in high entropy alloys, Front. Mater. 5 (2018) 42.
[10] L.R. Owen, E.J. Pickering, H.Y. Playford, H.J. Stone, M.G. Tucker, N.G. Jones, An assessment of the lattice strain in the CrMnFeCoNi high-entropy alloy, Acta Mater. 122 (2017) 11e18.
[11] S.Q. Xia, X. Yang, T.F. Yang, S. Liu, Y. Zhang, Irradiation resistance in AlxCoCrFeNi high entropy alloys, JOM 67 (2015) 2340e2344.
[12] P.K. Liaw, T. Egami, C. Zhang, F. Zhang, Y. Zhang, Radiation Behavior of High-Entropy Alloys for Advanced Reactors, CompuTherm, LLC, Madison, WI (United States), 2015. Final report (No. DOE/NEUP-11-3196). Univ. of Ten- nessee, Knoxville, TN (United States).
[13] B. Kombaiah, K. Jin, H. Bei, P.D. Edmondson, Y. Zhang, Phase stability of single phase Al0. 12CrNiFeCo high entropy alloy upon irradiation, Mater. Des. 160

(2018) 1208e1216.
[14] N.A.P.K. Kumar, C. Li, K.J. Leonard, H. Bei, S.J. Zinkle, Microstructural stability and mechanical behavior of FeNiMnCr high entropy alloy under ion irradia-tion, Acta Mater. 113 (2016) 230e244.
[15] C. Lu, T. Yang, K. Jin, G. Velisa, P. Xiu, M. Song, Q. Peng, F. Gao, Y. Zhang, H. Bei, W.J. Weber, Enhanced void swelling in NiCoFeCrPd high-entropy alloy by indentation-induced dislocations, Mater. Res. Lett. 6 (10) (2018) 584e591.
[16] M.R. He, S. Wang, S. Shi, K. Jin, H. Bei, K. Yasuda, S. Matsumura, K. Higashida, I.M. Robertson, Mechanisms of radiation-induced segregation in CrFeCoNi- based single-phase concentrated solid solution alloys, Acta Mater. 126 (2017) 182e193.
[17] S.J. Zinkle, Fusion materials science: overview of challenges and recent progress, Phys. Plasmas 12 (5) (2005) p.058101.
[18] M. Li, M.K. Miller, W.Y. Chen, Phase stability in thermally-aged CASS CF8 under heavy ion irradiation, J. Nucl. Mater. 462 (2015) 214e220.
[19] K. Tai, R.S. Averback, P. Bellon, Y. Ashkenazy, B. Stumphy, Temperaturedependence of irradiation-induced creep in dilute nanostructured CueW al-loys, J. Nucl. Mater. 422 (1e3) (2012) 8e13.
[20] K. Tai, R.S. Averback, P. Bellon, N. Vo, Y. Ashkenazy, S.J. Dillon, Orientation relationship formed during irradiation induced precipitation of W in Cu,J. Nucl. Mater. 454 (1e3) (2014) 126e129.
[21] D. Miracle, J. Miller, O. Senkov, C. Woodward, M. Uchic, J. Tiley, Exploration and development of high entropy alloys for structural applications, Entropy16 (1) (2014) 494e525.
[22] D. Ikeuchi, D.J.M. King, K.J. Laws, A.J. Knowles, R.D. Aughterson, G.R. Lumpkin, E.G. Obbard, Cr-Mo-VW: a new refractory and transition metal high-entropyalloy system, Scr. Mater. 158 (2019) 141e145.
[23] A.S. Gandy, B. Jim, G. Coe, D. Patel, L. Hardwick, S. Akhmadaliev, N. Reeves- McLaren, R. Goodall, High temperature and ion implantation-induced phase transformations in novel reduced activation Si-Fe-V-Cr (-Mo) high entropy alloys, Front. Mater. 6 (2019) 146.
[24] H. Huang, Y. Wu, J. He, H. Wang, X. Liu, K. An, W. Wu, Z. Lu, Phase-trans- formation ductilization of brittle high-entropy alloys via metastability engi-neering, Adv. Mater. 29 (30) (2017) 1701678.
[25] E. Fazakas, V. Zadorozhnyy, L.K. Varga, A. Inoue, D.V. Louzguine-Luzgin, F. Tian, L. Vitos, Experimental and theoretical study of Ti20Zr20Hf20Nb20X20 (X V or Cr) refractory high-entropy alloys, Int. J. Refract. Metals Hard Mater. 47 (2014) 131e138.
[26] N.N. Guo, L. Wang, L.S. Luo, X.Z. Li, R.R. Chen, Y.Q. Su, J.J. Guo, H.Z. Fu, Microstructure and mechanical properties of refractory high entropy (Mo0. 5NbHf0. 5ZrTi) BCC/M5Si3 in-situ compound, J. Alloy. Comp. 660 (2016) 197e203.
[27] A. Takeuchi, A. Inoue, Calculations of mixing enthalpy and mismatch entropy for ternary amorphous alloys, Mater. Trans., JIM 41 (11) (2000) 1372e1378.
[28] A. Takeuchi, A. Inoue, Classification of bulk metallic glasses by atomic size difference, heat of mixing and period of constituent elements and its appli- cation to characterization of the main alloying element, Mater. Trans. 46 (12)(2005) 2817e2829.
[29] Y. Zhang, Y.J. Zhou, J.P. Lin, G.L. Chen, P.K. Liaw, Solid-solution phase formation rules for multi-component alloys, Adv. Eng. Mater. 10 (6) (2008) 534e538.
[30] F. Otto, A. Dlouhý, C. Somsen, H. Bei, G. Eggeler, E.P. George, The influences oftemperature and microstructure on the tensile properties of a CoCrFeMnNi high-entropy alloy, Acta Mater. 61 (15) (2013) 5743e5755.
[31] M.C. Troparevsky, J.R. Morris, P.R. Kent, A.R. Lupini, G.M. Stocks, Criteria for predicting the formation of single-phase high-entropy alloys, Phys. Rev. X 5 (1) (2015), 011041.
[32] Sheng Guo, C.T. Liu, Phase stability in high entropy alloys: formation of solid- solution phase or amorphous phase, Prog. Nat. Sci.: Mater. Int. 21 (6) (2011) 433e446.
[33] X. Yang, Y. Zhang, Prediction of high-entropy stabilized solid-solution in multi-component alloys, Mater. Chem. Phys. 132 (2e3) (2012) 233e238.
[34] J.F. Zeigler, J.P. Biersack, U.N.D.U. Littmark, The stopping and range of ions insolids, Stop. Range. Ion. Matter 1 (1985). http://www.srim.org/.
[35] E.A. Brandes, G.B. Brook (Eds.), Smithells Metals Reference Book, Elsevier, 2013.
[36] L. Vegard, Die konstitution der mischkristalle und die raumfüllung der atome,Z. Phys. 5 (1) (1921) 17e26.
[37] C. Zheng, M.A. Auger, M.P. Moody, D. Kaoumi, Radiation induced segregation and precipitation behavior in self-ion irradiated Ferritic/Martensitic HT9 steel, J. Nucl. Mater. 491 (2017) 162e176.
[38] T. Chen, Y. Yang, L. He, B. Tyburska-Püschel, K. Sridharan, H. Xu, L. Tan, Enhanced diffusion of Cr in 20Cr-25Ni type alloys under proton irradiation at 670 C, Nucl. Mater. Energy. 17 (2018) 142e146.
[39] Z. Wu, Y. Gao, H. Bei, Thermal activation mechanisms and Labusch-type strengthening analysis for a family of high-entropy and equiatomic solid- solution alloys, Acta Mater. 120 (2016) 108e119.
[40] S. Xia, M.C. Gao, T. Yang, P.K. Liaw, Y. Zhang, Phase stability and microstruc- tures of high entropy alloys ion irradiated to high doses, J. Nucl. Mater. 480 (2016) 100e108.
[41] M.C. Gao, J.W. Yeh, P.K. Liaw, Y. Zhang, High-entropy Alloys: Fundamentals and Applications, Springer, 2016.
[42] B.S. Murty, J.W. Yeh, S. Ranganathan, High-Entropy Alloys, Butterworth-Hei- nemann, 2014.
[43] T. Yang, S. Xia, S. Liu, C. Wang, S. Liu, Y. Fang, Y. Zhang, J. Xue, S. Yan, Y. Wang,Precipitation behavior of Al x CoCrFeNi high entropy alloys under ion irra- diation, Sci. Rep. 6 (2016) 32146.
[44] Y. Zhang, T.T. Zuo, Z. Tang, M.C. Gao, K.A. Dahmen, P.K. Liaw, Z.P. Lu, Micro-structures and properties of high-entropy alloys, Prog. Mater. Sci. 61 (2014) 1e93.
[45] E.J. Pickering, N.G. Jones, High-entropy alloys: a critical assessment of their founding principles and future prospects, Int. Mater. Rev. 61 (2016) 183e202.
[46] D.B. Miracle, O.N. Senkov, A critical review of high entropy alloys and related concepts, Acta Mater. (2016) 1e64.
[47] F. Tancret, I. Toda-Caraballo, E. Menou, P.E.J.R. Díaz-Del, Designing high en- tropy alloys employing thermodynamics and Gaussian process statistical analysis, Mater. Des. 115 (2017) 486e497.
[48] A.M. Manzoni, H.M. Daoud, R. Voelkl, U. Glatzel, N. Wanderka, Influence of W, Mo and Ti trace elements on the phase separation in Al8Co17Cr17Cu8- Fe17Ni33 based high entropy alloy, Ultramicroscopy 159 (2015) 265e271.
[49] J.J. Licavoli, M.C. Gao, J.S. Sears, P.D. Jablonski, J.A. Hawk, Microstructure andmechanical behavior of high-entropy alloys, J. Mater. Eng. Perform. 24 (10) (2015) 3685e3698.
[50] M.H. Tsai, J.W. Yeh, High-entropy alloys: a critical review, Mater. Res. Lett. 2(2014) 107e123.
[51] E.J. Pickering, R. Muñoz-Moreno, H.J. Stone, N.G. Jones, Precipitation in the equiatomic high-entropy alloy CrMnFeCoNi, Scr. Mater. 113 (2016) 106e109.
[52] C. Dang, J.U. Surjadi, L. Gao, Y. Lu, Mechanical properties of nanostructured CoCrFeNiMn high-entropy alloy (HEA) coating, Front. Mater. 5 (2018) 41.
[53] Y. Long, X. Liang, K. Su, H. Peng, X. Li, A fine-grained NbMoTaWVCr refractoryhigh-entropy alloy with ultra-high strength: microstructural evolution and mechanical properties, J. Alloy. Comp. 780 (2019) 607e617.
[54] M. Victoria, N. Baluc, P. Spätig, Structural materials for fusion reactors, Nucl. Fusion 41 (8) (2001) 1047.
[55] O. El-Atwani, N. Li, M. Li, A. Devaraj, J.K.S. Baldwin, M.M. Schneider, D. Sobieraj, J.S. Wrobel, D. Nguyen-Manh, S.A. Maloy, E. Martinez, Outstanding radiation resistance of tungsten-based high-entropy alloys, Sci. Adv. 5 (3) (2019) 2002.
Y. Wang, K. Zhang, Y. Feng, Y. Li, W. Tang, B. Wei, Evaluation of radiation response in CoCrFeCuNi high-entropy alloys, Entropy 20 (11) (2018) 835

4.6. Additions to Published Paper

4.6.1 Self-Healing Process

This section will include further explanation of the self-healing mechanism which may be responsible for the irradiation resistance of HEAs as suggested in the published paper.

As previously discussed in Section 2.4: High Entropy Alloys: Irradiation, the lower volume swelling rate and defect density of HEAs after irradiation in comparison to traditional alloys, may be attributed to possible self-healing mechanism. Figure 4.1 below illustrates various proposed mechanisms for the self-healing process in HEAs.

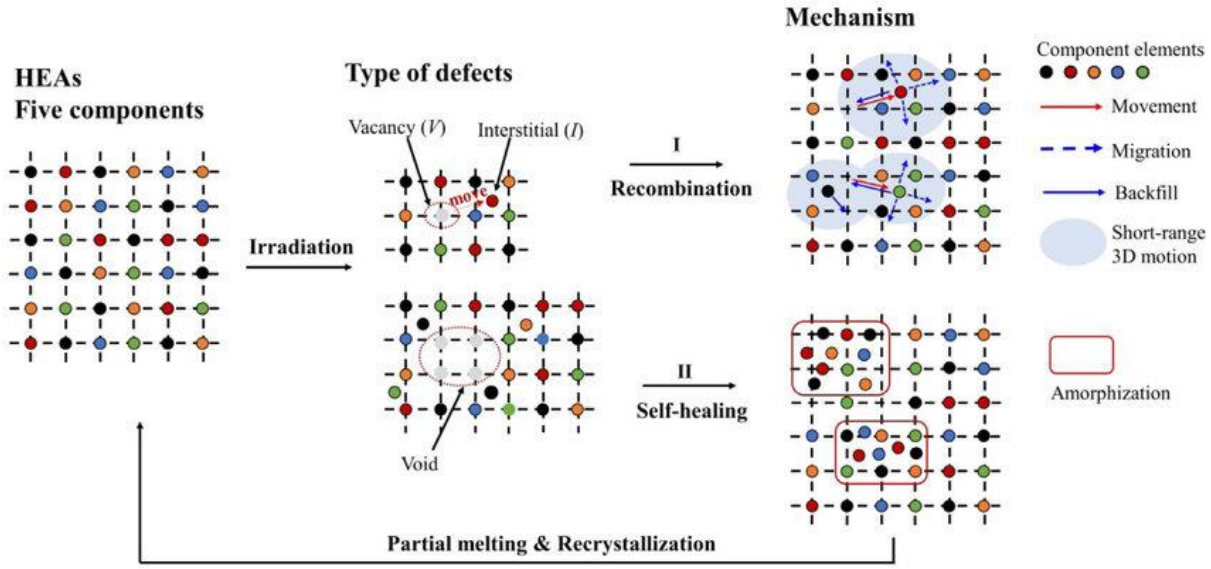

Figure 4.1: Schematic for the proposed self-healing mechanism of irradiation resistance in HEAs.

One suggested method of increased irradiation resistance arises from the high atomic-level stresses originating from mixing elements of varying atomic sizes in HEAs. This effect is attributed to the facilitation of amorphization of alloys. Areas of localised melting caused by the thermal spikes during particle irradiation can increase the order of the alloy and subsequently reduce the density of defects. Additionally, the decreased electron mean free path of HEAs (due to the increase in number of component elements) results in longer thermal spikes, which again, promotes recovery from the damaged state.

4.6.2. Experimental

There was an unintentional contamination of VCrMoW with a small concentration of cobalt (likely to have arisen from the melting process where contaminants can reside on the water-cooled copper crucible). Therefore, the alloy VCrMoW, with no contaminants, was fabricated

and assessed for high temperature homogenisation to determine if the elemental segregation present in the as-cast alloy can be reduced and the ideal duration of a 1600 °C heat treatment. The presence of a single BCC phase (which may be an overlapping of two very similar BCC phases) from the as-cast VCrMoW in Section 4.5. was evaluated for its hardness using nanoindentation to reveal the mechanical differences of the dendrite and interdendritic regions. This work also aids in the assessment for future low activation high entropy alloys and can be used to assess the optimal homogenisation heat treatment and if further high temperature experiments would be appropriate for further refractory alloys.

4.6.2.1 Homogenisation Treatments

To establish complete elemental homogenisation, a series of high temperature heat treatment were applied at 1600 °C for varying durations. The aim of this systematic approach to thermal treatment is to establish a suitable homogenisation heat treatment that could be applied to further refractory high entropy alloys with high melting points. For homogenisation of an alloy, typically a 0.5-0.8T_m temperature is applied, however, the duration of the heat treatment varies depending on the alloy composition and the alloy properties. Therefore, there is a need to establish a suitable effective homogenisation heat treatment that has the shortest possible duration. Firstly, the characterisation of the as-cast VCrMoW is required.

4.6.2.1.1 As-Cast

Raw elements of high purity were melted using the Vacuum Arc Melting (VAM) procedure extensively detailed in Chapter 3: Experimental Methodology. The fabricated ingot (20 g) was first analysed using X-ray Fluorescence (XRF) to obtain the actual alloy composition (at%) which was revealed to be $V_{42}Cr_{29}Mo_{18}W_{11}$. As with the VAM process in Section 4.5, the fabricated alloy in this work has a slightly different composition than the intended $V_{44}Cr_{21}Mo_{17.5}W_{17.5}$ most likely due to the melting procedure. The melting procedure calls for the additional doping of volatile elements which are likely to be decreased in content in the resulting alloy due to excess evaporation. However, sometimes the retainment of low boiling point elements occurs due to the lack of control parameters (temperature, heating/cooling rates) during the melting process. This is discussed in much further detail in Chapter 6. Throughout the rest of this work this alloy is simply referred to as VCrMoW.

Figure 4.2 shows the experimental XRD pattern for the as-cast VCrMoW. These peaks match a single disordered BCC phase and is analogous to a $V_{0.5}W_{0.5}$ structure [1] with a space group Im-3m (229) and a lattice parameter a≈3.09 Å.

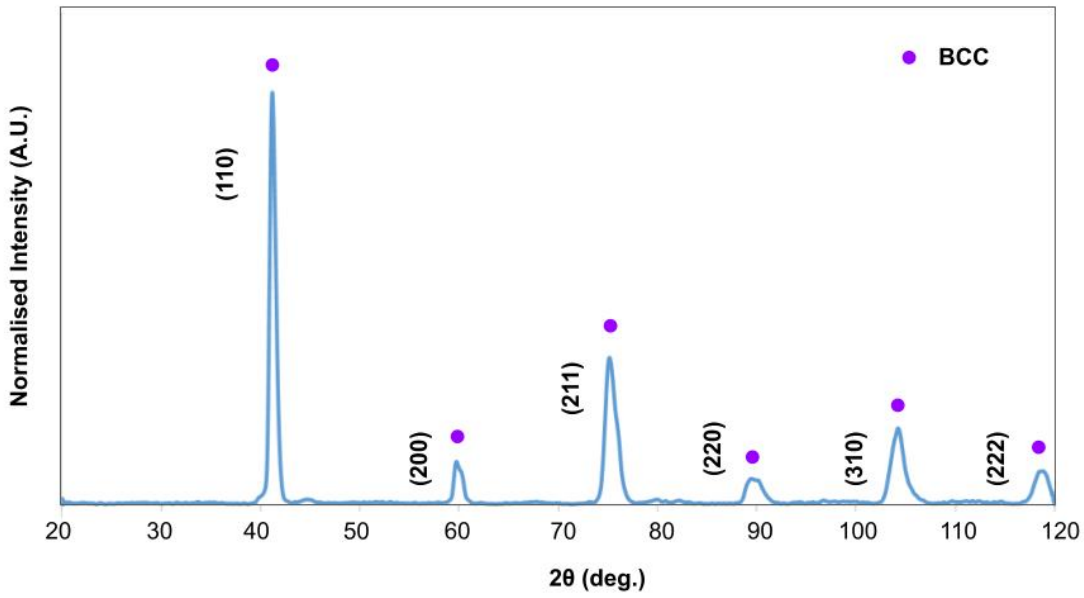

Figure 4.2: XRD pattern of the as-cast VCrMoW

This analysis correlates with the experimental XRD pattern of the as-cast VCrMoWCo which also displayed a single BCC structure with slightly broad peaks. This additionally corresponds with the HEA empirical parameters which suggest the formation of a stable BCC solid solution. The peaks in this XRD pattern are broad with leaning shoulders (as observed in the as-cast samples in Section 4.5.) which may be representative of the dendritic microstructure where two very similar BCC phases may be overlapping. As the peaks are overlapping, they cannot be individually resolved and indexed as two separate phases and so for simplicity is referred to as a single BCC phase. The small unidentified peaks could not be successfully matched.

Figure 4.3 shows the Thermo-Calc predictions using the SSOL4 database for VCrMoW which shows the presence of a single-phase disordered BCC A2 phase stable from melting until approximately 750 °C, below this temperature Thermo-Calc is unable to compute the equilibrium phases.

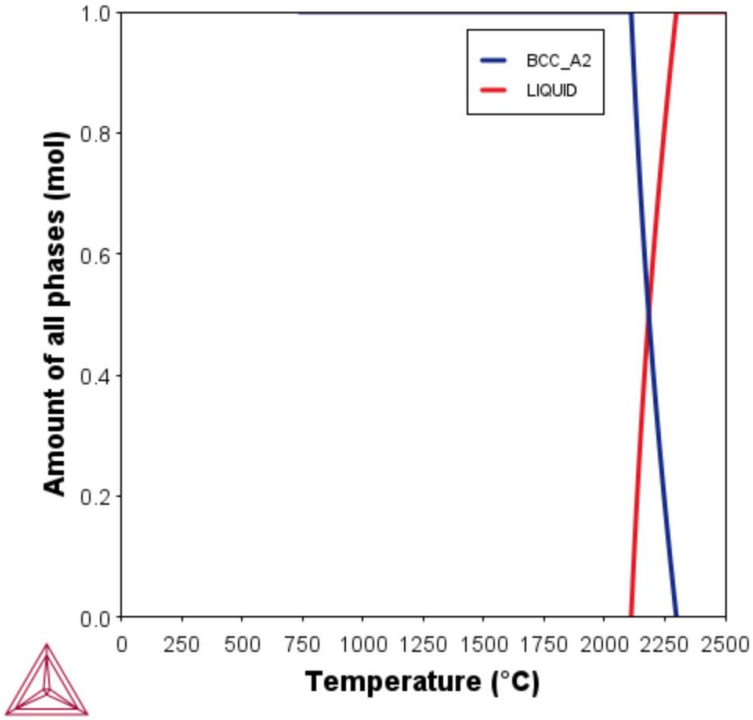

Figure 4.3: Thermo-Calc simulation of VCrMoW using the SSOL4 database

These results show yet further agreement of the design predictions, in this case using Thermo-Calc simulations, with the experimental verified data.

Figure 4.4 shows the SEM-BSE micrographs of the as-cast VCrMoW which displays the typically dendritic microstructure, where the dendritic arms are of darker contrast and the interdendritic regions are lighter in contrast. This microstructure is typical of VAM produced alloys and relates to the solidification of differing elements during the melting and cooling process. High melting point elements solidify first in the dendritic cores and the resulting lower melting point elements solidify in the interdendritic region [2].

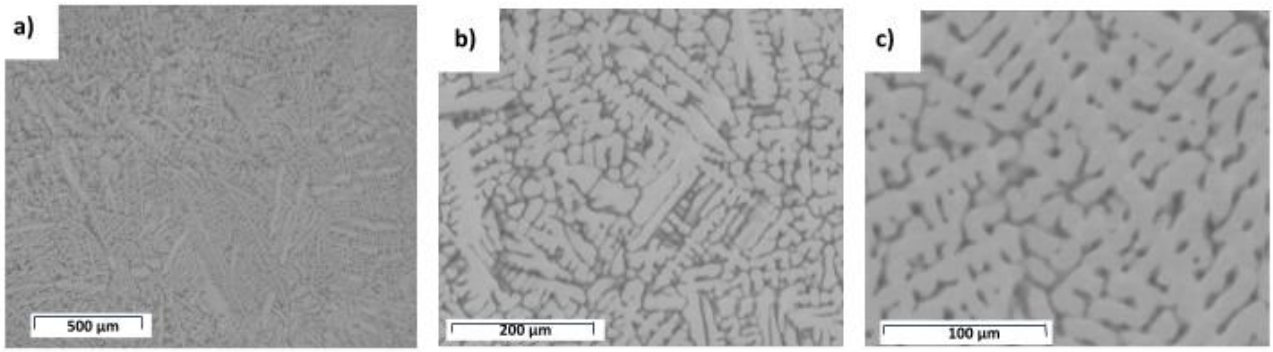

Figure 4.4: SEM-BSE micrographs of the as-cast VCrMoW at magnifications a) x150, b) x520, and c) x1200

Figure 4.5 shows the SEM-EDX elemental maps to establish the relationship of elements in the dendritic microstructure. Observed is the higher content of tungsten in the lighter dendritic arms with vanadium, chromium, and molybdenum in the darker interdendritic regions.

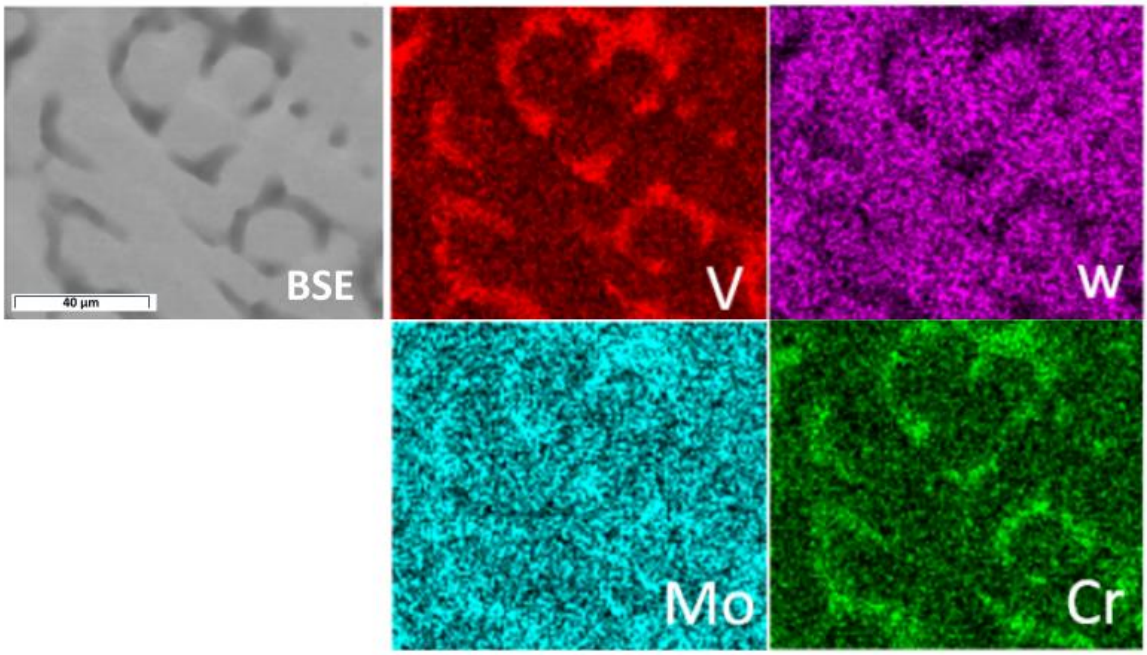

Figure 4.5: SEM-EDX elemental maps of as-cast VCrMoW

Table 4.1 displays the SEM-EDX point scans to quantify the extent of elemental segregation in dendritic microstructure. As expected, the lighter region – the dendritic arms, are composed mostly of tungsten, which has the highest melting point (3422 °C).

Table 4.1: Elemental concentrations (at%) of the two different regions of the as-cast VCrMoW alloy using SEM-EDX point scans (averaged from 5 separate point scans from each region). The Thermo-Calc predictions using the SSOL4 database are also included for the regional compositions.,

	Light region (at%)	**Dark region (at%)**	**Overall Alloy (at%)**
V	12.7±0.2	48.6±0.2	42
Cr	1.2±0.9	10±0.2	29
Mo	9±0.2	17±0.2	18
W	77±0.8	24±0.6	11
Thermo-Calc	BCC A2	BCC A2	BCC A2

Interestingly, from the results in Section 4.5., it would be expected that molybdenum would be homogenously spread (or as the second highest melting point, segregated in the dendrite arms). However, a high content of molybdenum is segregated in the interdendritic regions with only a smaller amount present in the dendrite regions.

The Thermo-Calc predictions of the elemental compositions of the dendritic arms and

interdendritic regions only show the formation of a disordered BCC A2 phase, no other phase or intermetallic compound formation is predicted. Therefore, this agrees with the XRD results

4.6.2.1.2. Homogenisation at 1600 °C for 24, 48, and 72 hours

Figure 4.6 shows the XRD patterns for the VCrMoW samples heat-treated at 1600 °C for 24, 48, and 72 hours. Each of the three heat treatments display two separate BCC phases, where the first BCC phases match with the as-cast phase. BCC 1 is analogous to a $V_{0.5}W_{0.5}$ structure [1] with a space group Im-3m (229) and a lattice parameter a≈3.09 Å. BCC 2 is analogous to a $Cr_{0.33}Mo_{0.34}W_{0.33}$ structure [3] with a space group Im-3m (229) and a lattice parameter a≈3.12 Å. BCC 3 is analogous to a pure Mo structure [4] with a Im-3m (229) space group and a lattice parameter a≈3.14 Å.

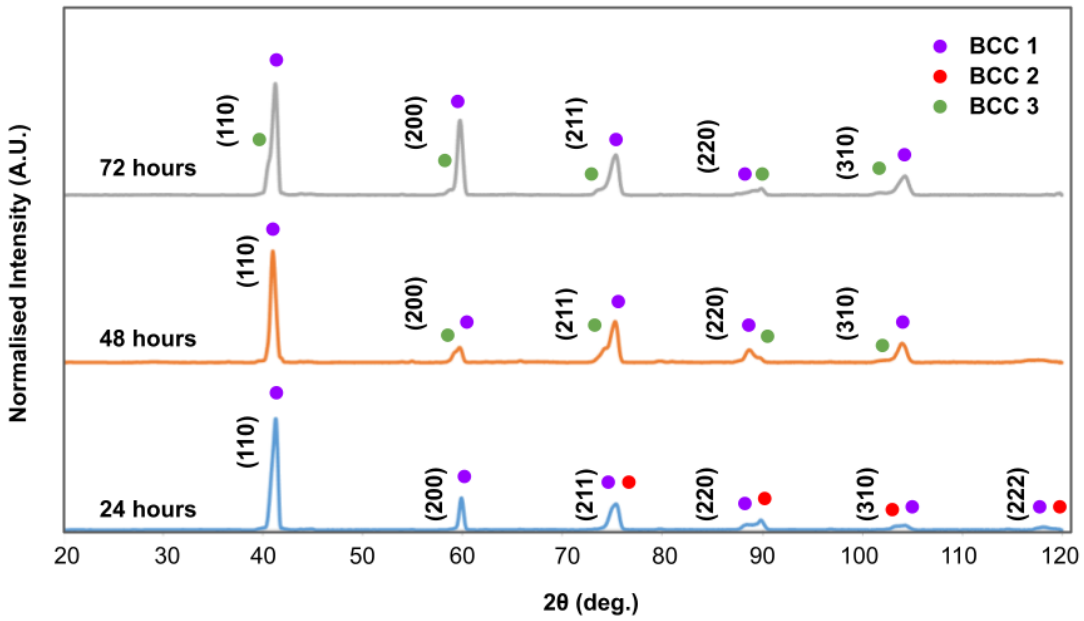

Figure 4.6: XRD patterns for VCrMoW heat treated at 1600 °C for 24 hours, 48 hours, and 72 hours.

From this figure, the evolution of phases from the homogenisation treatments can be observed. The homogenisation heat treatments of VCrMoW resulted in the additional formation of another BCC phase from as-cast condition. All of the VCrMoW samples heat treated at 1600 °C displayed two BCC phases, however increasing the duration from 24 hours to 48 and 72 hours changed the lattice parameter of the second BCC phase from a≈3.12 Å to a≈3.14 Å. Regardless, the observed expansion in lattice parameter is very minimal.

Figure 4.7 shows the SEM-BSE micrographs for the VCrMoW samples heat-treated at 1600 °C for 24, 48, and 72 hours at varying magnifications.

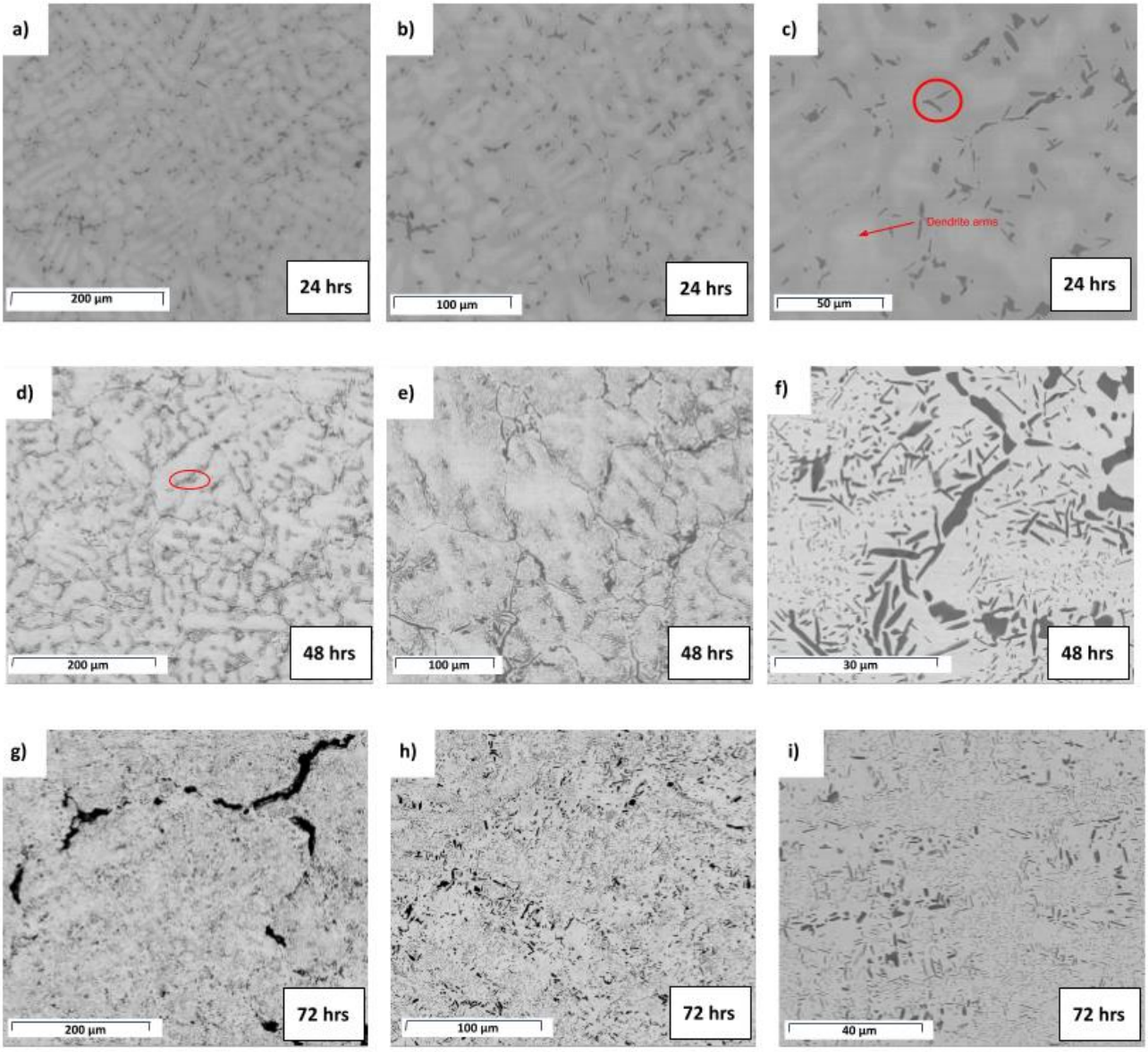

Figure 4.7: SEM-BSE micrographs of VCrMoW heat treated at 1600 C for a)-c) 24 hours d)-f) 48 hours, and g)-i) 72 hours

These SEM-BSE micrographs shows the microstructural evolution of VCrMoW upon heat treating at 1600 °C for varying durations. From a), d), and g) it can be observed that as the homogenisation heat treatment duration increases, the gradual loss of the dendritic microstructure occurs. The appearance of precipitation of dark grey precipitates (circled in red) in the interdendritic regions visible in VCrMoW heat treated for 24 hours increases in extent with longer heat treatments. Interestingly, as longer heat treatments are applied, the further loss of the interdendritic regions occurs (due to a higher volume fraction of the precipitates forming). With increasing duration, the precipitates become finer in morphology. King et al [5] suggested that for high entropy alloys, the cooling rate after the homogenisation process may affect the diffusion kinetics. In this study, the equiatomic high entropy alloy NbTiVZr was rapidly cooled (100 Ks^{-1}) and allowed to furnace cool. Rapid cooling resulted in a single BCC phase solid solution, whereas furnace cooling resulted in microsegregation. This disputes

previous reports of sluggish diffusion in HEAs as these cooling rates are sufficient for elements to segregate into secondary phases over a relatively short period of time. Therefore, for the reduction of this secondary BCC phase and precipitation, rapid cooling (for example cold water quenching) is recommended; at the time of this work, rapid quenching post homogenisation treatment was not available.

The experimental XRD of the heat-treated samples suggest the formation of an additional BCC phase which retains at longer heat treatment durations. This secondary BCC phase is likely formed from the interdendritic regions in the form of the precipitates. However, due to the small precipitation size, quantitative transmission electron microscopy is required for the confirmation of this hypothesis.

Figure 4.8 displays the SEM-EDX elemental maps which show the segregation of elements of VCrMoW heat treated at 1600 °C for a) 24 hours, b) 48 hours, and c) 72 hours.

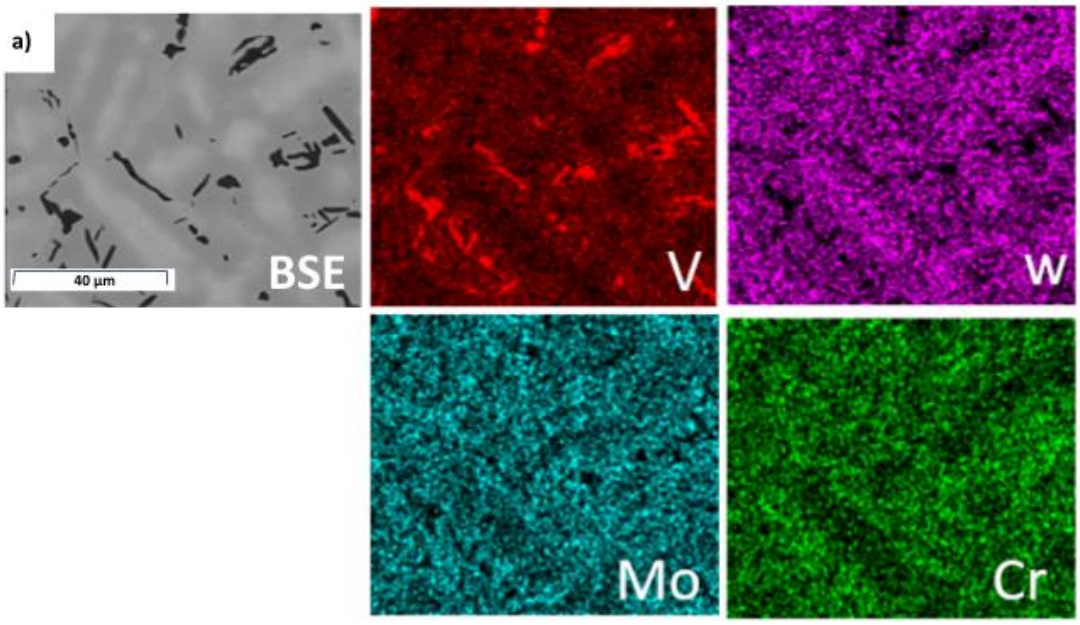

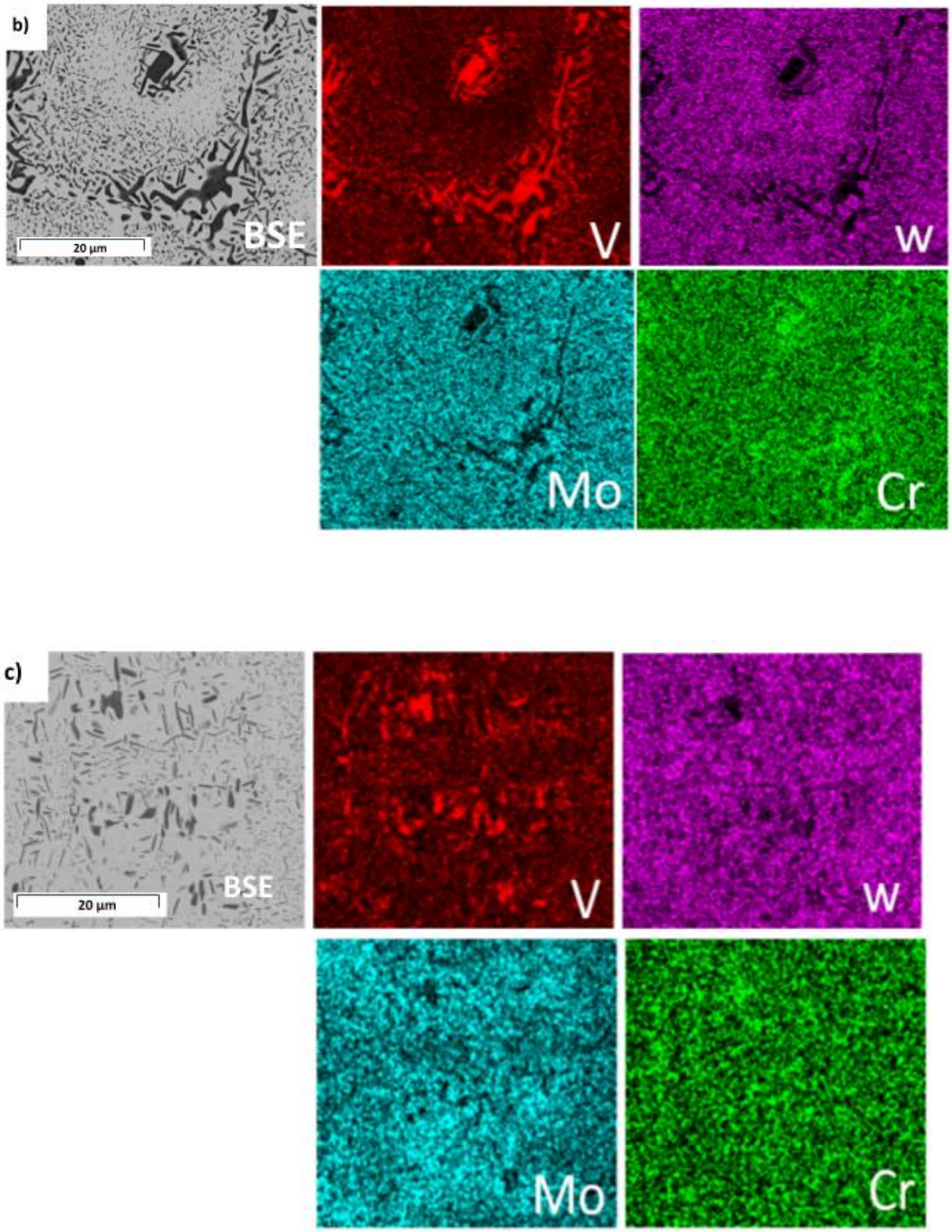

Figure 4.8: SEM-EDX elemental maps VCrMoW after heat treatment at 1600 °C for a) 24 hours, b) 48 hours, and c) 72 hours

From these elemental maps it can be clearly seen that the dark precipitation observed in the heat-treated SEM-BSE micrographs are predominately vanadium and chromium rich. With increasing duration of the homogenisation treatment, the grey interdendritic region (composing of V, Cr, and some Mo) is observed to slowly decrease in volume fraction – this region begins to form the fine black precipitates. Therefore, whilst there is a severe reduction in the dendritic microstructure, there remains elemental segregation of predominantly vanadium and chromium.

Table 4.2 shows the SEM-EDX point scans for each heat treated VCrMoW. Each region was probed for the quantitative elemental concentrations.

Table 4.2: Elemental concentrations (at%) of the three different regions of the heat treated VCrMoW alloy using SEM-EDX point scans (averaged from 5 separate point scans from each region). Thermo-Calc predictions using the SSOL4 database are also included for the regional compositions.

	Light region (at%)	**Dark region (at%)**	**Grey region (at%)**	**Overall Alloy (at%)**
24 hours				
V	15±0.25	93.8±0.3	25±0.25	42
Cr	2.25±0.25	2.6±0.3	5.5±0.25	29
Mo	8.25±0.25	0.98±0	13.9±0.25	18
W	74.5±1	2.6±0.3	55.4±0.76	11
Thermo-Calc	BCC A2	BCC A2	BCC A2	BCC A2
48 hours				
V	13.3±0.15	92±0.3	-	42
Cr	1.4±0.15	3.4±0.18	-	29
Mo	9.8±0.3	1.5±0.16	-	18
W	75.6±0.75	3±0.3	-	11
Thermo-Calc	BCC A2	BCC A2	-	BCC A2
72 hours				
V	10.8±0.4	82±1.5	45±1.2	42
Cr	1.2±0.2	1.2±0.5	0.9±0.4	29
Mo	17.5±0.7	1±0.5	5±0.5	18
W	70.5±1.2	16±1.4	49±1.5	11
Thermo-Calc	BCC A2	BCC A2	BCC A2	BCC A2

The XRD observations of VCrMoW heat treated at 1600 °C for all durations display two BCC phases very similar in lattice structure with comparable lattice parameters. The clear elemental segregation observed in the SEM-EDX points scans suggested the formation of two or three distinct regions with varying elemental concentrations. The chromium content of these different regions does not fluctuate greatly, however for the other constituents there is a clear trend: in the dendritic (light) regions tungsten is rich in content whereas for the interdendritic (grey) vanadium content increases. In the darker precipitates, these are rich in vanadium. Interestingly, for the 72-hour heat treated VCrMoW, the alloy demonstrates some elemental homogenisation – more of the tungsten content is observed in the darker precipitates and more molybdenum content is seen in the lighter dendritic arms. This may suggest that

homogenisation heat treatments more than 72 hours (for this alloy) may promote equilibrium phases.

The Thermo-Calc predictions, using the SSOL4 database only predict the formation of a disordered BCC A2 for the regional compositions present across all the heat treatments. This is also in agreement with the observed phases from the XRD patterns, where an additional BCC phase appears alongside the as-cast BCC phase.

4.6.2.1.3 Microhardness

Figure 4.9 shows the average values of the Vickers microhardness (GPa) for the as-cast and heat-treated conditions of VCrMoW, alongside the standard deviation for each data set. For each alloy a minimum of five separate microhardness indents were made. The as-cast VCrMoW has a microhardness of 5.09 ± 0.15 GPa. After heat treating at 1600 °C for 24 hours the alloy exhibited an increase in hardness to 5.83 ± 0.5 GPa. This heat treatment caused the alloy to have the highest microhardness as for the samples heat treated at 48 hours (2.81 ± 0.2 GPa) and 72 hours (2.72 ± 0.3 GPa) there was a significant decrease in hardness.

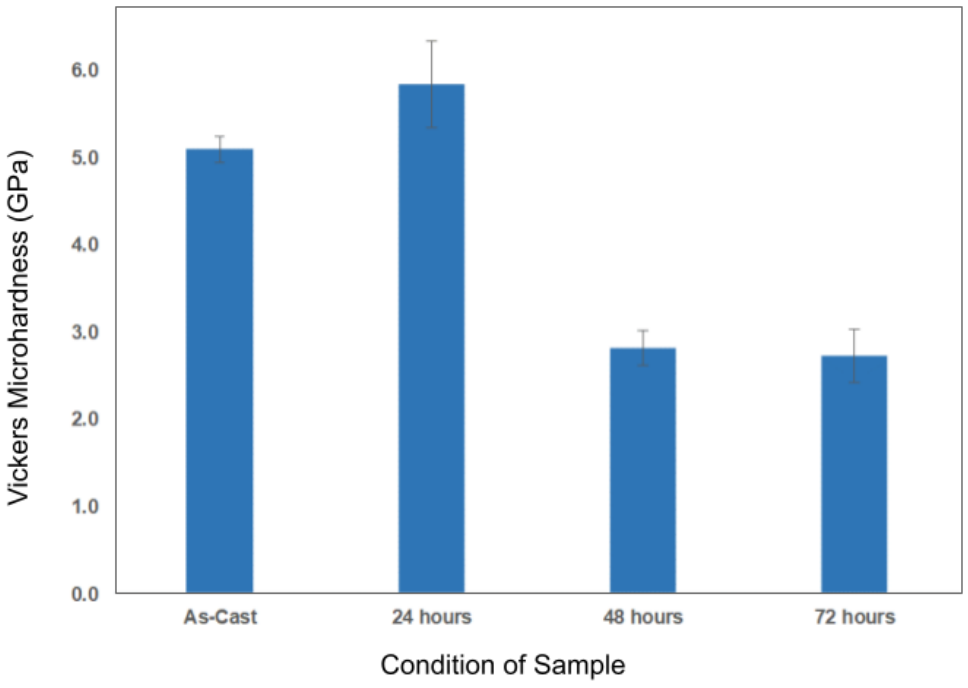

Figure 4.9: Graph of the Vickers microhardness values for VCrMoW in the as-cast condition and after heat treating at 1600 °C for 24, 48, and 72 hours.

Using the rule of mixtures approach (where the elemental microhardness is averaged considering the concentration of each constituent) the theoretical Vickers microhardness is approximately 12 GPa. However, none of the samples had hardness that matched this predicted value – all of the samples had much lower microhardness values. After 48- and 72-

hour homogenisation treatment, VCrMoW undergoes unexpected significant softening. Abbasi et al [6] reported a similar effect for the alloy CoCrFeMnNiNbC where after homogenisation the alloy softens from 114 HV to 100 HV. They attributed this effect to the as-cast dendritic microstructure which can impede dislocation sliding and therefore enhance the strength of the material, which may also be the mechanism for VCrMoW.

At 24 hours, the hardness of VCrMoW increased substantially this could indicate a more homogenous microstructure, however this is not observed in the SEM-EDX point scans. Additionally, the alloy with the highest hardness value also has the highest deviation observed in the error bar in the graph suggesting that this value had a high error associated with it. A possible explanation for the apparent reduced hardness value could be due to the dendritic microstructure of the as-cast VCrMoW – the theoretical Vickers microhardness is calculated assuming a single solid solution alloy which would benefit from solid solution hardening [7]. In the dendritic microstructure, this strengthening mechanism may not occur (and this may be evidence of two very similar BCC phases present likely not resolved by the XRD techniques).

The nanoindentation measurements of the dendritic arms and interdendritic regions of the as-cast VCrMoW is evaluated in the next section where nanoindentation of the dendritic microstructure was undertaken.

4.6.2.2. Nanoindentation

Mechanical testing of the as-cast VCrMoW was performed to determine hardness differences of the dendritic arms and interdendritic regions. A matrix of indents was performed over the sample to cover both regions for testing. A full description of this method is included in Chapter 3: Experimental Methodology. Figure 4.10 shows the Atomic Force Microscopy (AFM) micrograph used to probe the surface of the sample to observe the microstructure of the alloy for the determination of the placement of the indents. The contrast of the regions reflects the dendritic microstructure – the yellow regions represent the dendritic arms, and the red regions are the interdendritic regions.

Figure 4.10 shows the full AFM micrograph of the region that was indented which encompasses an area of 50 μm^2. The depth chart represents the surface morphology where the dendritic regions have a bigger depth (>350 nm) then the interdendritic region (<350 nm).

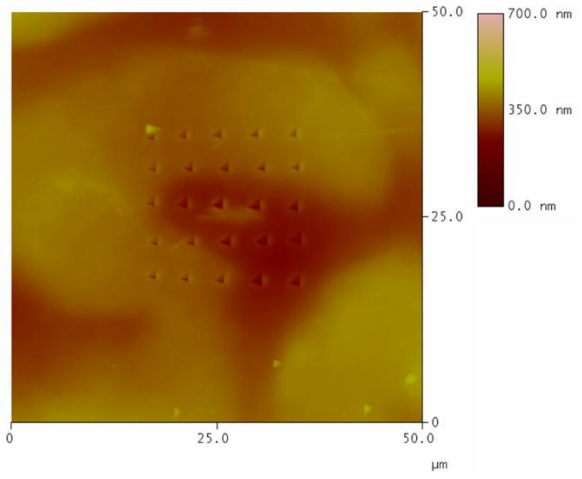

Figure 4.10: AFM micrograph of the indentation area of the as-cast VCrMoW

Figure 4.11 shows the area of indentation using AFM alongside the plotted hardness contour map of the region. As shown by the hardness data, the dendritic regions correlate with a higher average hardness (>9 GPa) and the interdendritic region has a lower overall hardness (<8.5 GPa).

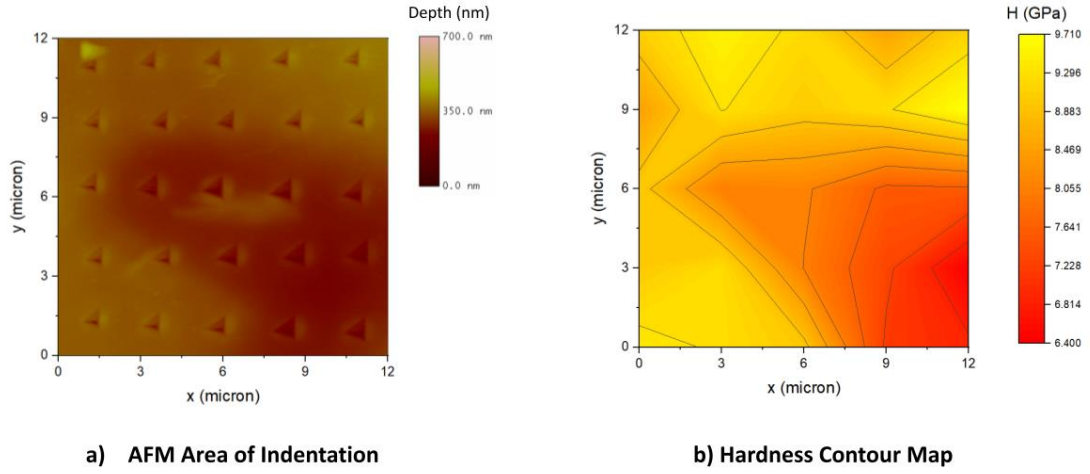

Figure 4.11: Nanoindentation results for as-cast VCrMoW of the a) AFM micrograph of the indentation matrix and b) the resulting hardness contour map of the corresponding region.

Additionally, from these micrographs, no further cracking of the indents in either the dendritic or interdendritic regions can be observed, indicating that VCrMoW in the as-cast sate could potentially have ductile behaviour at room temperature [8].

Table 4.3 shows the elemental concentrations identified using SEM-EDX point scans of the different regions of the as-cast VCrMoW with the corresponding theoretical hardness values (calculated using ROM) and the actual hardness values (using nanoindentation and Vickers microhardness).

Table 4.3: Elemental concentrations using SEM-EDX point scans for the dendritic microstructure of the as-cast VCrMoW. The corresponding hardness values for each region is also included.

	Light region (at%)	**Dark region (at%)**	**Overall Alloy (at%)**
V	12.7±0.2	48.6±0.2	42
Cr	1.2±0.9	10±0.2	29
Mo	9±0.2	17±0.2	18
W	77±0.8	24±0.6	11
Theoretical Hardness (GPa)	28.2	14.6	12
Experimental Hardness (GPa)	9.2±0.3	7.7±0.7	5.09

From these results it is clear that neither the nanoindentation or the Vickers microhardness data were comparable to the theoretical hardness of the different regions. Regardless for their reduced values, they are still consistent with the elemental concentrations for each region. The dendritic arms, much higher in content of tungsten (which has much higher corresponding elemental hardness value – 3430 MNm^{-2}) has a higher overall hardness value (9.2 GPa) than the interdendritic regions (which has less hard elemental constituents). These same results were also observed by Gorr et al [8] for the equimolar refractory high entropy alloy MoWAlCrTi. The dendritic region (richer in W-Mo) was significantly harder (685 HV) than the interdendritic region (330 HV) and the overall average hardness of the alloy.

4.6.2.3. Differential Scanning Calorimetry

For the assessment of phase transformations as a function of temperature, thermal analysis using differential scanning calorimetry (DSC) can be carried out. DSC measures the difference of heat flow between the reference pan and the sample as the material is heated and then cooled at a known rate. This technique is commonly used to evaluate thermal transitions including melting, evaporation, oxidation, and solidification. Chapter 3: Experimental Methodology details the procedure in more depth.

Figure 4.12 shows the a) heating and b) cooling DSC thermograms of the as-cast VCrMoW. Important features of interest are numbered in the heating curve, with the corresponding features highlighted in the cooling curve.

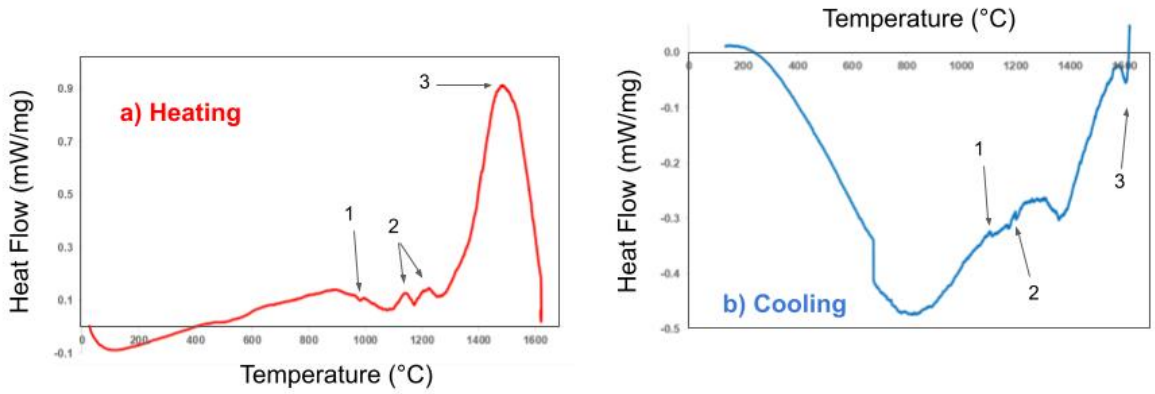

Figure 4.12: DSC curves upon a) heating and then subsequent b) cooling of the as-cast VCrMoW

From the heating DSC curve shown in a), the exothermic peak at around 1500 °C (labelled 3) could possibly correspond to the formation of the secondary BCC phase as this would correlate with the XRD observations in the homogenised VCrMoW at 1600 °C (for all durations tested).

There also appears to be no significantly intense sharp peaks in the heating portion of the DSC, however, there is a very small sharp peak in the heating thermogram indicated by 1). This could be attributed to the observed phase transformations from BCC to BCC, orthorhombic, and tetragonal following a long duration heat treatment at 1187 °C.

The broad increasing tendency up to 900 °C may be attributed to the diffusion of elements into a BCC solid solution This feature was also observed in DSC heating peaks up to 450 °C for FeNiCoAlCu as reported by [9].

From the cooling curve, the corresponding exothermic peaks observed at around 1200 °C can also be observed (labelled 2). However, they are shifted at a lower temperature (to around 1100 °C) and this is due to the supercooling effect on the cooling curves which shift them to lower temperatures [10].

From the heat treatments of VCrMoW detailed in Section 4.6.1. there was observation of the stability of the two BCC phases after applying longer duration homogenisation treatments at 1600 °C. Therefore, it could be expected that in the DSC curves of the as-cast VCrMoW there should be no endothermic or exothermic peaks (regardless of broadness) on the heating or cooling curves as there should be no phase transitions [11]. However, this was not experimentally observed.

Ideally, the DSC measurements of the heating and cooling cycle of the as-cast VCrMoW would

be repeated to ensure any peaks were not artefacts. Additionally, DSC experiments on the homogenised VCrMoW, would reveal any further phase transformations on the structurally stable alloy. However, due to time constraints and equipment availability this was not possible. Further work could include longer heat treatments between 1000 °C and 1300 °C to establish if any phase transformation is occurring in the temperature range.

4.6.2.4. Conclusions

The as-cast VCrMoW demonstrated comparable results to the alloy fabricated in Section 4.5., VCrMoW displayed a single BCC phase with a typical dendritic microstructure with tungsten rich dendritic arms and vanadium and chromium rich interdendritic regions. The thermal evolution of the as-cast VCrMoW was evaluated through homogenisation treatments for varying durations. Experimental XRD patterns shows that upon heat treating, VCrMoW transformed into two distinct disordered BCC phases which remained stable at all durations. Longer durations (for 72 hours) revealed fine precipitations with eradication of the dendritic microstructure. With each heat treatment, the morphology of the microstructure evolved and the degree of elemental microsegregation lessened. This suggests that for complete homogenisation of VCrMoW a longer duration heat treatment is required. Interestingly, VCrMoW in the as-cast and heat-treated conditions exhibited a relatively low hardness, though this could be attributed to the microstructure of the alloy. Nanoindentation results correlate with the elemental segregation – the dendritic arms containing more tungsten (a comparatively harder element) had hardness values that were higher than the interdendritic regions. Whilst molybdenum is a high activation element, these results can be utilised for the work of further novel low activation high entropy alloys. In particular, the thermal heat treatments showed that a longer duration homogenisation will likely be more successful in reducing elemental segregation.

4.6.3. References

[1] Gladyshevskii, E.I., Fedorov, T.F., Skolozdra, R.V. and Gorshkova, L.V., 1967. System WV-Si. Soviet Powder Metallurgy and Metal Ceramics, 6(5), pp.406-408.

[2] Senkov, O.N., Wilks, G.B., Scott, J.M. and Miracle, D.B., 2011. Mechanical properties of Nb25Mo25Ta25W25 and V20Nb20Mo20Ta20W20 refractory high entropy alloys. Intermetallics, 19(5), pp.698-706.

[3] Grum Grzhimailo N.V., Prokof`ev D.I. "AN X-RAY DIFFRACTION STUDY OF HIGH-TEMPERATURE SOLID SOLUTIONS IN THE CHROMIUM- MOLYBDENUM-TUNGSTEN SYSTEM". Russ. J. Inorg. Chem. (Engl. Transl.) 1961, 6, 590.

[4] Svechnikov V.N., Kobzenko G.F. "The chromium-molybdenum diagram". Dokl. Akad. Nauk SSSR 1964, 155, 611.

[5] King, D.J.M., Cheung, S.T.Y., Humphry-Baker, S.A., Parkin, C., Couet, A., Cortie, M.B., Lumpkin, G.R., Middleburgh, S.C. and Knowles, A.J., 2019. High temperature, low neutron cross-section high-entropy alloys in the Nb-Ti-V-Zr system. Acta Materialia, 166, pp.435-446.

[6] Abbasi, E. and Dehghani, K., 2019. Effect of Nb-C addition on the microstructure and mechanical properties of CoCrFeMnNi high entropy alloys during homogenisation. Materials Science and Engineering: A, 753, pp.224-231.

[7] Senkov, O.N., Wilks, G.B., Miracle, D.B., Chuang, C.P. and Liaw, P.K., 2010. Refractory high-entropy alloys. Intermetallics, 18(9), pp.1758-1765.

[8] Gorr, B., Azim, M., Christ, H.J., Mueller, T., Schliephake, D. and Heilmaier, M., 2015. Phase equilibria, microstructure, and high temperature oxidation resistance of novel refractory high-entropy alloys. Journal of Alloys and Compounds, 624, pp.270-278.

[9] Jin, G., Cai, Z., Guan, Y., Cui, X., Liu, Z., Li, Y. and Dong, M., 2018. High temperature wear performance of laser-cladded FeNiCoAlCu high-entropy alloy coating. Applied Surface Science, 445, pp.113-122.

[10] Chen, Y.Y., Duval, T., Hung, U.D., Yeh, J.W. and Shih, H.C., 2005. Microstructure and electrochemical properties of high entropy alloys—a comparison with type-304 stainless steel. Corrosion science, 47(9), pp.2257-2279.

[11] Guo, N.N., Wang, L., Luo, L.S., Li, X.Z., Su, Y.Q., Guo, J.J. and Fu, H.Z., 2015. Microstructure and mechanical properties of refractory MoNbHfZrTi high-entropy alloy. Materials & Design, 81, pp.87-94.

Chapter 5: Design of Novel Low Activation High Entropy Alloys

There is no established system for the design of high-temperature single-phase high entropy alloys. However, there are many different tools that aid the design process by predicting the formation of a single-phase solid solution over brittle, unwanted intermetallic compounds. In this chapter, the justification of the choice of elements is discussed in relation to some of the requirements of plasma-facing materials (PFM) including radiation damage tolerance, and mechanical and thermal properties. Additionally, some of the constraints of the alloy fabrication methods are discussed and taken into consideration during the alloy design process. Also examined in this chapter are some of the alloy design processes, which are evaluated for the optimisation of reduced activation high entropy alloy compositions. The empirical thermodynamic parameters for the design of solid solution compositionally complex alloys are also assessed to optimise the alloy compositions from equimolar concentrations. Finally, a suite of novel low activation high entropy alloys is presented as potential PFMs.

5.1. Low Activation Elements

A legislative requirement for plasma-facing components (PFCs) states that materials used must not produce long-lived (< 100 years) radioactive waste after their removal from the fusion reactor [1]. For this reason, the neutron-induced activation and surface dose rates of candidate materials are necessary to assess the application of these alloys. The decay heat and surfaces dose rates for some of the previous candidate plasma-facing materials are shown in Table 5.1 [2]. A high surface dose rate, for example molybdenum compared to tungsten, results in the PFC requiring surface cleaning after operation to reduce contamination. For this reason, as previously discussed in Chapter 2.1: Plasma-Facing Materials, the elements chosen for plasma-facing materials must be reduced activation elements.

Table 5.1: Decay heat after 1 day and surface dose rates for different potential plasma-facing components (Bolt et al, 2002).

Material	Decay heat after 1 day (kW/kg) (irrad. 4.15 MW/m2, 2.5y)	Decay time to reach a surface dose rate of 10-2 Sv(years) (irrad.5 MW/m2, 2.5y)
Tungsten	2 x 10-1	150
Molybdenum	3 x 10-2	2 x 105
Iron	10-2	60
SiC	10-3	10

From this information, we are limited in which elements we can use for the armour of the first wall. Moreover, this immediately renders most conventional high-temperature alloys (steels, zirconium alloys, and nickel-based superalloys) impractical for nuclear fusion applications due to their inclusion of high activation elements (Ni, Co, Hf, Mo, etc.).

5.2. Refractory Elements

Currently, pure tungsten, a high melting temperature refractory element, is the primary candidate for the armour component plasma-facing material (PFM) due to its high sputtering resistance at low plasma temperatures, high melting point, and tolerance of radiation damage. Unfortunately, the brittle nature of pure tungsten can lead to failure of the component during reactor operation. Alloying tungsten with further high temperature elements, to enhance the ductility of pure tungsten, is one of the suggested approaches to improve material performance under irradiation [3]. A full evaluation of tungsten and its alloys as candidates for the armour material is discussed in Chapter 2.1: Plasma-Facing Materials.

Alternative refractory metals, including tantalum and molybdenum, have also been considered for structural fusion materials in part due their retention of mechanical strength at high temperatures and high thermal conductivity. However, high atomic number elements can negatively impact the plasma by rapid cooling. Additionally, due to the higher neutron flux environment experienced by the plasma-facing components (PFCs) some refractory elements are activated above the allowed radiological dose limit and so must be excluded from these materials. Figure 5.1 shows the level of irradiation of several elements commonly found in

steels as a function of time (in years) after removal from a 3.6 GW nuclear fusion power reactor (after irradiating for 5 years) [4].

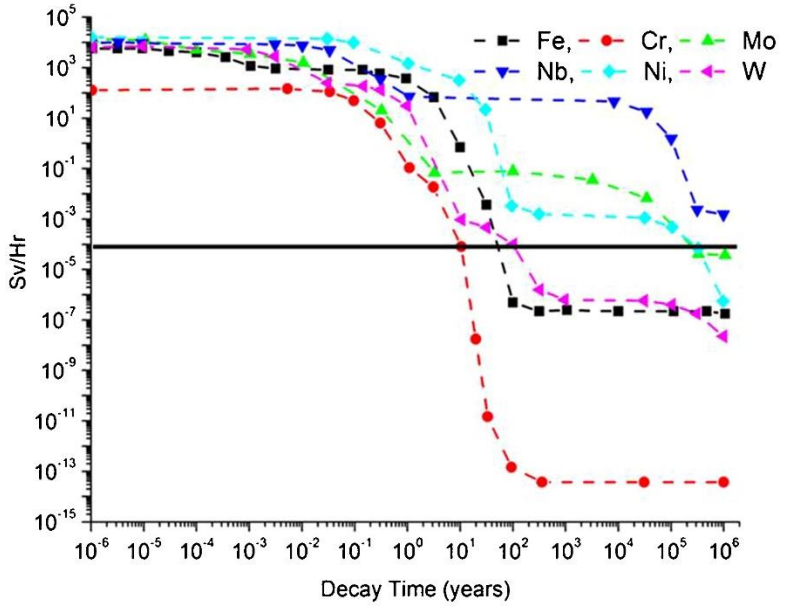

Figure 5.1: The length of time it takes for the level of irradiation to fall for several common elements found in steel [4].

Molybdenum, niobium, and nickel are significantly more activated after the 100-year limit than chromium, iron, and tungsten. Pure molybdenum has a high melting temperature (2623 °C) and low sputtering yield and was used as a first wall PFM in Alcator C-Mod (in 1991) and TEXTOR tokamaks [5]. However, this refractory metal was abandoned for use in ITER due to the long-lived radioactive products that would be formed after high neutron fluxes. So, whilst these refractory elements possess desirable high-temperature capabilities they must be restricted to mitigate the need for mid-level active waste.

In conclusion, whilst the physical properties of the pure refractory elements do not meet the PFC criteria, optimised alloyed compositions may meet some of the mechanical performance and radiation damage tolerant requirements. Development of ductile, strong materials which retain stability at high temperatures and neutron loads is paramount.

Figure 5.2 outlines the design process beginning with the selection of low activation elements with significant mechanical performance at elevated temperatures. To design of a range of alloys to systematically investigate, the high entropy alloy empirical parameters are first assessed. The maximisation of entropy, favourable elemental pair mixing, and minimisation of Gibbs free energy are all taken into consideration when identifying a series of low activation

high entropy alloys. The exploration of HEA empirical parameter boundaries, as discussed in Chapter 2.3: High Entropy Alloys, specifically for the prediction of the stability of a BCC solid solution is probed for refractory HEAs.

Once a set of alloys has been identified several considerations are required: 1) vacuum arc melting restrictions (minimisation of volatile elements, etc.), 2) phase diagram and 3) PFC considerations (reduction of brittle phases in the operating temperature range), and 4) Thermo-Calc predictions (for the likelihood of secondary phases and intermetallic compounds) are considered to refine the alloy composition from equimolar amounts.

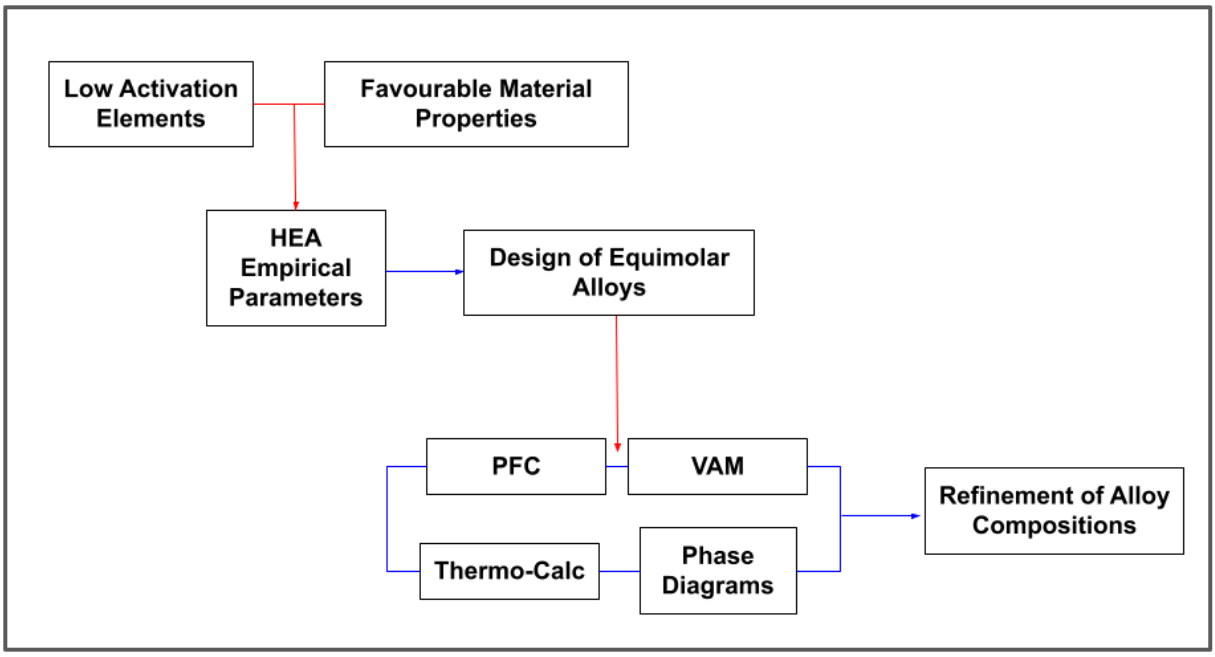

Figure 5.2: Flowchart summarising the design process steps for the range of novel refractory high entropy alloys.

Section 5.3. establishes some potential elements, including some low activation refractory elements, detailing those that have the capacity to be alloyed together to form a single BCC phase solid solution.

5.3. Determination of Refined Alloy Compositions

Overall, the design of candidate reduced activation HEAs for fusion applications can be an iterative process. Figure 5.3 outlines the flowchart of the entire design process for refinement of alloy composition.

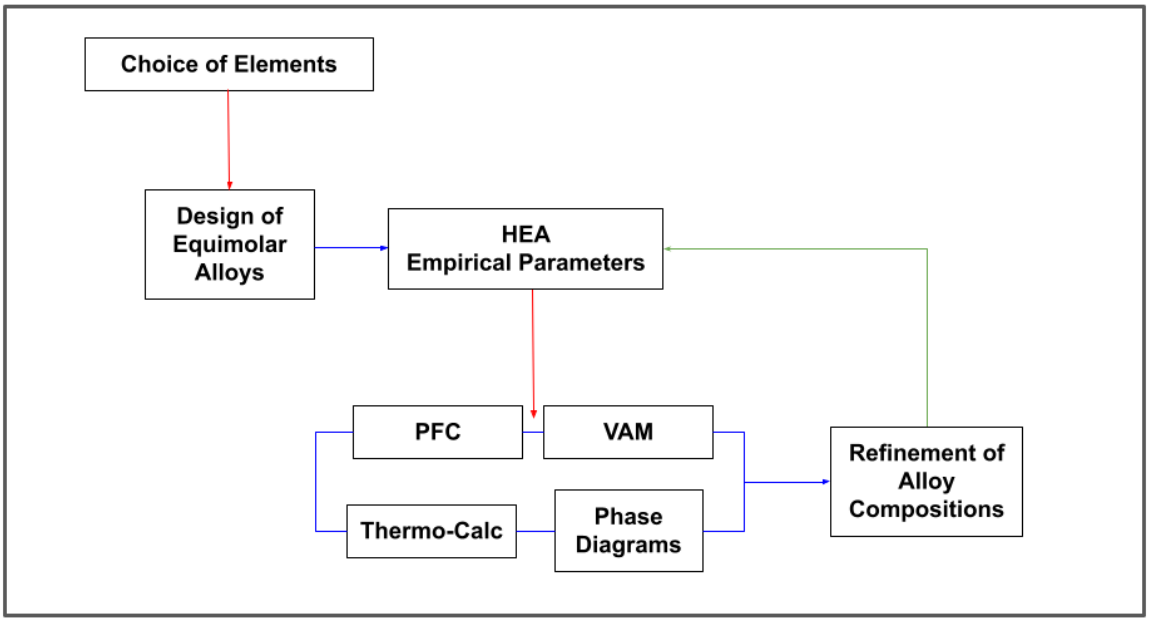

Figure 5.3: Flowchart of the overall design process highlighting the iterative stages for refinement of alloy composition.

Once the elements have been selected and the combination of components decided upon, the HEA thermodynamic parameters can be calculated for the equimolar compositions. At this stage, diversion from the equimolar concentrations, due to any requirements from fabrication methods, or application requirements need to be taken into consideration. For multicomponent alloys, the thermodynamic parameters used in this work can be applied to assess a suitable compositional range of alloys to determine the likelihood of formation of a solid solution. These compositions can then be used in Thermo-Calc to calculate property diagrams over the in-service temperature range. From these diagrams, molar amounts of equilibrium phases that are anticipated can be observed. Minimisation of brittle or undesirable phases can be calculated by computing the elemental dependencies on the phase. Reduction of these components will then allow for a greater proportion of the disordered solid solution to occur.

The refinement process can be an iterative process; to reduce any unwanted phases predicted in the property diagrams the alloy composition can be slightly altered in accordance with the dependent elements in these phases. This new composition, with an allowable range of concentrations for a component, can then be evaluated for the HEA thermodynamic parameters to establish a disordered solid solution as the majority phase. Any particular compositions which encourage the formation of a solid solution can then be re-assessed in Thermo-Calc to inspect the diminution of the unwanted phases. These last two stages may then be repeated for other components of the alloy and may need to be revised at each stage

to monitor the phases anticipated. Finally, once the successful determination of an alloy composition has been achieved then the alloy can be fabricated and experimentally characterised.

In this work, the enhanced alloy compositions calculated from the Thermo-Calc process was evaluated for the HEA empirical parameters. As these values remain within the parameter boundaries, there is no need to further adjust the elemental compositions of the alloys. Therefore, the Thermo-Calc design step is the final stage of the refinement process.

5.4. Choice of Low Activation Elements

An evaluation of candidate elements is detailed below with regards to their high temperature capability, low activation properties, and alloying restrictions. The rationale behind the alloy design process is to find a suitable replacement for the high activation element molybdenum in the alloy VCrMoW (detailed in Chapter 4: VCrMoWCo). The low activation elements assessed below are investigated for their high temperature properties and capability to form a single-phase BCC solid solution. There are several considerations that need to be considered including: vacuum arc melting constraints, solid solution requirements, and PFC property needs.

Table 5.2 lists the elemental data for all the low activation elements considered for the novel high entropy alloys.

Table 5.2: Thermo-physical properties for the low activation elements.

Element	Melting Point (°C)	Boiling Point (°C)	Atomic radii (nm)	Atomic number	Crystal structure	VEC
Vanadium	1910	3407	0.1316	23	BCC	5
Chromium	1907	2671	0.1249	24	BCC	6
Manganese	1246	2061	0.1350	25	Cubic	7
Iron	1538	2861	0.1241	26	BCC	8
Tantalum	3017	5458	0.1430	73	BCC	5
Tungsten	3422	5555	0.1367	74	BCC	6

5.4.1. Tantalum

There has been prior interest in the highly corrosion-resistant refractory metal tantalum as a candidate material for fusion applications. Tantalum and tantalum-based alloys offer many favourable properties for nuclear and high temperature applications. Compared to other

refractory metals, pure tantalum possesses superior ductility, workability, and weldability, though these properties may not persist in a tantalum containing alloy [6]. They have been proposed for use as both bulk materials for the first wall or as a surface coating. Adding alloying elements to tungsten, the primary candidate for PFCs, results in an increase in ductility and reduction of the DBTT. For example, to improve on the ductility of tungsten, alloying with tantalum which in its elemental form has excellent ductility, can enhance the mechanical performance of the PFC under irradiation. Pure tantalum has a total elongation of up to 50% at room temperature and retains ductility (approximately 5%) even at extremely low temperatures (-196 °C) [7]. A selection of tantalum-tungsten alloys (Tantaloy) with tungsten concentrations ranging from 2.5 wt% to 10 wt% provide increasing hardness and yield strength and decreasing ductility [8].

5.4.2. Vanadium

Advanced vanadium alloys have been considered as structural materials for fusion reactors; in particular, the prospective alloy V-4Cr-4Ti has been identified for its low induced radioactivity, resistance to neutron irradiation, and good high temperature strength [9]. In addition, V-4Cr-4Ti has been researched for its low thermal expansion and low elastic modulus which renders this alloy beneficial for retaining low thermal stresses at high heat fluxes. This alloy also uses reduced activation elements meeting the legislative criterion of reaching low-level waste after reactor shutdown. However, one of the major drawbacks of vanadium alloys for fusion applications is low temperature irradiation embrittlement, which would need to be improved for potential use in future advanced reactors. The moderate thermal conductivity and very different thermal expansion coefficients present challenges in the robust joining of a tungsten-vanadium component.

5.4.3. Chromium

Chromium and chromium-based alloys have been previously considered for high temperature applications including for use in jet engines. Pure chromium exhibits a high melting point (1863 °C) and excellent corrosion resistance however, chromium alloys also tend to suffer from a high DBTT which results in low toughness and ductility and further effects their ability to be shaped, welded, and manufactured [10]. The pursuit of chromium-based alloys for nuclear fusion applications is in part due to their excellent low activation and high service temperature (up to 1000 °C) capabilities. However, the advent of high temperature nickel superalloys for the aerospace industry meant that further research of chromium alloys was hampered. Thermomechanical testing of commercially available Plansee chromium alloys highlighted deficiencies in room temperature ductility.

5.4.4. Iron

Ferritic alloys are an important class of materials that have been considered as first wall components of nuclear reactors. A variety of steels (as well as nickel, titanium, and refractory-based alloys) can provide nanometre sized phases dispersed in the host metals matrix, demonstrating the capability of improving the materials strength under high temperature neutron service [11]. Specifically, iron-based oxide dispersion steels (ODS) have been developed with 9-12 wt% of chromium, with a primary focus for fusion applications. Oxide nanoclusters have shown to successfully pin the ferritic grains and will block dislocation movement, and therefore improve strength and creep resistance. Upon irradiation, they also serve as sinks for irradiation-induced defects and helium atoms and so expedite recovery of irradiation damage. Fe-12-16%Cr nanostructured ferritic alloys (NFAs) are a variation of ODS steels with prospective properties such as high tensile, fatigue, and creep strengths over a range of temperatures. However, much like chromium alloys, significant developments in their fabricability, joining, and cost is required for the industrial application of these alloys.

5.4.5. Manganese

As previously discussed, ferritic alloys have shown some potential for use as a structural material for fusion applications. Manganese is an important alloying element for stabilisation of the austenitic structure and to increase the hardness and strength of steel. Development of low activation manganese stainless steels (for example, Mn-Cr-Fe) to replace the high activation element nickel, has garnered interest for their higher hardness, yield strength, and ultimate tensile strength compared to standard austenitic stainless steels [12]. However, to maintain their good ductility and to minimise production of intermetallic compounds, only limited concentrations of manganese (below 35 wt%) can be used. Notably, Fe-Cr-Mn stainless steels are robust candidate materials to replace conventional Fe-Cr-Ni austenitic stainless steels which typically produce residual long-term radioactivity.

A problematic feature of elemental manganese in relation to alloy processing is the low boiling point (2061 °C) which is much lower than the melting point of tungsten (3422 °C). In addition, there is considerable varying densities between the two elements (Mn~ 7.26 g/cm^3 and W~19.3 g/cm^3). These disparate material properties form an obstacle when attempting to cast alloy with substantial elemental concentrations. As a result, there are very few data available on the Mn-W system and so some assumptions need to be made for potential secondary phase formation. Additionally, this means that the content of manganese in the designed alloys must be limited to around 10 at%. Nonetheless, manganese is hypothesised to exhibit some solubility in tungsten due to them both possessing the same BCC crystal structure at high

temperature. Additionally, manganese displays solubility in chromium and molybdenum and recent efforts have demonstrated a maximum of 12 at% manganese in tungsten [13].

5.5. Alloy Selection

For the design of an array of novel low activation multicomponent alloys, a review of current literature is required to assess which alloys have already been investigated. Many quaternary systems have been investigated [14], [15], [16], [17]. Chapter 4: VCrMoWCo discusses the preliminary studies of VCrMoW with a small amount of Co addition. This has led to a primary motive for the investigation of replacing the activation element molybdenum with low activation elements. As stipulated in Section 5.3., the manganese content in the designed alloys must be restricted to allow for the successful melting of dissimilar elements. To maintain a high configurational entropy an additional component is required. For this reason, simply replacing molybdenum from VCrMoW with a small amount of manganese may not necessarily result in a high configurational entropy. Furthermore, the addition of another refractory element can increase the melting point of the overall alloy therefore increasing the operating temperature range of the component.

Consequently, a systematic approach has been developed to design a novel range of alloys that all contain vanadium, chromium, and tungsten. The design process shown in Figure 5.3 indicates the first step as identifying potential elements; in this study the elements V, Cr, Mn, Fe, Ta, and, W are all considered. The next step is to use the HEA empirical parameters to generate a selection of alloys which maximises the formation of a stable BCC solid solution. By adhering to the thresholds of these parameters, the investigation of these thermodynamic criteria can also be reviewed. Therefore, the overall design procedure not only addresses the low activation requirement of PFMs, but also probes the fundamental principles of high entropy alloys.

The overall aim of designing a suite of alloys is to establish a system where a range of criteria can be examined in addition to identifying any potential candidates for PFMs. Table 5.3 outlines the requirements from three conditions of the alloy specifications: vacuum arc melting restrictions, high entropy alloy criteria, and plasma-facing component operating criteria. These requirements encompass the fabrication of the alloy, the fundamental properties of the class of alloy, and the application for the material. These conditions all need to be taken into consideration when choosing the elemental components of the alloys and when refining the alloy compositions from equimolar amounts.

Table 5.3: Summary of list of properties/ effects and requirements from the fabrication method, high entropy alloy parameters, and plasma-facing component requirements.

VAM	HEA	PFC
Low manganese content (between 5 - 10 at%)	'High entropy' effect (maximise number of elements/equimolar composition)	High temperature strength (by maximising the alloy's melting point)
Lower tungsten content (<35 at%)	Effect of elemental substitution on the alloy	Low activation elements (identified in Figure 5.1)
Minimisation of freezing range (limit to a 100 - 200 °C)	Formation of solid solution	Mitigation of brittle intermetallic compounds (below 0.2 mol and limit to lower temperature below 500 °C)
		Reduction of high atomic number elements (<35 at% of tungsten and tantalum)
		Stability of BCC solid solution over operational temperature range (between 750 - 1000 °C)

Highlighted in Table 5.3 is the restriction of manganese and tungsten due to the fabrication methods. Highly volatile and low boiling point elements can be challenging to incorporate into the alloy using vacuum arc melting (this is discussed further in Chapter 3: Experimental Methodology). Therefore, it is important to reduce the concentration of these elements) to a low amount. In this work, manganese is restricted to between 5-10 at% and tungsten is limited to below 35 at%. Limiting the amounts of these elements will ultimately reduce the overall entropy of the alloy and in order to investigate the high entropy effect on the formation of a solid solution the entropy must be increased. To compensate for the reduction in entropy additional components can be added to the alloy. For this reason, manganese-containing alloys contained at least 5 components, compared to VCrMoW which is a quaternary alloy.

Once the constituents have been chosen for the alloys, the elemental concentrations can be refined. In terms of alloy composition, as mentioned in detail in Chapter 2.3: High Entropy Alloys, equimolar concentrations are not necessarily the optimal elemental concentration for the encouragement of a single phase solid solution, regardless of the maximised configurational entropy. Deviation from the equimolar composition may mitigate the formation of brittle unwanted intermetallic compounds by reduction of problematic elements which accelerate the precipitation of intermetallic compounds. For this evaluation, inspection of binary and ternary phase diagrams is required to highlight any featured intermetallic formation. This is to identify any potential secondary phase formation for higher order systems (this method is fully assessed in Section 5.7. Phase Diagrams).

In Section 5.5. Chosen Suite of Alloys, a more in-depth analysis of the factors highlighted in Table 5.3 are discussed in relation to the chosen array of alloys.

5.6. Chosen Suite of Alloys

The five low activation refractory high entropy alloys designed for this investigation are:

1. **VCrMnFeTaW**
2. **VCrMnFeW**
3. **VCrMnTaW**
4. **VCrFeTaW**
5. **VCrFeTa**

As mentioned previously, these five high entropy alloys were specifically chosen for their predicted disordered BCC solid solution and their low activation nature. Most of these alloys are based on the ternary alloy VCrW-X established from the work in Chapter 4: VCrMoWCo where the substitution of the high activation element molybdenum was discussed. As mentioned earlier, a small addition of manganese, specifically restricted by the fabrication methods, is not sufficient to increase the entropy to the same degree as VCrMoW. To reproduce the same radiation-tolerant properties as the molybdenum-containing alloy for the novel low activation alloys, an increase in entropy by supplementing with an additional component is required. Therefore, two further alloys (with the additional elements iron and tantalum) VCrMnFeW and VCrMnTaW have been devised. The third alloy, VCrMnFeTaW has been designed based on all of the discussed low activation elements. The motivation for the composition of this alloy is described in further detail below. The final two low activation multicomponent alloys in this study are based on the restrictions of the fabrication methods used. For instance, the reduction of manganese, which, due to its low boiling point, can prove

problematic when trying to incorporate into refractory alloys; and also the reduction of tungsten, which, due to its high melting point can become difficult to melt when alloyed with much lower melting temperature elements. For this reason, the alloys VCrFeTaW and VCrFeTa are also investigated. Table 5.4 summarises the chosen alloy compositions and their design rationale.

Table 5.4: The designed series of novel low activation high entropy alloys alongside the rationale for each alloy and the motive for the substitution of elements.

Alloy composition	**Justification / purpose of study**
VCrMnFeW	Effects of substitution of Fe on alloy
VCrMnTaW	Effects of substitution of Ta on alloy
VCrMnFeTaW	● Near equimolar for study of all elements in one alloy ● Highest entropy alloy
VCrFeTaW	Removal of manganese for ease of melting
VCrFeTa	Removal of tungsten for ease of melting

A more detailed discussion of the motivation for the investigation of each of these alloys is detailed below. Considerations that need to be taken into account can be compiled into two groups: firstly, restrictions determined by fabrication methods and PFM requirements and secondly, high entropy alloy conditions. The high entropy alloy thermodynamic parameters predict the likelihood of the formation of a disordered solid solution. Manipulation of these parameters and comparison to known multicomponent alloys which form stable solid solutions will reveal further insights into fundamental attributes. Substitution of elements with varying thermodynamic properties (for example, different mixing enthalpies, atomic sizes, etc.) and the resultant effect on the phases present in the alloys will facilitate greater understanding behind the design approach of multicomponent alloys.

5.6.1. VCrMnFeW and VCrMnTaW

The first two alloys in this series to be investigated for potential as a PFM are VCrMnFeW and VCrMnTaW. Substitution of iron for tantalum will allow for a direct comparison between VCrMnFeW and VCrMnTaW and the resultant effect of these elements on the microstructure and phases present. A similar approach was undertaken by Hillel et al [18] in an attempt to isolate the effect of each element on the microstructure and composition of phases in AlCoCrFeNi. They investigated the quinary AlCoCrFeNi HEA by systematically casting five quaternary alloys by removing one element at a time.

By substituting elements, assessments on the thermo-physical properties of the elements and the interactions between the elements can be considered with regards to the thermodynamic parameters. For example, the atomic radii and valence electron concentration of both iron and tantalum vary and so will influence the overall equations which dictate the probability of formation of a disordered solid solution (this is discussed in depth in Section 5.6. High Entropy Alloy Design for a BCC Solid Solution). Reduction of the overall Gibbs free energy of the solid solution may also influence the propensity of ordered phases or intermetallic precipitates. Substitution of these elements may give an insight into the types of secondary phases that are inhibited or promoted.

Additionally, the mixing of enthalpies of the binary pairs of tantalum and iron with the corresponding elements will also be of interest. The importance of binary mixing enthalpies and melting points on the solidification of the melt occurring at rapid cooling rates will also influence the phases formed in the as-cast alloys; this process is deliberated in further detail for the fabricated alloys in Chapter 6: Experimental Assessment of Novel High Entropy Alloys.

In terms of elemental concentrations, deviations from equimolar concentration are required for the fabrication of the alloy. As mentioned previously, reduction of manganese for all of the alloys is required due to its low boiling point (and in part due to the tungsten content increasing the melting point of the alloy). Further reduction of iron and tantalum is also needed to mitigate the probability of unfavourable intermetallic compounds and unfavourable phases. This is discussed in further detail in the Section 5.7. Phase Diagrams.

5.6.2. VCrFeTaW and VCrFeTa

For the first two alloys, the thermodynamic parameters were the primary focus of investigation, however for VCrFeTaW and VCrFeTa, the primary aim was to enhance the manufacturing

process of low activation multicomponent alloys. For VCrFeTaW, removal of the problematic volatile element manganese may improve the ease of melting the alloy during fabrication.

For VCrFeTa, removal of the high melting point element tungsten, in addition to the low boiling point element manganese, is expected to further aid the ease of melting the alloying mixture. This alloy is particularly interesting due to the high propensity of all of the elements forming the brittle Laves phase. Using the methods employed in Section 5.6. High Entropy Alloy Design for a BCC Solid Solution, it can be seen that the mixing enthalpy of Fe-Ta is extremely negative compared to any other binary pair. Additionally, V-Fe and Cr-Ta have the same negative values. The study of combining strongly attracting elements which readily form intermetallic compounds, even though the alloy composition predicts the formation of a disordered BCC solid solution, will be an insightful investigation into the usefulness of the thermodynamic parameters for alloy design in these systems.

5.6.3. VCrMnFeTaW

The alloy design of VCrMnFeTaW was approached in a different manner compared to the other alloys in this work. The system applied for this alloy is akin to the strategy employed by Cantor et al [19], where an equimolar alloy containing all the elements in interest is fabricated. This is to ascertain whether a stable solid solution matrix is formed from any combination of components in the alloy. After fabrication of the alloy, examination of the phases present using typical characterisation methods (detailed in the Chapter 3: Experimental Methodology) can be used to determine any solid solution formation. For example, XRD analysis can establish the crystal structure of the solid solution in the alloy and SEM-EDX can be used for confirmation of the concentration of the components in the phase. This new composition can then be fabricated as a novel alloy with the prediction of a single-phase formation, however kinetic and thermodynamic considerations also need to be considered. It is worth noting that this strategy is only theorised to highlight favourable compositions for the formation of a stable solid solution. So, rather than rely solely on this method, this procedure forms one part of the design process of a suite of alloys.

However, for the elemental composition of VCrMnFeTaW an important caveat must be made - the concentration of manganese would again have to be significantly reduced. For the equimolar composition, 16 at% of Mn would still be an excessive amount to incorporate into a refractory based alloy. Additionally, as shown in Section 5.5. Chosen Suite of Alloys, this alloy composition possesses the highest entropy as most components are near equimolar, resulting in the ‘high entropy’ effect being able to be investigated.

5.7. High Entropy Alloy Design for a BCC Solid Solution

This section will address the empirical thermodynamic parameters for the formation of a solid solution for multicomponent alloys. The equations used for the prediction of a single-phase solid solution are discussed in full in Chapter 2.3: High Entropy Alloys. Deviation from equimolar concentrations, as discussed previously, will allow for the reduction in problematic formation of intermetallic compounds and unfavourable secondary phases. Comparison of equimolar compositions with the enhanced compositions is needed to ensure that whilst the requirements of fabrication are being met, the empirical parameters for a stable solid solution are also being fulfilled.

Below is a summary of the equations and parameters used to quantitatively determine the propensity for the range of alloys to form a BCC solid solution. These equations do not predict the formation of secondary phases or intermetallic compounds; however, they are able to gauge the tendency for stoichiometric compounds to form in relation to the disordered solid solution. The difficulty in assessing this method, however, arises from the endeavour in predicting the unknown phases which may occur including the calculation of crystal structure and elemental stoichiometry.

Equations 1-3 are temperature dependent and so to compare the calculated parameters, temperature was kept at a constant for all of the equations. The following equations were calculated for the equimolar low activation alloy compositions:

$$\Delta G_{mix} = \Delta H_{mix} - T\Delta S_{mix} \qquad \textit{Equation 5.1}$$

$$\Delta H_{mix} = \sum_{i=1}^{n} \Omega_{ij} c_i c_j \qquad \textit{Equation 5.2}$$

$$\Delta S_{mix} = -R \sum_{i=1}^{N} c_i Ln c_i \qquad \textit{Equation 5.3}$$

$$\delta = \sqrt{\sum_{i=1}^{N} c_i (1 - \frac{r_i}{\bar{r}})^2} \qquad \textit{Equation 5.4}$$

$$\Omega = \frac{T_{m\,\Delta S_{mix}}}{\Delta H_{mix}} \qquad \textit{Equation 5.5}$$

$$\text{VEC} = \sum_{i=1}^{n} c_i (VEC)_i \qquad \textit{Equation 5.6}$$

$$T_m = \sum_{i=1}^{n} c_i (T_m)_i \qquad \textit{Equation 5.7}$$

Firstly, these equations and parameters were calculated for equimolar concentrations of the novel alloys to determine if a disordered BCC solid solution was likely to occur. The python script, of which details are explained fully in Chapter 3: Experimental Methodology, is written to calculate the thermodynamic parameters for a range of alloy compositions where each element is between 5 at% and 35 at%. This has the potential to output a large range of data with large numbers of alloy compositions, especially for higher ordered systems. Alternatively, some of the low activation alloys (VCrFeTa and VCrFeTaW) only resulted in a few compositions where the calculated parameters were within specified boundaries. Table 5.5 shows these upper and lower thresholds which are set in the python script and are obtained from literature values based on experimental data (further detail of this can be found in Chapter 2.3: High Entropy Alloys). Alloy compositions which satisfy these criteria are predicted to form a BCC solid solution.

Table 5.5: Thermodynamic parameters and the specified boundaries estimated for the prediction of a single-phase solid solution.

	Lower limit	**Upper limit**	**Reference**
Omega	1.1	-	Yang and Zhang (2012) [20]
Atomic size difference (%)	0	6.6	Wang et al (2014) [21]
Entropy ($JK^{-1}mol^{-1}$)	11	19.5	Guo and Liu (2011) [22]
Enthalpy ($kJmol^{-1}$)	-10	5	Zhang (2014) [23]
VEC	-	6.87	Wang et al (2014) [21]

An important detail to appreciate is the origin of upper and lower limits of the parameters set to identify the formation of a solid solution. Experimental data of as-cast multicomponent alloys from literature was collected and evaluated. Characterisation results determining the phases present in the high entropy alloys were compiled in relation to their thermodynamic properties. Ranges of values where solid solutions were observed for a variety of alloys provide the basis for the upper and lower limits for the thermodynamic parameters. As these limits are set by as-cast alloys only and not specifically equilibrium phases they may not accurately determine if an alloy in these ranges will explicitly form a disordered solid solution. Another disadvantage to this method of designating boundaries where solid solutions form, is that an array of high entropy alloys was considered without any distinction towards elements included in the alloys and/or whether this had any effect on the formation of a solid solution. For these reasons, the thermodynamic parameters are not to be stringently adhered to, especially when compromise was required (i.e., to comply with arc melting restraints).

Table 5.6 and Table 5.7 displays the calculated results from the python script for the equimolar concentrations of the alloys. In correspondence with the parameters thresholds all the alloys are predicted to obtain a BCC crystal structure solid solution.

Table 5.6: Data calculated from the python script for the equimolar compositions of the chosen alloys

Equimolar Alloy Compositions	Omega	Atomic size difference (%)	Entropy ($JK^{-1}mol^{-1}$)	Enthalpy ($kJmol^{-1}$)	VEC
$V_{0.2}Cr_{0.2}Mn_{0.2}Fe_{0.2}W_{0.2}$	63492	3.99	13.38	-0.48	6.4
$V_{0.2}Cr_{0.2}Mn_{0.2}Ta_{0.2}W_{0.2}$	15372	4.44	13.38	-2.24	5.8
$V_{0.16}Cr_{0.16}Mn_{0.16}Fe_{0.16}Ta_{0.16}W_{0.16}$	10845	5.00	14.62	-3.18	5.92
$V_{0.2}Cr_{0.2}Fe_{0.2}Ta_{0.2}W_{0.2}$	5502	5.41	13.38	-6.4	6
$V_{0.25}Cr_{0.25}Fe_{0.25}Ta_{0.25}$	3305	5.78	11.53	-8.25	6

Table 5.7: Data calculated from the python script for the equimolar compositions of the chosen alloys

Equimolar Alloy Compositions	Gibbs free energy ($kJmol^{-1}$)	Melting Temperature (°C)	Predicted solid solution
$V_{0.2}Cr_{0.2}Mn_{0.2}Fe_{0.2}W_{0.2}$	-3988	2005	BCC
$V_{0.2}Cr_{0.2}Mn_{0.2}Ta_{0.2}W_{0.2}$	-3990	2300	BCC
$V_{0.16}Cr_{0.16}Mn_{0.16}Fe_{0.16}Ta_{0.16}W_{0.16}$	-4360	2086	BCC
$V_{0.2}Cr_{0.2}Fe_{0.2}Ta_{0.2}W_{0.2}$	-3994	2359	BCC
$V_{0.25}Cr_{0.25}Fe_{0.25}Ta_{0.25}$	-3443	2093	BCC

As mentioned previously in Chapter 2.3, the enthalpy of mixing equation (Equation 2) does not take into consideration any outlying binary pairs. Equation 2 averages the magnitudes of the binary pairs enthalpies of mixing but does not highlight if any of the elements bear highly negative or positive values when considered with any one of the other elements. The enthalpy of mixing is a criterion which determines the proclivity of a binary pair to form a strong intermetallic bond. An extremely negative value would suggest an intermetallic formation of the binary pair, whilst an overly positive value would indicate poor mixing of the elements and allude to elemental segregation.

Table 5.8 displays the values of the enthalpies of mixing for the binary pairs of elements in this study. From all the possible binary pairs of low activation elements included in this study the enthalpy of mixing for iron-tantalum is by far the most negative and highest in magnitude. This indicates that alloys with both iron and tantalum will likely form a secondary phase containing at least these two elements.

Table 5.8: The values of enthalpies of mixing (kJmol^{-1}) for the binary pairs of elements in this work. These values were obtained from [24].

	Vanadium	Chromium	Manganese	Iron	Tantalum
Chromium	-2				
Manganese	-1	2			
Iron	-7	-1	0		
Tantalum	-1	-7	-4	-15	
Tungsten	-1	1	6	0	-7

Figure 5.4 displays the Fe-Ta binary phase diagram which shows the crystallographic data as a function of temperature [25].

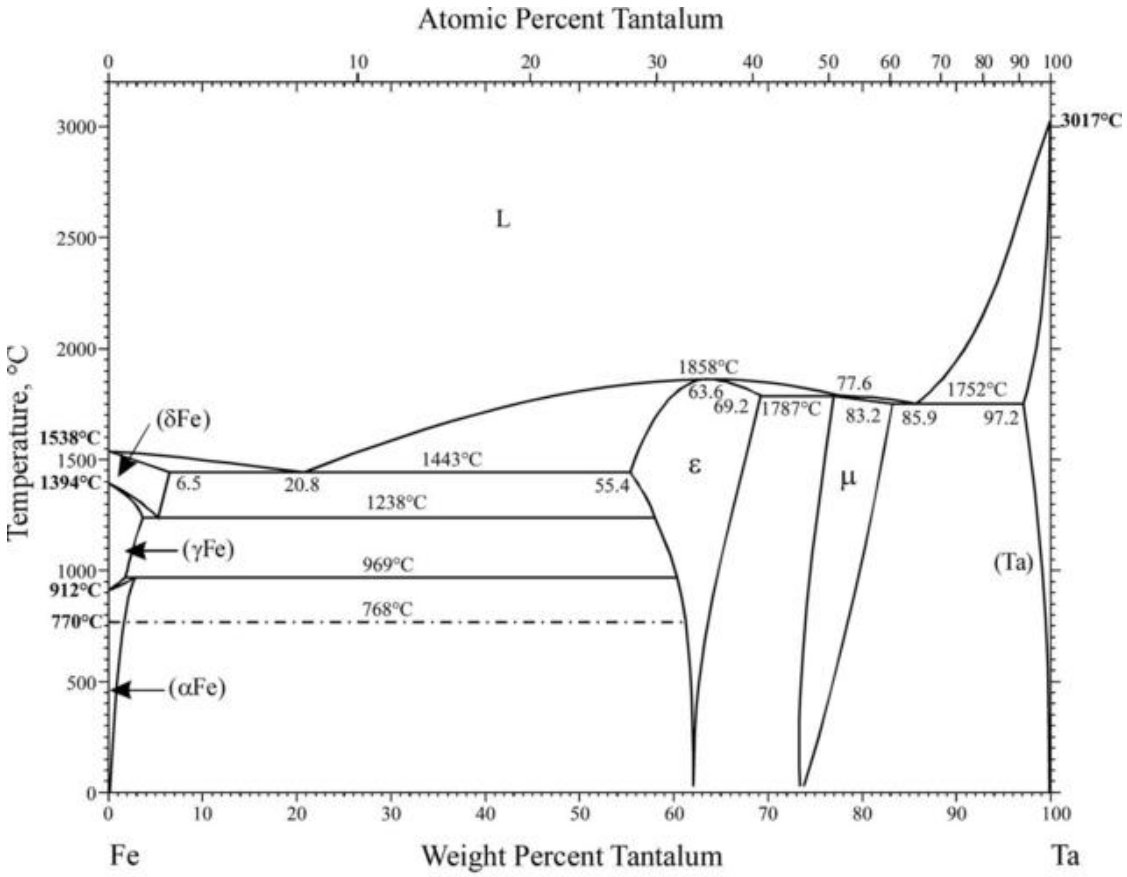

Figure 5.4: Binary phase diagram for Fe-Ta [25].

From the binary phase diagram, we can observe that intermetallic compounds and secondary phases readily form at a range of temperatures. For example, the μ phase and the ε phase are both intermetallic phases which are present at higher proportions of tantalum from melting to cooling of the binary alloy. This is discussed further in the next Section 5.7. Phase Diagrams where a range of likely binary phases are evaluated.

At the end of this chapter, the calculated empirical values for the equimolar compositions are compared with the refined composition values (determined from Thermo-Calc predictions) to ensure the parameters remain within the set boundaries. Refinement of the alloy compositions away from equimolar concentrations is necessary to comply with the fabrication methods and nuclear fusion applications. Therefore, it is necessary to re-evaluate the thermodynamic parameters for the newly designed alloys to see the effect of the change in composition with respect to the mixing enthalpies, entropy, and Gibbs free energy. Remaining within the upper and lower limits ensures the greatest likelihood for the formation of a disordered BCC solid solution. An assessment of this method is also provided at the end, with emphasis on the change in composition whilst retaining a stable BCC solid solution.

5.8. Phase Diagrams

As phase diagrams exhibit equilibrium conditions, slow heating and cooling rates must be used when considering data. This typically fluctuates from industrially made engineering alloys where kinetic effects and diffusion and reaction rates often contribute to phase formation. This can inhibit phase changes by increasing the time needed for a reaction to occur. For example, under rapid cooling rates, as demonstrated in VAM, the change in phase develops at a lower temperature than for equilibrium circumstances where cooling is much slower. Regardless of the imprecision of conventional alloy manufacturing compared to equilibrium environments, phase diagrams contain a wealth of knowledge concerning the potential phases an alloy composition may obtain.

An important aspect in the alloy design process is to assess the phase diagram of the candidate alloy. Construction of phase diagrams of multicomponent systems requires extensive generation of complex data. So, when considering the broad range of potential alloys that can be produced from the periodic table, as the number of components in the system increases, so does the number of possible elements.

Table 5.9 shows the possible number of systems for different phase diagrams. From this table, it is evident that the possible number of quaternary alloys runs into the millions. It is evident that most quaternary and higher-ordered phase diagrams are far from being fully experimentally determined, and thus for this reason, it is mostly binary and ternary (with a few quaternary) phase diagrams that have been experimentally verified so far.

Table 5.9: Possible number of systems depending on the number of components in the system out of 90 elements where n= number of elements considered, and m = number of components in the system [26].

Order of the system	**n! / m!(n-m)!**
Binary	90! / 2!(88)! = 4005
Ternary	90! / 3!(87)! = 117480
Quaternary	90! / 4!(86)! = 2255190

For the design of the low activation high entropy alloys in this study, well-established phase diagrams documented in the online ASM Handbook [27] were taken into consideration and tabulated. The critical study of these phase diagrams is of great importance as they can highlight any potential phase formation, including metastable phases, across a wide range of temperatures. However, it is important to note that whilst it is imperative to study available binary and ternary phase diagrams, phases and precipitates involving higher order systems are likely to form in multicomponent alloys and cannot accurately be predicted using the experimentally established phase diagrams of fewer elements. Therefore, it is crucial to consult materials design tools like Thermo-Calc for the prediction of higher order systems, as is discussed in greater depth in Section 5.8. Thermo-Calc. Furthermore, if a binary system within a more complex alloy is assessed in one of the thermodynamic databases in Thermo-Calc (that is, thermodynamic data underlying the binary phase diagram is captured within the database) then the calculated ternary system will be more accurate. For systems not experimentally verified in the ASM handbook, predictive methods such as Thermo-Calc can be a particularly useful tool in the design process.

Figure 5.5 shows the binary phase diagrams of V-Cr and V-W sourced from the ASM online Handbook [27].

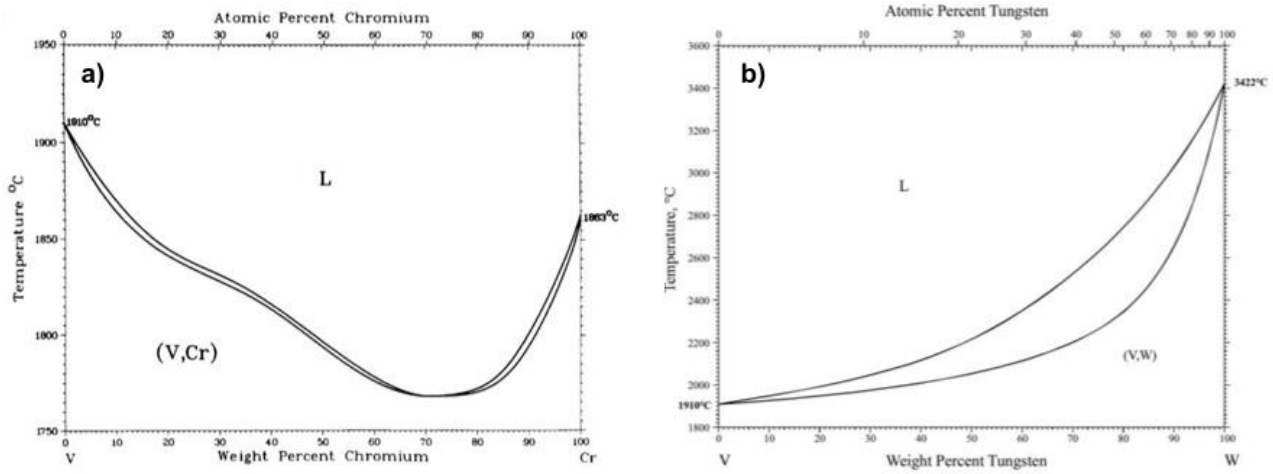

Figure 5.5: Binary phase diagrams a) V-Cr and b) V-W [27].

Both binary phase diagrams of the base VCrW alloy, V-Cr and V-W, are isomorphous systems - i.e., the elements demonstrate complete solubility with one another (across all temperatures) and so form one solid phase below the solidus. This is in part enabled by the elements all possessing bcc crystalline structures and similar atomic sizes. The ternary phase diagram of VCrW is discussed in the next section regarding the experimental verification of the equimolar alloy composition.

The binary phase diagrams of the low activation elements used in this study have been evaluated to assess the potential intermetallic precipitates and ordered compounds that may occur. Table 5.10 shows the potential ordered phases that are likely to form due to the combination of elements chosen including the Laves phase, σ phase, and μ phase.

Table 5.10: Comparison of some of the ordered intermetallic phases that occur in the binary phase diagrams for the elements included in the designed low activation alloys. The prototype of the compound is included (if the exact stoichiometry of the phase is unknown) as well as the space group and crystal structure [27]

Cr-Fe **Cr-Mn** **Fe-V** **Mn-V**	**Cr-Ta**	**Fe-Ta**	**Fe-W**	**Ta-V**
σ CrFe Tetragonal P42/mnm	α Cr_2Ta Hexagonal P63/mmc	ε $MgZn_2$ Hexagonal P63/mmc	μ Fe_7W_6 Trigonal R3m	α TaV_2 Cubic Fd-3m
	β Cr_2Ta Cubic Fd-3m	μ Fe_7W_6 Trigonal R3m	δ FeW Orthorhombic P212121	β TaV_2 Hexagonal P63/mmc

From this table it can be seen that the compound CrFe with a tetragonal crystal structure, also known as the sigma phase (σ phase), is present amongst several binary diagrams. For the binary diagrams not containing either chromium or iron, the CrFe structure is a prototype for the elements in the binary system being studied. For example, in the binary phase diagram Cr-Mn this phase would be present as CrMn with a defined stoichiometry. The propensity of the σ phase across a range of binary systems suggests that this phase is readily formed between these elements. Similarly, the Laves phase is present in the binary phase diagrams of Cr-Ta and Ta-V in both forms where the hexagonal crystal structure correlates with the C14 Laves phase and the cubic crystal structures is the C15 Laves phase. The σ phase and Laves phase belong to a class of phases defined as Frank Kasper phases. In high entropy alloys these phases are prevalent; the Laves phase is the most frequent intermetallic phase identified in HEAs, almost all of the Laves phases observed belong to the C14 variant [28]. This is theorised to be due to the hexagonal C14 Laves phase having a higher flexibility to accommodate atoms of varying sizes compared to the cubic C15 Laves phase. It is for this

reason that C14 Laves phases can stabilise at off-stoichiometric compositions whereas the C15 variant is only stable at the stoichiometric composition.

The formation of a single-phase BCC solid solution stable over a wide range of temperatures would be the ideal condition. However, from the binary phase diagrams there is strong evidence of the precipitation of ordered phases, particularly inclined to occur at lower temperatures. This may not be entirely detrimental to the overall mechanical performance of the multicomponent alloy, depending on the distribution and sizes of precipitates. Often, the introduction of high melting temperature transition metal based Laves phases helps to retain the alloy's strength at high temperature. However, precipitation of the Laves phase along the grain boundary will not provide strengthening to the alloy. Proper control on the amount, size, and morphology of these phases can be achieved using heat treatments and during the cooling process (this is explored further in Chapter 2.3: High Entropy Alloys). On the other hand, alloys predominantly formed of Laves or σ phases are notably brittle and so are unsuitable for use in many structural applications. Further work on the exploration of both the detrimental and beneficial effects of the Laves phase in reduced activation ferritic martensitic steels for fusion applications can be found in Chapter 2.1: Plasma-Facing Materials.

A further application of the binary phase diagrams is for the consideration of improving the fabrication methods of these refractory high entropy alloys. As detailed extensively in Chapter 3: Experimental Methodology there are some concerns when melting very high melting point elements with elements which possess low boiling/melting points. Pre-alloying some of the elements in the alloy to reduce the melting temperature for the ease of incorporating the volatile elements in a secondary melt is a common technique used for alloys with disparate components. Binary phase diagrams are used to identify a combination of components which reduces the solidus sufficiently to facilitate the mixing of problematic elements by the reduction of evaporation of these elements. Unfortunately, in this case, due to the high proportion of tungsten in these alloys, there was no suitable combination of elements which would adequately reduce the melting point. Therefore, the melting procedure identified in Chapter 3: Experimental Methodology was employed.

5.9. Thermo-Calc

The next stage of the alloy design process is to calculate the property diagrams of the equimolar alloy compositions. The HEA thermodynamic rules only consider the likelihood of the formation of a simple solid solution and serve to predict the crystal structure of the solid solution. Therefore, it is imperative to establish the probability of the formation of any ordered

or intermetallic compounds over a wide temperature range. Thermo-Calc is a computer software program which uses the CALPHAD method to predict equilibrium phase diagrams of novel alloy compositions [29]. In this work the Thermo-Calc 2021a version was used. The phases generated by Thermo-Calc are equilibrium phases as the model used to calculate the phase diagrams, CALPHAD, relies on thermodynamic principles and experimental binary, ternary, and higher-order phase diagram data. A description of the methodology of Thermo-Calc can be found in Chapter 3: Experimental Methodology.

For novel materials, construction of phase and property diagrams firstly involves the careful selection of a thermodynamic database. Usually, this is based on the principal element as typical for conventional engineering alloys. For example, for a novel steel composition the TCFE8 (v8.2) database, based on the iron phase diagrams, is appropriate to use. This approach is suitable for conventional alloys but as HEAs do not possess a dominant component, special considerations must be considered when selecting the most appropriate database. The databases contain thermodynamic information regarding the binary and ternary phase diagrams and each one differs by which phase diagrams are included. For example, the TCNI8 (v8.2) database contains data for a range of nickel binary, ternary and higher-order phase diagrams including phase information of elements which would likely be included in a Ni-based alloy. Whilst there is a dedicated HEA database (TCHEA44 v4.2) for multicomponent alloys, at the time of this work, this database has not yet been evaluated for refractory-based alloys. In this research, only a short-term trial version of the TCHEA4 database was available, therefore only the equimolar alloy compositions were investigated.

Inaccurate predictions of equilibrium phases can occur if an unsuitable thermodynamic database is chosen. If the appropriate phase diagrams are not assessed, then the calculation of incorrect crystal structures is more likely to occur. More importantly, if the binary phase diagrams of the components of a system are not evaluated in the database, then phases that are likely to occur (as predicted from the binary phase diagrams) will not appear in the Thermo-Calc property diagrams. Therefore, the selection of a database which encompasses all the relevant phase diagrams across the full compositional range is most preferable. For refractory alloys, there is no defined thermodynamic database, therefore the solid solution database (SSOL4) was selected, as it contains a wide selection of elements in the considered binary, ternary, and higher-order phase diagrams. The SSOL4 database was used to assess the equimolar compositions of the chosen alloys in this work to determine an enhanced alloy composition which mitigates the formation of any secondary intermetallic phases.

Table 5.11 shows the number of phases and systems included in the TCHEA4 and SSOL4 databases. The brackets highlight the number of phase diagrams assessed in the full compositional range and the relevant ternary phase diagrams which are included in the database. Systems evaluated for SSOL4 only included a minimum number of systems included as updated versions from 2004 are not available.

Table 5.11: A summary of the phases, elements, and systems included in the TCHEA4 and SSOL4 databases.

Thermodynamic database	**Elements**	**Binary systems**	**Ternary and higher-order systems**	**Solution and intermetallic phases**
SSOL4 (v4.9)	78 (all included)	115 Not included: Cr-Mn Cr-Ta Fe-Ta Ta-W V-W V-Ta	59 Included: Cr-Fe-W (relevant) C-Cr-Fe-Mn	600
TCHEA4 (v4.2)	26 (all included)	271 Not included: Mn-W	400+ (136 full-range) Included: Cr-Fe-V Fe-Ta-W Cr-Ta-W Cr-Fe-W	438

It is important to note that binary and ternary phase diagrams do not encompass an exhaustive list of all the possible phases that may occur - phases that are composed of several elements will only appear in multicomponent phase diagrams. As explained in Section 5.7. Phase Diagrams, only binary and ternary (and a few quaternary) experimental data are available in the databases due to the plethora of possible quaternary systems when considering the number of elements in the periodic table. This renders most of the higher-order phase diagrams far from being experimentally verified.

In this work, the SSOL4 (v4.9) and TCHEA44 (v4.2) were used to ascertain which equilibrium phases would be exhibited in the phase diagrams after alloying. Both thermodynamic databases were evaluated for comparison of low activation refractory HEAs.

Figure 5.6 displays the flowchart of the design process route using the two Thermo-Calc thermodynamic databases, TCHEA44 and SSOL4.

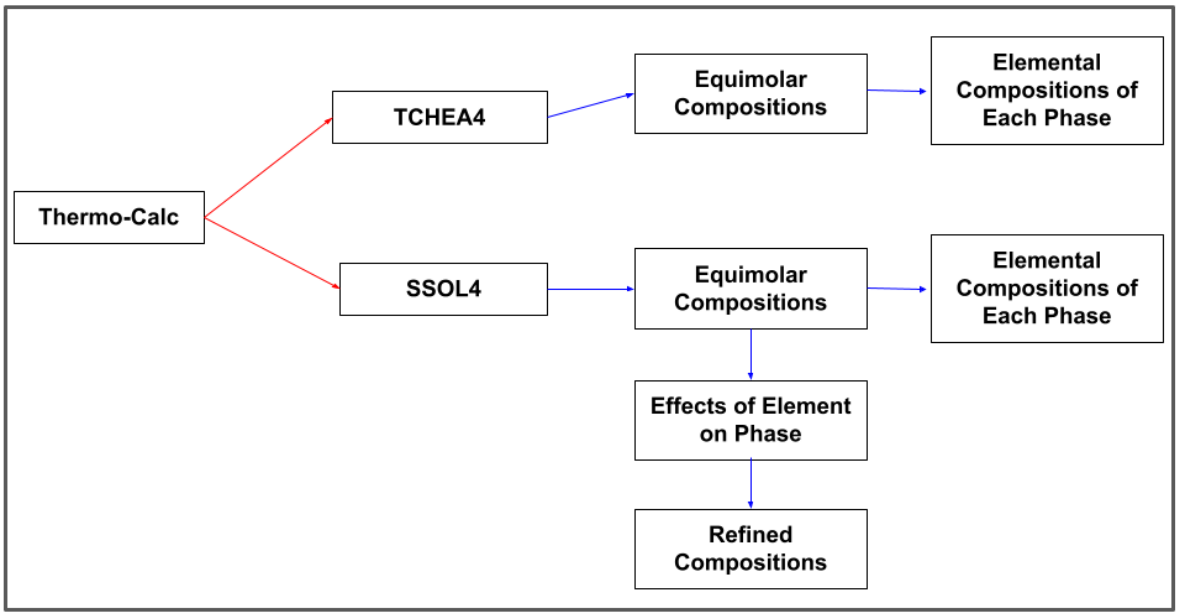

Figure 5.6: The flowchart outlining the design process route using the Thermo-Calc databases TCHEA4 and SSOL4

From this flowchart it can be observed that the design of the optimal alloy composition is an iterative process where the systematic modification of each element for the minimisation of an unfavourable phase (discussed in Section 5.7. Phase Diagrams) results in the design of a new alloy composition. This new composition is re-evaluated for the empirical HEA thermodynamic parameters to ensure the solid solution formed is still likely to have a BCC crystal structure.

Firstly, the equimolar alloy compositions (evaluated in the python script) were considered in Thermo-Calc using both the SSOL4 and TCHEA4 database for comparison of these databases. Property diagrams, where the amount of a phase produced as a function of temperature is given, were computed for each equimolar alloy using Thermo-Calc. Property diagrams differ from traditional phase diagrams in that the alloy composition is fixed so only the effect of a change in temperature influences the phases expected. However, the effect of concentration of each element for a given phase can also be computed, thus providing a relationship between the formation of a phase as a function of each elemental concentration. Establishment of a particular element's influence on the precipitation of an unfavourable ordered phase is vital. The mitigation of the formation of intermetallic compounds (highlighted

in Chapter 2.3: High Entropy Alloys) and encouragement of single-phase solid solutions may be necessary for evaluation of the radiation damage tolerant properties of HEAs. SSOL4 was primarily used to alter the equimolar alloy composition by adjusting each element's concentration separately to observe the subsequent changes in the property diagrams of the resultant alloy composition. This refinement process is repeated for all the elements in the alloy until a desirable composition is established and is a significant stage in the alloy design process for the minimisation of detrimental phases. The generation of property diagrams identifies any possible equilibrium phases that is likely to form across a wide range of temperatures. Ideally, a stable single-phase solid solution would be readily formed upon fabrication of the alloy with little to no precipitation of ordered phases at intermediate temperatures.

5.10. Preliminary Study of Ternary VCrW

A preliminary study was conducted for the evaluation of the Thermo-Calc predictions for a fabricated refractory alloy in the as-cast state. The experimental verification of the base alloy, VCrW, is explored in this work due to this favourable combination of elements, across a wide range of compositions, consistently being predicted to form a stable single BCC phase. Figure 5.7 shows the established ternary phase diagram, VCrW, at 1000 °C [30]. From this diagram the elements exhibit full miscibility with one another and possess a BCC phase solid solution in addition to a mixture of two BCC solid solutions at high concentrations of tungsten and chromium.

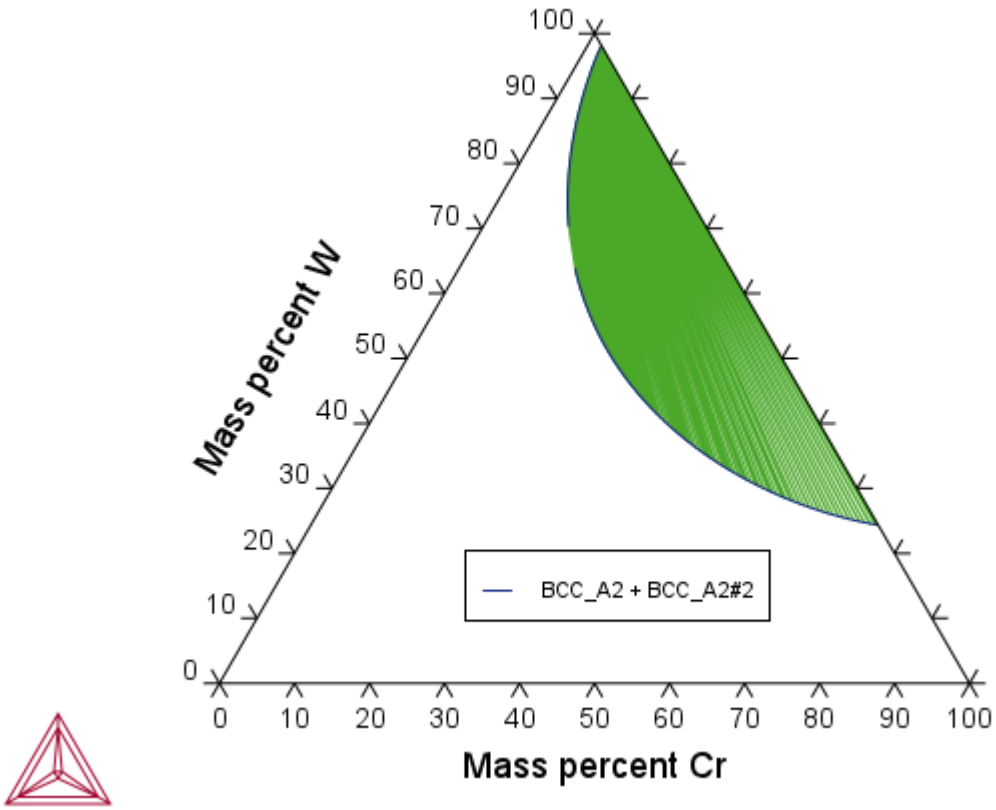

Figure 5.7: Isothermal ternary phase diagram of VCrW at 1000 °C

In the first instance, to establish the capabilities of Thermo-Calc for refractory alloys and to compare with the established isothermal ternary phase diagram, the property diagram for the alloy $V_{33}Cr_{33}W_{33}$ was calculating using the SSOL4 database. Figure 5.8 shows the property diagram of $V_{33}Cr_{33}W_{33}$ calculated using the SSOL4 database and includes the equilibrium phases predicted to occur. The property diagram confirms that a disordered BCC solid solution occurs across a wide range of temperatures, with a mixture of two disordered BCC phases below 1100 °C.

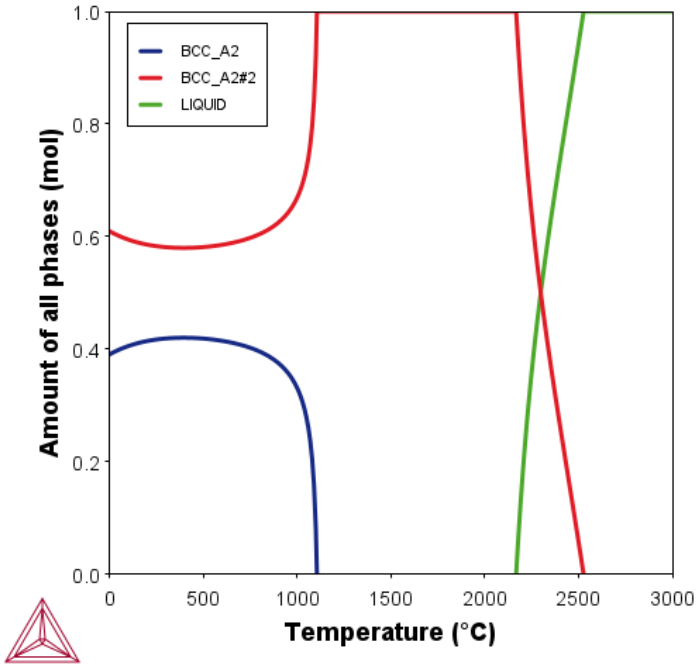

Figure 5.8: Property diagram of $V_{33}Cr_{33}W_{33}$ calculated using the SSOL4 database in Thermo-Calc

For experimental verification, the ternary VCrW alloy was fabricated using VAM (the full experimental details can be read in Chapter 3: Experimental Methodology) and characterised using X-ray diffraction (XRD) for phase identification. Figure 5.9 displays the XRD pattern of the as-cast ternary equimolar VCrW alloy and clearly shows a single-phase BCC phase with some micro-segregation.

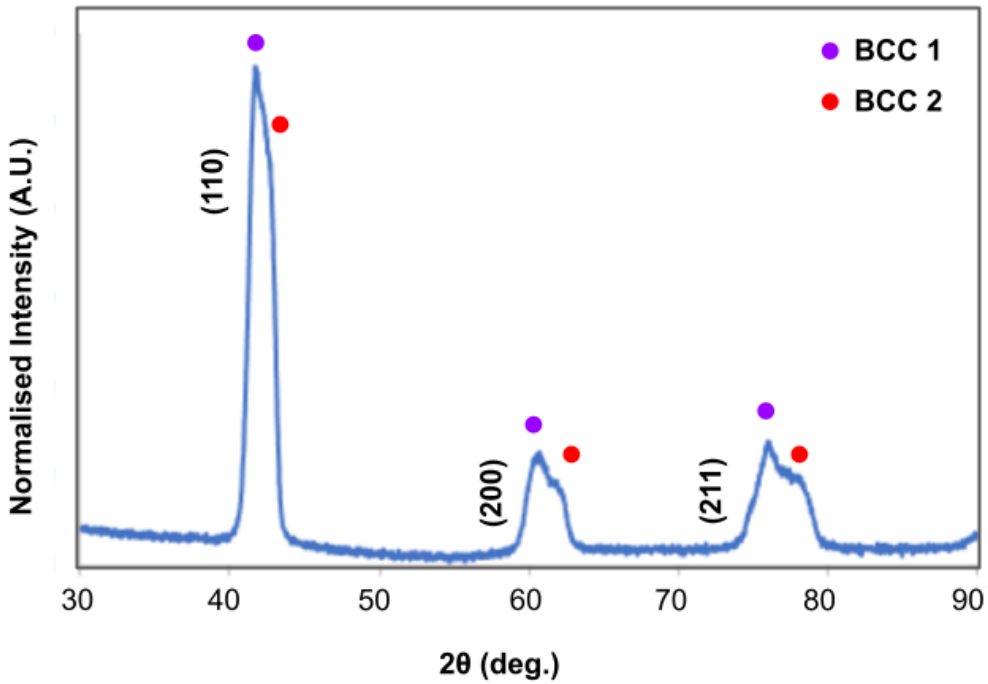

Figure 5.9: XRD pattern for the as-cast $V_{33}Cr_{33}W_{33}$ equimolar alloy

The broad peaks and slight splitting indicate that two BCC phases with very similar lattice parameters may be present but are overlapping due to their similarities. These results are in accordance with the ternary VCrW phase diagram and Thermo-Calc predictions and therefore suitable preliminary verifications so far have been made for this design tool. The predictions of a stable single BCC phase from Thermo-Calc, the available ternary diagram, and the experimentally verified results suggest that the maximisation of V, Cr, W (where permitted by the fabrication restrictions) in the designed alloys will strengthen the formation of this favourable BCC matrix.

The next section investigates the Thermo-Calc predictions for the equimolar alloy compositions and details the refinement process for each of the alloys investigated in this work.

5.11. Refinement of $V_{25}Cr_{25}Fe_{25}Ta_{25}$

Figure 5.10 shows the Thermo-Calc property diagrams for the equimolar VCrFeTa using both the SSOL4 and TCHEA4 databases. Both databases predict a BCC phase, as was also determined by the empirical parameters. However, the TCHEA4 database predicts a C15 Laves phase as the predominate phase across all temperatures, whilst the SSOL4 suggests a BCC solid solution upon solidification to around 1000 °C.

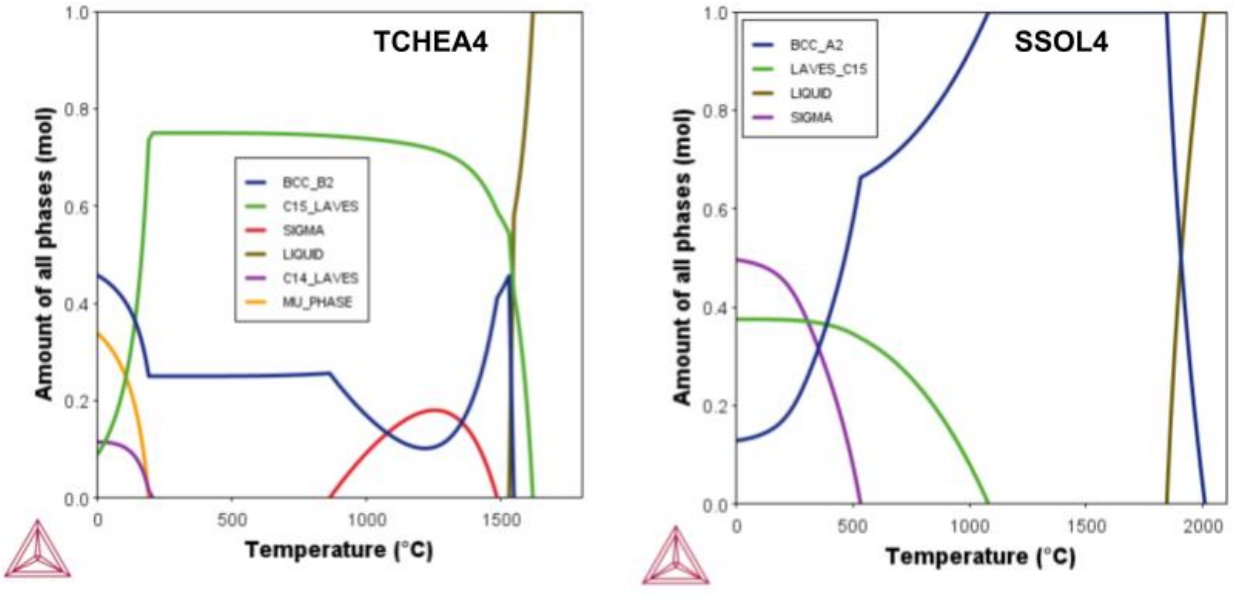

Figure 5.10: The property diagrams for $V_{25}Cr_{25}Fe_{25}Ta_{25}$ determined by the SSOL4 and TCHEA4 databases in Thermo-Calc.

Using the TCHEA4 database, $V_{25}Cr_{25}Fe_{25}Ta_{25}$ upon solidification displays a majority C15 Laves phase (around 0.9 mol) with fluctuating additions of the ordered BCC B2 (0.5 mol – 0.1 mol) and σ phases (0.2 mol). All three of these phases are ordered brittle phases and so are deemed unfavourable for fusion applications in significant proportions.

Table 5.12 details the constituents (and their concentrations) of phases present in $V_{25}Cr_{25}Fe_{25}Ta_{25}$ as determined by the TCHEA4 database using Thermo-Calc. The amount of each element in the phases present in $V_{25}Cr_{25}Fe_{25}Ta_{25}$ are determined as a function of temperature.

Table 5.12: The relative concentration of components in the phases present in $V_{25}Cr_{25}Fe_{25}Ta_{25}$ from the TCHEA4 database

Phase	Amount of component in the phase from the largest concentration to smallest
BCC B2	V>Cr>Fe>Ta
Laves C15	Ta>Fe>Cr>V
σ	V>Fe>Cr>Ta

From these plots it can be observed that vanadium is the majority component for both the ordered BCC B2 and σ phase. This can be rationalised by the property diagram of $V_{25}Cr_{25}Fe_{25}Ta_{25}$ which exhibits the inverse relationship between the two phases. One hypothesis could be that both phases are competing for the same elements, therefore when one phase is in a higher proportion, there is less vanadium available and so the other phase is diminished in comparison. On the other hand, tantalum is the major component of the C15 Laves phase and has the least concentration in both the BCC B2 and σ phases. Therefore, there is no competition between these phases and no resultant fluctuation of concentration in relation to them.

In comparison, for the same equimolar alloy composition, the SSOL4 database calculates a majority disordered BCC A2 matrix with significant amounts of Laves C15 and σ phases forming below 1100 °C (as shown in Figure 5.10). This is like the predictions made by TCHEA4 database, in that a BCC, C15 Laves, and σ phase are all predicted, however, there is a discrepancy in the amounts of each phase predicted. Another notable difference between SSOL4 and the newer TCHEA4 database is the prediction of ordered phases and their disordered counterparts. The bulk ordered BCC B2 phase in the equimolar composition predicted by the TCHEA4 database differs from the disordered BCC A2, suggested by the

SSOL4 database. To successfully extrapolate higher-ordered systems for the TCHEA4 database, ordered and disordered systems are modelled with the partitioning model which aims to fully describe second-order transformations. Furthermore, another disparity can be observed in predicted phases suggested by Thermo-Calc. From the $V_{25}Cr_{25}Fe_{25}Ta_{25}$ property diagrams, the TCHEA4 database predicts the dominance of the C15 Laves phase (compared to the C14 Laves phase) compared to the SSOL4 database which suggests the sole formation of the C15 Laves phase. When considering the literature survey of prevalent phases formed in HEAs (as discussed in Chapter 2.3: High Entropy Alloys), the C14 Laves phase is observed to a much greater extent in fabricated alloys compared to the C15 Laves variant. However, for this particular alloy and database, Thermo-Calc still consistently predicts the formation of the C15 Laves phase. This may be due to the prevalence of both varieties, C14 and C15, of the Laves phases in the corresponding binary phase diagrams. Therefore, this is clearly an aspect of this design tool that needs further development.

Figure 5.11 shows the change in concentration of chromium for VCr_xFeTa and the resulting effect of the formation of equilibrium phases. From this diagram it can be observed that reducing the chromium content of VCr_xFeTa significantly reduces the undesirable C15 Laves phase and promotes their formation at lower temperatures.

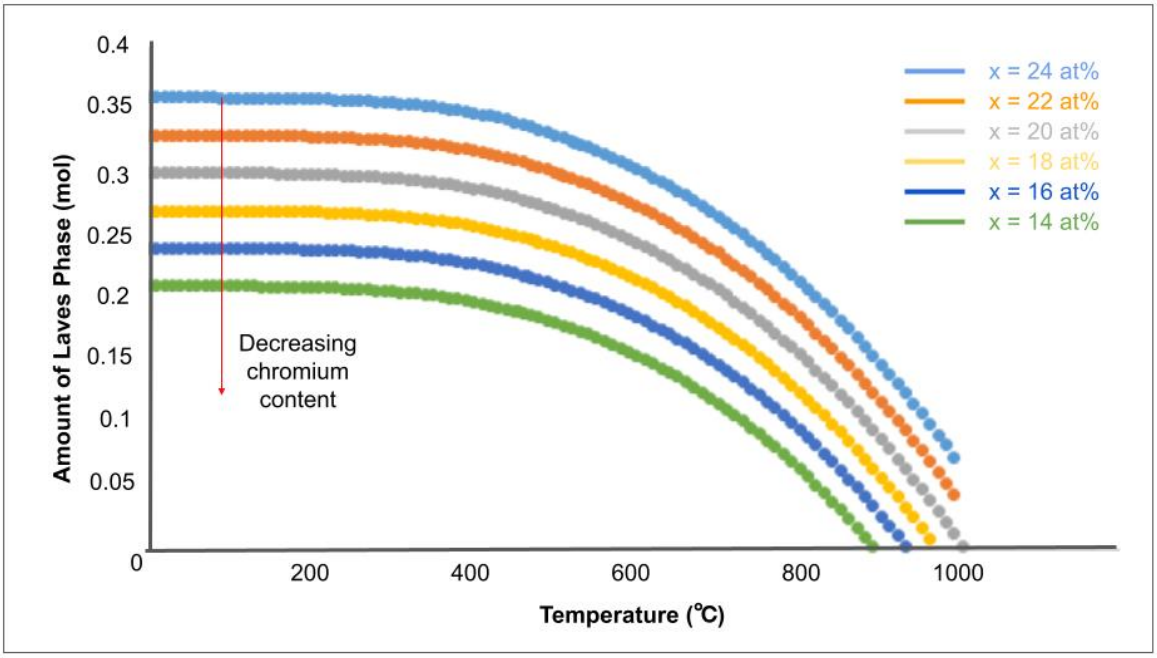

Figure 5.11: The effect of change in concentration of Cr in VCr_xFeTa on the equilibrium phase formation

By reducing the chromium content from 25 at% to 15 at% there is approximately a reduction of approximately 0.16 mol of the unfavourable C15 Laves phase. However, to accommodate for the reduction of chromium, there must be an increase in another alloy constituent. As chromium has been sufficiently reduced to minimise the C15 Laves phase, increasing the

tantalum content will not further increase the C15 Laves phase. To increase the overall melting point of the alloy a bigger proportion of the highest melting point element is added. For VCrFeTa, increasing the content of tantalum will increase the melting point of the alloy.

Figure 5.12 shows the property diagram of $V_{25}Cr_{15}Fe_{35}Ta_{25}$, the refined composition of VCrFeTa, predicted using the SSOL4 database. In the compositional refinement of the alloy VCrFeTa, the equimolar composition does not result in a single-phase alloy but altering the concentration of the elements does cause a change in the equilibrium phases.

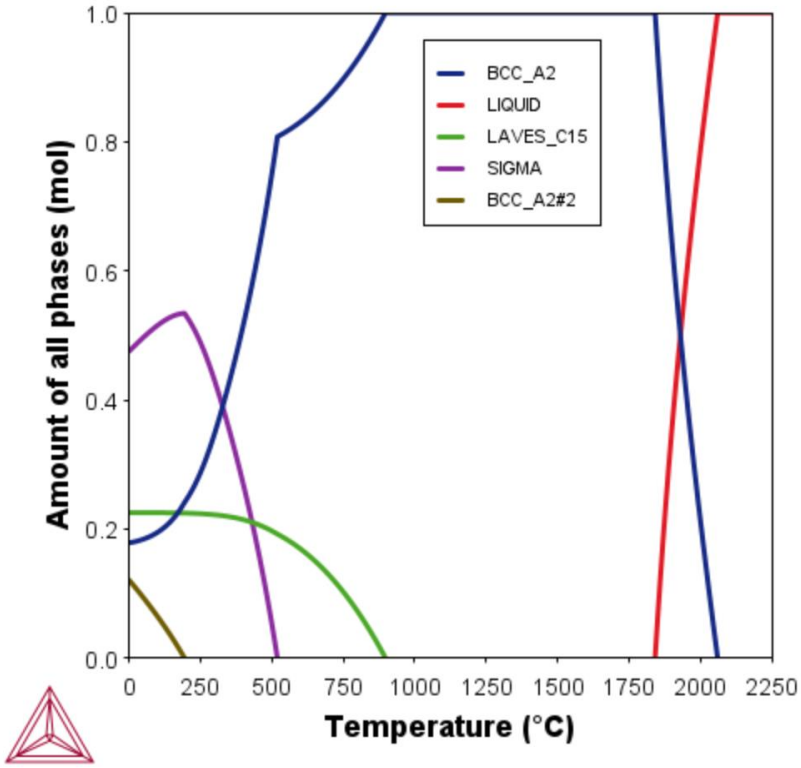

Figure 5.12: The property diagram of the refined alloy composition, $V_{25}Cr_{15}Fe_{35}Ta_{25}$, using the SSOL4 database.

Compared to the property diagram of $V_{25}Cr_{25}Fe_{25}Ta_{25}$ (also using the SSOL4 database) there is an overall reduction of Cr from 25 at% to 15 at% which corresponds to a successful decrease in the concentration of the Laves phase from a maximum of 0.9 mol to 0.24 mol. Whilst there is a small increase in the maximum amount of the σ phase from 0.5 mol to 0.55 mol, this only occurs at around 250 °C which is an insignificant temperature for the alloy's application. There is also an additional disordered BCC A2 phase. It should be noted that #n (where n is an integer) denotes the same morphology of crystal structure but with the elements residing in different site occupations. However, this phase is only present below 250 °C with a maximum concentration of 0.1 mol. Whilst this alloy does not solely exhibit a single BCC phase across all temperatures, between 500 °C and 900 °C there is only a maximum 0.2 mol

of C15 Laves phase (and 0.8 mol of disordered BCC) and above this temperature (until melting) there is only a disordered BCC phase predicted.

5.12. Refinement of $V_{20}Cr_{20}Fe_{20}Ta_{20}W_{20}$

Figure 5.13 shows the Thermo-Calc property diagrams for the equimolar VCrFeTaW using both the SSOL4 and TCHEA4 databases. For $V_{20}Cr_{20}Fe_{20}Ta_{20}W_{20}$, TCHEA4 predicts the formation of several different phases (ordered BCC B2, C15 and C14 Laves, μ phase); there is no one predominant phase over a wide temperature range. On the other hand, the SSOL4 database predicts a disordered BCC A2 phase, a C15 Laves phase, and a σ phase.

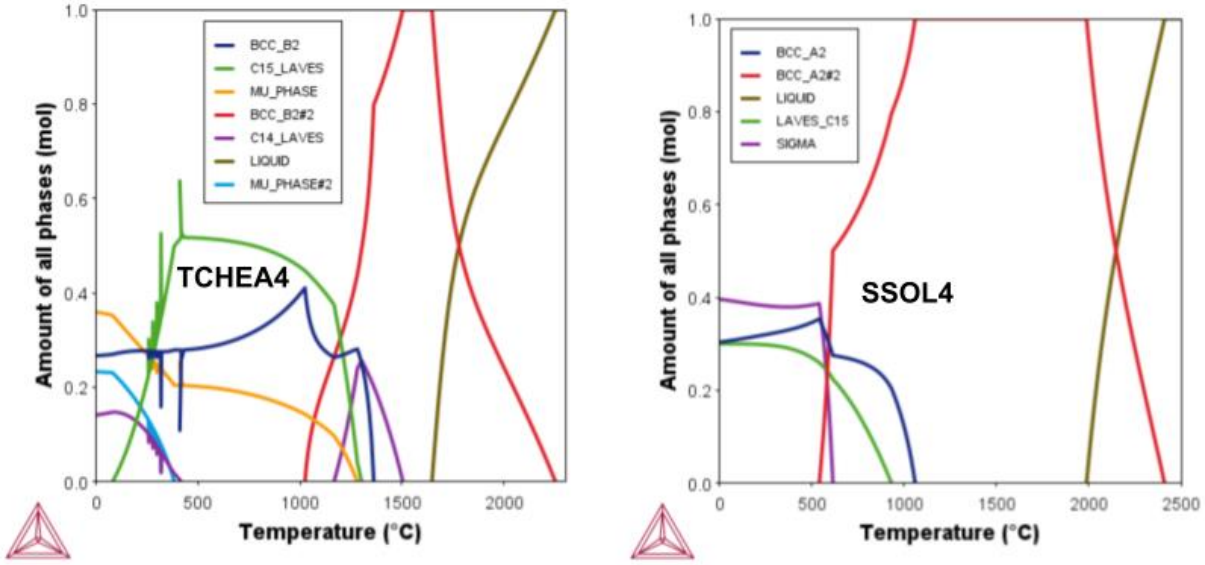

Figure 5.13: The property diagrams for $V_{20}Cr_{20}Fe_{20}Ta_{20}W_{20}$ determined by the SSOL4 and TCHEA4 databases in Thermo-Calc.

The $V_{20}Cr_{20}Fe_{20}Ta_{20}W_{20}$ property diagram generated by the SSOL4 database is more akin to the equilibrium phases predicted for $V_{25}Cr_{25}Fe_{25}Ta_{25}$. There is a predominant disordered BCC phase which is the majority phase until 1000 °C, below this temperature there is around 0.4 mol of either the σ, C15 Laves, and an additional disordered BCC A2 phase.

There are vast differences between the TCHEA4 and SSOL4 predictions for $V_{20}Cr_{20}Fe_{20}Ta_{20}W_{20}$. For the TCHEA4 database, the C15 Laves phase encompasses almost half of the microstructure of the alloy between 400 °C and 1300 °C. This is like $V_{25}Cr_{25}Fe_{25}Ta_{25}$ (using the same database) where the C15 Laves phase was the predominant phase predicted. The same C15 Laves phase is predicted using the SSOL4 database for $V_{20}Cr_{20}Fe_{20}Ta_{20}W_{20}$, however in much smaller proportions (maximum 0.3 mol below 1000 °C). Also, like $V_{25}Cr_{25}Fe_{25}Ta_{25}$, the TCHEA4 database consistently predicts the formation of both the C15 and C14 Laves phase for $V_{20}Cr_{20}Fe_{20}Ta_{20}W_{20}$, whilst the SSOL4 database only predicts the

C15 Laves variant. Another distinct difference between the TCHEA4 and SSOL4 database predictions is the formation of the σ phase. For $V_{20}Cr_{20}Fe_{20}Ta_{20}W_{20,}$ the SSOL4 database predicts the formation of the σ phase, whilst the TCHEA4 database does not suggest any formation of the σ phase. In the experimental assessment of VCrFeTaW the identification of the σ phase from experimental XRD validates the prediction of the σ phase using the SSOL4 database (this is discussed in depth in Chapter 6: Experimental Assessment of Novel High Entropy Alloys).

Table 5.13 details the constituents (and their concentrations) of phases present in $V_{20}Cr_{20}Fe_{20}Ta_{20}W_{20}$ as determined by the TCHEA4 database using Thermo-Calc. The amount of each element in the phases present in $V_{20}Cr_{20}Fe_{20}Ta_{20}W_{20}$ are determined as a function of temperature.

Table 5.13: The relative concentration of components in the phases present in equimolar VCrFeTaW from the TCHEA4 database

Phase	Amount of component in the phase from the largest concentration to smallest
BCC B2	V>W>Ta>Cr>Fe
BCC B2 #2	V=W=Ta=Cr=Fe
Laves C15	Fe>Ta>Cr>V
Laves C14 (low temperature)	Fe>Ta>Cr
Laves C14 (high temperature)	Fe>Ta>Cr>W
μ phase	Cr>W>Ta>Fe

Another difference between the TCHEA4 and SSOL4 is the prediction of the Mu phase, which only appears in the TCHEA4 database for $V_{20}Cr_{20}Fe_{20}Ta_{20}W_{20.}$ A significant amount (0.2 mol rising to 0.35 mol below 500 °C) is predicted to form. From the binary diagrams of both Fe-Ta and Fe-W there is the formation of the intermetallic compound Fe_7W_6 (an analogous structure in the Fe-Ta phase diagram) which possesses a trigonal crystal structure and is termed the μ phase. $V_{20}Cr_{20}Fe_{20}Ta_{20}W_{20}$ contains a higher proportion of Fe, Ta, and W compared to the other alloys in this system, so the probability of the μ phase forming is increased. However, the μ phase observed in the property diagram of $V_{20}Cr_{20}Fe_{20}Ta_{20}W_{20}$ (using TCHEA4) contains a moderate proportion of Cr, Fe, Ta, and W (as observed in Table 5.13) suggesting a higher-ordered phase which cannot be directly inferred from the binary phase diagram.

From Table 5.13 it can be observed that there is a compositional difference between the ordered BCC B2 phases predicted by TCHEA4. At temperatures below 1000 °C, the ordered BCC B2 dominates over the ordered BCC B2 #2 variant phase. The lower temperature dominant phase is mostly rich in vanadium and tungsten whereas higher temperature BCC phase has components which are roughly equimolar in composition. However, this higher temperature phase is unstable and rapidly decomposes below 1500 °C.

For the refinement of $V_{20}Cr_{20}Fe_{20}Ta_{20}W_{20}$ the relative concentrations of components in the equilibrium phases (Table 5.13) were taken into consideration. It is likely that the minimisation of the iron content is likely to reduce both variants of the Laves phase. This calculation was considered in Thermo-Calc as a first step to reduce the Laves phases.

Figure 5.14: The effect of reducing the iron content from 20 at% to 10 at% whilst keeping the rest of the alloy equimolar for $VCrFe_xTaW$ on the equilibrium phase formation.

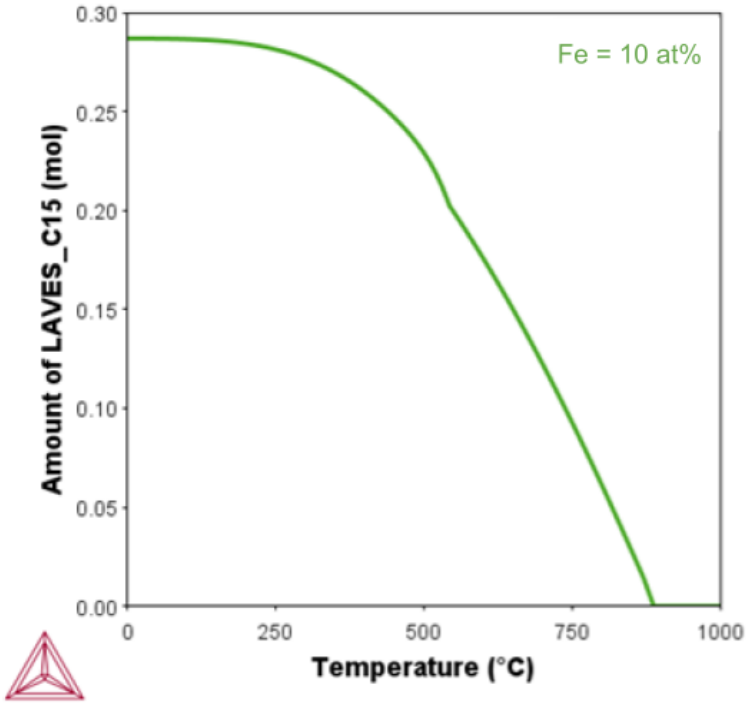

Figure 5.14: The property diagrams for $V_{0.225}Cr_{0.225}Fe_{0.1}Ta_{0.225}W_{0.225}$ determined by the SSOL4 database using Thermo-Calc

Compared to the equimolar VCrFeTaW property diagram, the concentration of the C15 Laves phases has remained the same around 0.3 mol in concentration, whilst the temperature of formation is reduced by approximately 100 °C. Therefore, again using the results from Table 5.13, to encourage the formation of the BCC phase, the vanadium content was increased from 20 at% to 30 at%. Additionally, the increase of tungsten to 30 at% is also hypothesised to

encourage a single BCC solid solution. However, the composition of tungsten cannot be increased further as a higher amount of tungsten would rapidly increase the melting temperature of the alloy which could hinder the melting process. To compensate for these elemental changes, there must be a reduction in either (or both) tantalum or chromium.

To decrease the unfavourable Laves phases, the alloy $V_{0.3}Cr_xFe_{0.1}Ta_xW_{0.3}$ has been designed. Three separate alloy compositions were computed in Thermo-Calc to determine the most optimised alloy.

1. Equal content of chromium and tantalum (Cr=15 at%, Ta=15 at%)
2. High chromium content, low tantalum content (Cr=20 at%, Ta=10 at%)
3. Low chromium content, high tantalum content (Cr=10 at%, Ta=20 at%)

Figure 5.15 shows the three property diagrams for $V_{0.3}Cr_{0.15}Fe_{0.1}Ta_{0.15}W_{0.3}$, $V_{0.3}Cr_{0.2}Fe_{0.1}Ta_{0.1}W_{0.3}$, and $V_{0.3}Cr_{0.1}Fe_{0.1}Ta_{0.2}W_{0.3}$ using the SSOL4 database of Thermo-Calc. Higher content of chromium leads to the highest proportion of the C15 Laves phase (though the amount of Laves phase for this alloy is still less than the equimolar VCrFeTaW. Equal proportions of chromium and tantalum lead to a further decrease of the Laves phase.

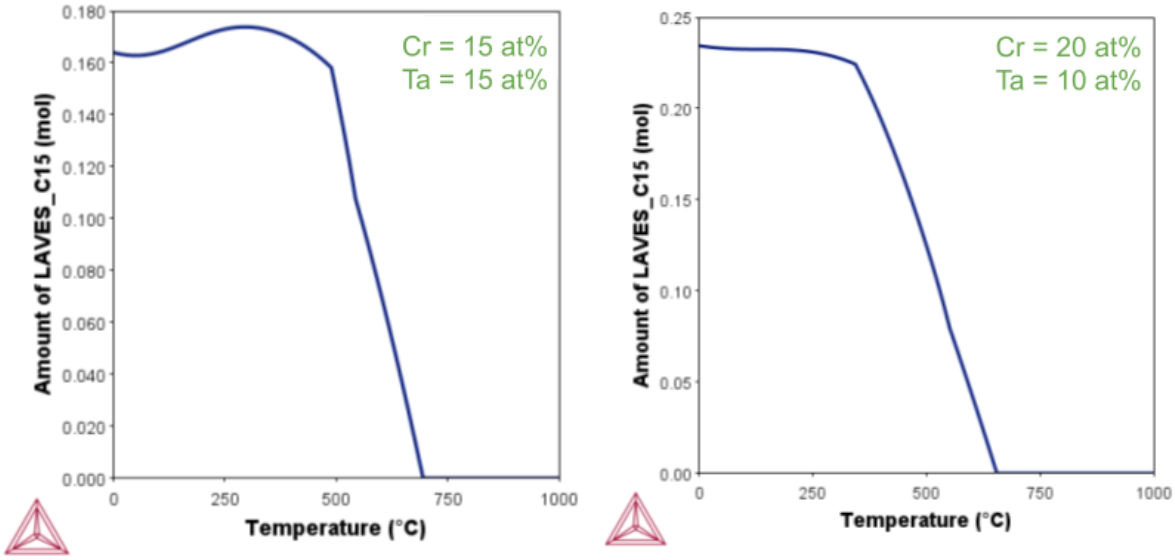

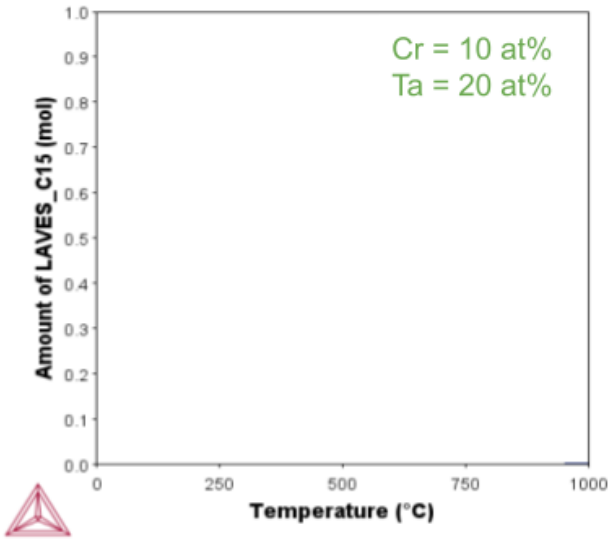

Figure 5.15: Three property diagrams of $V_{0.3}Cr_{0.15}Fe_{0.1}Ta_{0.15}W_{0.3}$, $V_{0.3}Cr_{0.2}Fe_{0.1}Ta_{0.1}W_{0.3}$, and $V_{0.3}Cr_{0.1}Fe_{0.1}Ta_{0.2}W_{0.3}$ using the SSOL4 database of Thermo-Calc

However, it is obvious from these results that that an increase of tantalum content to 20 at% (therefore chromium content will be 10 at%) will completely diminish the C15 Laves phase.

Figure 5.16 shows the property diagram of $V_{30}Cr_{10}Fe_{10}Ta_{20}W_{30}$, the refined composition of VCrFeTaW, predicted using the SSOL4 database. The predominant phases from the melting point to 750 °C is the disordered BCC phase (at 1100 °C there is also a second BCC phase with a slightly different composition). Below 600 °C there is a negligible amount of a C15 Laves phase (less than 0.1 mol).

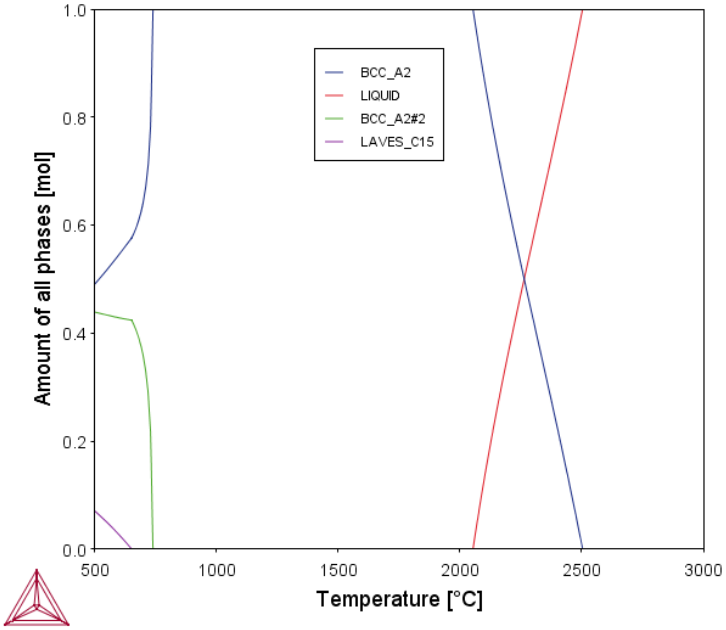

Figure 5.16: The property diagram of the refined alloy composition, $V_{30}Cr_{10}Fe_{10}Ta_{20}W_{30}$, using the SSOL4 database.

5.13. Refinement of $V_{20}Cr_{20}Mn_{20}Fe_{20}W_{20}$

Figure 5.17 shows the Thermo-Calc property diagrams for the equimolar VCrMnFeW using both the SSOL4 and TCHEA4 databases. For $V_{20}Cr_{20}Fe_{20}Ta_{20}W_{20}$, TCHEA4 predicts the formation an ordered BCC B2 stable upon cooling until 1000 °C. Below 1000 °C the formation of a predominant σ phase occurs (0.6 mol) with a moderate amount of an ordered BCC B2 #2 phase (0.4 mol). On the other hand, the SSOL4 database predicts a stable disordered BCC A2 phase from cooling until 550 °C (with a minor addition of a second ordered BCC B2 #2). Below 550 °C there are several σ phases predicted up to 0.4 mol in concentration.

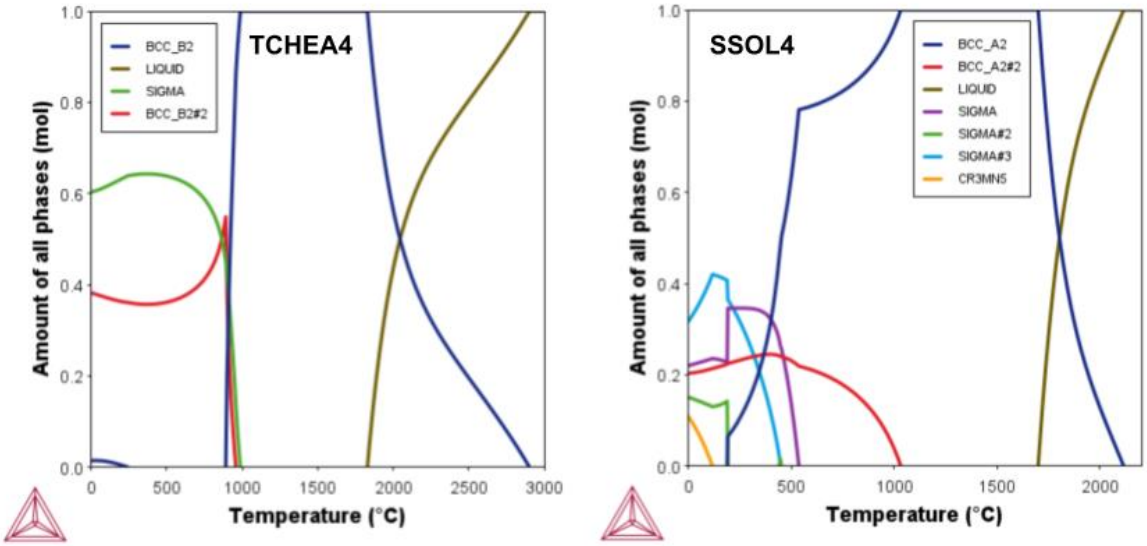

Figure 5.17: The property diagrams for $V_{20}Cr_{20}Mn_{20}Fe_{20}W_{20}$ determined by the SSOL4 and TCHEA4 databases in Thermo-Calc.

A slight difference between TCHEA4 and SSOL4 for the equimolar composition of VCrMnFeW is the prediction of a small amount of the intermetallic compound Cr_3Mn_5 (a cubic phase analogous to the α Mn phase with the A12 structure) below 100 °C. However, the inaccuracies of Thermo-Calc predictions below a few 100 °C means that this phase can be neglected.

Table 5.14 details the constituents (and their concentrations) of phases present in $V_{20}Cr_{20}Mn_{20}Fe_{20}W_{20}$ as determined by the TCHEA4 database using Thermo-Calc. The amount of each element in the phases present in $V_{20}Cr_{20}Mn_{20}Fe_{20}W_{20}$ are determined as a function of temperature.

Table 5.14: The relative concentration of components in the phases present in equimolar VCrMnFeW from the TCHEA4 database

Phase	Amount of component in the phase from the largest concentration to smallest
BCC B2	W>Mn>V>Cr>Fe
BCC_B2#2	W>V>Mn>Cr>Fe
σ	Fe>Cr>V>Mn>>W

As discussed in previous sections, whilst the prediction of the σ phase was absent from the TCHEA4 predictions for $V_{20}Cr_{20}Fe_{20}Ta_{20}W_{20}$, for $V_{20}Cr_{20}Mn_{20}Fe_{20}W_{20}$ a significant proportion of the microstructure is composed of the σ phase (0.6 mol) which is due to form at temperatures below 1000 °C. The σ phase is also due to form using the SSOL4 predictions albeit at lower temperatures (550 °C) than that predicted by TCHEA4. In addition, the contents of the phases also differ: Fe-V rich and lower in Cr is predicted using the SSOL4 database compared to the higher proportion of Fe-V-Cr for the TCHEA4 predictions. This may be likely due to the higher proportion of the σ phase being evident in the TCHEA4 predictions (0.6 mol) compared to the SSOL4 predictions (0.4 mol). On the other hand, the same predilection the TCHEA4 database has for predicting an ordered BCC matrix over a disordered one (and vice versa for SSOL4) also appears to be the case for VCrMnFeW.

The striking similarities between the two database predictions for $V_{20}Cr_{20}Mn_{20}Fe_{20}W_{20}$, compared to the previous alloys, may result from the lack of Ta binary phase diagrams assessed in SSOL4. A consequence of this is the reliance of further computational extrapolations needed to predict the phases that may form for Ta-based alloys; the lack of experimental data for the Ta-binary systems may result in the calculation of unreliable phases that would not occur experimentally.

VCrMnFeW differs from the previous alloy compositions in that the inclusion of manganese, a volatile element with a low boiling point, yields further special considerations. As previously discussed, the low boiling point of manganese increases the tendency of evaporation during the melting process resulting in an alloy with a lower concentration of manganese. Also, elemental manganese has a propensity to oxide rapidly in air and despite gentle removal of this outer oxide scale prior to melting, some oxygen may still be introduced in the alloying process. To mitigate these issues, a moderate reduction amount of manganese is accepted in the design process. However, even limited amounts of a component can still have dramatic effects on the microstructure and crystalline structure. In the TCHEA4 database, even though 271 binary systems are assessed, the Mn-W phase diagram is not evaluated. The

experimental binary phase diagram is also missing from the ASM handbook [29]. So it is clear that further experimental work in the Mn-W binary system is needed and as a result the formation of Mn-W phases cannot be accurately predicted in this process.

The refinement process of VCrMnFeW begins with the fabrication restriction of minimising volatile elements. For all the alloys, manganese is reduced to below 10 at%. An extremely large solidification range is apparent in both equimolar VCrMnFeW property diagrams (Figure 5.17). For the TCHEA4 prediction the freezing range is approximately 700 °C, whilst for the SSOL4 property diagram the range is around 350 °C. To avoid further melting issues during fabrication, the concentration of manganese is set to the minimum 5 at%. For the refinement of $V_{0.2}Cr_{0.2}Mn_{0.05}Fe_{0.2}W_{0.2}$ the relative concentrations of components in the equilibrium phases (Table 5.14) was taken into consideration. Increasing the content of tungsten and vanadium will likely promote the formation of the BCC phase. For this reason, the concentrations of both vanadium and tungsten are set to the maximum 35 at%. To compensate for these elemental changes, there must be a reduction in either (or both) iron and chromium. As shown in Table 5.14 the σ phase has a high concentration of iron whilst the BCC matrix is lean in this element. Therefore, by decreasing the content of iron, it is theorised that the amount of σ phase formed is also diminished. However, an investigation into the relationship between the iron and chromium content on the formation of the σ phase is undertaken to justify this hypothesis.

To maximise the BCC phase and to adhere to fabrication restrictions, the alloy $V_{0.35}Cr_xMn_{0.05}Fe_xW_{0.35}$ has been designed. Four separate alloy compositions were computed in Thermo-Calc to determine the most optimised alloy for the decrease the unfavourable σ phase. Decreasing content of chromium and increasing concentration of iron (and vice versa) was calculated where:

1. Cr=20 at%, Fe=5 at%
2. Cr=15 at%, Fe=10 at%
3. Cr=10 at%, Fe=15 at%
4. Cr=5 at%, Fe=10 at%

Figure 5.18 shows the three property diagrams for $V_{0.3}Cr_{0.15}Fe_{0.1}Ta_{0.15}W_{0.3}$, $V_{0.3}Cr_{0.2}Fe_{0.1}Ta_{0.1}W_{0.3}$, and $V_{0.3}Cr_{0.1}Fe_{0.1}Ta_{0.2}W_{0.3}$ using the SSOL4 database of Thermo-Calc. Higher content of chromium leads to the highest proportion of the C15 Laves phase (though the amount of Laves phase for this alloy is still less than the equimolar VCrFeTaW. Equal proportions of chromium and tantalum lead to a further decrease of the Laves phase.

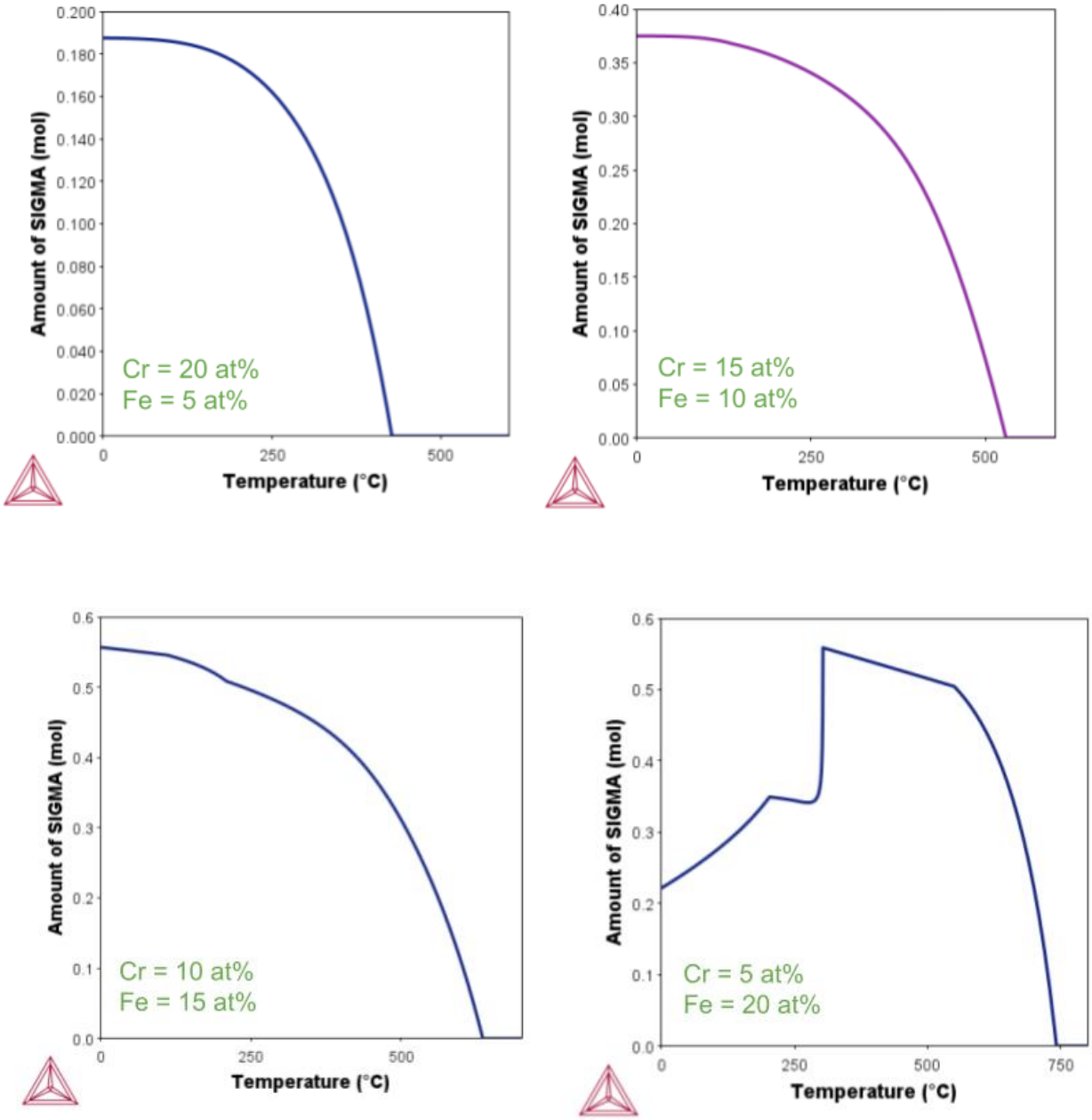

Figure 5.18: Four property diagrams for $V_{0.35}Cr_{0.2}Mn_{0.05}Fe_{0.05}W_{0.35}$, $V_{0.35}Cr_{0.15}Mn_{0.05}Fe_{0.1}W_{0.35}$, $V_{0.35}Cr_{0.1}Mn_{0.05}Fe_{0.15}W_{0.35}$, and $V_{0.35}Cr_{0.05}Mn_{0.05}Fe_{0.1}W_{0.35}$ calculated using the SSOL4 database of Thermo-Calc

The composition of chromium and iron that reduces the formation of the σ phase the most is Cr=20 at% and Fe=5 at%. Therefore, the overall alloy composition designed in this investigation is $V_{35}Cr_{20}Mn_5Fe_5W_{35}$.

Figure 5.19 shows the property diagram of $V_{35}Cr_{20}Mn_5Fe_5W_{35}$, the refined composition of VCrFeTaW, predicted using the SSOL4 database. On first inspection, the amount of equilibrium phases present in the property diagram is dramatically reduced compared to $V_{20}Cr_{20}Mn_{20}Fe_{20}W_{20}$.

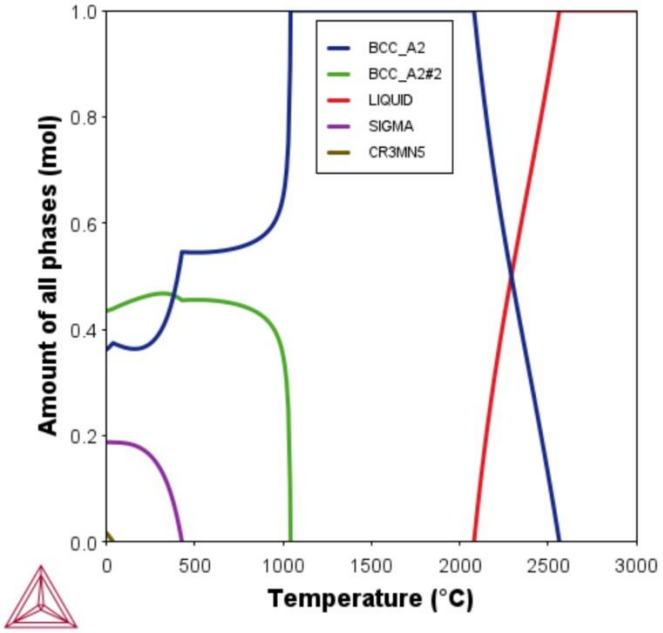

Figure 5.19: The property diagram of the refined alloy composition, $V_{35}Cr_{20}Mn_5Fe_5W_{35}$, using the SSOL4 database.

The concentration of the σ phase for $V_{35}Cr_{20}Mn_5Fe_5W_{35}$ dramatically reduces to 0.2 mol and is formed at temperatures below 500 °C. However, the refined $V_{35}Cr_{20}Mn_5Fe_5W_{35}$ alloy only has one σ phase composition and a negligible amount of Cr_3Mn_5 present in the predicted property diagram. This is compared to the equimolar alloy which was predicted to have three different compositions of the σ phase and a small amount of Cr_3Mn_5. Overall, at all temperatures above 500 °C there is a predominant disordered BCC A2 phase (with a small amount of a secondary disordered BCC A2 phase).

5.14. Refinement of $V_{20}Cr_{20}Mn_{20}Ta_{20}W_{20}$

Figure 5.20 shows the Thermo-Calc property diagram for the equimolar VCrMnTaW using both the SSOL4 and TCHEA4 databases. As with the previous alloys using the SSOL4 database, the most prevalent phase is the disordered BCC A2 phase formed upon cooling until 1000 °C. Below 1000 °C, a secondary disordered BCC A2 phase forms (0.1 mol) and a C15 Laves phase begins to precipitate (to a maximum 0.3 mol at 400 °C). Below 400 °C a small amount of a Cr_3Mn_5 phase begins to precipitate (0.3 mol). Interestingly, the TCHEA4 database has predicted a C14 Laves phase instead of the C15 variant. This coincides with experimental observations of HEAs (as discussed in Section 5.7. Phase Diagrams) as may reflect the improvement of inclusion of experimental HEA data for the TCHEA4 database. Additionally, the TCHEA4 database predicts the formation of a μ phase below 1000 °C.

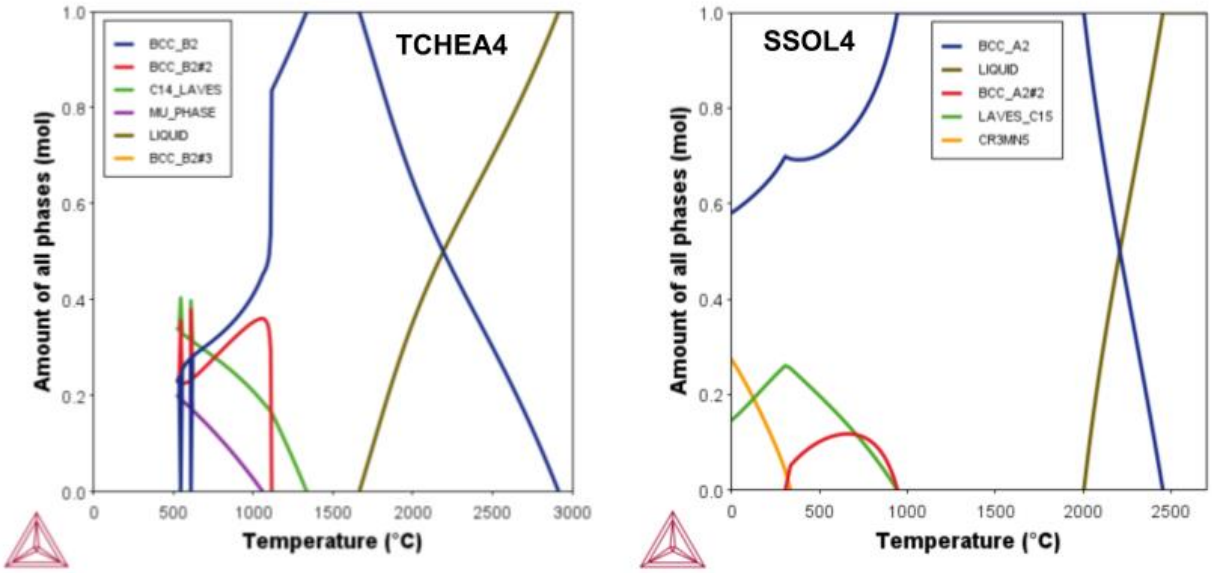

Figure 5.20: The property diagram for $V_{20}Cr_{20}Mn_{20}Ta_{20}W_{20}$ determined by the TCHEA4 and SSOL4 databases in Thermo-Calc

These predicted phases are typical for the alloy compositions in this work, in particular, for the alloy $V_{20}Cr_{20}Mn_{20}Fe_{20}W_{20}$ there was also a predicted Cr_3Mn_5 phase most likely due to the presence of chromium and manganese in high proportions.

Table 5.15 details the constituents (and their concentrations) of phases present in $V_{20}Cr_{20}Mn_{20}Ta_{20}W_{20}$ as determined by the TCHEA4 database using Thermo-Calc. The amount of each element in the phases present in $V_{20}Cr_{20}Mn_{20}Ta_{20}W_{20}$ are determined as a function of temperature. From this data the C15 Laves phase only consists of chromium and tantalum.

Table 5.15: The relative concentration of components in the phases present in equimolar VCrMnTaW from the SSOL4 database.

Phase	Amount of component in the phase from the largest concentration to smallest
BCC A2	W>V>Mn>Ta>Cr
Laves C15	Cr>Ta

The amount of manganese in $V_{20}Cr_{20}Mn_{20}Ta_{20}W_{20}$ needs to be reduced for ease of alloying. Therefore, as with VCrMnFeW, the reduction of manganese from 20 at% to 5 at% is necessary. From Table 5.15, for the reduction of the unfavourable C15 Laves phase, as with VCrFeTa, the chromium content also needs to be reduced. This reduction will also inhibit the formation of the Cr_3Mn_5 phase which forms in moderate amounts below 1000 °C in the

equimolar composition. From this property diagram we can observe the relationship between the elements and the phases present in the alloy.

Figure 5.21 shows the fluctuation of elemental concentrations which comprise the disordered BCC A2 phase of $V_{20}Cr_{20}Mn_{20}Ta_{20}W_{20}$ as a function of temperature using the SSOL4 database.

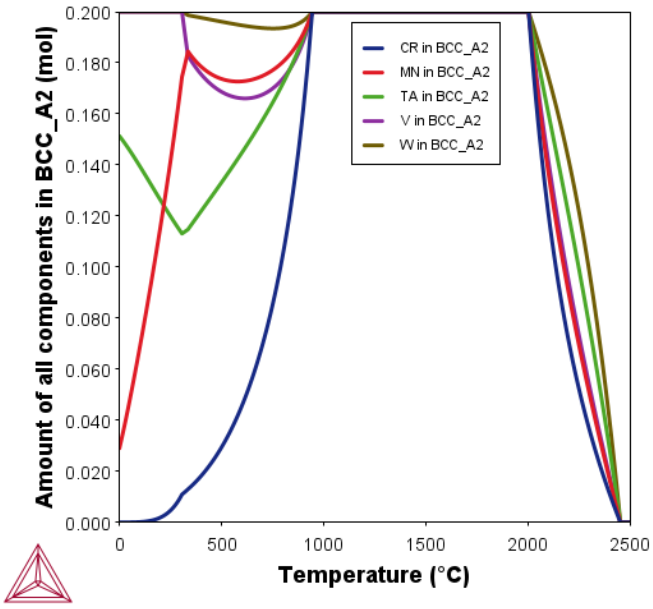

Figure 5.21: The concentrations of elements present in the disordered BCC A2 matrix as a function of temperature for $V_{20}Cr_{20}Mn_{20}Ta_{20}W_{20}$ generated using the SSOL4 database.

The first element to precipitate from the decomposing disordered BCC matrix, with decreasing temperature from 1000 °C, is chromium which is present in the C15 Laves and Cr_3Mn_5 phases. Interestingly, the decreasing content of tantalum in the disordered BCC matrix directly corresponds to the formation of the C15 Laves phase and this is supported by Table 5.15 which displays the dominance of chromium in the C15 Laves phase. Ideally, both chromium and tantalum concentrations would be decreased in the refined composition to diminish the formation of both the Laves C15 and Cr_3Mn_5 phases. However, to adhere to the design rules, the composition of VCrMnTaW is aligned in accordance with $V_{35}Cr_{20}Mn_5Fe_5W_{35}$. This means that the resulting microstructural effects of substitution of tantalum and iron on VCrMnW-X can be evaluated. Additionally, the considerable reduction of tantalum (from 20 at% to 5 at%) is sufficient alone to reduce the amount of C15 Laves phase formed.

Figure 5.22 shows the property diagram of $V_{35}Cr_{20}Mn_5Ta_5W_{35}$, the refined composition of VCrMnTaW, predicted using the SSOL4 database. The predicted amount of the Cr_3Mn_5 phases is completely diminished to a negligible amount, whilst the C15 Laves phase is dramatically reduced to less than 0.2 mol below 400 °C. There is retainment of the

predominant disordered BCC A2 phase with 0.4 mol of a secondary disordered BCC A2 phase below 1000 °C.

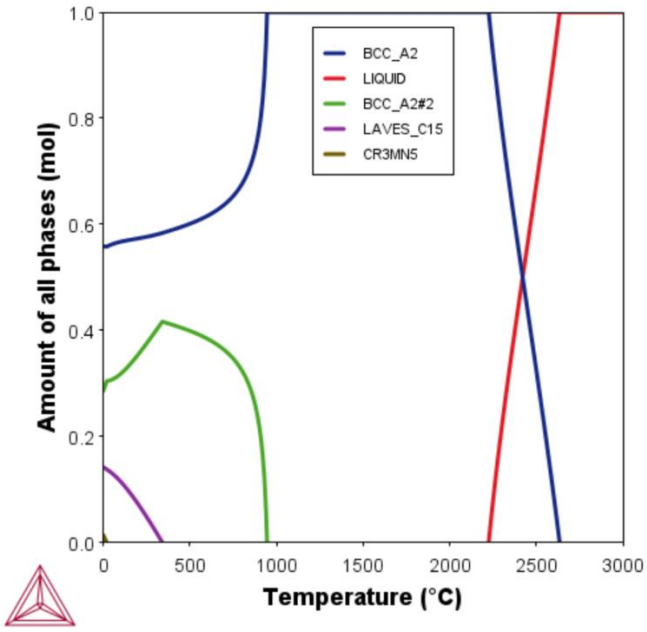

Figure 5.22: The property diagram of the refined alloy composition, $V_{35}Cr_{20}Mn_5Fe_5W_{35}$, using the SSOL4 database.

From the property diagrams we can also evaluate and assess the likely fluidity and microstructural effects of the alloying melt during fabrication. This phenomenon is discussed more in depth in Chapter 6 where the solidification processes of the fabricated samples are evaluated. For both $V_{35}Cr_{20}Mn_5Ta_5W_{35}$ minimisation of the freezing range, identified by the difference between the solidus and liquid temperatures, in the refined composition results in a higher quality cast ingot. From the property diagram of $V_{20}Cr_{20}Mn_{20}Ta_{20}W_{20}$, the solidification range is approximately 500 °C, and after the refinement process for $V_{35}Cr_{20}Mn_5Ta_5W_{35}$, this is reduced to around 350 °C. For refractory alloys, where high homogenisation temperatures are costly and sometimes impractical, reducing the freezing range can advantageously impact the microstructure of the cast alloy. This beneficial effect may also overcome some of the adverse requirements of vacuum arc melting and consequently yield an improved cast alloy.

5.15. Refinement of $V_{16.6}Cr_{16.6}Mn_{16.6}Fe_{16.6}Ta_{16.6}W_{16.6}$

Figure 5.23 shows the Thermo-Calc property diagram for the equimolar VCrMnFeTaW using both the TCHEA4 and SSOL4 databases. As with the previous alloys using the SSOL4 database, the most prevalent phase is the disordered BCC A2 phase formed upon cooling until 500 °C. Below 900 °C, a secondary disordered BCC A2 phase forms (0.3 mol) and a C15 Laves phase begins to precipitate (to a maximum 0.25 mol at 400 °C). Below 500 °C there is

a significant proportion of σ phase formation (0.4 mol). And below 300 °C a small amount of a Cr_3Mn_5 phase begins to precipitate (0.2 mol). Again, as for $V_{0.2}Cr_{0.2}Mn_{0.2}Ta_{0.2}W_{0.2}$, the TCHEA4 database predicts the formation of the C14 Laves phase instead of the C15 variant and there is also the additional μ phase predicted around 1000 °C.

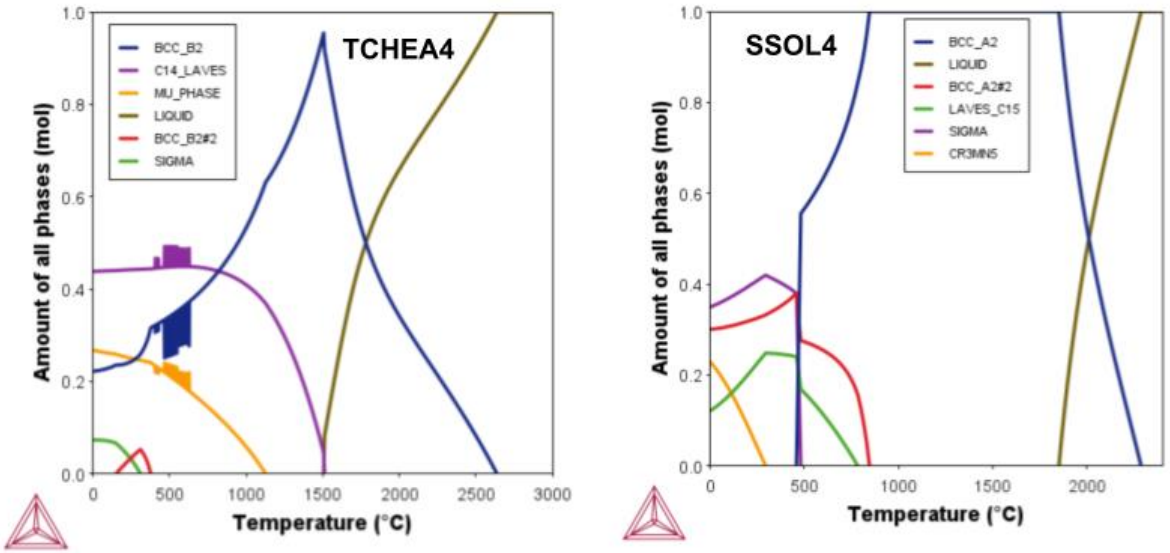

Figure 5.23: The property diagram for $V_{16.6}Cr_{16.6}Mn_{16.6}Fe_{16.6}Ta_{16.6}W_{16.6}$ determined by both the TCHEA4 and SSOL4 databases in Thermo-Calc

When comparing the equilibrium phases of the equimolar alloy VCrMnFeTaW there is evidence of some competition between the C15 Laves phase and the σ phase. This is akin to the equimolar VCrFeTa predictions, where there is competition between the two minor phases BCC B2 and σ, where vanadium is the dominant component of both phases. For VCrMnFeTaW the influential element is iron. The first element to precipitate out of the BCC matrix is iron which forms the majority of the σ phase (followed by vanadium then manganese). This is confirmed from the binary phase diagrams of Fe-V and Fe-Mn where the predominant intermetallic compound is analogous to CrFe with a tetragonal crystal structure which is termed the σ phase.

In this work, the compositional refinement of equimolar VCrMnFeTaW is based on a different approach compared to the other alloys (this strategy is discussed in detail in Section 5.5.3.). For this reason, the refined composition will not greatly differ from the equimolar composition. However, for VCrMnFeTaW an important caveat is that the concentration of manganese included would again have to be significantly reduced (to a maximum of 10 at%). In the equimolar composition the concentration of manganese (16 at%) would still be an excessive amount to incorporate into a refractory-based alloy. Additionally, to increase the ease of melting, the concentration of iron (an additional element with significantly lower melting point

compared to the other elements) was slightly reduced (to 15 at%) as well as a reduction in tungsten content (also to 15 at%) due to its excessively high melting point.

Figure 5.24 shows the property diagram of $V_{20}Cr_{20}Mn_{10}Fe_{15}Ta_{20}W_{15}$, the refined composition of VCrMnFeTaW, predicted using the SSOL4 database. There is little difference between the equimolar and refined VCrMnFeTaW property diagrams, likely due to the small change in composition.

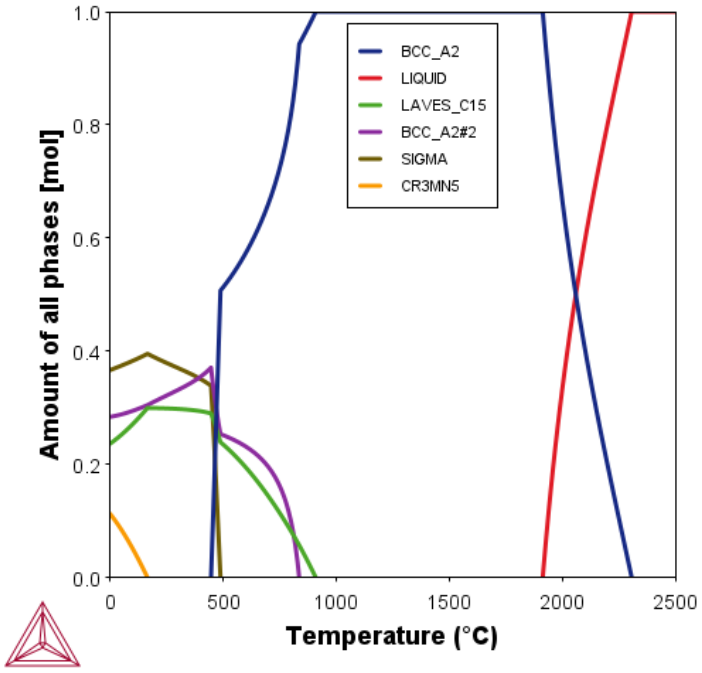

Figure 5.24: The property diagram of the refined alloy composition, $V_{20}Cr_{20}Mn_{10}Fe_{15}Ta_{20}W_{15}$, using the SSOL4 database.

Both property diagrams display a similar morphology for the same phases with a small decrease in concentration of the Cr_3Mn_5 intermetallic compound for the refined composition. Using the binary phase diagram of Cr-Mn, the Cr_3Mn_5 is an intermetallic compound that will form at high concentrations of manganese (91-100 wt%). To minimise this unwanted phase, maximising the ratio of Cr/Mn to 3:1 has been previously recommended [31]. For the alloys VCrMnTaW and VCrMnFeTaW this guidance is implemented, whereas for VCrMnFeW the ratio of Cr:Mn is approximately 15:1 and will serve as a good comparison to verify this method. In the VCrMnFeTaW property diagram, at 400 °C and below, the C15 Laves phase (composed of Cr and Ta) begins to decompose from 0.25 mol. In the same temperature range, the precipitation of Cr_3Mn_5 begins. This trend also follows for the refined composition of VCrMnFeTaW and equimolar VCrMnTaW property diagrams.

5.16. Summary of Thermo-Calc Predictions

Table 5.16 shows a summary of the predicted phases for the refined alloy compositions and compares the two thermodynamic databases TCHEA44 and SSOL4 of Thermo-Calc. Those highlighted in blue are negligible amounts or amounts present below 500°C. There is a consistent prediction of a major BCC phase for all of the alloys using the SSOL4 database– this corresponds with the HEA empirical rules (for the equimolar and refined compositions) which predicts a majority BCC solid solution. Deviation of this main phase can be observed in the TCHEA predictions. For VCrFeTaW and VCrFeTa a major C15 Laves phase is predicted to be more stable at higher and intermediate temperature than the ordered BCC phase. Interestingly, for the VCrMnTaW and VCrMnFeTaW alloys, the TCHEA database predicted the formation of the C14 variant Laves phase whilst for the same alloys the SSOL4 database predicted the C15 variant.

Additionally, the TCHEA database only predicted an ordered BCC B2 phase whilst the SSOL4 database only predicted the formation of a disordered BCC A2 phase.

Table 5.16: The predicted phases expected to occur across the entire temperature range of the equimolar and refined alloy compositions using Thermo-Calc. Both the TCHEA4 and SSOL4 databases are used for comparison.

Alloy	Composition	TCHEA4 phases	SSOL4 phases
VCrMnFeW	**equimolar**	BCC_B2 σ	BCC_A2 σ Cr_3Mn_5
	refined		BCC_A2 (and #2) Σ
VCrMnTaW	**equimolar**	BCC_B2 Laves_C14 μ phase	BCC_A2 Laves_C15 Cr_3Mn_5
	refined		BCC_A2 Laves_C15
VCrMnFeTaW	**equimolar**	BCC_B2 Laves_C14 μ phase σ	BCC_A2 Laves_C15 σ Cr_3Mn_5

	refined		BCC_A2 Laves_C15 σ Cr_3Mn_5
VCrFeTaW	**equimolar**	Laves_C15 (and C14) BCC_B2 μ phase	BCC_A2 Laves_C15 Σ
	refined		BCC_A2 Laves_C15
VCrFeTa	**Equimolar**	Laves_C15 (and C14) BCC_B2 σ μ phase	BCC_A2 Laves_C15 σ
	Refined		BCC_A2 Laves_C15 σ

5.17. Empirical Parameters for Refined Alloy Compositions

Table 5.17 and Table 5.18 show the results from the HEA empirical parameter calculations for the refined alloy compositions. In comparison to the equimolar composition values, there are some general trends which all the alloys adhere to and some exceptions which dispute the trend.

Table 5.17: Data calculated from the python script for the refined compositions of the chosen alloys

Refined Alloy Compositions	Omega	Atomic size difference (%)	Entropy ($JK^{-1}mol^{-1}$)	Enthalpy ($kJmol^{-1}$)	VEC
$V_{0.35}Cr_{0.2}Mn_{0.05}Fe_{0.05}W_{0.35}$	34475	3.51	11.28	-0.87	5.8
$V_{0.35}Cr_{0.2}Mn_{0.05}Ta_{0.05}W_{0.35}$	25268	3.67	11.28	-1.22	5.65
$V_{0.2}Cr_{0.2}Mn_{0.1}Fe_{0.15}Ta_{0.2}W_{0.15}$	8930	5.21	14.67	-4.12	6
$V_{0.3}Cr_{0.1}Fe_{0.1}Ta_{0.2}W_{0.3}$	7001	4.61	12.51	-5.04	5.7
$V_{0.25}Cr_{0.15}Fe_{0.35}Ta_{0.25}$	2739	5.84	11.19	-9.51	6.2

Table 5.18: Data calculated from the python script for the refined compositions of the chosen alloys

Refined Alloy Compositions	Gibbs free energy ($kJmol^{-1}$)	Melting Temperature (°C)	Predicted solid solution
$V_{0.35}Cr_{0.2}Mn_{0.05}Fe_{0.05}W_{0.35}$	-3361	2385	BCC
$V_{0.35}Cr_{0.2}Mn_{0.05}Ta_{0.05}W_{0.35}$	-3362	2461	BCC
$V_{0.2}Cr_{0.2}Mn_{0.1}Fe_{0.15}Ta_{0.2}W_{0.15}$	-4376	2235	BCC
$V_{0.3}Cr_{0.1}Fe_{0.1}Ta_{0.2}W_{0.3}$	-3733	2548	BCC
$V_{0.25}Cr_{0.15}Fe_{0.35}Ta_{0.25}$	-3342	2056	BCC

As with the equimolar compositions, the calculated VEC values are still in the range for a predicted stable BCC solid solution. The VEC values for the refined compositions are lower than those predicted for the equimolar compositions, but as the elements have remained the same, the most reasonable crystal structure for the solid solution is still BCC. Additionally, the Gibbs free energy values for all the refined compositions are significantly more negative than the equimolar equivalents. This indicates that the solid solution is more stable and more energetically favourable to form for the refined alloys which is advantageous for the design of radiation-tolerant materials. For all the alloys, as the refined compositions deviate from the maximum configurational entropy, there is a decrease in the entropy value for the refined alloy

compositions compared to the equimolar alloys. However compositional changes deviating from equal concentrations are needed to adhere to other requirements. Additionally, the difference between the atomic sizes is also generally lower for the refined alloys compared to the equimolar compositions.

The overall enthalpy values for the refined alloys are still within the set limits, however there is variance in whether the enhanced alloy composition has increased or decreased compared to its equimolar concentration. This is due to the change in elemental concentration of the alloys; whilst the individual values for each of the binary pairs of mixing enthalpies remain the same, lowering the concentration of a pair can reduce the magnitude of its effect on the alloy's overall enthalpy. In the examined alloys, VCrMnFeW and VCrFeTa have much more negative values for the refined composition compared to the respective equimolar alloys. For example, for VCrFeTa rising the content of iron (to 35 at%) would increase the influence of the Fe-Ta mixing enthalpy (which has the highest magnitude – 15 $kJmol^{-1}$), therefore makes the overall mixing enthalpy more negative.

Overall, the refined alloy compositions have a higher melting point than their equimolar counterparts except for VCrFeTa. The higher proportion of iron (and corresponding decrease in chromium content) which has a relatively low melting point results in a lower overall alloy melting point. Overall, the newly generated HEA empirical parameters remain within the set threshold identified.

5.18. Conclusion

For the design of novel high entropy system, several design tools and methods were evaluated. The assessment of low activation elements and refractory metals with high temperature capabilities were firstly considered. From these elements, a range of suitable alloys were designed to probe validity of the HEA thermodynamic criteria for these systems. The highest entropy of each alloy composition was computed using the criteria and it was determined that for all five alloys a stable BCC solid solution was predicted to form. To determine if any potential favourable solid solution formation would occur from any of the chosen elements an alloy with all the constituents was designed – VCrMnFeTaW. The effect of substitution of elements was also investigated; in this work iron and tantalum were substituted for the alloys VCrMnFeW and VCrMnTaW.

Fabrication restrictions were taken into concentrations to reduce the number of volatile elements (like manganese, <10 at%) and very high melting point elements (like tungsten <35

at%) for ease of melting. For these reasons two alloys – VCrFeTa and VCrFeTaW – were designed to investigate removal of these problematic elements on the melting process.

Assessment of the binary and available ternary phase diagrams identified possible intermetallic phases that could form at a range of temperatures. Most notably, the elements V, Cr, Fe, and Ta all have a high propensity to form a σ phase. The alloy VCrFeTa was designed to have a high configurational entropy to determine if this increases the tendency of a multicomponent σ phase formation.

Thermo-Calc simulations for each equimolar alloy revealed possible minor phase formation of C15 Laves phase, σ phase, and a Cr_3Mn_5 phase in addition to a main BCC phase. In addition, the thermodynamic databases TCHEA4 and SSOL4, identified as the most appropriate databases for these alloys, were compared. The TCHEA4 database consistently predicted a predominant ordered BCC B2 phase for the alloys, whilst the SSOL4 database identified the majority phase as a disordered BCC A2 phase. Furthermore, when predicting the Laves phase the TCHEA4 database preferred predicting the C14 variant of the Laves phase whilst for the same alloys the SSOL4 database predicted the C15 variant.

Finally, Thermo-Calc was used to investigate effect of reducing/increasing constituents for each alloy on the prediction of equilibrium phases. The fabrication restrictions on elemental concentrations were taken into consideration as well as the minimisation of unfavourable phases predicted by Thermo-Calc.

To ensure the HEA empirical parameters were still within the allowed thresholds, each criterion was re-calculated for the enhanced alloy compositions to ensure a BCC solid solution formation.

To conclude, in this chapter, several design tools were used to refine the compositions of five novel refractory high entropy alloys:

1. $V_{0.35}Cr_{0.2}Mn_{0.05}Fe_{0.05}W_{0.35}$
2. $V_{0.35}Cr_{0.2}Mn_{0.05}Ta_{0.05}W_{0.35}$
3. $V_{0.2}Cr_{0.2}Mn_{0.1}Fe_{0.15}Ta_{0.2}W_{0.15}$
4. $V_{0.3}Cr_{0.1}Fe_{0.1}Ta_{0.2}W_{0.3}$
5. $V_{0.25}Cr_{0.15}Fe_{0.35}Ta_{0.25}$

In Chapter 6 the experimental assessment of these alloys is undertaken and subsequent validation of Thermo-Calc, the HEA empirical parameters, and binary phase diagrams is given.

5.19. References

[1] Zucchetti, M., Candido, L., Khripunov, V., Kolbasov, B. and Testoni, R., 2018. Fusion power plants, fission and conventional power plants. Radioactivity, radiotoxicity, radioactive waste. Fusion Engineering and Design, 136, pp.1529-1533.

[2] Bolt, H., Barabash, V., Federici, G., Linke, J., Loarte, A., Roth, J. and Sato, K., 2002. Plasma facing and high heat flux materials–needs for ITER and beyond. Journal of Nuclear Materials, 307, pp.43-52.

[3] Hancock, D., Homfray, D., Porton, M., Todd, I. and Wynne, B., 2018. Refractory metals as structural materials for fusion high heat flux components. Journal of Nuclear Materials, 512, pp.169-183.

[4] Gorley, M.J., 2015. Critical Assessment 12: Prospects for reduced activation steel for fusion plant. Materials Science and Technology, 31(8), pp.975-980.

[5] Rubel, M., 2006. Analysis of plasma facing materials: material migration and fuel retention. Physica Scripta, 2006(T123), p.54.

[6] Byun, T.S. and Maloy, S.A., 2008. Dose dependence of mechanical properties in tantalum and tantalum alloys after low temperature irradiation. Journal of nuclear materials, 377(1), pp.72-79.

[7] Tietz, T.E. and Wilson, J.W., 1965. Behavior and properties of refractory metals.

[8] Campbell, F.C. ed., 2008. Elements of metallurgy and engineering alloys. ASM International.

[9] Zinkle, S.J., Matsui, H., Smith, D.L., Rowcliffe, A.F., Van Osch, E., Abe, K. and Kazakov, V.A., 1998. Research and development on vanadium alloys for fusion applications. Journal of nuclear materials, 258, pp.205-214.

[10] Holzwarth, U. and Stamm, H., 2002. Mechanical and thermomechanical properties of commercially pure chromium and chromium alloys. Journal of Nuclear Materials, 300(2-3), pp.161-177.

[11] Odette, G.R., 2018. On the status and prospects for nanostructured ferritic alloys for nuclear fission and fusion application with emphasis on the underlying science. Scripta Materialia, 143, pp.142-148.

[12] Eissa, M.M., El-Kameesy, S.U., El-Fiki, S.A., Ghali, S.N., El Shazly, R.M. and Saeed, A., 2016. Attenuation capability of low activation-modified high manganese austenitic stainless steel for fusion reactor system. Fusion Engineering and Design, 112, pp.130-135.

[13] Elsebaie, O. and Jaansalu, K.M., 2018. A study of the manganese–tungsten binary phase diagram. International Journal of Refractory Metals and Hard Materials, 72, pp.332-340.

[14] Dominguez, L.A., Goodall, R. and Todd, I., 2015. Prediction and validation of quaternary high entropy alloys using statistical approaches. Materials Science and Technology, 31(10), pp.1201-1206.

[15] Coury, F.G., Butler, T., Chaput, K., Saville, A., Copley, J., Foltz, J., Mason, P., Clarke, K., Kaufman, M. and Clarke, A., 2018. Phase equilibria, mechanical properties and design of quaternary refractory high entropy alloys. Materials & Design, 155, pp.244-256.

[16] Nguyen, V.T., Qian, M., Shi, Z., Song, T., Huang, L. and Zou, J., 2018. A novel quaternary equiatomic Ti-Zr-Nb-Ta medium entropy alloy (MEA). Intermetallics, 101, pp.39-43.

[17] Huang, Y.C., Lai, Y.C., Lin, Y.H. and Wu, S.K., 2021. A study on the severely cold-rolled and annealed quaternary equiatomic derivatives from quinary HfNbTaTiZr refractory high entropy alloy. Journal of Alloys and Compounds, 855, p.157404.

[18] Hillel, G., Natovitz, L., Salhov, S., Haroush, S., Pinkas, M. and Meshi, L., 2020. Understanding the Role of the Constituting Elements of the AlCoCrFeNi High Entropy Alloy through the Investigation of Quaternary Alloys. Metals, 10(10), p.1275.

[19] Cantor, B., Chang, I.T.H., Knight, P. and Vincent, A.J.B., 2004. Microstructural development in equiatomic multicomponent alloys. Materials Science and Engineering: A, 375, pp.213-218.

[20] Yang, X. and Zhang, Y., 2012. Prediction of high-entropy stabilized solid-solution in multi-component alloys. Materials Chemistry and Physics, 132(2-3), pp.233-238.

[21] Wang, Z., Guo, S. and Liu, C.T., 2014. Phase selection in high-entropy alloys: from nonequilibrium to equilibrium. Jom, 66(10), pp.1966-1972.

[22] Sheng, G.U.O. and Liu, C.T., 2011. Phase stability in high entropy alloys: Formation of solid-solution phase or amorphous phase. Progress in Natural Science: Materials International, 21(6), pp.433-446.

[23] Zhang, F., Zhang, C., Chen, S.L., Zhu, J., Cao, W.S. and Kattner, U.R., 2014. An understanding of high entropy alloys from phase diagram calculations. Calphad, 45, pp.1-10.

[24] Takeuchi, A. and Inoue, A., 2005. Classification of bulk metallic glasses by atomic size difference, heat of mixing and period of constituent elements and its application to characterization of the main alloying element. Materials Transactions, 46(12), pp.2817-2829.

[25] Fe (Iron) Binary Alloy Phase Diagrams, Alloy Phase Diagrams, Vol 3, ASM Handbook, Edited By H. Okamoto, M.E. Schlesinger, E.M. Mueller, ASM International, 2016, p 340–361

[26] Parker, G., 2001. Encyclopedia of materials: science and technology.

[27] Baker, H. and Okamoto, H., 1992. ASM Handbook. Vol. 3. Alloy Phase Diagrams. ASM International, Materials Park, Ohio 44073-0002, USA, 1992. 501.

[28] Stein, F. and Leineweber, A., 2020. Laves phases: a review of their functional and structural applications and an improved fundamental understanding of stability and properties. Journal of Materials Science, pp.1-107.

[29] Kaufman, L. and Bernstein, H., 1970. Computer calculation of phase diagrams. With special reference to refractory metals.

[30] English, J.J., 1961. Binary and ternary phase diagrams of columbium, molybdenum, tantalum, and tungsten (Vol. 152). Defense Metals Information Center, Battelle Memorial Institute.

[31] Zhu, K., Gui, N., Jiang, T., Zhu, M., Lu, X., Zhang, J. and Li, C., 2014. The development of the low-cost titanium alloy containing Cr and Mn alloying elements. Metallurgical and Materials Transactions A, 45(4), pp.1761-1766.

Chapter 6: Experimental Assessment of Novel High Entropy Alloys

The refined alloy compositions determined in Chapter 5: Alloy Design were fabricated using vacuum arc melting (VAM) and then experimentally characterised, in their as-cast state, by X-ray diffraction (XRD), scanning electron microscopy (SEM) and elemental analysis by X-ray fluorescence spectroscopy (XRF) and energy dispersive X-ray analysis (EDX), and hardness measurements taken using Vickers microhardness. A summary of the characterisation techniques used can be seen in Chapter 3: Experimental Methods. Then, with the use of Thermo-Calc, a range of suitable heat treatments were identified to facilitate homogenisation and to evaluate precipitation at lower temperatures. Small sections of the fabricated alloys were heat treated using these calculated temperatures and, using the methods applied to the as-cast alloys, characterised to investigate any thermally induced phase transformations and microstructural evolution. This chapter discusses these effects with regards to the alloy's composition, designed using parameters such as elemental substitution, reduction of volatile and high melting point elements, and the design of materials with a focus on the formation of a BCC solid solution. The primary aim of this investigation is to determine the most attractive candidate low activation high entropy alloy for nuclear fusion armour applications.

6.1. Fabrication of Alloys

The masses of elements corresponding to the five novel high entropy alloy compositions designed in Chapter 5: Alloy Design were weighed and melted according to the melting procedures outlined in Chapter 3: Experimental Methods. Table 6.1 displays the optimal alloy compositions calculated from the design processes for the five refractory-based high entropy alloys alongside the actual atomic percentages determined from XRF analysis.

Table 6.1: The refined compositions designed using high entropy alloy empirical thermodynamic parameters and Thermo-Calc calculations and actual alloy compositions gathered from experimentally obtained data using XRF, also included are the standard deviation errors from the separate scans.

Alloy Composition	V (at%)	Cr (at%)	Mn (at%)	Fe (at%)	Ta (at%)	W (at%)
VCrMnFeW	35	20	5	5	-	35
	35±0.33	33±0.79	2±0.19	12±0.80	-	18±1.39
VCrMnTaW	35	20	5	-	5	35
	46±0.36	3±0.75	1±0.17	-	10±0.35	40±0.72
VCrMnFeTaW	20	20	10	15	20	15
	21±0.37	18±0.56	9±0.22	17±0.49	20±1.32	15±1.27
VCrFeTaW	30	10	-	10	20	30
	36±1.46	18±0.67	-	8±0.42	17±0.70	21±1.18
VCrFeTa	25	15	-	35	25	-
	26±0.18	17±0.34	-	32±0.45	25±0.55	-

The samples were first analysed by X-ray Fluorescence (XRF) to obtain the actual alloy compositions of the fabricated novel high entropy alloys. Table 6.1 displays the results obtained gathered from an average of at least five separate XRF scans for each alloy alongside the standard deviation of these scans. These experimental elemental compositions can be compared to the compositions designed from Chapter 5: Alloy Design. From this table it can be observed that there is some enrichment of some elements and depletion of other elements for all the alloys.

The discrepancies between the designed and experimentally obtained alloy compositions can be related to the fabrication process of the novel refractory HEAs. Most notably, there is a severe decline in the manganese content of all the alloys made using VAM. As detailed in Chapter 3: Experimental Methods, the propensity of evaporation of volatile elements (for example, manganese) increases when the content of higher melting point elements (for example tungsten) increases. This can be observed in VCrMnTaW where the resultant tungsten content is increased (from 35 at% to 40 at%) and the manganese content is depleted (from 5 at% to 1 at%).

The design process rationale for the comparison between VCrMnFeW and VCrMnTaW was based on the elemental substitution of iron and tantalum. However, for VCrMnTaW, the effects of the fabrication process have resulted in the unintentional loss of the volatile elements chromium and manganese as displayed in Table 6.1. This has proportionally increased the

concentrations of vanadium and tungsten. The higher amount of tantalum (which has a higher melting point than iron) has considerably increased the melting point of the overall alloy (from the Thermo-Calc property diagrams this approximates to an increase by almost 500 °C for the equimolar compositions). The increase in temperature results in an even greater likelihood of evaporation of manganese which has a boiling point (2061 °C) lower than that of the melting point of VCrMnTaW (2892 °C). Conversely, for VCrMnFeW, the deliberate doping of potentially volatile elements (as described in Chapter 5: Alloy Design) has unintentionally resulted in the increased concentration of chromium. Therefore, the VCrMnW base of both alloys differs slightly in concentrations, specifically $V_{46}Cr_3Mn_1W_{40}$-Ta_{10} compared to $V_{35}Cr_{33}Mn_2W_{18}$-Fe_{12}. Nonetheless, a comparison between the two alloys can still be made with regards to elemental substitution.

Table 6.2 shows the experimentally measured densities of three of the novel HEAs calculated using the pristine ingot formed from VAM by applying the Archimedes' methods detailed in Chapter 3: Experimental Methods. The theoretical densities were determined using the rule of mixtures using the densities of the elements and the elemental compositions obtained from the XRF data. It can be seen from the table that the experimentally measured densities of the fabricated ingots are consistently smaller than the theoretical densities.

Table 6.2: The theoretical and experimentally measured densities of the novel alloys. The measured densities were calculated using six average measurements and includes the standard error of these measurements.

Alloy Composition	Theoretical density (g/cm^3)	Measured density (g/cm^3)
$V_{35}Cr_{33}Mn_2Fe_{12}W_{18}$	9.5	8.6±0.04
$V_{46}Cr_3Mn_1Ta_{10}W_{40}$	13	12.2±0.05
$V_{36}Cr_{18}Fe_8Ta_{17}W_{21}$	11.7	11.7±0.02

For VCrFeTaW the theoretical density is identical to the experimentally measured density which may correspond to a fully disordered solid solution. Senkov et al [1] reported for the near equiatomic WNbMoTaW that the theoretical density was also identical to the measured density due to the presence of a fully disordered BCC solid solution. However, for VCrMnFeW and VCrMnTaW both have lower measured densities than theoretically calculated. This is consistent with a small amount of porosity formed from the arc melting process. Porosity due to shrinkage occurs during solidification and is a type of defect which can reduce mechanical

performance of cast parts. Shrinkage porosity is caused by the density change from liquid to solid; it forms when the liquid melt cannot feed the volume contraction of an alloy during solidification [2]. This type of porosity occurs late in solidification and therefore form in the remaining spaces between dendrites [3]. Gas porosity is another common casting defect which can severely deteriorate materials properties. Gas porosity is formed by gas entrapment during the melt and the solubility of the dissolved gasses decreases during the cooling process [4]. Unlike the formation of shrinkage pores, this mechanism occurs much earlier in solidification resulting in spherical shaped pores. This phenomenon has been previously reported for VAM refractory HEAs, including ReMoTaW which displayed three disordered solid solution phases and had a measured density 0.48% less than the theoretical density calculated using the rule of mixtures [5].

Due to the discrepancy between the theoretically calculated alloy compositions and the experimentally measured compositions, the alloy design processes were revised for the XRF obtained elemental compositions. The HEA thermodynamic parameters, to determine the stability of a solid solution, and the Thermo-Calc predictions for the formation of equilibrium phases were both recalculated for the fabricated alloys. Table 6.3 shows the python results for the measured elemental compositions (using XRF) for each of the alloys. The empirical parameters which determine the formation of a solid solution in relation to the entropy, enthalpy, and Gibbs free energy are also included.

Table 6.3: Data calculated from the python script for the experimentally measured compositions of the chosen alloys

Experimental composition of the alloy	Omega	Atomic size difference (%)	Entropy ($JK^{-1}mol^{-1}$)	Enthalpy ($kJmol^{-1}$)	VEC
$V_{35}Cr_{33}Mn_2Fe_{12}W_{18}$	12669	3.6	11.43	-2.16	5.91
$V_{46}Cr_3Mn_1Ta_{10}W_{40}$	12520	3.0	9.19	-2.12	5.45
$V_{21}Cr_{18}Mn_9Fe_{17}Ta_{20}W_{15}$	8087	5.2	14.64	-4.54	6.02
$V_{36}Cr_{18}Fe_8Ta_{17}W_{21}$	7486	4.7	12.53	-4.45	5.63
$V_{26}Cr_{17}Fe_{32}Ta_{25}$	2897	5.8	11.33	-9.15	6.13

Table 6.4: Data calculated from the python script for the refined compositions of the chosen alloys

Experimental composition of the alloy	Gibbs free energy ($kJmol^{-1}$)	Melting Temperature (°C)	Predicted solid solution
$V_{35}Cr_{33}Mn_2Fe_{12}W_{18}$	-3408	2123	BCC
$V_{46}Cr_3Mn_1Ta_{10}W_{40}$	-2740	2619	BCC
$V_{21}Cr_{18}Mn_9Fe_{17}Ta_{20}W_{15}$	-4367	2235	BCC
$V_{36}Cr_{18}Fe_8Ta_{17}W_{21}$	-3739	2385	BCC
$V_{26}Cr_{17}Fe_{32}Ta_{25}$	-3385	2067	BCC

It can be observed by these results that regardless of the compositional changes occurred from the fabrication process, all the alloys still predict the stable formation of a BCC solid solution.

After the fabrication of the novel alloys and the experimental validation of the alloy compositions and densities, the five refractory HEAs were fully characterised in the as-cast conditions. Samples of each alloy were then annealed in furnaces and experimentally characterised for comparison to the as-cast conditions. The results of these characterisation techniques are detailed in the section below.

Figure 6.1 outlines the order of the experimental procedures for the as-cast and heat treated samples. The details of the experimental characterisation techniques can be found in Chapter 3: Experimental Methods.

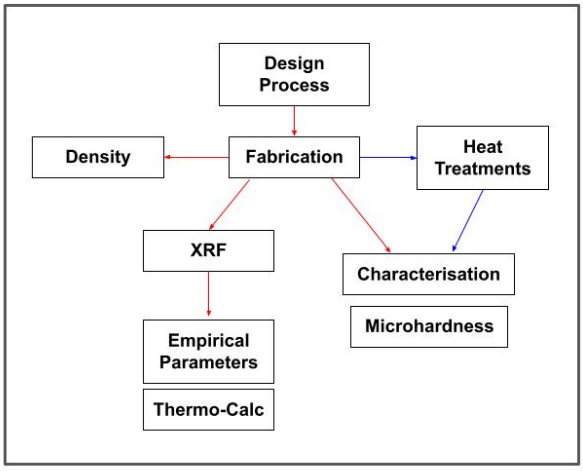

Figure 6.1: Flowchart of the experimental assessment of the designed refractory HEAs.

6.2. As-Cast Condition

Figure 6.2 displays a compilation of the SEM-BSE micrographs from the novel high entropy alloys investigated in this work. The evolution of the microstructures of the alloys upon annealing can be observed. As a general trend, most of the alloys in the as-cast condition displayed a dendritic microstructure which is typical of ingots fabricated using VAM, due to the solidification in the arc melting process which leads to a segregation of the elements [6]. However, the morphologies of the dendrites, for example the width of the dendritic arms, vary depending on the alloy's composition.

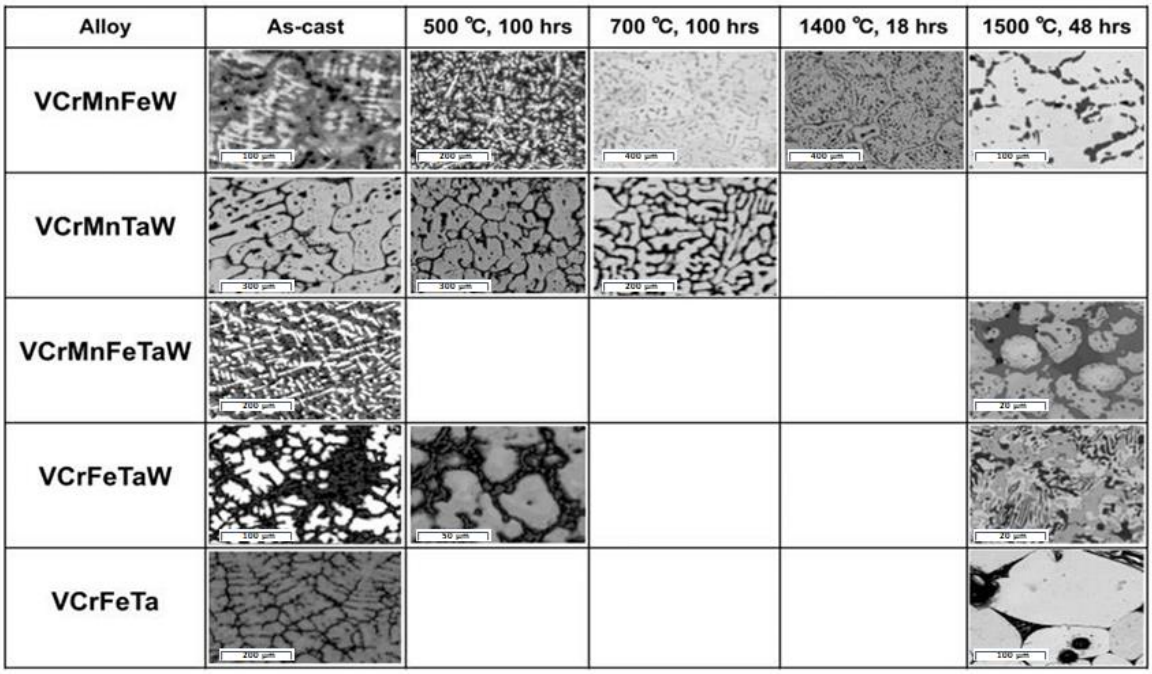

Figure 6.2: A composite image of the SEM-BSE micrographs of the five novel refractory HEAs. The as-cast states of the alloys are displayed alongside the microstructural evolution of the alloy as a function of temperature.

During the melting process, the exposed region of the ingot (typically facing the argon atmosphere) undergoes slower cooling compared to the region in contact with the water-cooled crucible. This microstructure is most common in alloys which contain elements with vastly different melting points (for example, tungsten melts at 3342 °C and manganese melts at 1246 °C). The main fabrication routes of bulk refractory high entropy alloys (RHEAs) include arc melting, hot isostatic pressing, and arc melting followed by annealing. Alloy compositions containing constituent elements of vastly varying melting points, including refractory multicomponent alloys, experience exacerbated effects of elemental segregation. Therefore, subsequent homogenisation treatments are normally required to mitigate these effects.

Microsegregation occurs due to the formation of the solid having a different composition compared to the liquid state. The higher melting point element solidifies first in the dendrite arms, whilst the lower melting point elements enrich the interdendritic regions resulting in microsegregation. This dendritic microstructure develops from the partition of alloying elements in the separate liquid and solid phases and is intensified when the solidification process is slow. This enrichment of the rest of the elements will form the interdendritic regions between the dendrite arms [7]. As explained above, this will depend on the partition coefficients and melting points of the elements and is reflective of a slow cooling rate. Additionally, if the difference between the temperatures of the liquidus and solidus is large enough, enhanced microsegregation of elements can also occur. The temperature range of solidification can be observed in the Thermo-Calc property diagrams of the experimental alloy compositions. Table 6.5 shows the liquidus and solidus temperature range from the calculated Thermo-Calc property diagrams for each of the experimentally validated novel alloys.

Table 6.5: The predicted solidification ranges of the experimental alloys identified from the property diagrams calculated in Thermo-Calc using the SSOL4 database

Alloy Composition	Liquidus-Solidus Range (°C)
$V_{35}Cr_{33}Mn_2Fe_{12}W_{18}$	1897 - 2156
$V_{46}Cr_3Mn_1Ta_{10}W_{40}$	2416 - 2624
$V_{21}Cr_{18}Mn_9Fe_{17}Ta_{20}W_{15}$	1916 - 2316
$V_{36}Cr_{18}Fe_8Ta_{17}W_{21}$	2101 - 2501
$V_{26}Cr_{17}Fe_{32}Ta_{25}$	1843 - 2052

From this table it can be observed that VCrMnFeTaW has a particularly large temperature range of solidification which could explain the resultant fine dendritic microstructure.

Contrastingly, VCrMnTaW and VCrFeTa have smaller liquidus-solidus ranges which may reflect the larger, more globular dendrites observed by the SEM-BSE micrographs.

Further discussion of the microsegregation of high entropy alloys in the as-cast condition is detailed in Chapter 2.3: High Entropy Alloys. To reduce these unfavourable effects, small ingots (~20 g) were produced and were re-melted and flipped more than 7 times whilst also ensuring the ingot remained in a liquid state for approximately 30 seconds in each melting event. Further detail on the experimental procedure is described fully in Chapter 3: Experimental Methods. Additionally, to facilitate the removal of microsegregation, annealing treatments to homogenise the alloys was undertaken (described in the next section).

Figure 6.3 displays the XRD patterns of all the alloys investigated in their as-cast condition, with different crystal structures identified and labelled accordingly. VCrMnTaW is the only alloy to obtain a single BCC phase, however, VCrMnFeW displayed a dual BCC phase and VCrFeTaW showed three very similar BCC phases. Interestingly, VCrFeTa exhibited a single HCP phase and VCrMnFeTaW demonstrated three distinct FCC phases; for both of these alloys these phases were not predicted for.

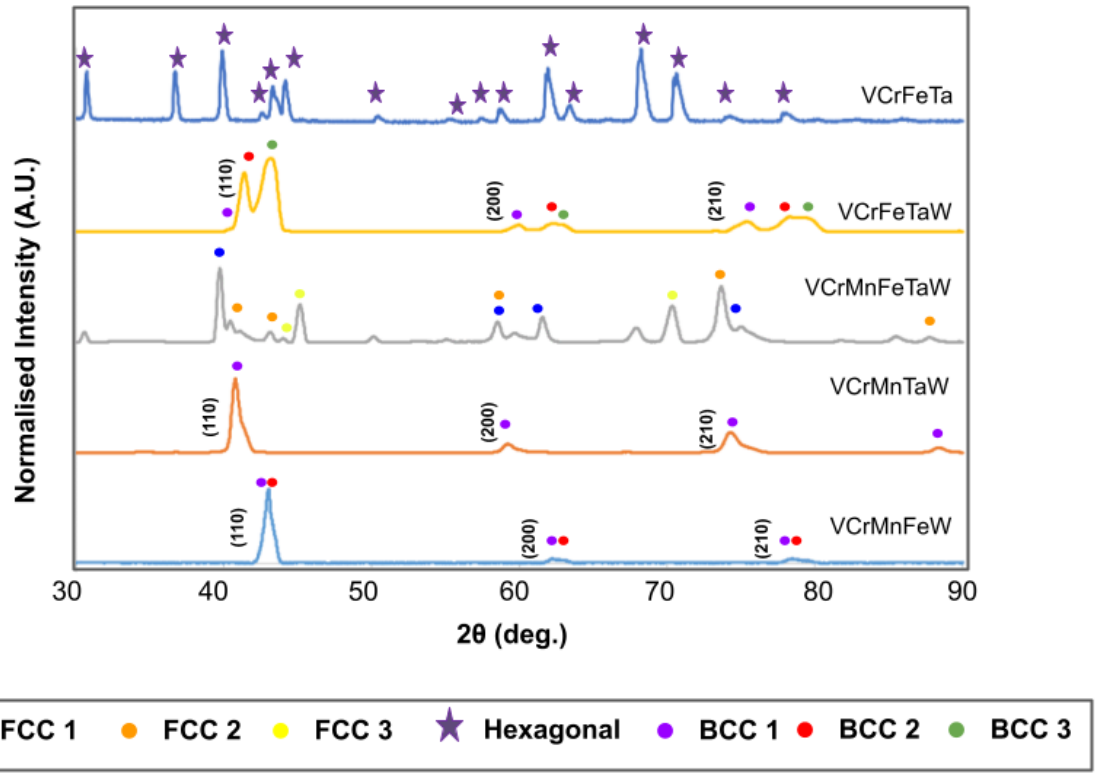

Figure 6.3: A composite image of the experimental XRD patterns of the five novel refractory HEAs in the as-cast condition.

It is clear from Figure 6.3 that many of these alloys did not form the BCC crystal structure designed for. From the results of the computational design tools (described in Chapter 5: Alloy Design), these alloy compositions were predicted to form single-phase BCC alloys. There could be many reasons for the disagreement between the design processes and the experimental results. As explained in the previous section, elemental segregation is inevitable due to dendritic growth. For this reason, it is important to evaluate the thermal stability of these as-cast phases and to achieve chemical homogeneity.

6.3. Heat-Treated Conditions

Heat treating samples of the novel alloys is required to evaluate the thermal stability of these phases. Ideally, long-term intermediate temperature annealing would be the preferred method for investigating the most stable equilibrium phases formed during the in-service temperatures. However, due to time constraints, this isn't always possible. A high temperature (0.6 - 0.8 T_m), relatively short heat treatment can result in the homogenisation of the alloy by reducing the defects and microsegregation apparent in the as-cast state. Table 6.6 displays the calculated melting points of the fabricated alloys using the python script in Chapter 6: Alloy Design compared to the temperature range required for homogenisation.

Table 6.6: The theoretical melting points of the novel alloys ascertained from the rule of mixtures, and the corresponding temperature range for the homogenisation heat treatment for each alloy.

	Melting Point (°C)	**0.6 - 0.8T_m (°C)**
$V_{35}Cr_{33}Mn_2Fe_{12}W_{18}$	2123	1274 - 1698
$V_{46}Cr_3Mn_1Ta_{10}W_{40}$	2619	1571 - 2095
$V_{21}Cr_{18}Mn_9Fe_{17}Ta_{20}W_{15}$	2235	1341 - 1788
$V_{36}Cr_{18}Fe_8Ta_{17}W_{21}$	2385	1431 - 1908
$V_{26}Cr_{17}Fe_{32}Ta_{25}$	2067	1240 - 1653

From these calculated temperature ranges it is clear to see that in order to homogenise all of the alloys in a single short heat treatment ideally an annealing treatment at ~1800 °C would be recommended. However, for refractory alloys, and other high melting point alloys, procurement of high-temperature furnaces can be problematic. For this reason, the highest temperature available for this research was 1500 °C for 48 hours and 1400 °C for 18 hours which can be observed from Table 6.6 to be on the lower side of the homogenisation temperature range. These high temperature heat treatments were followed by water

quenching the samples to ensure the retainment of only the high-temperature phases. A second heat treatment was also applied for a longer duration at a much lower temperature to ascertain the production of any low-temperature intermetallic precipitation. From the Thermo-Calc diagrams, much of the secondary phase formation occurs below 1000 °C. To evaluate the degree of intermetallic/secondary phase formation, heat treatments below 1000 °C are required. At lower temperatures, due to lower kinetic energy, the time taken to attain equilibrium phases will be much longer than the homogenisation heat treatments. Two heat treatments at 500 °C and 700 °C (both for 100 hours) were conducted and again followed by water quenching to trap these phases. The heat treatments applied depended on the facilities available at the time. The experimental details of the heat treatments are fully explained in Chapter 3: Experimental Methods.

The following sections describe, in detail, the experimental characterisation of each of the novel refractory HEAs investigated in this work. A flowchart of the experimental procedures implemented can be seen in Figure 6.4. The fabricated samples are characterised in their as-cast condition using scanning electron microscopy (SEM) for microstructural morphology, combined with energy dispersive X-ray spectroscopy (EDX) for regional elemental concentrations. The composition of each region is then re-inputted into Thermo-Calc to identify possible phases that may form. X-ray diffraction is then used for phase identification of the alloy. An assessment of hardness is made using Vickers microhardness. Sections of the alloy undergoes different heat treatments and then subsequent characterisation is followed.

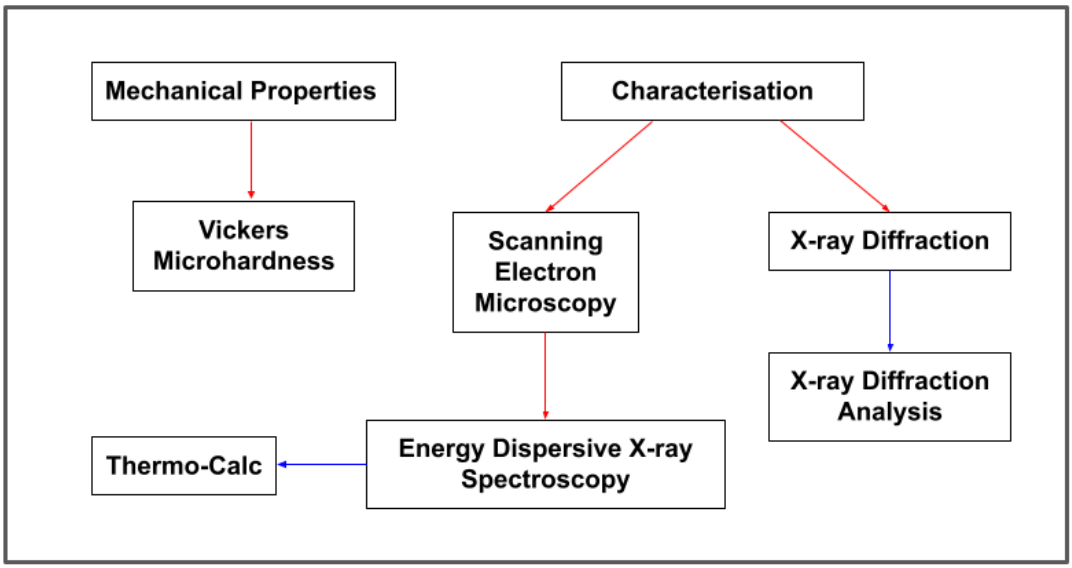

Figure 6.4: Flowchart of the experimental assessment of the designed refractory HEAs.

Both the as-cast and heat-treated conditions were evaluated, and an assessment of the experimental results were made. In the following work, samples heat treated at high

temperatures were referred to as ‘homogenised’ due to the realisation that incomplete homogenisation is likely. This is likely due to insufficient heat treatment times and inadequate heat treatment temperatures, as explained in the section above. Full alloy compositions will be identified at the beginning of each section but throughout the section each alloy will be referred to in shortened form.

6.4. $V_{0.21}Cr_{0.18}Mn_{0.09}Fe_{0.17}Ta_{0.2}W_{0.15}$

6.4.1. As-Cast

Figure 6.5 shows the experimental XRD pattern for the as-cast VCrMnFeTaW. These peaks matched three separate face-centered cubic phases indicated by a green circle (FCC1), blue triangle (FCC2) and red square (FCC3). The first cubic phase (FCC1) is analogous to a $InSb_{0.85}Te_{0.15}$ structure [8] with a space group F43m (216) and lattice parameter a≈6.43 Å. The second cubic phase (FCC2) is analogous to a CuScNiIn structure [9] with a space group Fm-3m and a lattice parameter a≈6.30 Å. The third cubic phase (FCC3) is analogous to $ZrCo_2$ [10] with a space group Fd-3m and a lattice parameter a≈6.95 Å.

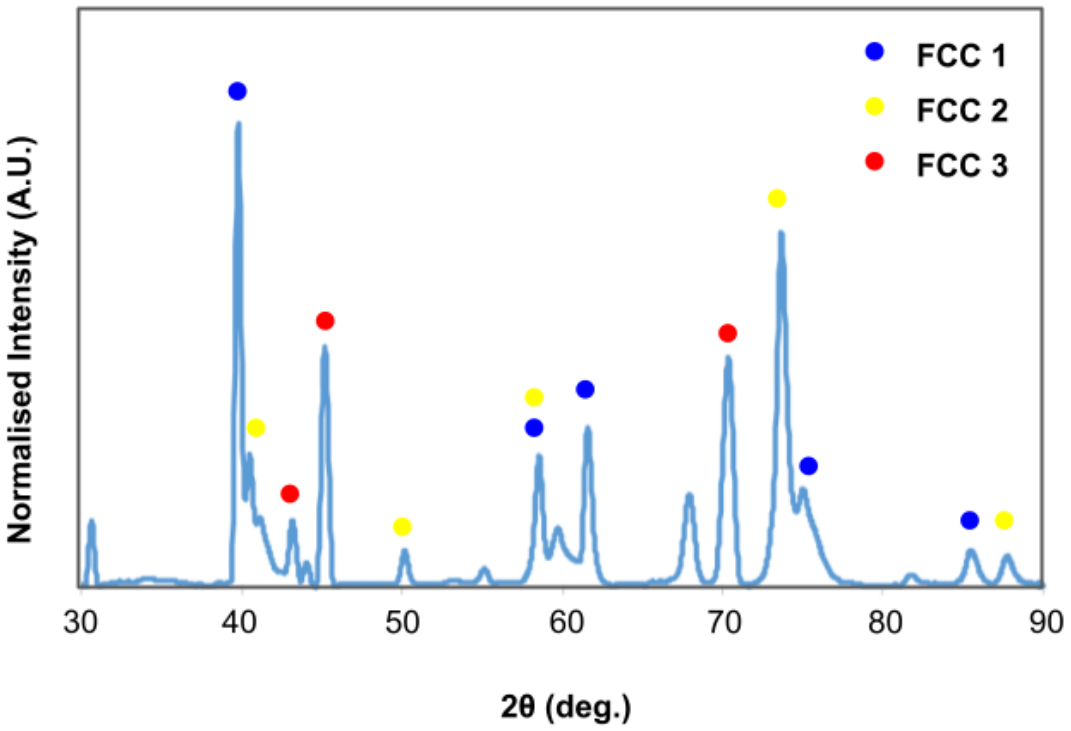

Figure 6.5: XRD pattern of the as-cast $V_{0.21}Cr_{0.18}Mn_{0.09}Fe_{0.17}Ta_{0.2}W_{0.15}$

It should be noted that these FCC phases were the best patterns which matched the experimental XRD pattern, however there are still some peaks which were unable to be

successfully matched. This means that although these FCC phases were matched using XRD, they may not entirely represent the phases in the as-cast VCrMnFeTaW. Further experimental techniques, such as high-resolution TEM, are required to determine the diffraction pattern of the alloy.

Table 6.7 summarises the XRD analysis and includes prototype structures that are analogous to the phases identified in the XRD pattern. The crystalline structures of these three face-centered cubic (FCC) phases are very similar and they all possess comparable lattice parameters.

Table 6.7: Three phases identified by the experimental XRD of as-cast VCrMnFeTaW.

	FCC1	**FCC2**	**FCC3**
Space group	F43m (216)	Fm-3m (225)	Fd-3m (227)
Prototype	ZnS	$AlCu_2Mn$	Cu_2Mg
Name	Zincblende (B3) structure	Heusler (L21) Structure	Cubic Laves Structure (C15)
Structure	Wurtzite/Diamond	BCC/D03	Diamond
Pearson symbol	cF8	cF16	cF24
Lattice parameter (Å)	a ≈6.43	a≈6.30	a≈6.95
Availability in TC	SSOL4	TCHEA4	SSOL4, TCHEA4

Figure 6.6 displays the three different cubic structures analogous to the three phases identified in the experimental XRD pattern: a) Zincblende, b) Heusler L21 structure, and c) cubic C15 Laves phase (Mehl et al 2017).

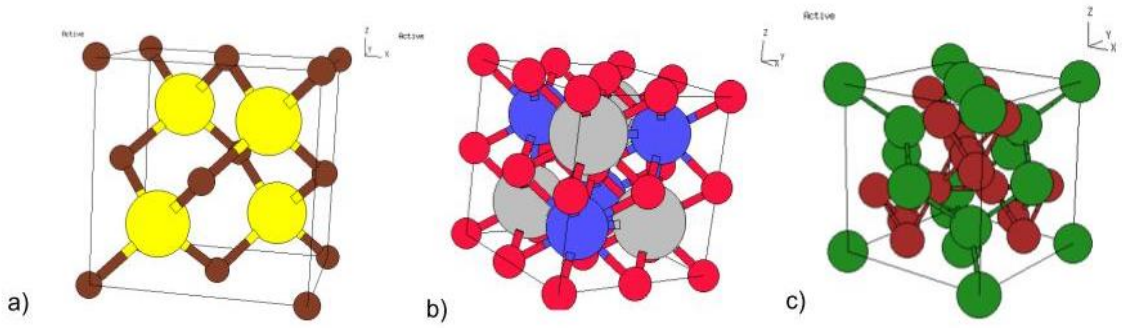

Figure 6.6: The three different cubic structures analogous to the three phases identified in the experimental XRD pattern: a) Zincblende, b) Heusler L21 structure, and c) cubic C15 Laves phase (Mehl et al, 2017).

The Zincblende (B3) and Cubic Laves (C15) structure can be represented as deviations of the diamond structure, whereas the Heusler (L21) structure is more related to a variance in the BCC structure reduced to the crystallographically-equivalent D03 lattice. These three cubic phases matched very well to the experimental XRD pattern; the peak positions of the analogous structures overlapped precisely with the experimental XRD peaks. However, there were many other PDF cards identified to match some of the same peak positions. For example, the structure $Sc_{0.7}Ti_{0.3}Ni$ [11] with a space group Pm-3m (221) and a lattice parameter a≈3.13 Å and Pearson symbol cP2 was a match with some of the peaks in the XRD pattern. This structure is identified with the ordered BCC B2 structure (analogous to the CsCl structure). $Sc_{0.7}Ti_{0.3}Ni$ is very similar to the Zincblende B3 structure in that they both have cubic crystal structures, but they have different lattice parameters and Pearson symbols, resulting in a marginally deviated lattice structure. A possible reason for multiple successful matches with structures of differing atomic lattice positions could be due to the large number of peaks present in the XRD pattern. The probability of finding analogous structure with phases that match these peaks increases as the number of peak positions increase. Additionally, when matching the XRD peaks to an analogous structure it is important to find a phase which has the multiple peaks that match the experimental XRD pattern. The three chosen FCC peaks all had multiple peaks (at least three peaks per phase) which matched the peak positions of the experimental XRD pattern. During the XRD analysis many phases were matched to the XRD pattern, however, the combination of different phases sometimes resulted in some peaks not being fitted to a phase. The closest matching combination of peaks, which takes into consideration the greatest number of peaks, were the three FCC phases reported in Table 6.7.

Figure 6.7 displays the SEM-BSE micrographs of the as-cast VCrMnFeTaW which show three regions with varying contrast: white, grey, and black displaying the characteristic fine dendritic microstructure. The white regions represent the dendritic arms, and the grey area depicts the interdendritic regions. The black precipitates are dispersed in the interdendritic regions and are highlighted in Figure 6.7b) by a red circle.

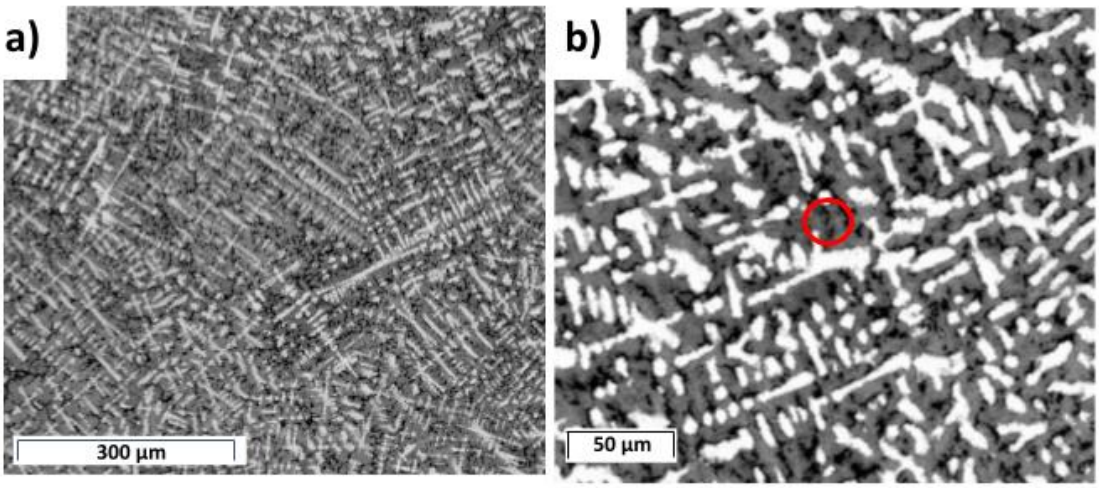

Figure 6.7: SEM-BSE micrographs of the as-cast $V_{0.21}Cr_{0.18}Mn_{0.09}Fe_{0.17}Ta_{0.2}W_{0.15}$ at magnifications a) x400 and b) x1300

Figure 6.8 shows the SEM-EDX elemental maps which highlight the constituent distribution of the as-cast VCrMnFeTaW. As expected, the brighter areas are richer in heavier atoms, like tungsten and tantalum, and more deficient in lighter atoms like iron, chromium, and vanadium. For the darker region (defined as grey) the opposite applies, and these regions are more abundant in tantalum, iron, and chromium. The small black regions appear to be vanadium-rich precipitates.

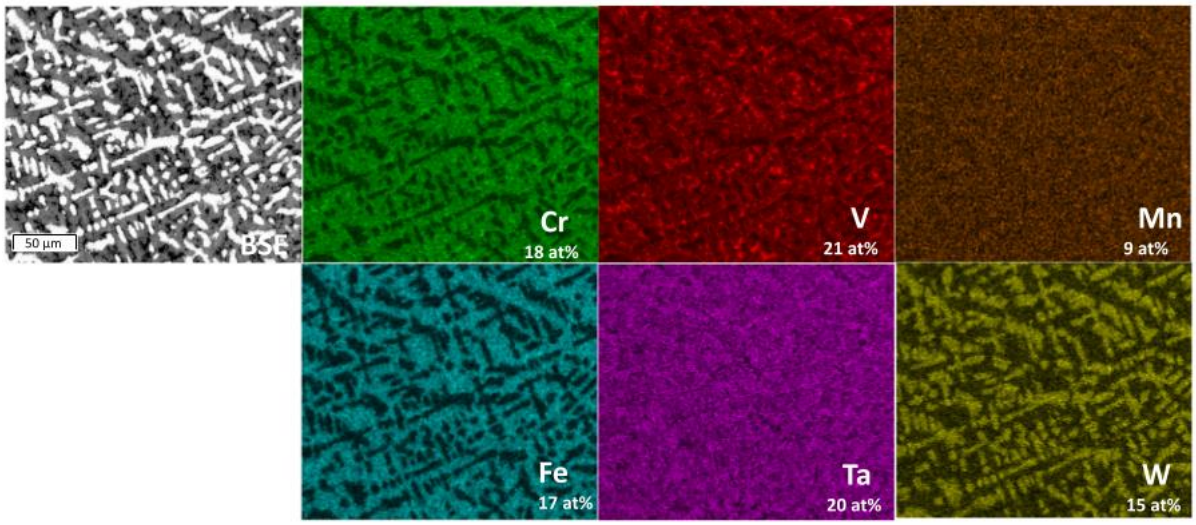

Figure 6.8: SEM-EDX elemental maps of the as-cast $V_{0.21}Cr_{0.18}Mn_{0.09}Fe_{0.17}Ta_{0.2}W_{0.15}$ at magnification x1300

Table 6.8 displays the elemental compositions of the three regions determined by SEM-EDX point scans. Whilst the composition of each phase varies, each region contains all the components in the alloy. The comparable lattice parameters (a ≈6.43, a≈6.30, and a≈6.95) of

the three FCC phases identified by the XRD analysis is also a reflection of the elemental distribution across the three phases.

Table 6.8: Elemental concentrations (at%) of the three different regions of the VCrMnFeTaW alloy in the as-cast state using SEM-EDX point scans (averaged from 5 separate point scans from each region). The corresponding Thermo-Calc predictions of the equilibrium for each regional composition are also stated. The averaged XRF values of the overall VCrMnFeTaW composition is included for comparison.

	White region (at%)	**Grey region (at%)**	**Black region (at%)**	**Overall Alloy (at%)**
C	-	-	-	29
V	17±0.9	20±0.6	42±2	15
Cr	9±0.9	21±0.4	20±0.8	11
Mn	0.2±0.2	0.1±0.1	0.04±0.1	8
Fe	4±0.7	22±0.6	17±1.8	11
Ta	26±0.4	27±1.1	8±1.5	14
W	44±1.9	10±0.3	13±2.4	12
Thermo-Calc predictions (SSOL4)	BCC A2	BCC A2 C14 Laves	BCC A2 C14 Laves	BCC A2 σ C15 Laves

As with the previous alloys in the as-cast state, the concentration of manganese is too small to be quantitatively calculated by SEM-EDX point scans for reasons already discussed. To determine whether these compositions would yield the crystal structures observed in the XRD patterns, the average compositions, as determined by the SEM-EDX point scans, were inputted back into Thermo-Calc. For the grey (equimolar but slightly deficient in tungsten) and black (rich in vanadium, chromium, and iron) regions. Thermo-Calc predicts a BCC and a C14 Laves phase to be present; whilst for the white phase, Thermo-Calc only predicts a BCC phase. Furthermore, for the overall alloy composition, it is shown that there is a considerable amount of carbon contamination within the alloy, likely arising from the VAM process. Whilst the amount of carbon in each region was unable to be accurately determined, EDX area scans of the alloy suggested a substantial amount of carbon contaminated within the sample.

Figure 6.9 shows the Thermo-Calc predictions using the TCHEA4 and SSOL4 database for $V_{0.21}Cr_{0.18}Mn_{0.09}Fe_{0.17}Ta_{0.2}W_{0.15}$. Similar phases include the main BCC phase (disordered in the SSOL4 prediction and ordered in the TCHEA4 prediction) and a σ phase at lower temperatures (below 500 °C).

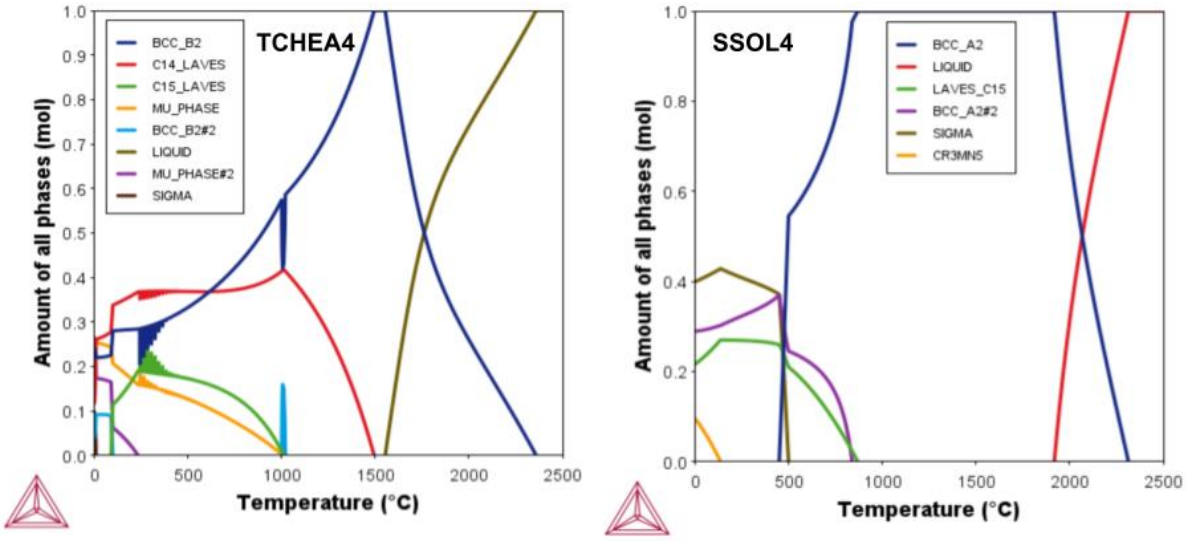

Figure 6.9: The Thermo-Calc predictions for $V_{0.21}Cr_{0.18}Mn_{0.09}Fe_{0.17}Ta_{0.2}W_{0.15}$ using the TCHEA4 and SSOL4 database

For the overall alloy, the TCHEA4 database incorrectly predicts the formation of both a C15 Laves phase and a C14 Laves phase. However, the SSOL4 database correctly predicts a cubic C15 Laves phase as a secondary phase for the overall composition of VCrMnFeTaW. As with the empirical HEA parameters, the crystal structure of the predominant phase is predicted by both TCHEA4 and SSOL4 to be a disordered BCC A2 phase, yet this is not identified in the experimental XRD pattern. This is likely, in part, due to the introduction of carbon as an interstitial within the lattice, thus causing significant change in the crystal structure.

Further shortfalls of some of these predictions may arise for several reasons: firstly, Thermo-Calc contains different possible phases and phase constitutions depending on the thermodynamic database used. Table 6.8 displays the difference in TCHEA4 and SSOL4 and shows that neither of the databases contains all three as-cast phases suggested by the XRD analysis. This may be due to no indication of these FCC crystal structures in the binary phase diagrams of the components in VCrMnFeTaW. This could suggest that these as-cast FCC phases are metastable as opposed to equilibrium phases due to the formation under non-equilibrium solidification conditions.

However, from the SEM-EDX point scans it is evident that all three FCC phases are composed of all the elements, therefore higher-ordered phase diagrams are needed to calculate the tendency of the formation of a cubic crystal structure akin to those experimentally observed. This leads to the second reason - manganese is not accounted for by SEM-EDX in these point

scan calculations, Additionally, as there is evidence of significant addition of carbon within the alloy, this is likely to create enough distortion to change the lattice structure and may be the reason for the formation of multiple unexpected FCC phases.

This means that the Thermo-Calc predictions cannot be entirely accurate regardless of the database used. Additionally, both the binary phase diagrams and Thermo-Calc only take into consideration of equilibrium phases and so the as-cast phases present in VCrMnFeTaW may have formed due to non-equilibrium cooling (i.e., fast cooling) and may not be stable after heat treating. These results suggest, therefore, that whilst the empirical rules for the prediction of a single-phase solid solution can be used to determine an FCC, BCC, σ, or Laves phase, they cannot be used to determine specific crystal structures like Heulser or Zincblende structures. In the current literature, there are no set boundaries for the calculation of a diamond-type structure single-phase solid solution.

6.4.2 1500 °C, 48 hours

Figure 6.10 shows the SEM-BSE micrograph of VCrMnFeTaW after a high temperature heat treatment (1500 °C for 48 hours). Large cellular structures of white contrast (approximately 10-20 μm in diameter) with grey precipitation inside the grains and grey and black regions dispersed outside of these globular grains (indicated by the red arrows) can be observed.

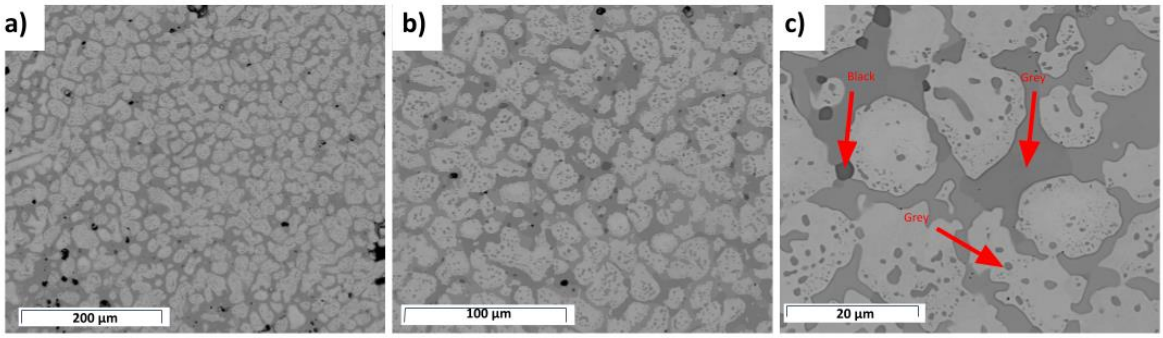

Figure 6.10: SEM-BSE micrograph of $V_{0.21}Cr_{0.18}Mn_{0.09}Fe_{0.17}Ta_{0.2}W_{0.15}$ after heat treatment at 1500 °C for 48 hours at magnifications a) x600 b) x1300 and c) x5000

It is evident from these micrographs that there has been a major change in the microstructure of the as-cast sample, specifically, there is no longer evidence of the dendritic microstructure.

Figure 6.11 displays the SEM-EDX elemental maps which show the distribution of elements in the 'homogenised' VCrMnFeTaW. The white cellular regions are mainly composed of

tungsten, whereas the grey precipitates inside the cells and the grey region surrounding the cells are rich in all the remaining elements.

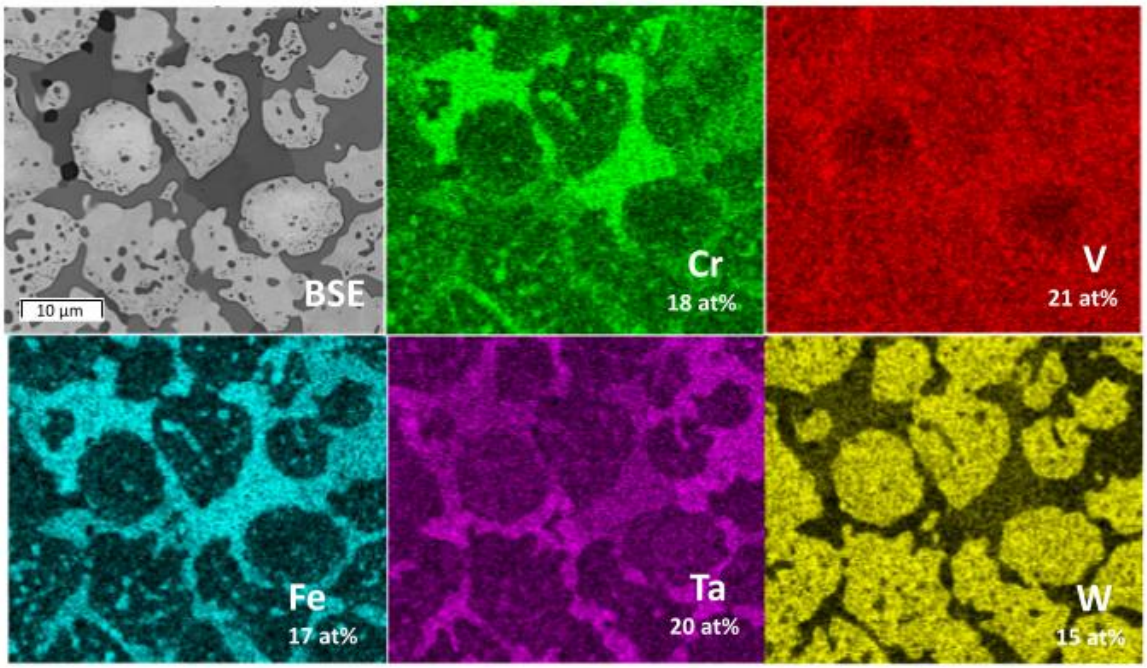

Figure 6.11: SEM-EDX elemental maps of $V_{0.21}Cr_{0.18}Mn_{0.09}Fe_{0.17}Ta_{0.2}W_{0.15}$ after heat treatment at 1500 °C for 48 hours at magnification x5000

The strong proclivity of iron, tantalum, and chromium forming in the same interdendritic regions could be due to very negative enthalpies of mixing values for the binary pairs. For example, Cr-Ta (-7 kJ/mol) and Fe-Ta (-15 kJ/mol) are two pairs of elements that have the most negative values of ΔH_{mix}. This indicates a strong attraction between these elements and represents the tendency for the formation of intermetallic compounds (i.e., α and β Cr_2Ta or the analogous structures of ε $MgZn_2$ or μ Fe_7W_6 for Fe-Ta compounds).

Table 6.9 lists the chemical compositions for all four regions of contrast ascertained from the SEM-BSE micrographs. The dark grey precipitates inside the cells were found to have the same composition as the black regions surrounding the cells, therefore it can be concluded that these two regions are the same. The white cells appear to be richer in tungsten (and deficient in chromium and iron) whereas the light grey region surrounding the cells is observed to be enriched in tantalum (and lacking in tungsten).

Table 6.9: Elemental concentrations (at%) of the three different regions of the 'homogenised' VCrMnFeTaW alloy in the as-cast state using SEM-EDX point scans (averaged from 5 separate point scans from each region). The corresponding Thermo-Calc predictions of the equilibrium phases for each regional composition are also stated. The averaged XRF values of the overall VCrMnFeTaW composition is included for comparison.

	White region (at%)	**Light Grey region (at%)**	**Dark Grey region (at%)**	**Black region (at%)**	**Overall Alloy (at%)**
C	-	-	-	-	42
V	14±2	19±0.4	17±0.3	17	10
Cr	6±0.4	15±0.2	22±1.2	24	7
Mn	-	-	-	-	5
Fe	2±1.5	20±0.3	22±1.3	23	6
Ta	25±2	41±0.3	26±0.6	26	13
W	53±0.7	5±0.2	13±2.9	10	17
Thermo-Calc predictions (SSOL4)	BCC A2	BCC A2 C14 Laves	BCC A2 C14 Laves	BCC A2 C14 Laves	BCC A2

By comparing the compositions of the different phases in the as-cast sample (Table 6.9) with the phases present in the heat-treated sample, the following microstructural evolution is suggested. The white contrast dendritic region, rich in tungsten, increases in volume fraction and forms a spherical grain-like structure; the black and light grey interdendritic regions, richer in tantalum, forms in between the boundaries of these grains upon heat treating. Whilst this high temperature heat treatment transformed the microstructure, there is still evidence of elemental microsegregation as shown by the SEM-EDX elemental maps. As with all the alloys in this work, a higher temperature (ideally around 1800 °C) would be more appropriate in achieving a homogenised alloy.

Interestingly, the SEM-EDX data obtained from each phase observed in the 'homogenised' alloy is somewhat comparable to the corresponding regions observed in the as-cast alloy (shown in Table 6.8). Therefore, whilst the microstructure of the alloy dramatically changed during the homogenization heat treatment, the degree of elemental redistribution was small. A slight difference in the 'homogenised' VCrMnFeTaW is the composition of the black region. In the as-cast alloy the black precipitates contained all the components but were vanadium-rich. Post-homogenisation, the composition of this phase is more akin to the darker grey region. This is explained in more detail further in the section. Prolonged heat treatment of the

alloy (beyond 48 hours) or heat treating at higher temperatures may be sufficient to reduce this segregation.

The dark grey precipitates formed inside the grains have a similar composition to the lighter grey region surrounding the grains. However, the composition inside the grains contains a slightly higher proportion of tungsten (13 at%) compared to the grey region outside the grain (5 at%) which is attributed to the increased concentration of tungsten within the grains. This may be due to the excess of concentration of tungsten within the white grains (53 at%) therefore the precipitates which are enclosed within these grains are likely to contain a higher abundance of tungsten due to the diffusion of tungsten.

As with the as-cast sample, the quantitative elemental concentration of manganese was not detected by the SEM-EDX point scans. The SEM-EDX data does indicate that each region of the "homogenised" VCrMnFeTaW is mutlicomponent in nature (considering the lack of manganese data). Thermo-Calc was used to determine the equilibrium phases predicted to form from the compositions identified by SEM-EDX point scans for each region. These results are listed in Table 6.9. For the black and both grey regions a disordered BCC and C14 Laves phase was expected to form, whereas, for the white region, a stable BCC phase was predicted, which correlates with the corresponding regions in the as-cast sample.

Figure 6.12 shows the XRD pattern for the 'homogenised' VCrMnFeTaW and displays two FCC phases. The first FCC phase (FCC1) is indicated by a green circle and is analogous to $Ni_{1.91}SnZr$ [12] with a space group Fm-3m (225) and a lattice parameter a≈6.27 Å. The second FCC phase (FCC2) is represented by a blue triangle and is analogous to $Ti_{1.8}Mn_{0.3}Co_{0.9}$ [13] with a space group Fd-3m (227) and a lattice parameter a≈11.34 Å.

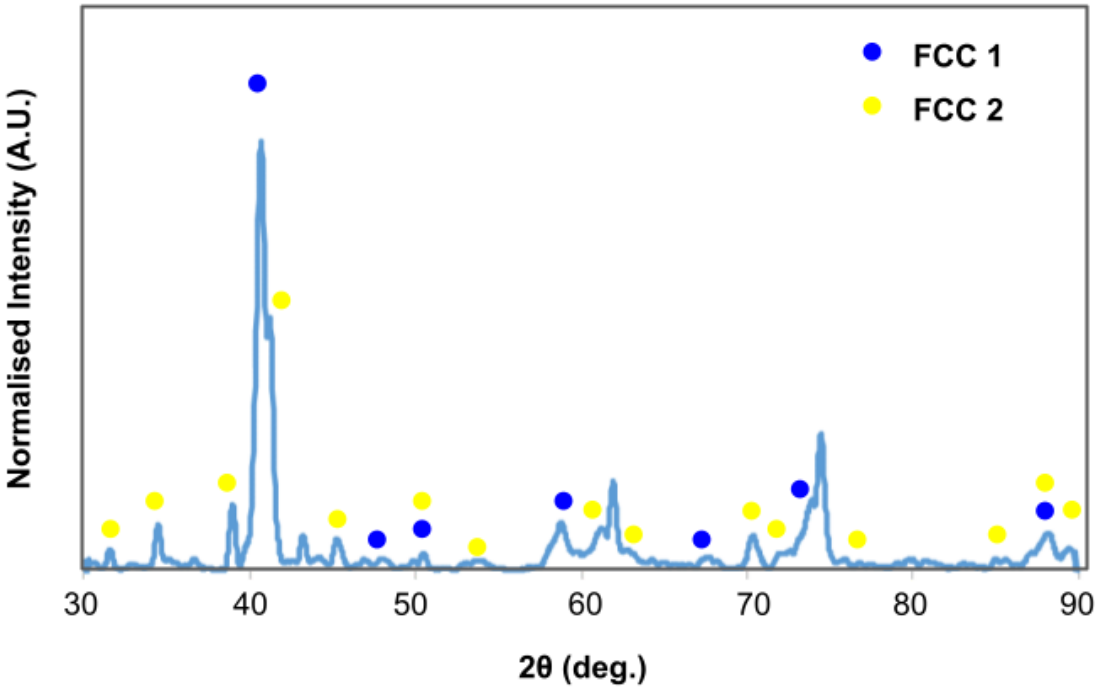

Figure 6.12: XRD pattern of $V_{0.21}Cr_{0.18}Mn_{0.09}Fe_{0.17}Ta_{0.2}W_{0.15}$ after heat treatment at 1500 °C for 48 hours

In the as-cast VCrMnFeTaW XRD pattern, there were three distinct FCC phases with the space groups F43m (216), Fm-3m (225), and Fd-3m (227). Upon heat treatment, the FCC phase with space group F43m (216) does not appear in the 'homogenised' XRD pattern, however the two FCC phases with space groups Fm-3m (225), and Fd-3m (227) identified reflect the two of the same phases in the as-cast XRD pattern. These phases are summarised in Table 6.10.

Table 6.10: Two FCC phases identified by the experimental XRD of the homogenised VCrMnFeTaW. These are derived from the PDF cards which will be analogous to the phases found experimentally.

	FCC1	**FCC2**
Space group	Fm-3m (225)	Fd-3m (227)
Prototype	$AlCu_2Mn$	$NiTi_2$
Name	Heusler (L21) Structure	NiTi2 Structure
Structure	BCC/D03	FCC
Pearson symbol	cF16	cF96
Lattice parameter (Å)	a≈6.27	a≈11.34
Availability in Thermo-Calc	TCHEA4	TCHEA4, SSOL4

The F43m (216) phase appears to have dissolved at high temperature, yet there is retention of the Fm-3m (225) and Fd-3m (227) phases. However, the Fd-3m (227) phase differs slightly in the homogenised condition compared to the phase identified in the as-cast XRD pattern. Firstly, the Pearson symbol has changed from cF24 (as-cast) to cF96 ('homogenised') indicating a change in the structure of the lattice. The $NiTi_2$ structure analogous to the 'homogenised' phase appears to accommodate more of the elements as the lattice parameter has expanded substantially from the as-cast Fd-3m (227) phase (from 6.95 Å to 11.34 Å respectively).

The reduction of phases in the homogenised alloy, identified using XRD, is also explained by the loss of vanadium precipitation from the as-cast alloy also observed by the SEM-EDX elemental maps. After the high-temperature heat treatment, there is a clear reduction in the vanadium-based precipitates which coincides with the decomposition of the FCC1 (Zincblende structure, F43m (216)) phase. This suggests that this phase is only stable at lower temperatures and is metastable in the as-cast alloy.

The experimental XRD pattern correlates with the SEM-EDX regional compositions for the 'homogenised' alloy: the light grey, dark grey, and black regions all contain very similar elemental compositions and can be considered analogous in structure to the Fd-3m FCC

phase. The majority white region is most likely akin to the Fm-3m FCC phase for this reason. At 1500 °C, Thermo-Calc predicts from the property diagrams of VCrMnFeTaW for there to be a single BCC phase. There are no apparent secondary phases or intermetallic compounds predicted at this temperature. However, at much lower temperatures there is a small amount of σ (0.4 mol below 700 °C) and C15 Laves phase (0.3 mol below 1200 °C) predicted to form.

6.5. $V_{0.26}Cr_{0.17}Fe_{0.32}Ta_{0.25}$

6.5.1. As-Cast

Figure 6.13 shows the experimental XRD pattern of the as-cast VCrFeTa alloy and displays a single hexagonal close-packed (HCP) crystal structure (with a space group of P63/mmc). All the peaks featured in the XRD pattern matched with a single HCP phase analogous to $Cr_{66}Ta_{33}$ [14] with lattice parameters a≈4.89 Å and c≈7.99 Å.

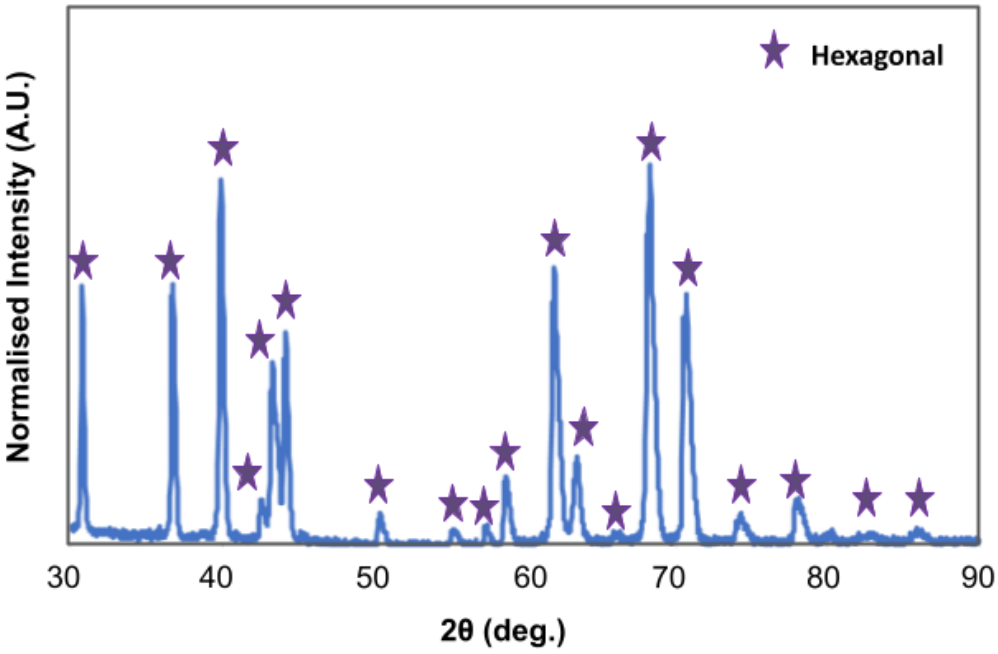

Figure 6.13: XRD pattern of the as-cast $V_{0.26}Cr_{0.17}Fe_{0.32}Ta_{0.25}$

This is surprising given the extensive design processes (discussed in depth in Chapter 5: Alloy Design) used to enhance the formation of a BCC solid solution of these novel high entropy alloys. The specific HCP crystal structure (with a Pearson symbol hP12) is based on the hexagonal Laves structure of the C14 variant where the atoms are positioned in the hexagonal diamond sites. This analysis is further reinforced by the ICDD PDF-4+ Web software which gives this crystal structure an extremely high 'goodness of match' (GoM) - a criterion used to measure the PDF's pattern of best fit to the experimental peaks with no shifting or broadening

of the peaks. All 22 experimental peaks matched the exact positions of the HCP PDF card. The large number of X-ray peaks provides a higher accuracy in matching the peaks to an analogous structure and determining the lattice parameters. The predictions from the thermodynamic parameters in Chapter 5: Alloy Design indicate a stable BCC solid solution. Very few single-phase HCP HEAs have been experimentally observed [15], [16], [17]. And it has been hypothesised by Zhang et al [18] that single phase HCP HEAs are likely to form if the constituents are rare earth elements as they all have similar atomic sizes and crystal structures and so can form isomorphous solid solutions. However, recent work by Krapivka and Firstov [19] have indicated the propensity of a fully disordered Laves phase (or σ or μ phase) depending on the average valence electron concentration (VEC) per atom and other empirical parameters. For example, if the alloying components each have an average VEC between 6-7 then the overall alloy may form a laves solid solution. VCrFeTa does not follow this stipulation (aside from chromium which has a VEC of 6) as most components have a VEC slightly outside of this boundary. However, for the alloy's overall average VEC (for the experimental composition), the VEC is 6.13 which does adhere to this rule. From the same work, another criterion for the formation of a Laves phase is the total negative enthalpy of mixing to be lower than -7 kJ/mol. VCrFeTa meets this requirement and has an overall mixing enthalpy of -9.15 kJ/mol, which is by far the lowest value of the novel alloys. Whilst the authors suggest that all the criteria must be met for a 100% laves phase, the deficiencies highlighted by VCrFeTa in some of these rules may be explained by an unstable Laves phase being formed in the as-cast state from the non-equilibrium fabrication conditions. This hypothesis is challenged by the subsequent heat treatment where the hexagonal Laves solid solution may undergo a phase transformation.

Figure 6.14 shows the Thermo-Calc predictions using the TCHEA4 and SSOL4 database for $V_{0.26}Cr_{0.17}Fe_{0.32}Ta_{0.25}$. There are vast differences between the TCHEA4 and SSOL4 database predictions. The major phase predicted by SSOL4 is the disordered BCC A2 phase (as for all of the alloys in this work), however the most stable predominant phase calculated by TCHEA4 is the C15 Laves phase. An ordered BCC B2 phase is predicted below 750 °C and a σ phase is present at higher temperatures (500 °C – 1500 °C). For SSOL4, the C15 Laves phase also appears but at much lower concentrations (less than 0.3 mol) and below 1000 °C. Similarly, the σ phase is also low-temperature dependent but at much higher proportions (0.6 mol) than calculated for TCHEA4.

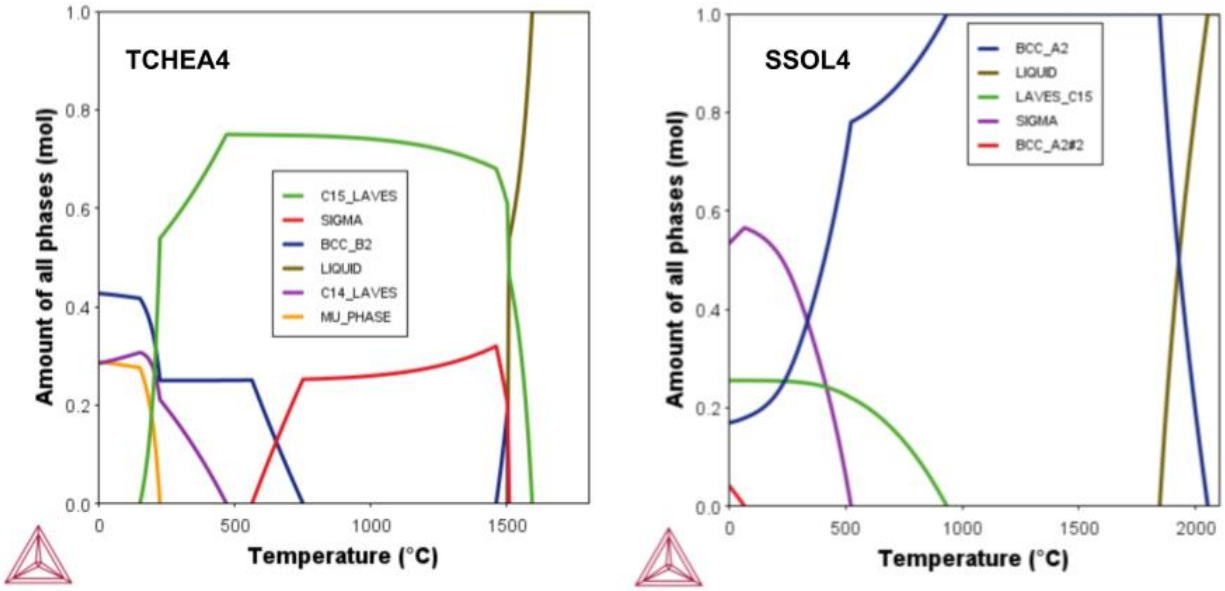

Figure 6.14: The Thermo-Calc predictions for $V_{0.26}Cr_{0.17}Fe_{0.32}Ta_{0.25}$ using the TCHEA4 and SSOL4 database

From this figure the Thermo-Calc predictions (using both databases) for VCrFeTa also suggest the formation of the Laves phase. Even though the predominant matrix is expected to be a disordered BCC solid solution, the SSOL4 database predicts a C15 Laves phase below 1000 °C and the TCHEA4 database predicts a majority C15 Laves phase with a negligible amount of the C14 Laves variant. The HCP phase proposed from the XRD analysis suggests that the Laves phase is of the C14 variant, which is also the most exhibited Laves variation observed in fabricated high entropy alloys [20] (this is explained further in Chapter 5: Alloy Design). Furthermore, the analogous structure which matched with the experimental XRD pattern, $Cr_{66}Ta_{33}$, has the same structure as the prototype $MgZn_2$ which correlates with the hexagonal C14 Laves phase. Solid solutions with wide homogeneity ranges are formed based on the C14 Laves intermetallic compounds for this reason.

Figure 6.15 displays the SEM-BSE micrographs of the as-cast VCrFeTa which reveal a typical dendritic microstructure with the black regions representing the dendrites and the grey and white regions showing the interdendritic regions.

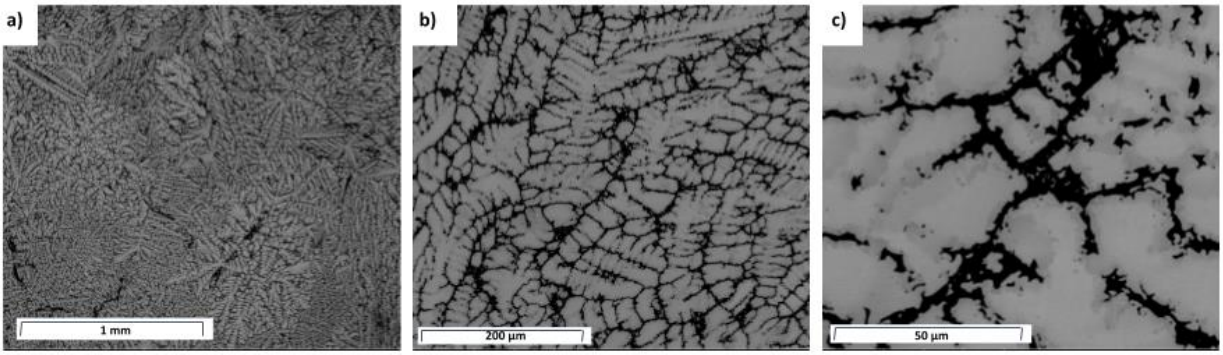

Figure 6.15: SEM-BSE micrographs of the as-cast $V_{0.26}Cr_{0.17}Fe_{0.32}Ta_{0.25}$ at magnifications a) x150 b) x600 and c) x3000

Figure 6.16 shows the SEM-EDX elemental maps of the as-cast VCrFeTa. These maps exhibit a small amount of elemental segregation with vanadium, chromium, and iron enriching the interdendritic regions. In this area tantalum content appears to be diminished.

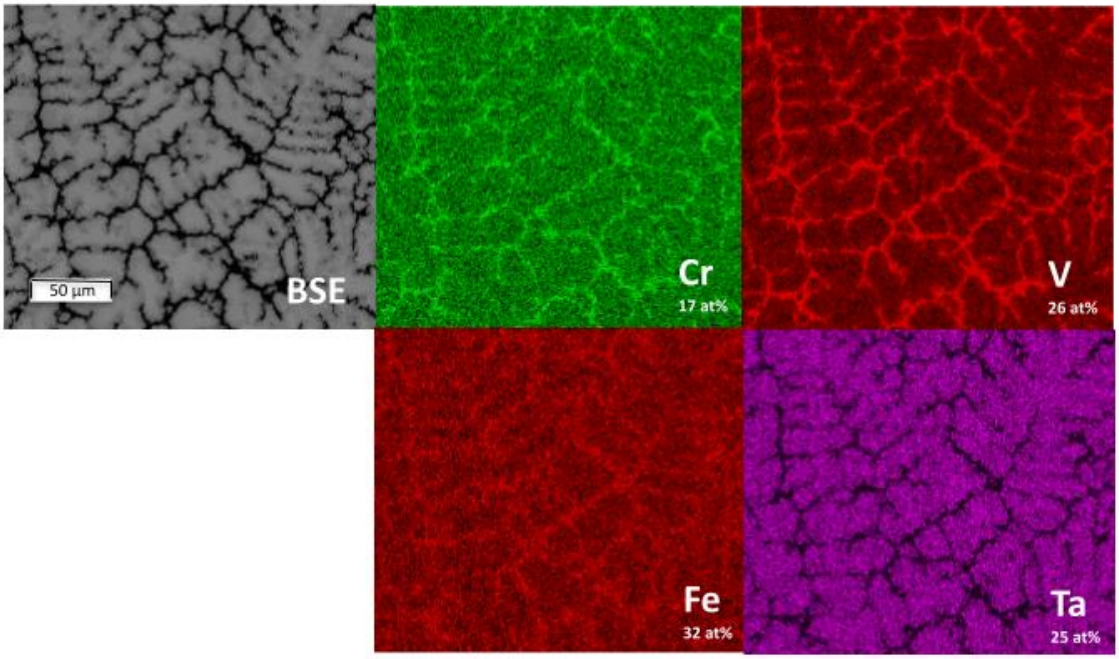

Figure 6.16: SEM-EDX elemental maps of the as-cast $V_{0.26}Cr_{0.17}Fe_{0.32}Ta_{0.25}$ at magnification x1300

The identification of a single BCC phase in the experimental XRD pattern for the equimolar MoNbTaVW high entropy alloy in the as-cast state was reported by Senkov et al [1]. There was evidence of elemental segregation due to the dendritic microstructure in the SEM-EDX elemental maps. The observed microsegregation of the constituents was attributed to the non-equilibrium solidification within the liquidus and solidus temperatures. This kinetically restricts the homogeneous distribution of the alloying elements in the growing solid phases and results in microsegregation according to their respective melting temperature. These findings coincide

with the results found in this work and further solidifies that regardless of metastable microstructures a single-phase alloy can be formed. Whilst in general there is homogeneity between the elements in VCrFeTa, there is a slight microsegregation between vanadium and tantalum. Findings from Zhang et al [21] have shown that for the alloys $Cr_{0.5}$MoNbTaVW and Cr_2MoNbTaVW there was elemental microsegregation in the solidification microstructure as shown by the SEM-EDX elemental maps. The constituents with a higher atomic number, tungsten, tantalum, and molybdenum solidify first in the dendrite arms, whilst niobium, vanadium, and chromium enrich the interdendritic regions. As with the studies from Senkov et al [1] and Zhang et al [19] investigated the elemental compositions of each region and calculated the partition coefficients for each element to quantify the microsegregation [22]. For the alloys $Cr_{0.5}$MoNbTaVW and Cr_2MoNbTaVW the microsegregation between vanadium and tantalum in the as-cast state are apparent and reflect the same arrangement found in the as-cast VCrFeTa. This segregation between tantalum and vanadium, specifically in regard to the work by Zhang et al [21] is discussed further in a later section: as-cast VCrMnTaW.

Table 6.11 shows the elemental compositions of the dendritic and interdendritic regions of the as-cast VCrFeTa from SEM-EDX point scans. These point scans are necessary to quantify the microsegregation and to determine if the interdendritic regions are completely void of tantalum.

Table 6.11: Elemental concentrations (at%) of the three different regions of the refined VCrFeTa alloy in the as-cast state using SEM-EDX point scans (averaged from 5 separate point scans from each region). The corresponding Thermo-Calc predictions of the equilibrium phases for each regional composition are also stated. The averaged XRF values of the overall VCrFeTa composition is included for comparison.

	White region (at%)	**Grey region (at%)**	**Black region (at%)**	**$K=C_{da}/C_{idr}$**	**Overall alloy (at%)**
V	19±0.2	22±0.4	41±5.6	1.36	26
Cr	16±0.2	15±0.1	16±0.7	1	17
Fe	32±0.04	33±0.2	35±0.8	0.91	32
Ta	33±0.2	30±0.4	8±5.9	4.13	25
Thermo-Calc predictions (SSOL4)	BCC A2	BCC A2	BCC A2		BCC A2 C15 Laves σ

The SEM-EDX point scans display the mostly homogenous microstructure which alludes to a single-phase HCP structure. However, the black region (dendritic region) displays some enrichment in vanadium (41 at%) and depletion in tantalum (8 at%) and the contrast of this

region also correlates with the average atomic number of the composition of the region. The partition coefficients, K, calculated from the SEM-EDX point scan averages indicate that chromium and iron are ~1 which indicate an even distribution of these elements in both the dendritic and interdendritic regions. For vanadium and tantalum, these values are much greater and reflect the microsegregation between these elements. These results are discussed further in Section: as-cast VCrMnTaW.

These compositions, whilst again are not equilibrium phases as they were formed in non-equilibrium conditions, were calculated in Thermo-Calc to give insight into the possible phases that may form. These are also depicted in Table 6.11 and interestingly, Thermo-Calc predicts a single disordered BCC A2 phase for the three compositions which correlates with the initial overall refined composition of VCrFeTa. And for the overall alloy, a majority disordered BCC A2 phase is predicted until 1250 °C when the formation of a cubic C15 Laves phase and σ phase are predicted to occur.

6.5.2. 1500 °C, 48 hours

Figure 6.17 shows the SEM-BE micrograph of the 'homogenised' VCrFeTa which displays a homogenised alloy with defined grains. The grain sizes vary in diameter between 50 and 150 µm.

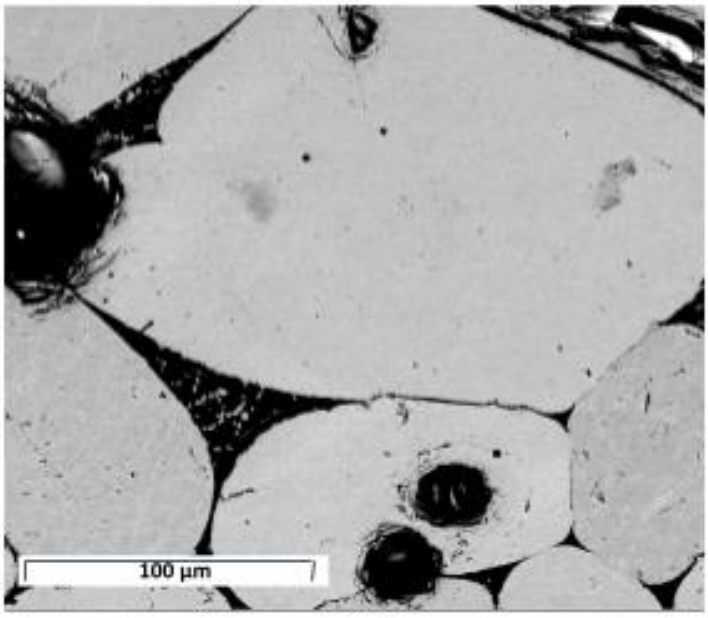

Figure 6.17: SEM-BSE micrograph $V_{0.26}Cr_{0.17}Fe_{0.32}Ta_{0.25}$ after heat treatment at 1500 °C for 48 hours at magnification x1300

Figure 6.18 shows the SEM-EDX elemental maps of $V_{0.26}Cr_{0.17}Fe_{0.32}Ta_{0.25}$ after heat treatment at 1500 °C for 48 hours. There is some elemental segregation along and between the grains

identified by the SEM-EDX elemental maps. These areas are rich in vanadium, chromium and iron, much like in the as-cast state where tantalum is depleted in these regions.

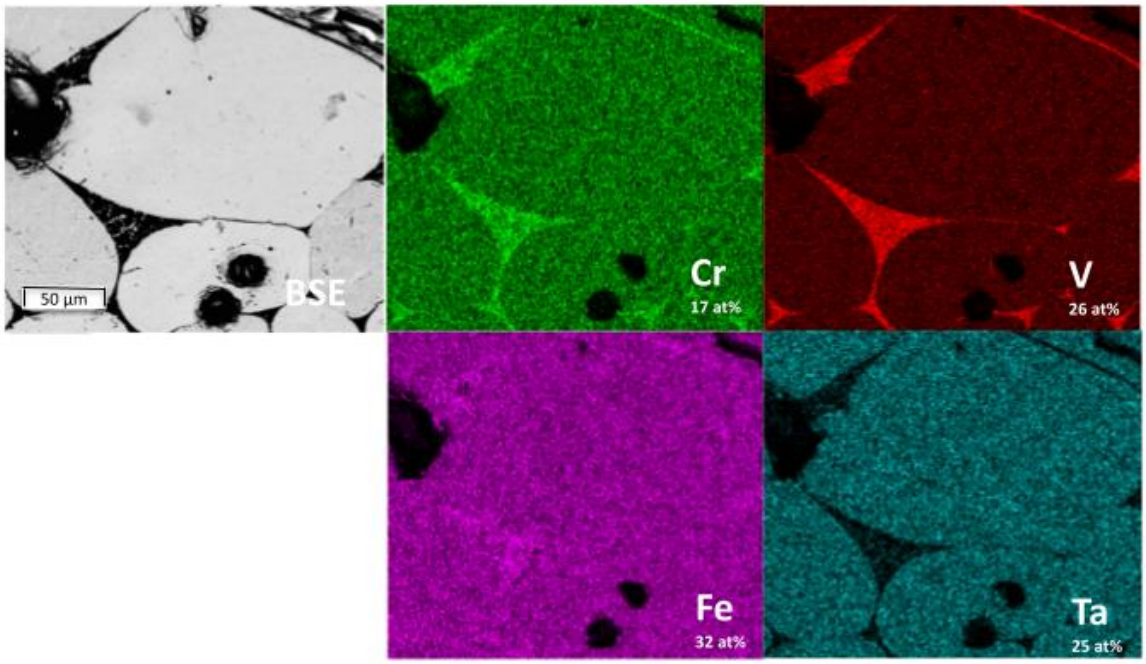

Figure 6.18: SEM-EDX elemental maps of $V_{0.26}Cr_{0.17}Fe_{0.32}Ta_{0.25}$ after heat treatment at 1500 °C for 48 hours at magnification x1300

This pattern of elemental segregation is also observed in other alloys studied in this system, for example, in the homogenised VCrFeTaW. The homogenisation of VCrFeTa can be regarded in most part as a successful heat treatment and resulted in the eradication of dendrites and formation of a granular microstructure. This may be due to the lower melting point of the refined VCrFeTa (2067 °C) which would require a lower temperature homogenisation heat treatment to achieve homogeneity. VCrMnFeW also has a similar predicted melting point (2123 °C) and may confirm that the lower melting point alloys have a more successful homogenisation treatment.

Table 6.12 shows the elemental compositions of the granular area and interdendritic regions of the 'homogenised' VCrFeTa from SEM-EDX point scans. From this table there is little difference between the as-cast VCrFeTa of the equivalent regions.

Table 6.12: Elemental concentrations (at%) of the three different regions of the 'homogenised' VCrMnFeTaW alloy in the as-cast state using SEM-EDX point scans (averaged from 5 separate point scans from each region). The corresponding Thermo-Calc predictions of the equilibrium phases for each regional composition are also stated. The averaged XRF values of the overall VCrMnFeTaW composition is included for comparison.

	White region (at%)	**Black region (at%)**	**Overall alloy (at%)**
O	-	-	11
V	22±0.2	46±0.2	22
Cr	15±0.3	15±1.2	14
Fe	36±0.3	36±0.8	31
Ta	27±0.2	3±1.1	22
Thermo-Calc predictions (SSOL4)	BCC A2 C15 Laves σ	BCC A2 σ C15 Laves	BCC A2 C15 Laves σ

A notable difference between the regional elemental concentrations of the 'homogenised' VCrFeTa is the difference between the vanadium and tantalum concentrations. Additionally, there is evidence of an oxygen contamination within the sample, likely arising from the heat treatment process. The amount of oxygen in each region was unable to be determined due to the inherent limitations of EDX, however the presence of oxygen in the overall alloy (determined using area scans) was quantified at 11 at%.

Figure 6.19 displays the experimental XRD pattern of VCrFeTa after heat treating at 1500 °C for 48 hours with a hexagonal phase (depicted by a purple star) and an FCC phase (shown by a green circle). The hexagonal phase is analogous to $TaV_{0.6}Fe_{1.4}$ [23] and the FCC phase is analogous to Nb_3Ni_3O [24].

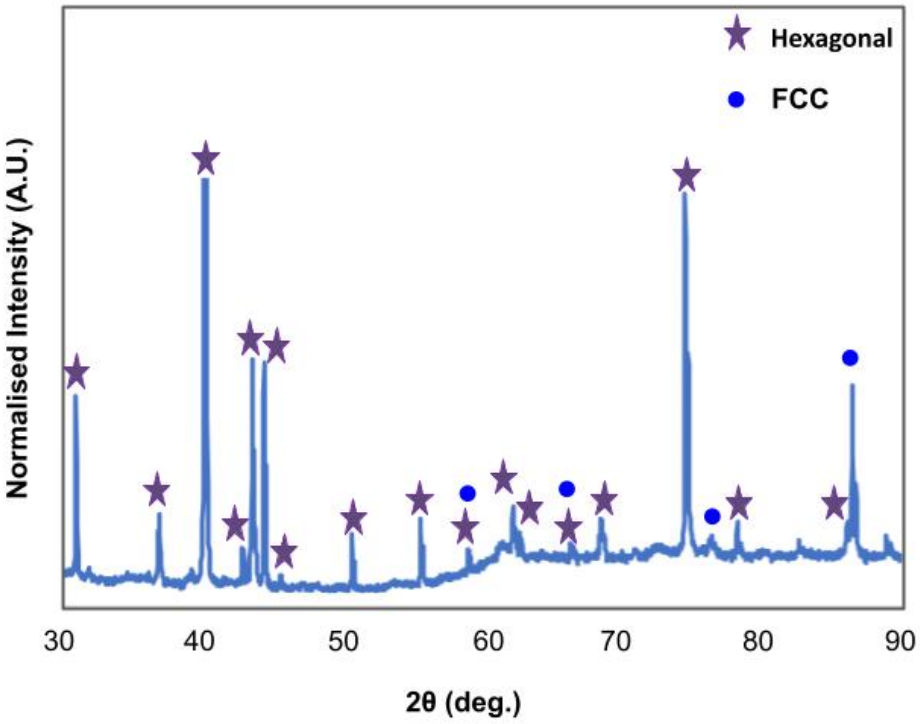

Figure 6.19: XRD pattern $V_{0.26}Cr_{0.17}Fe_{0.32}Ta_{0.25}$ after heat treatment at 1500 °C for 48 hours

Due to the high intensity of the peak at 40 °, the peak intensity of the next highest peak was used to give the relative intensity of the other peaks. The secondary FCC phase has been identified as an oxide phase, Nb_3Ni_3O. Whilst Nb and Ni are not present in this alloy, these elements can be substituted with elements V, Cr, Fe, or Ta alongside oxygen, which has also been identified in the EDX scans. Therefore, it can be concluded that after a homogenisation treatment, the hexagonal phase remained, and an oxide phase formed likely due to air contamination during the heat treatment.

The analogous XRD phases and associated parameters are summarised in Table 6.13.

Table 6.13: Two phases identified by the experimental XRD of the 'homogenised' VCrFeTa. These are derived from the analogous structures which have the same XRD pattern to the phases found experimentally.

	HCP1	**FCC1**
Space group	P63/mmc (194)	Fd-3m
Prototype	$MgZn_2$	Fe_3W_3C
Name	Hexagonal C14 Laves	E93 Structure
Structure	Hexagonal diamond	FCC
Pearson symbol	hP12	cF112
Lattice parameter (Å)	a≈4.89, c≈7.98	a≈11.2

In the as-cast state, VCrFeTa displayed a single-phase hexagonal close-packed crystal structure, specifically the hexagonal C14 Laves structure. After a high-temperature heat treatment (1500 °C for 48 hours) the experimental XRD pattern exhibits a similar hexagonal phase as observed in the as-cast condition. From Figure 6.14, the TCHEA4 database calculates a majority C15 Laves phase over a wide temperature range, in addition to a C14 Laves phase below 500 °C. The C15 Laves phase was also observed in the experimental XRD pattern of the as-cast VCrMnFeTaW. However, the XRD pattern of the 'homogenised' VCrFeTa has indicated the presence of an FCC phase like the C15 Laves phase but with a slightly different structure.

6.6. $V_{0.46}Cr_{0.03}Mn_{0.01}Ta_{0.1}W_{0.4}$

6.6.1. As-Cast

Figure 6.20 shows the XRD pattern of the as-cast VCrMnTaW which displays a single BCC phase analogous to $V_{0.5}W_{0.5}$ [25] with a space group Im-3m (229) and a lattice parameter a≈3.09 Å.

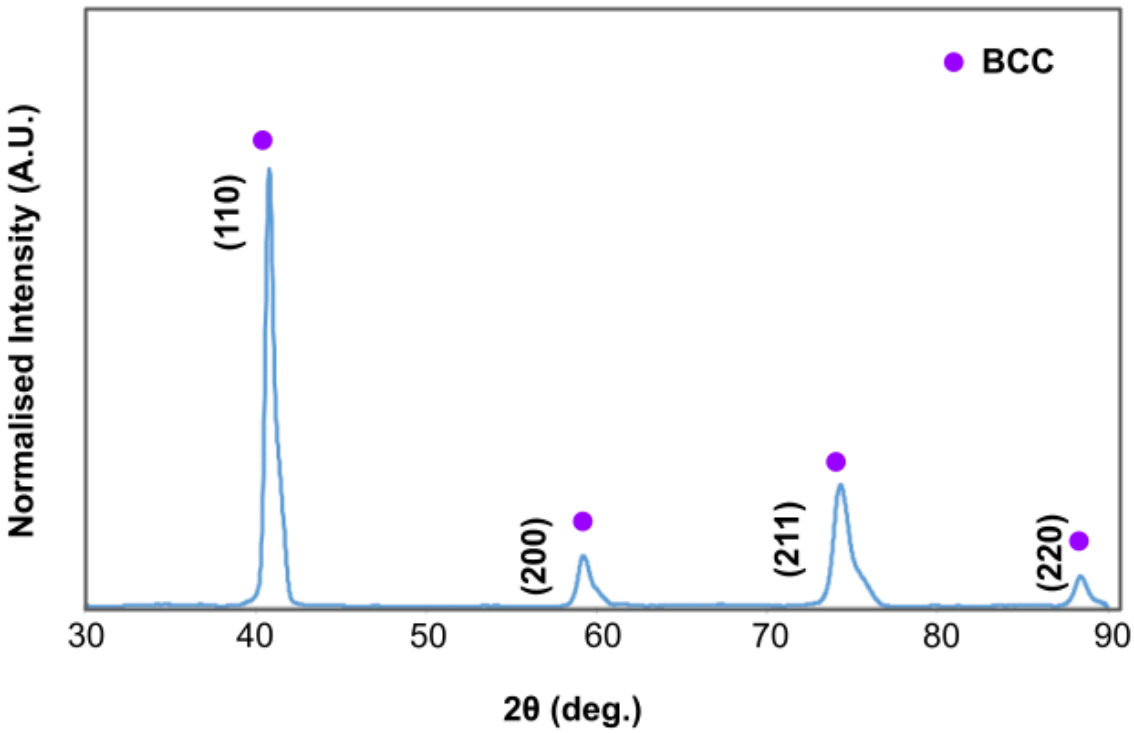

Figure 6.20: XRD pattern of as-cast $V_{0.46}Cr_{0.03}Mn_{0.01}Ta_{0.1}W_{0.4}$

For the as-cast VCrMnTaW alloy, the experimental XRD pattern displays no peak splitting, suggesting a single BCC solid solution phase. However, in the higher theta peaks (75 °) there appears to be a slight 'leaning' shoulder on the peaks suggesting a secondary phase with very similar lattice parameters.

Figure 6.21 shows the Thermo-Calc predictions using the TCHEA4 and SSOL4 database for $V_{0.46}Cr_{0.03}Mn_{0.01}Ta_{0.1}W_{0.4}$. From both databases, the majority phase is the BCC phase (disordered for SSOL4 and ordered for TCHEA4). Minor phases at very low temperatures are also predicted but only in very small quantities, therefore can be discounted.

.

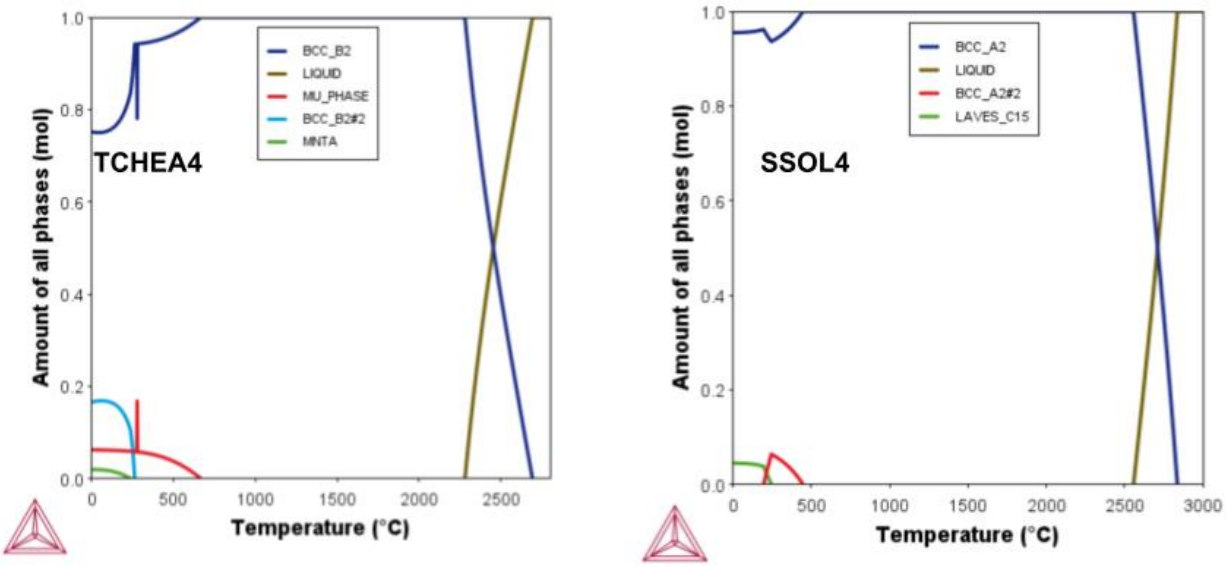

Figure 6.21: The Thermo-Calc predictions for $V_{0.46}Cr_{0.03}Mn_{0.01}Ta_{0.1}W_{0.4}$ using the TCHEA4 and SSOL4 databases

Figure 6.22 presents the SEM-BSE micrographs of the as-cast VCrMnTaW which display the typical dendritic microstructure. These dendrites have a more globular appearance rather than the fine dendritic microstructure of previous alloys in this work (for example from the SEM-BSE micrographs of the as-cast VCrMnFeW). There are also some fine precipitates within the grains which have the same contrast as the black interdendritic regions.

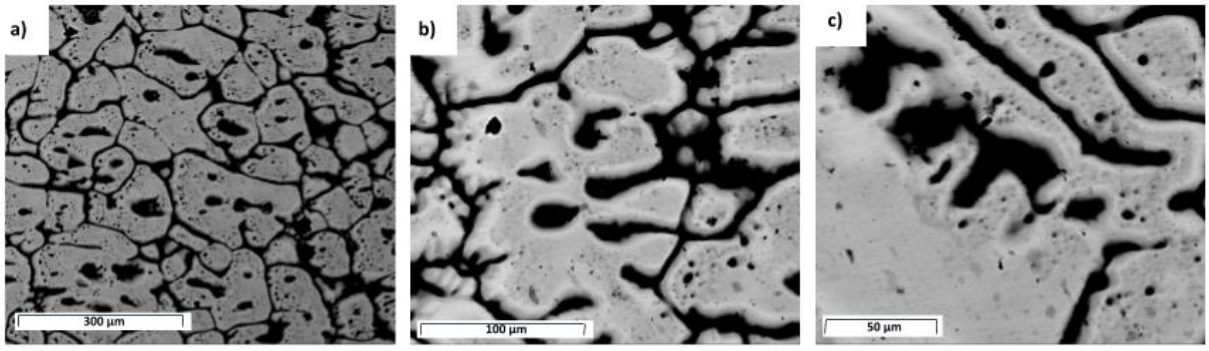

Figure 6.22: SEM-BSE micrograph of the as-cast $V_{0.46}Cr_{0.03}Mn_{0.01}Ta_{0.1}W_{0.4}$ at magnification a) x400 b) x1200 c) x1600

Figure 6.23 exhibits the SEM-EDX elemental maps which present the elemental distribution of the as-cast VCrMnTaW. The black interdendritic regions and the black precipitates appear to be rich in chromium and vanadium whilst the dendrites are abundant in tungsten. From these elemental maps, tantalum and manganese resemble a homogeneous distribution.

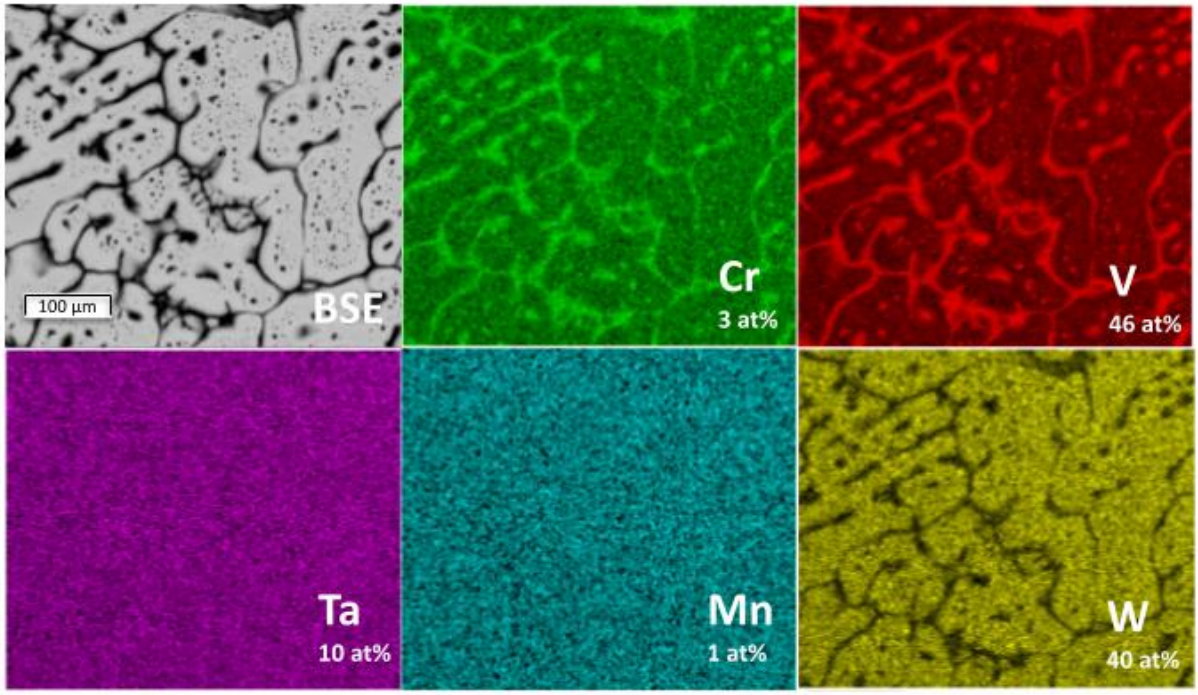

Figure 6.23: SEM-EDX elemental maps of as-cast $V_{0.46}Cr_{0.03}Mn_{0.01}Ta_{0.1}W_{0.4}$ at magnification x600

Whilst the experimental XRD pattern suggests the formation of a single BCC phase, the SEM-EDX elemental maps reveal some elemental microsegregation with two distinct regions of different chemical compositions. This is in disagreement with previous studies where the number of regions of different chemical compositions directly reflects the amount of phases observed in the correlating experimental XRD pattern. However, the 'shoulders' of some of the peaks reveal that a secondary BCC phase with very similar lattice parameters may be apparent. This is typically observed in some of the alloys in this work, for example VCrMoWCo (this is discussed in Chapter 4).

The inverse relationship between vanadium and tungsten as represented by the SEM-EDX elemental maps is apparent in the as-cast alloy VCrMnTaW. The heavier atomic mass (and higher melting point) element, tungsten solidifies in the dendritic regions, whilst vanadium is enriched in the interdendritic regions. This is reflective of the elemental distribution observed in VCrMnFeW after a low heat treatment at 500 for 100 hours. Another prevalent elemental-pairing distribution is the alignment of chromium with the dispersion of vanadium. This compositional dependence is observed across many alloys in the as-cast state and after heat treating (including the as-cast VCrMoW, as-cast and 'homogenised' VCrFeTa, as-cast and 'homogenised' VCrMnFeW, and as-cast and low temperature heat treated VCrFeTaW) and could be due to several reasons. Firstly, the similar melting points of vanadium (1910 °C) and chromium (1907 °C) could result in this elemental attraction of the solidification

microstructures observed (as discussed in Section 6.2: As-Cast Condition of this Chapter). Secondly, the enthalpy of mixing for the binary pair, V-Cr has a fairly low value (-2 kJ/mol) resulting in a strong elemental attraction in the melt pool during fabrication. Finally, the V-Cr binary phase diagram displays an isomorphous system which only forms a BCC phase across all temperatures. This is a similar case as demonstrated by the as-cast VCrMnFeW which displayed a strong V-W formation due to the V-W binary phase diagram having an isomorphous system.

The alloy VCrFeTa in the as-cast state, also displays this typical V-Cr formation, however this alloy in the as-cast and 'homogenised' state also demonstrated microsegregation between vanadium and tantalum. This type of microsegregation between these elements is not apparent in the as-cast state of VCrMnTaW, from the SEM-EDX elemental maps tantalum appeared to be homogenous across the microstructure. This may be due to the difference in the crystalline structures of the phases formed in both of these elements - the as-cast VCrFeTa displayed a single HCP phase in the XRD pattern whilst the as-cast VCrMnTaW demonstrated a single BCC phase. The XRD pattern of the 'homogenised' VCrFeTa revealed an HCP phase and an FCC phase indicating that the single HCP phase was not the most stable form of the alloy. The microsegregation of vanadium and tantalum observed in VCrFeTa may be due to the unstable HCP and FCC phases. Table 6.14 displays the values for the enthalpy of mixing of the binary pairs of elements for VCrFeTa. The most negative values (-15 and -7 kJ/mol) belong to Fe-Ta and Cr-Ta respectively indicating a strong attraction for these elements. This is also reflective of the tendency for the intermetallic compound formation (where the analogous structures are: α Cr_2Ta, β Cr_2Ta, ε $MgZn_2$, and μ Fe_7W_6).

Table 6.14: The values of enthalpies of mixing (kJ/mol) for the binary pairs of elements in VCrFeTa.

	Vanadium	**Chromium**	**Iron**
Chromium	-2		
Iron	-7	-1	
Tantalum	-1	-7	-15

Whilst all of the elemental pairs have negative enthalpy of mixing terms, indicating a favourable attraction during melting between all of the alloy constituents, the ΔH_{mix} for Ta-V (-1 kJ/mol) has one of the smallest magnitude values. During solidification as the dendrites form, due to the high melting point and due to having the smallest magnitude of ΔH_{mix} for Ta-V, tantalum forms in the dendrite bulk whereas vanadium solidifies in the interdendritic regions. Additionally, as the proportion of tantalum in VCrFeTa is much greater (25 at%) compared to

the content in VCrMnTaW (10 at%) this may explain why the exacerbated microsegregation is only observed in VCrFeTa.

Alternatively, a difference between these alloys is the addition of tungsten in VCrMnTaW which may influence the tantalum distribution. As the melt pool cools during the fabrication process, the higher melting point elements tantalum forms in the dendrites and vanadium and manganese solidifies in the interdendritic regions. Due to the similar melting points of tungsten and tantalum (3422 °C and 3017 °C respectively) these elements will solidify in the same dendritic regions. The very negative magnitude of the enthalpy of mixing of Cr-Ta (-7 kJ/mol) also forces the tantalum enrichment of the interdendritic regions (where chromium content is also enhanced). Overall, it could be the balance between these properties that results in the homogenous distribution of tantalum in VCrMnTaW. Interestingly, for both of these alloys the evidence of microsegregation between these elements does not mitigate the single phase crystalline structures of both of these alloys. As previously mentioned in the as-cast VCrFeTa section, Senkov et al [1] reported of a single BCC phase identified by XRD for the equimolar MoNbTaVW despite evidence for microsegregation from the SEM-EDX elemental maps. In this alloy, tantalum was, for the most part, uniformly distributed whilst tungsten solidified first in the dendrite arms and vanadium enriched the interdendritic regions. They attributed the addition of vanadium to the increase in observed microsegregation of tungsten and tantalum in the interdendritic region compared to MoNbTaW. The dependence of the excess concentration of an alloying element inside the dendrite arm with respect to the melting temperature of the element was investigated. It was found that the segregation of an element increases with the increase in ΔT_i (which is the change in temperature between the melting point of the element, i, and the calculated melting temperature of the overall alloy). Therefore, the as-cast alloy MoNbTaW demonstrated that tantalum was homogeneously distributed, and the dendrite arms were enriched in tungsten. On the addition of vanadium, the as-cast MoNbTaVW displayed a finer grain structure and a change in the distribution of elements with tantalum and tungsten showing more segregation from the interdendritic regions (by 7.3 and 2 at% respectively). Whilst this study does not reflect the constituent distribution of the as-cast VCrMnTaW this clearly demonstrates the correlation between an excess/deficiency of an element in the dendritic arm relative to its concentration in the overall alloy composition. All of the alloys in this work contain vanadium and for VCrMnTaW the content of vanadium is the highest (46 at%). However, the as-cast VCrMnTaW displays a homogeneous distribution of tantalum rather than encouraging the segregation of this constituent as suggested by Senkov et al [1]. This suggests that the change in distribution of an element may also depend strongly on the other alloying constituents; this work does not include alloys with niobium or molybdenum due to the high activation of these elements.

Findings from Zhang et al [21] reported that for $Cr_xMoNbTaVW$, increasing the chromium content changed the solidification microstructure from cellular to dendritic and this directly influences the elemental distribution of tantalum. For x=0.5 the as-cast cellular microstructure demonstrated the typical tantalum-vanadium microsegregation where tantalum predominantly solidifies in the cellular region and vanadium settles in the interdendritic region. This alloy demonstrated a single BCC phase in the experimental XRD pattern. Increasing the chromium content, for x=2, the microstructure evolves to be more dendritic in morphology and the same elemental distribution remains but is exacerbated for all elements. The partition coefficient for all of the elements increases where the higher end is represented by tungsten which value close to 12:1. Additionally, CALPHAD modelling predicts phase decomposition occurring for the increased chromium content for this alloy composition which is reflected in the XRD pattern where a secondary BCC is detected. In this work the small content of chromium (3 at%) of VCrMnTaW may reflect the homogeneously distributed tantalum (K=1.13). The elemental distribution of VCrMnTaW in the as-cast state also reflects that for $Cr_xMoNbTaVW$: tungsten is abundant in the dendrite arms (K=4.31) whereas the interdendritic region is enriched mostly in chromium (K=0.33) and then vanadium (K=0.45). The globular dendrites of the as-cast VCrMnTaW may also explain the homogeneously distributed tantalum, as they best reflect the morphology of the cellular structure of $Cr_{0.5}MoNbTaVW$ and this is comparable by the similar partition coefficients of tantalum in both alloys (K=1.14 for $Cr_{0.5}MoNbTaVW$ and K=1.13 for VCrMnTaW). For $Cr_xMoNbTaVW$, the increasing content of chromium was correctly predicted to destabilised the BCC phase by the predicted formation of a C15 Laves phase. Similarly, for this work, the alloy VCrMnTaW (as with VCrFeTa) was predicted to form the C15 Laves phase and Cr_3Mn_5 in the equimolar compositions where the chromium content was sufficiently high enough to promote these secondary phases (this is discussed in Chapter 5: Alloy Design).

Table 6.15 lists the elemental compositions of the regions of the as-cast VCrMnTaW composed from the SEM-EDX point scans. These results show the vanadium enrichment in the black interdendritic regions and the tungsten enrichment in the white dendritic region. Whilst both regions are multicomponent in nature and vary in chemical composition, the Thermo-Calc predictions for both regions indicated the formation of a stable single BCC phase.

Table 6.15: Elemental concentrations (at%) of the two different regions of the VCrMnTaW alloy in the as-cast state using SEM-EDX point scans (averaged from 5 separate point scans from each region). The corresponding Thermo-Calc predictions of the equilibrium phases for each regional composition are also stated. The averaged XRF values of the overall VCrMnTaW composition is included for comparison.

	White (at%) Dendritic arms	**Black (at%) Interdendritic region**	**$K=C_{da}/C_{idr}$**	**Overall Alloy (at%)**
V	33±2.5	73±4.2	0.45	46
Cr	20±0.2	6±0.7	0.33	3
Mn	0.1±0.06	0.1±0.06	-	1
Ta	9±0.2	8±0.4	1.13	10
W	56±2.5	13±4.5	4.31	40
Thermo-Calc predictions (SSOL4)	BCC A2	BCC A2		BCC A2

The Thermo-Calc calculations are formed using the experimental SEM-EDX elemental compositions for the distinct regions and correlate with the experimental XRD pattern of the as-cast VCrMnTaW which display a single BCC phase. Additionally, structure that was analogous to the peaks in the experimental XRD pattern, $V_{0.5}W_{0.5}$ [25] reflects the relative chemical composition of the alloy.

As previously mentioned in Section: as-cast VCrFeTa, the partition coefficients, K, for each element was calculated using the SEM-EDX point scan averages of each region of the alloy. Tungsten has the highest value (4.31) and this is reflected in the SEM-EDX elemental maps where tungsten is enriched in the dendrite arms. Tantalum has a value ~1 which confirms the homogenous distribution between both regions.

6.6.2. 700 °C, 100 hours

A higher temperature homogenisation heat treatment was unavailable for VCrMnTaW however; two lower temperature heat treatments were applied.

Figure 6.24 shows the SEM-BSE micrographs for VCrMnTaW heat treated at 700 °C for 100 hours. The morphology of the dendrites, for the most part, remains from the as-cast sample. The dendritic region appears to be slightly finer in the heat treated sample (with an average 50-100 μm in length), though this may just be due to the inhomogeneity of the cooling rates within the fabrication process.

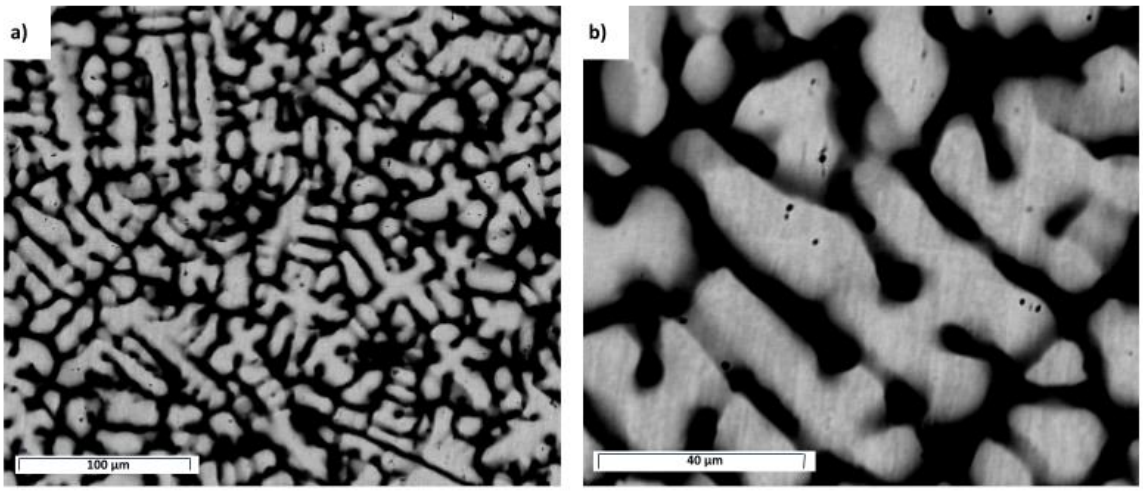

Figure 6.24: SEM-BSE micrograph of $V_{0.46}Cr_{0.03}Mn_{0.01}Ta_{0.1}W_{0.4}$ heat treated at 700 °C for 100 hours at magnification a) x900 b) x3000

Figure 6.25 displays the SEM-EDX elemental maps showing the chemical distribution of the heat treated VCrMnTaW. As with the as-cast sample, the chromium-vanadium enrichment in the interdendritic regions remains alongside the segregation of tungsten in the dendritic regions. Tantalum and manganese distribution is again evenly dispersed throughout.

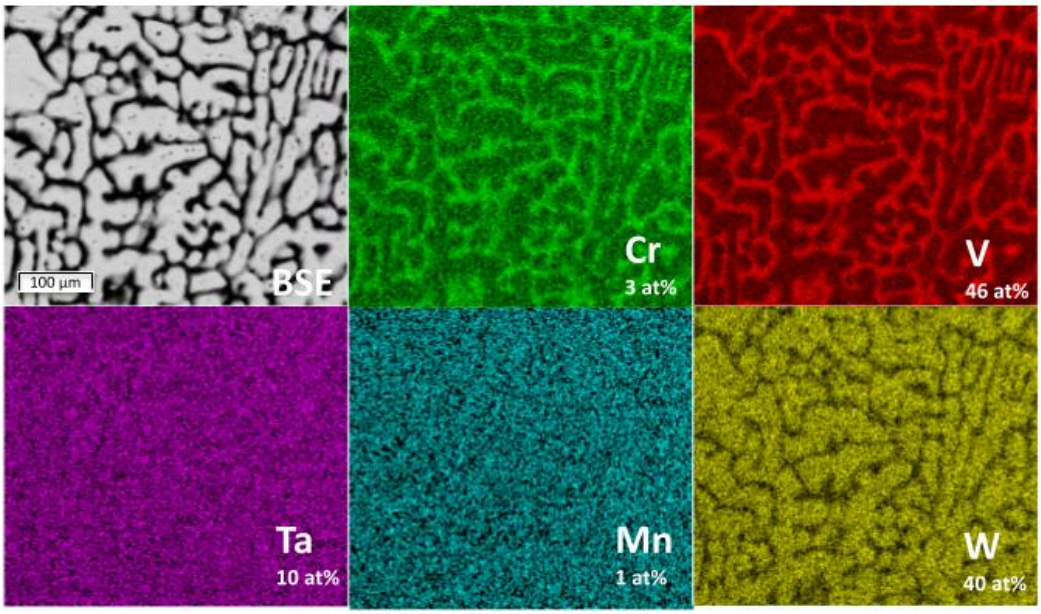

Figure 6.25: SEM-EDX elemental maps of $V_{0.46}Cr_{0.03}Mn_{0.01}Ta_{0.1}W_{0.4}$ heat treated at 700 °C for 100 hours at magnification x1000

Figure 6.26 shows the experimental XRD pattern of VCrMnTaW heat treated at 700 °C for 100 hours. The XRD pattern match with the same structure in the as-cast state: a single BCC phase analogous to $V_{0.5}W_{0.5}$ [25] with a space group Im-3m (229) and a lattice parameter a≈3.09 Å.

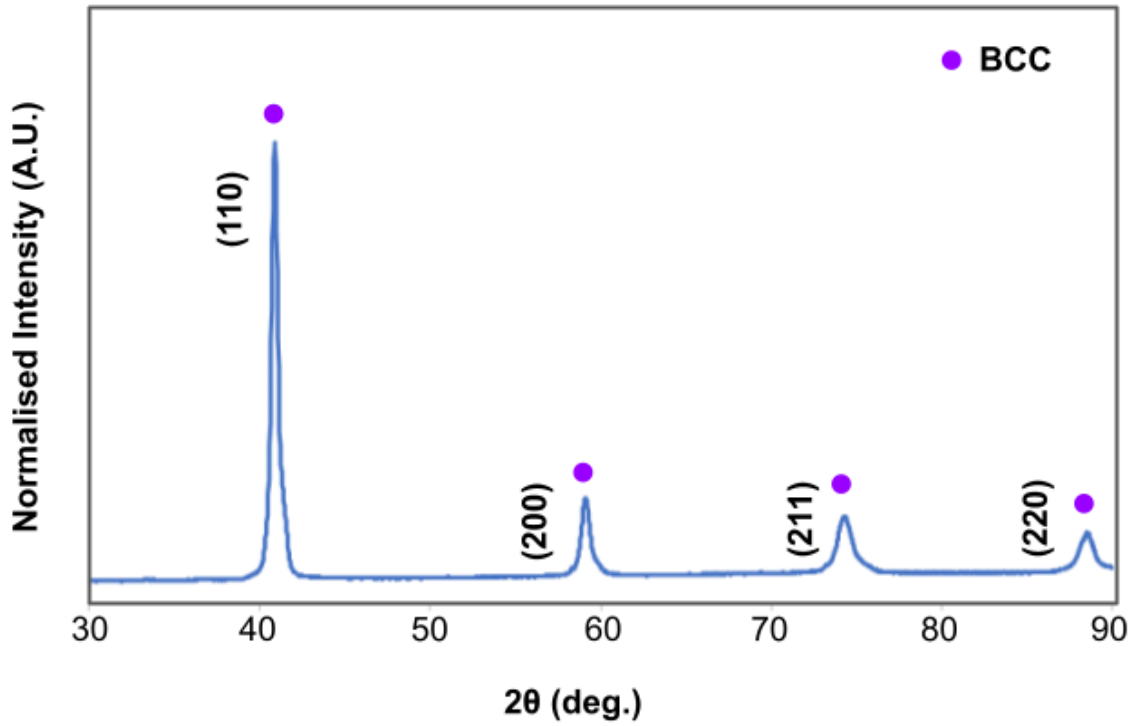

Figure 6.26: XRD pattern of $V_{0.46}Cr_{0.03}Mn_{0.01}Ta_{0.1}W_{0.4}$ heat treated at 700 °C for 100 hours

Overall, there appears to be no change in the microstructure or phases of the heat treated VCrMnTaW.

6.6.3. 500 °C, 100 hours

Figure 6.27 shows the SEM-BSE micrograph for VCrMnTaW heat treated at 500 °C for 100 hours. The morphology of the dendrites appears to be of the same size and structure as from the as-cast sample.

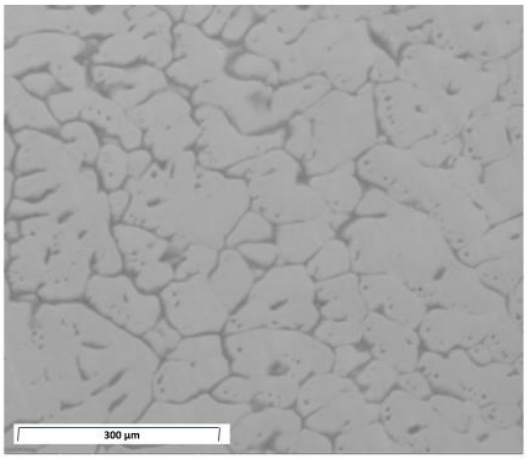

Figure 6.27: SEM-BSE micrograph of $V_{0.46}Cr_{0.03}Mn_{0.01}Ta_{0.1}W_{0.4}$ heat treated at 500 °C for 100 hours at magnification x400

Figure 6.28 displays the SEM-EDX elemental maps showing the distribution of the elements in the heat treated VCrMnTaW. The same constituent microsegregation appears as the as-cast and VCrMnTaW heat treated at 500 °C for 100 hours. V-Cr enrichment occurs in the interdendritic regions and segregation of tungsten in the dendrites occurs. Tantalum and manganese distribution is again evenly dispersed throughout.

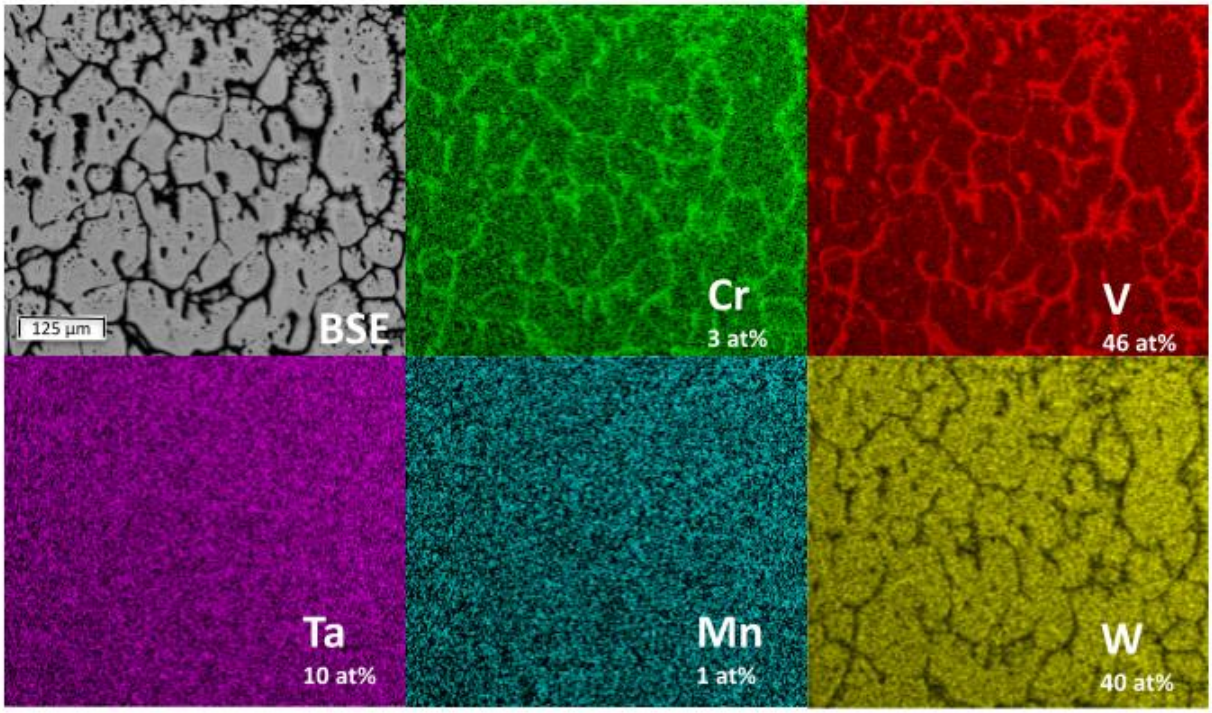

Figure 6.28: SEM-EDX elemental maps of $V_{0.46}Cr_{0.03}Mn_{0.01}Ta_{0.1}W_{0.4}$ heat treated at 500 °C for 100 hours at magnification x1000

Table 6.16 presents the SEM-EDX point scans of the dendritic and interdendritic regions showing the elemental compositions in these areas. The SEM-EDX point scans of the heat-treated reveal that the compositions of the two regions are the same as in the as-cast state.

Table 6.16: Elemental concentrations (at%) of the two different regions of the VCrMnTaW alloy heat-treated at 500 °C for 100 hours using SEM-EDX point scans (averaged from 5 separate point scans from each region). The corresponding Thermo-Calc predictions of the equilibrium phases for each regional composition are also stated. The averaged XRF values of the overall VCrMnTaW composition is included for comparison.

	White region (at%)	Black region (at%)	Overall Alloy (at%)
V	38±0.5	76±2.5	46
Cr	2±0.2	5±0.3	3
Mn	-	-	1
Ta	9±0.4	8±0.1	10
W	58±0.5	11±2.6	40
Thermo-Calc predictions (SSOL4)	BCC A2	BCC A2	BCC A2

Figure 6.29 shows the experimental XRD pattern of the VCrMnTaW heat treated at 500 °C for 100 hours. The pattern exhibited the same single BCC phase analogous to $V_{0.5}W_{0.5}$ [25] with a space group Im-3m (229) and a lattice parameter a≈3.09 Å.

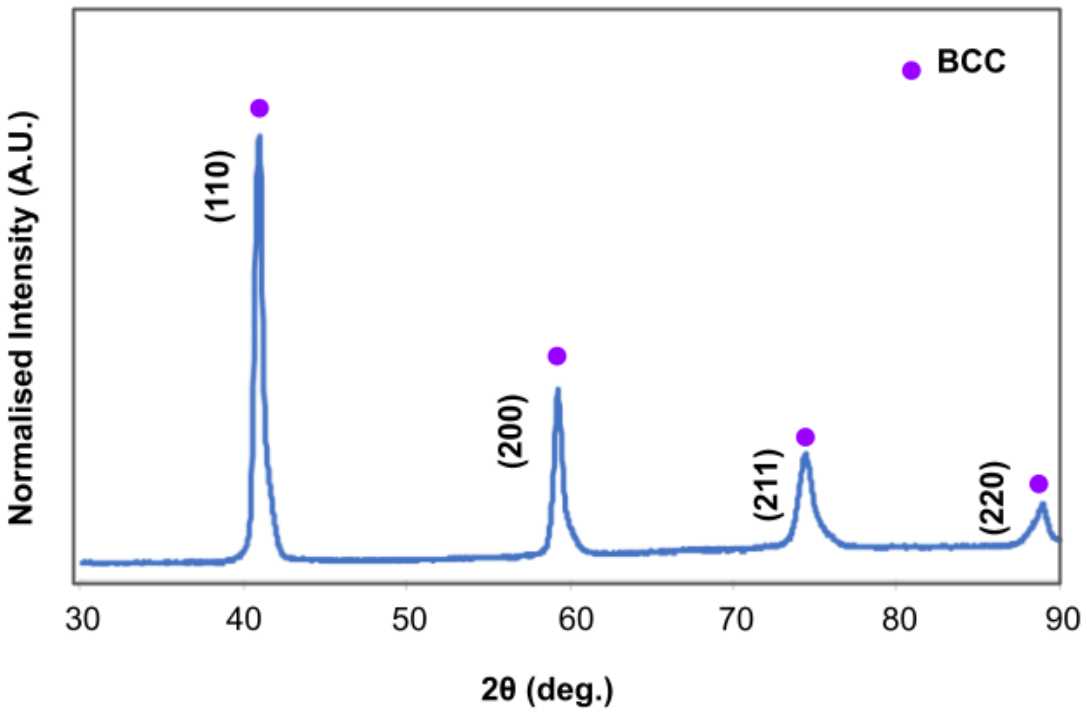

Figure 6.29: XRD pattern of $V_{0.46}Cr_{0.03}Mn_{0.01}Ta_{0.1}W_{0.4}$ heat treated at 500 °C for 100 hours

This single BCC phase remained after both heat treatments matching the same structure. Whilst there is no change at the lower temperature heat treatments, a higher temperature homogenisation heat treatment is still required to ascertain if a single phase BCC matrix is still stable at elevated temperatures. Due to the unintentional evaporation of chromium and manganese the overall entropy of the alloy composition of VCrMnTaW has dramatically decreased and so may not be an ideal candidate for the evaluation of high entropy alloy properties.

6.7. $V_{0.36}Cr_{0.18}Fe_{0.08}Ta_{0.17}W_{0.21}$

6.7.1 As-Cast

Figure 6.30 displays the SEM-EDX elemental maps which show the elemental distribution within the microstructure. From these elemental maps there is segregation between the constituent elements with areas rich in chromium, iron, and vanadium and opposing areas of segregated tungsten dispersed between these elements. Tantalum appears to be distributed evenly

across the alloy with a small amount concentrated in the regions of high vanadium.

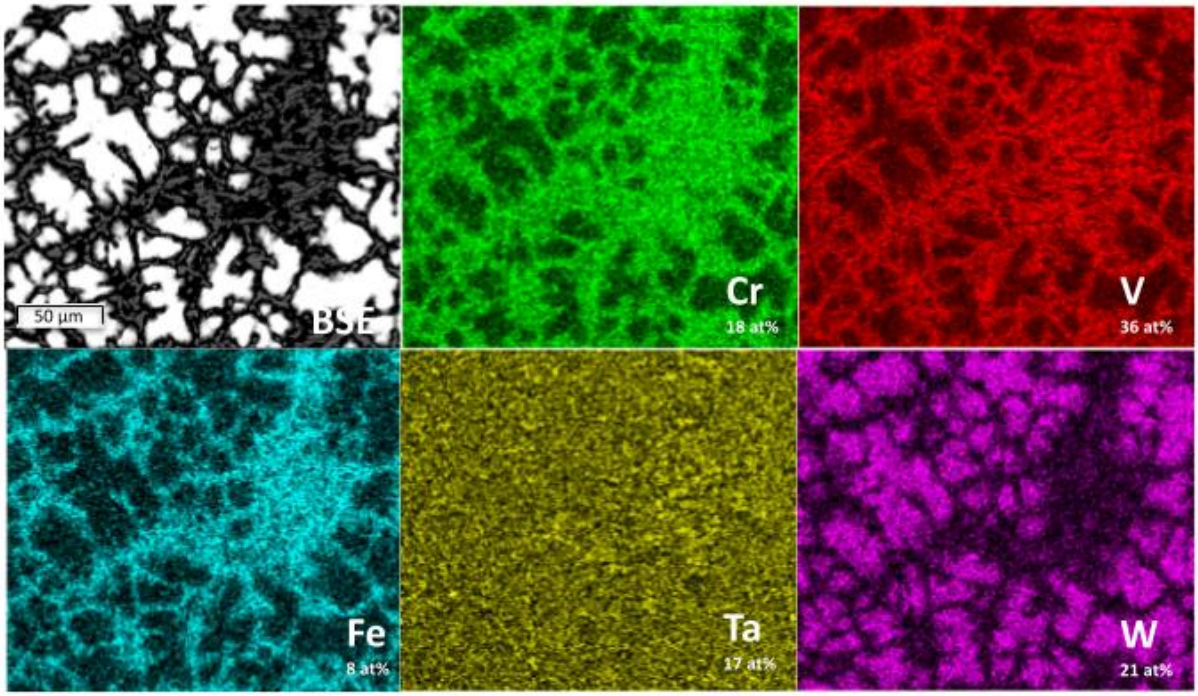

Figure 6.30: SEM-EDX elemental maps of the as-cast $V_{0.36}Cr_{0.18}Fe_{0.08}Ta_{0.17}W_{0.21}$ at magnification x1300

Figure 6.31 shows the XRD pattern of the as-cast VCrFeTaW and is revealed to have three separate BCC phases (space group Im-3m) with very similar lattice parameters (a≈3.16 Å, a≈3.02 Å, a≈2.09 Å).

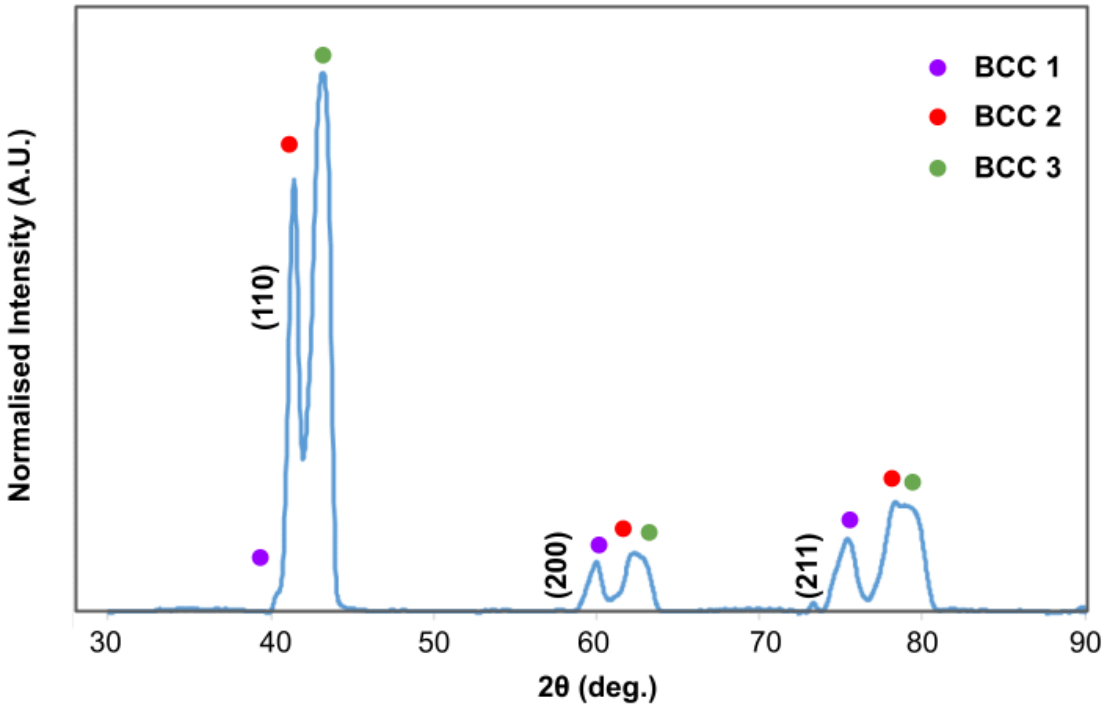

Figure 6.31: XRD pattern of as-cast $V_{0.36}Cr_{0.18}Fe_{0.08}Ta_{0.17}W_{0.21}$

A summary of these phases can be observed in Table 6.17. The analogous structures which best fit the three sets of peaks shown in the as-cast XRD pattern complement the elemental segregation observed in the SEM-EDX: pure W [26], $Ta_{0.09}V_{0.91}$ [27], and $Cr_{0.4}Fe_{0.2}V_{0.4}$ [28].

Table 6.17: The three analogous structures which best match the three sets of peaks displayed in the as-cast VCrFeTaW XRD pattern.

	BCC1	**BCC2**	**BCC3**
Composition	W	$Ta_{0.09}V_{0.91}$	$Cr_{0.4}Fe_{0.2}V_{0.4}$
Lattice parameter	a≈3.16	a≈3.02	a≈2.09
Space Group	Im-3m (229)	Im-3m (229)	Im-3m (229)

An intriguing comparison can be made for the experimentally obtained lattice parameters of both the as-cast states of VCrFeTaW and VCrMnFeTaW. The approximate lattice parameters of the three BCC phases determined by the XRD analysis of the as-cast VCrFeTaW are

a≈3.16 Å, a≈3.02 Å, and a≈2.09 Å. The approximate lattice parameters of the three FCC phases determined by the XRD analysis of the as-cast VCrMnFeTaW are a ≈6.43 Å, a≈6.30 Å, and a≈6.95 Å. It appears that the addition of manganese to VCrFeTaW increases the lattice parameter by an average of 138 %. It is speculated that the increase in the overall alloy atomic size difference (from 4.7 % to 5.2 %) on the addition of approximately 1 at% of manganese (which has an atomic radii of 0.135 nm) is responsible for the expansion of the cubic lattice parameter. However, the difference between the crystal structures of these alloys must also be taken into consideration. The transformation from three similar BCC phases to three FCC of slightly varying lattice structures may be an effect of the atomic mismatch from accommodating an element with a relatively large atomic radius. This coincides with the results found by Tan et al [29] who observed the expansion of lattice parameters by 1.33 % with the addition of manganese to the high entropy alloy, CrFeCoNi. They attributed the increasing lattice parameter to not only the accommodation of a larger atomic radius element, but also due to the chemical complexity of the high entropy alloy.

Figure 6.32 shows the Thermo-Calc predictions for $V_{0.36}Cr_{0.18}Fe_{0.08}Ta_{0.17}W_{0.21}$ using the TCHEA4 and SSOL4 databases. As with the other alloys in this work, the dominant phase has a BCC crystal structure (ordered for TCHEA4 and disordered for SSOL4) stable at higher and intermediate temperatures. At lower temperatures the TCHEA4 database predicts a C15 Laves phase and small additions of μ phases (below 0.2 mol). For the SSOL4 database, moderate amounts of a σ phase and a C15 Laves phase is predicted.

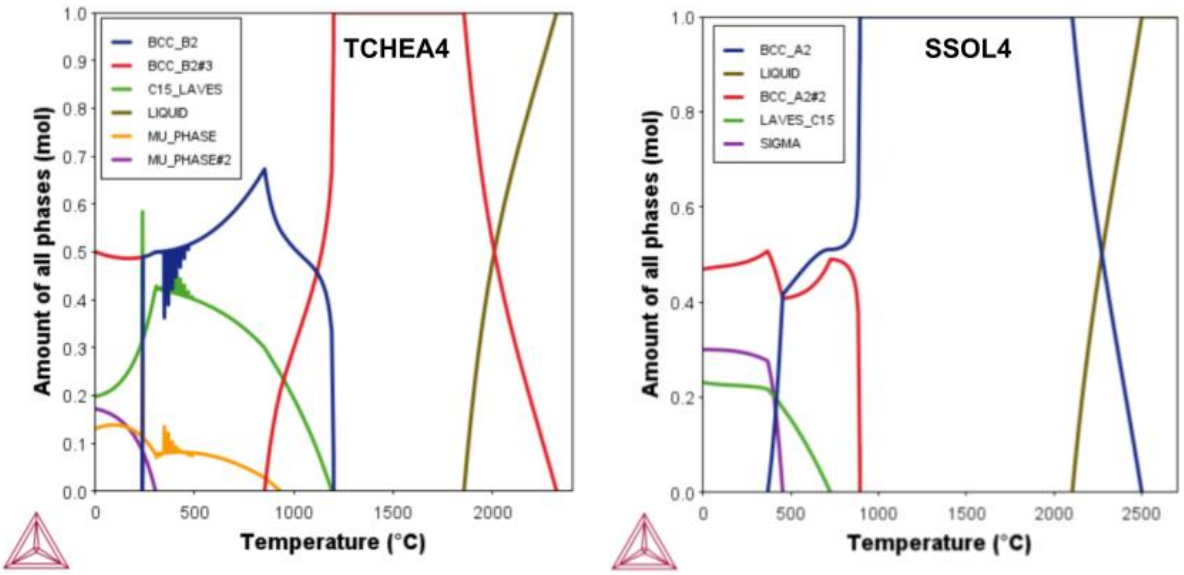

Figure 6.32: The Thermo-Calc predictions for $V_{0.36}Cr_{0.18}Fe_{0.08}Ta_{0.17}W_{0.21}$ *using the TCHEA4 and SSOL4 databases*

The dominant BCC phase predicted by both databases may account for the observed BCC phases identified by the experimental XRD pattern.

Figure 6.33 shows the SEM-BSE micrographs of the as-cast VCrFeTaW which also confirm the three regions of segregation which are represented by areas of black, dark grey, and white contrast.

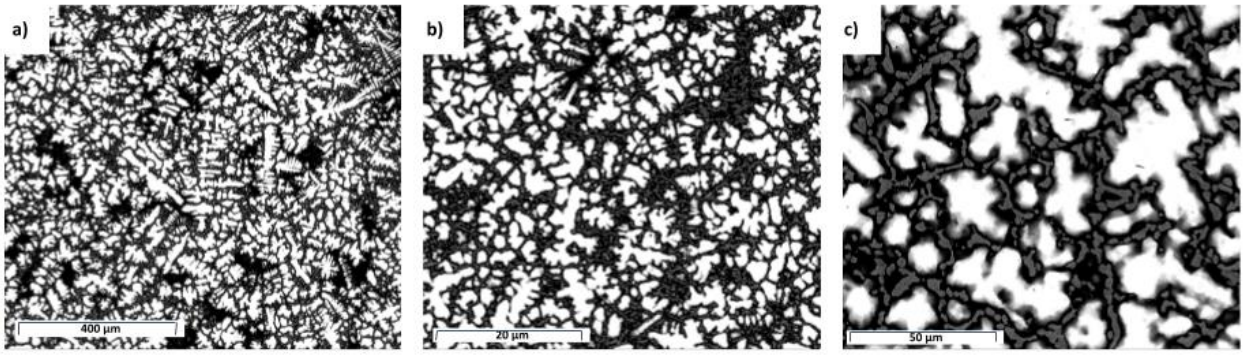

Figure 6.33: SEM-BSE micrograph of as-cast $V_{0.36}Cr_{0.18}Fe_{0.08}Ta_{0.17}W_{0.21}$ *at magnification a) x300, b) x500, and c) x2000*

VCrFeTaW is one of the alloys in this work that did not exhibit a dendritic microstructure in the as-cast state. However, instead of possessing a single-phase grain microstructure, there are areas of elemental segregation as shown by the contrast in the SEM-BSE micrographs. The black and dark grey regions display a fine phase separation, characteristic of a needle-type microstructure, that occurs in between the white zones which are more globular in appearance. The areas which are brighter, in contrast, contain a greater proportion of higher atomic number elements, including tungsten, and the areas which are darker contain an increased proportion of lower atomic number elements, including vanadium. Using the SSOL4 predictions of the overall composition of VCrFeTaW, two disordered BCC equilibrium phases are expected to occur. The additional phase observed in the experimental XRD of the as-cast alloy may be attributed to the pure W phase which is most likely to be the third BCC phase due to elemental tungsten having a BCC crystal structure.

6.7.2. 1500 °C, 48 hours

Figure 6.34 displays the SEM-BSE micrographs of VCrFeTaW after annealing at 1500 °C for 48 hours. Much like in the as-cast condition, there are three distinct regions of contrast: black, grey, and white.

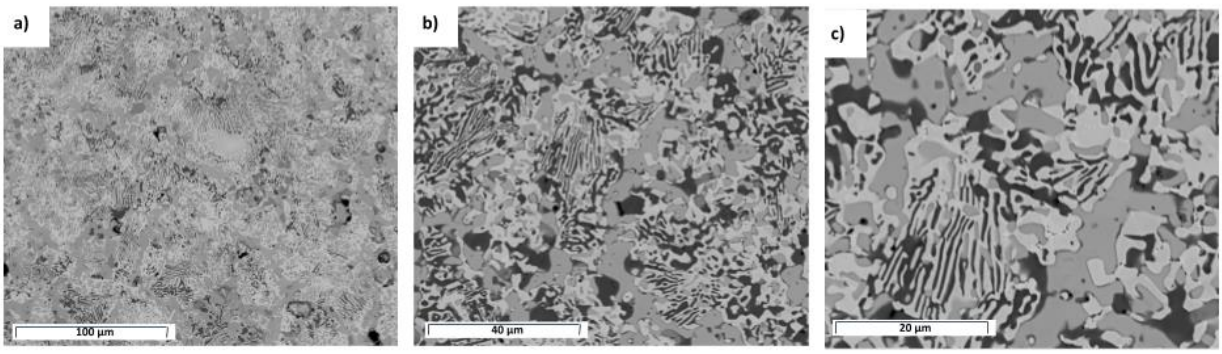

Figure 6.34: SEM-BSE micrograph of $V_{0.36}Cr_{0.18}Fe_{0.08}Ta_{0.17}W_{0.21}$ *heat treated at 1500 °C for 48 hours at magnification a) x1200, b) x3000, and c) x6000*

The morphology of these different regions retains the needle-type microstructure of the as-cast alloy. However, after the high-temperature heat treatment, a lamellar-like formation has spread from its localised regions in between and around the brighter grains and has instead formed a basis of the granular structure. Table 6.18 presents the elemental compositions of the three regions observed in the SEM-BSE micrographs and shows that each region is multicomponent in nature with some areas having enhanced concentrations of certain elements whilst being depleted in others.

Table 6.18: The elemental compositions (at%) of different regions within the 'homogenised' VCrFeTaW alloy using SEM-EDX point scans (averaged from 5 separate point scans from each region). The corresponding Thermo-Calc predictions of the equilibrium phases for each regional composition are also stated. The averaged XRF values of the overall VCrFeTaW composition is included for comparison.

	White region (at%)	**Grey region (at%)**	**Black region (at%)**	**Overall Alloy (at%)**
V	23±1.0	18±0.7	82±1.9	36
Cr	8±0.2	12±0.4	5±0.2	18
Fe	2±0.1	29±0.8	0.7±0.2	8
Ta	9±0.6	36±0.2	11±0.3	17
W	58±1.5	5±0.5	2±1.1	21
Thermo-Calc predictions (SSOL4)	BCC A2 σ C15 Laves	BCC A2 σ C15 Laves	BCC A2 C15 Laves	BCC A2

In the homogenised state, VCrFeTaW displays the typical segregation between vanadium and tantalum also observed in VCrFeTa. Additionally, in the as-cast state, the VCrFeTaW alloy displayed a fairly homogeneous spread of tantalum, however, after a high-temperature heat

treatment (1500 °C for 48 hours) elemental segregation is exacerbated and is reduced (11 at%) in areas of high vanadium (82 at%) concentration (i.e. the black region).

Figure 6.35 shows the SEM-EDX elemental maps for the ‘homogenised’ VCrFeTaW which displays the microsegregation between different constituents.

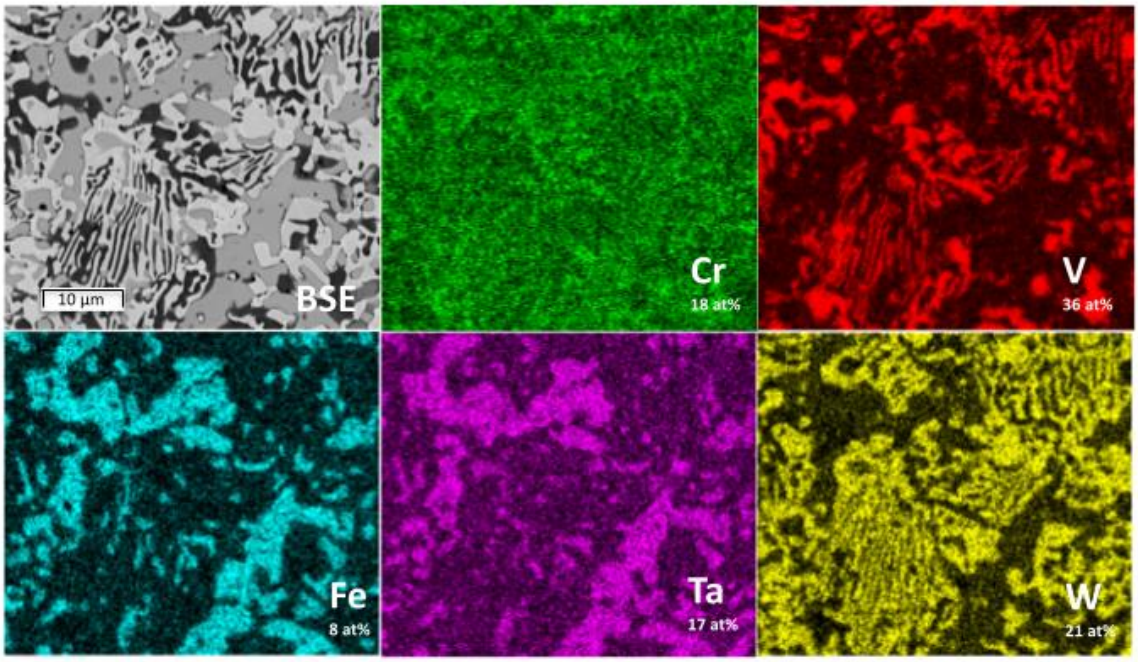

Figure 6.35: SEM-EDX elemental maps of V0.36Cr0.18Fe0.08Ta0.17W0.21 *heat treated at 1500 °C for 48 hours* at magnification x6000

Figure 6.36 shows the experimental XRD pattern of the ‘homogenised’ VCrFeTaW which also reflects the three different regions observed in the SEM-BSE micrographs. The XRD pattern appears to match three different crystal structures: a tetragonal crystal structure, an FCC phase, and a primitive phase (denoted by green circle, blue triangle, and red square respectively).

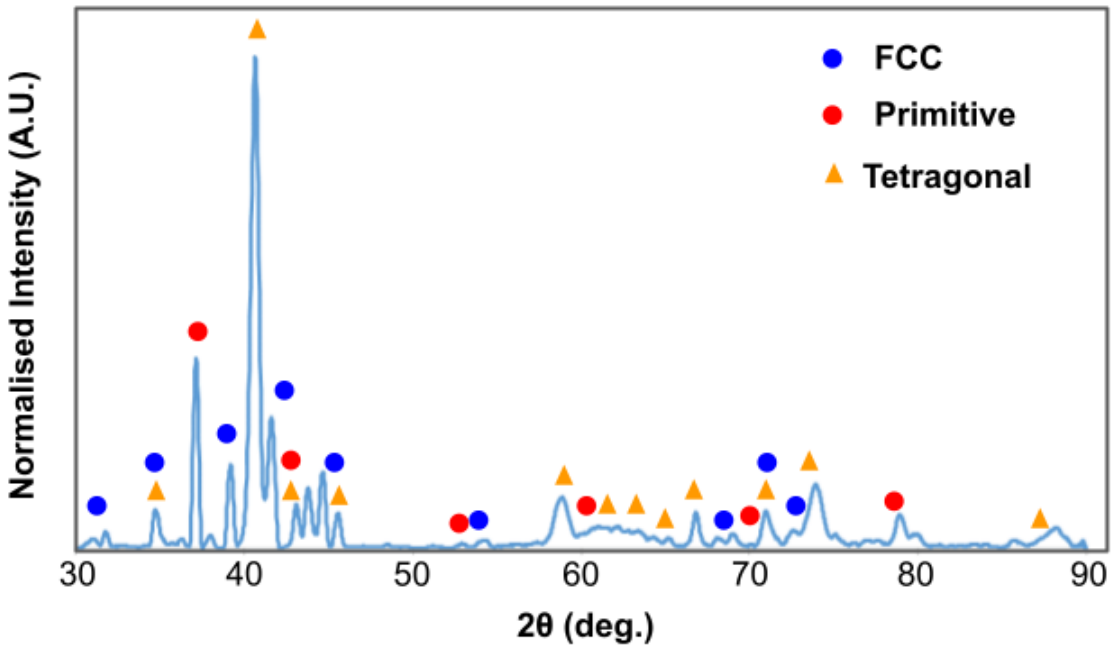

Figure 6.36: XRD pattern of $V_{0.36}Cr_{0.18}Fe_{0.08}Ta_{0.17}W_{0.21}$ heat treated at *heat treated at 1500 °C for 48 hours*

The analogous structures of these phases and their corresponding lattice parameters are listed in Table 6.19. The tetragonal phase was analogous to YZn_{12} [30], the FCC phase was analogous to Ni_2W_4C [31], and the primitive phase was analogous to $Ba(YNbO_6)_{0.5}$ [32].

Table 6.19: The XRD analysis of the experimental peaks of the 'homogenised' VCrFeTaW, which matched with three different analogous structures and corresponded to the following parameters.

	Tetragonal	**FCC1**	**Primitive1**
Prototype	Mn12Th (D2b) structure	Fe_3W_3C (E93 Structure)	Cubic Perovskite (E21 Structure)
Lattice parameter	a≈8.88, c≈5.13	a≈11.25	a≈4.20
Pearson Symbol	tI26	cF112	cP5
Space Group	I4/mmm (139)	Fd-3m (227)	Pm-3m (221)

Much like in the as-cast condition, the number of phases represented in the 'homogenised' SEM-BSE micrographs correlate with the number of phases identified in the 'homogenised' XRD pattern. However, identifying which phases correspond to the regions in the microstructure proved to be problematic. The structure analogous to the phases established in the XRD pattern did not correspond to the constituent elements in the alloy - their crystallographic positions merely mimic the peaks represented in the experimental XRD pattern. To determine the stable phases likely to form in each region observed in the SEM-

BSE micrographs, Thermo-Calc analysis was carried out on the SEM-EDX point scan elemental at% averages. These findings are represented in Table 6.18 where property diagrams were calculated for the three contrasting regions identified in the SEM-EDX point scans. Each of the three regions are predicted to form a majority BCC phase across a range of temperatures with small amounts of secondary phases at lower temperatures. These results are discussed in further detail in the next section. However, it is clear that the Thermo-Calc predictions of the regional compositions do not necessarily correlate with the 'homogenised' alloy XRD observations and further analysis is required.

The Thermo-Calc predictions using the SSOL4 database for the experimental composition of VCrFeTaW (Figure 6.32) suggests the formation of 0.2 - 0.3 mol of both a σ and C15 Laves phase at lower temperatures below 1000 °C. These phases directly correspond to the observed phases from the 'homogenised' experimental XRD data denoted in Table 6.19. As mentioned previously, the σ phase can be compared to the tetragonal I4/mmm (139) crystal structure and the C15 Laves phase is related to the cubic Fd-3m (227) phase (denoted as the FCC phase). However, it is important to note that the FCC phase identified by XRD has a slightly different lattice structure to the C15 Laves phase. Both the FCC phase identified by XRD and the C15 Laves phase predicted from the overall composition of VCrFeTaW using Thermo-Calc both have the same space group Fd-3m. However, the XRD phase is based on the Fe_3W_3C (E93) structure with a Pearson symbol of cF112 (unlike the C15 Laves phase which has a Pearson symbol of cF24 and is analogous to the Cu_2Mg structure) and so there is a small difference in the atomic positions within the lattice much like the homogenised VCrFeTa Fd-3m phase.

Table 6.20 shows the Thermo-Calc predictions for the constituents of the C15 Laves phase and the σ phase for $V_{0.36}Cr_{0.18}Fe_{0.08}Ta_{0.17}W_{0.21}$ using the SSOL4 database.

Table 6.20: Thermo-Calc predictions of the elemental concentrations of the C15 Laves phase and the σ phase for $V_{0.36}Cr_{0.18}Fe_{0.08}Ta_{0.17}W_{0.21}$.

Phase	Amount of component in the phase from the largest concentration to smallest
C15 Laves phase	Cr>Ta
σ phase	V>Fe>Cr

Specifically, Thermo-Calc predicts the C15 Laves phase to be composed primarily of chromium and tantalum and the σ phase to be predominantly vanadium and iron with small

amounts of chromium. However, these elemental proportions are not reflective of the regional compositions calculated from SEM-EDX point scans listed in Table 6.18 and so further analysis is required.

Secondly, using the regional compositions from the 'homogenised' alloy and inputting the SEM-EDX point scans of the different regions (Table 6.18), Thermo-Calc can be used to predict the possible equilibrium phases that may occur. The grey and white regions are expected to have a small amount of a σ and C15 Laves phase at lower temperatures whilst the black region is only predicted to have a negligible amount of C15 Laves phase. The primitive crystal structure identified by the XRD analysis is not incorporated in the SSOL4 database but does appear in the TCHEA4 database under ALFESI_TAU3, ALTI3N_E21, and TI3ALC_E21. These phase constituents are composed of their respective elements (i.e. aluminium, iron, silicon, titanium, nitrogen, and carbon). Aside from iron, none of these elements are present in VCrFeTaW and so this may be the reason for the lack of prediction of the Fd-3m phase.

However, regardless of the chemical stoichiometry, the XRD analysis takes into consideration a wider range of crystallographic structures with structures that are analogous and not necessarily composed of the same constituent elements. The XRD pattern matching with the FCC phase is analogous with Ni_2W_4C and suggests that the elements are comparatively positioned in the lattice structure. Whilst for the as-cast VCrFeTa alloy, the single hexagonal phase PDF card had a high GOM value, not all the PDF cards in this study matched with such a high degree of confidence. Therefore, it can be concluded that similar PDF cards, with the same space group but with slightly differing atomic positions, may also match the experimental XRD pattern.

From Table 6.19, the black region is the only area completely devoid of iron and is predominant in vanadium (82 at%) and tantalum (11 at%) with very small amounts of chromium (5 at%) and tungsten (2 at%). Evaluation of the Ta-V binary phase diagram suggests the formation of an αTaV_2 intermetallic compound (with a space group of Fd-3m and Pearson symbol cF24) which has the prototype Cu_2Mg with a cubic C15 Laves phase structure. This lattice structure is like the Fd-3m phase identified by the experimental XRD (as previously discussed) and coincides with the Thermo-Calc prediction of the regional composition. This indicates that the black region could potentially be the Fd-3m phase. However, the grey region, composed of almost equal proportions of V (18 at%), Cr (12 at%), Fe (29 at%), and Ta (36 at%) is also a candidate for the FCC phase. Much like the homogenised VCrFeTa alloy, the high entropy of this phase composition has the potential to drive the formation of the Fd-3m FCC phase.

However, the depletion of tantalum in the homogenised VCrFeTa and the enrichment of tantalum in this homogenised alloy suggests that this grey phase may not be the FCC phase. Instead, it can be hypothesised that the grey region is likely to be the tetragonal crystalline phase, also named the σ phase, with a space group I4/mmm (139). In this alloy, the σ phase is composed of a near-equimolar concentration of tantalum, iron, vanadium, and chromium. As previously discussed, work by Krapivka and Firstov [19] hypothesised that increasing the number of components that are likely to form a σ phase (i.e. σ phase forming pairs like V-Mn, V-Fe, Cr-Mn, Cr-Fe, etc.) the more likely a larger proportion of the σ phase will precipitate in the alloy. The grey region has the highest concentration of vanadium, chromium, and iron all of which readily form a σ phase and so it can be concluded that this region is likely to be a multi-principal element σ phase.

As a result, the white region is identified as the primitive phase (with space group Pm-3m) analogous to the $Ba(YNbO_6)_{0.5}$ structure (Pearson symbol of cP5). The space group Pm-3m is also shared with the ordered BCC B2 structure (with a cP2 Pearson symbol) which shares a primitive-type structure. The ordered B2 BCC phase is consistently predicted by the TCHEA4 database of Thermo-Calc to be a stable equilibrium phase for all of the high entropy alloys in this study (this is discussed in Chapter 5: Alloy Design). As previously discussed, some of the insufficiencies arising in the XRD analysis of peak matching may result in the inaccurate prediction of the specific crystalline structure. Therefore, the primitive Pm-3m identified by the experimental XRD pattern may be analogous to an ordered BCC B2 phase.

6.7.3. 500 °C, 100 hours

Figure 6.37 exhibits the SEM-BSE micrographs of VCrFeTaW annealed at 500 °C for 100 hours. The micrographs exhibit a white grain-like structure with black and grey needle-like precipitation in the grain boundaries.

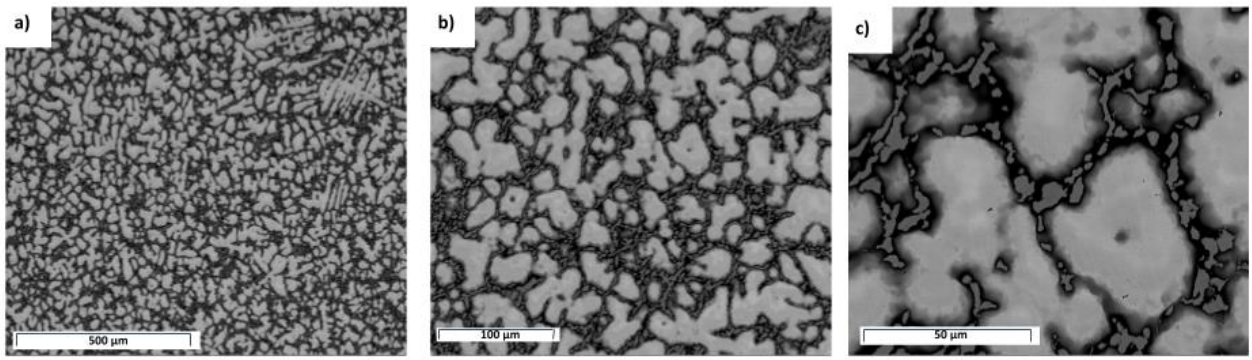

Figure 6.37: SEM-BSE micrograph of $V_{0.36}Cr_{0.18}Fe_{0.08}Ta_{0.17}W_{0.21}$ *heat treated at 500 °C for 100 hours at magnification a) x1200, b) x3000, and c) x6000*

Figure 6.38 shows the SEM-EDX elemental maps collected for VCrFeTaW annealed at 500 °C for 100 hours. Typical of other alloys investigated in this work, vanadium and chromium show preference for enriching the boundaries surrounding the ‘grains’, whilst the grains are higher in tungsten content.

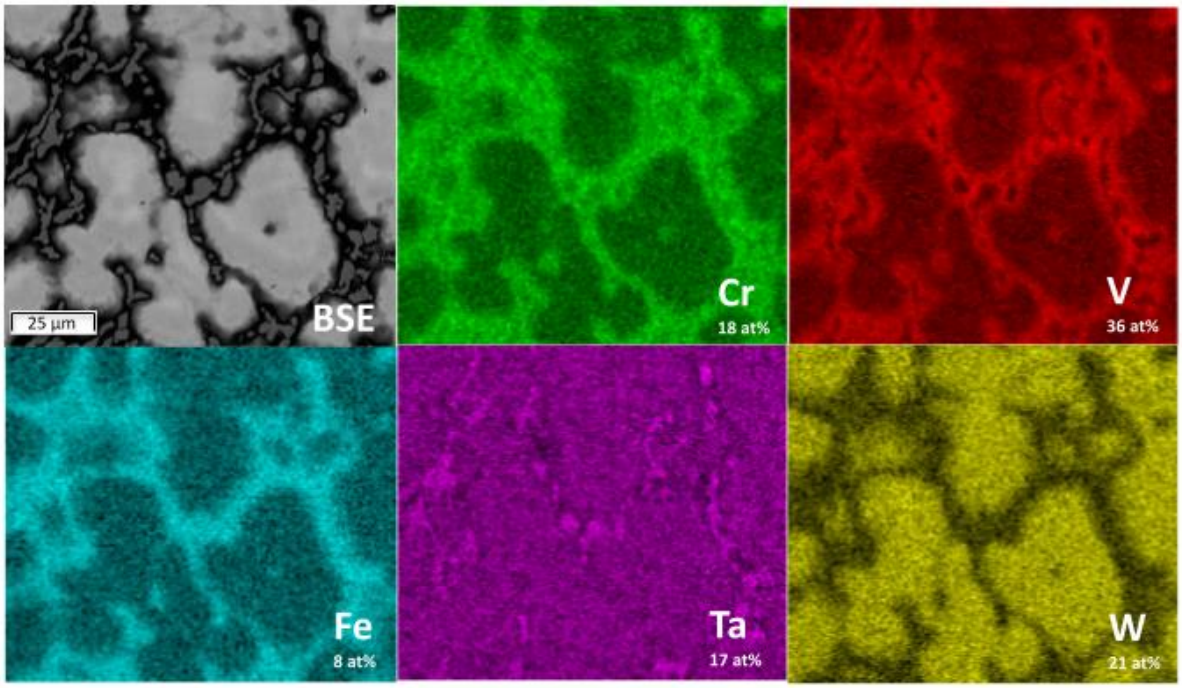

Figure 6.38: SEM-EDX elemental maps $V_{0.36}Cr_{0.18}Fe_{0.08}Ta_{0.17}W_{0.21}$ *heat treated at 500 °C for 100 hours at magnification a) x6000*

Table 6.21 displays the SEM-EDX point scans of the three regions of VCrFeTaW heat treated at 500 C for 100 hours as shown in the SEM-BSE micrographs. Alongside the elemental compositions the Thermo-Calc predictions of the equilibrium phases stable for each region are given.

Table 6.21: The elemental compositions (at%) of different regions within the low temperature heat treated VCrFeTaW alloy using SEM-EDX point scans (averaged from 5 separate point scans from each region). The corresponding Thermo-Calc predictions of the equilibrium phases for each regional composition are also stated. The averaged XRF values of the overall VCrFeTaW composition is included for comparison.

	White region (at%)	Grey region (at%)	Black region (at%)	Overall Alloy (at%)
V	32±0.7	33±7.1	41±9.7	36
Cr	12±0.4	21±1.2	23±0.8	18
Fe	3±0.3	21±1.7	16±3.6	8
Ta	15±0.3	21±6.4	13±8.7	17
W	38±1.1	4±0.3	7±2.3	21
Thermo-Calc predictions (SSOL4)	BCC A2	BCC A2 σ C15 Laves	BCC A2 σ	BCC A2 σ C15 Laves

The SEM-EDX point scans of the white region of the low temperature heat treated sample is comparable to the elemental compositions of the white region in the high temperature heat treatment.

Figure 6.39 displays the experimental XRD pattern of VCrFeTaW heat treated at 500 °C for 100 hours. The pattern matches with two disordered BCC phases (both with space groups Im-3m) with lattice parameters (a≈3.16 Å and a≈8.51 Å) respectively. BCC1 is analogous to a pure W [33] and BCC2 is analogous to Ho_4FeGa_{12} [34]. The experimental peak at ~40° is very broad and contains three separate peaks – two matching BCC2 and one matching BCC1.

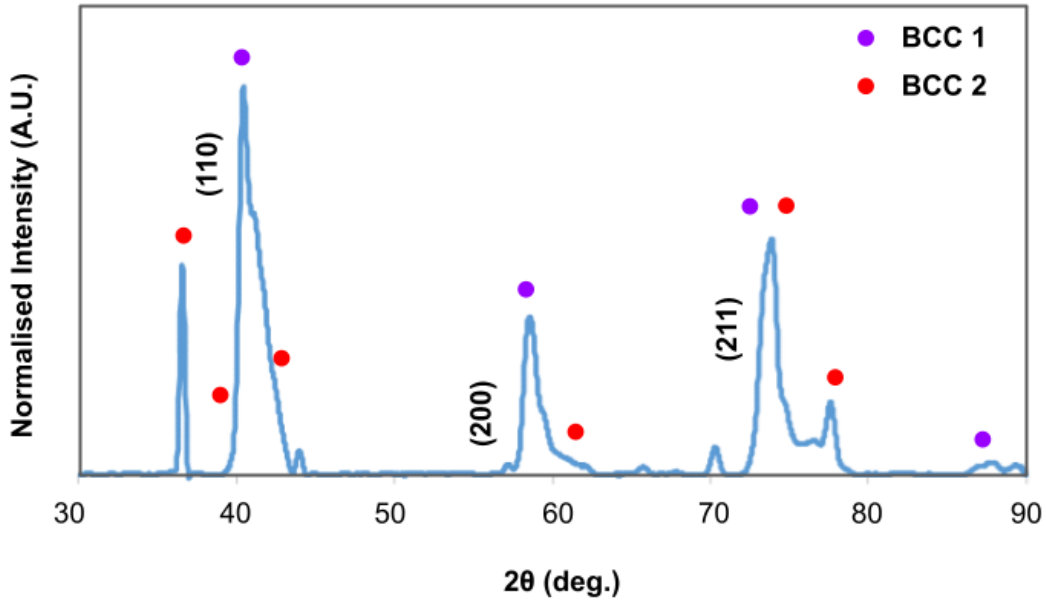

Figure 6.39: XRD pattern of $V_{0.36}Cr_{0.18}Fe_{0.08}Ta_{0.17}W_{0.21}$ heat treated at *heat treated at 500 °C for 100 hours*

This further verifies the matching of the primitive Pm-3m phase to the ordered BCC B2 structure in the 'homogenised' VCrFeTaW discussed previously. The elemental concentrations of the white region (exhibited in the SEM-BSE micrographs) of both the 'homogenised' and the low temperature VCrFeTaW are very similar (confirmed by the respective SEM-EDX regional point scans). Therefore, as the low temperature VCrFeTaW white region likely matched one of the BCC phases from the experimental XRD pattern, it can be concluded that the two white regions may be similar in crystal structure. The white region in the 'homogenised' VCrFeTaW is anticipated to have ordered BCC B2 structure (with a Pm-3m space group) and the low temperature heat treatment VCrFeTaW has a disordered BCC A2 structure (with a space group Im-3m).

The second BCC phase can be attributed to both the black and grey phases which are rich in all the elements bar tungsten. The grey precipitates are slightly richer in tantalum (21 at%) and have an equal amount of chromium (21 at%) and the black region is richer in chromium (23 at%) compared to the concentration of tantalum (13 at%). As with the higher temperature heat treatment, all three regions are composed of multiple components in high proportions. The majority phase which appears in the Thermo-Calc predictions for these two regions is an equilibrium BCC crystal structure which is stable across a wide temperature range. For the overall Thermo-Calc predictions of the alloy VCrFeTaW, at 500 °C (listed in Table 6.21) the equilibrium phases predicted is a disordered BCC A2 phase (0.5 mol), a σ phase (0.3 mol) and a C15 Laves phase (0.2 mol). The BCC phases identified by the XRD pattern coincide with the disordered BCC A2 phase predicted by Thermo-Calc using the SSOL4 database, however, there appears to be no evidence of a C15 Laves phase or a Tetragonal crystal structure in the XRD pattern.

6.8. $V_{0.35}Cr_{0.33}Mn_{0.02}Fe_{0.12}W_{0.18}$

6.8.1. As-Cast

Figure 6.40 displays the experimental XRD pattern of the as-cast VCrMnFeW which exhibits two BCC phases with very similar lattice parameters and whose peaks are similar enough that they overlap slightly.

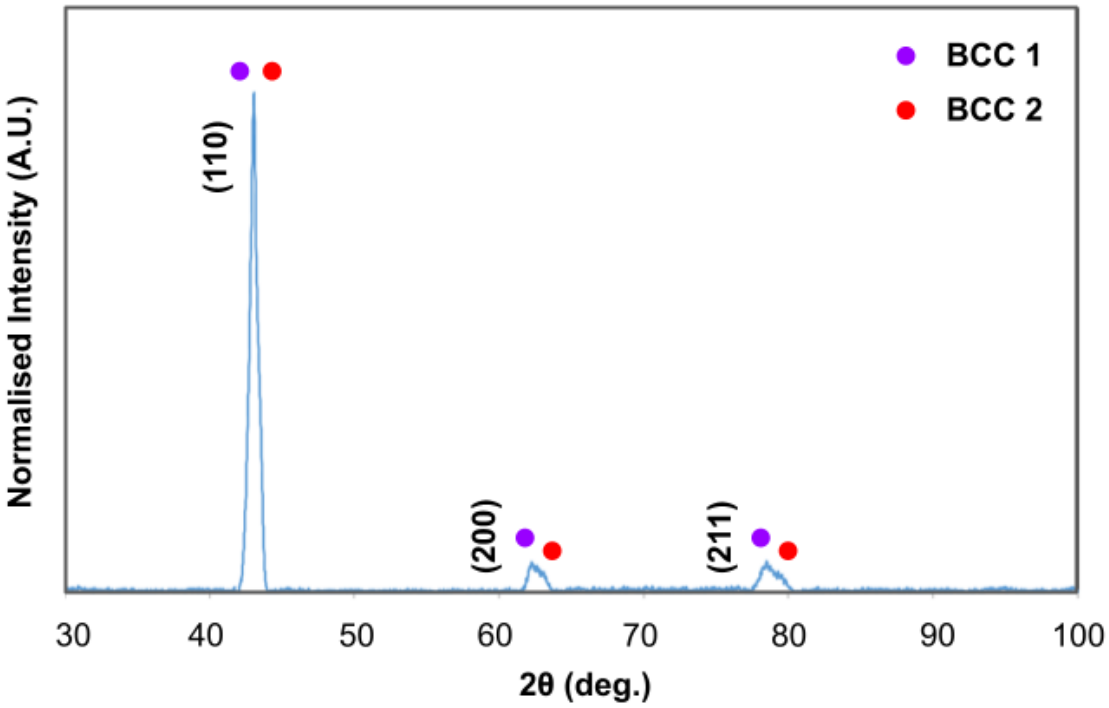

Figure 6.40: XRD pattern of as-cast $V_{0.35}Cr_{0.33}Mn_{0.02}Fe_{0.12}W_{0.18}$

The first BCC phase is analogous to $Fe_{0.5}Rh_{0.5}$ [35] with a space group Im-3m (and lattice parameter a≈2.98 Å) and is represented by a purple circle. The second BCC phase is analogous to $Fe_{0.5}Al_{0.5}$ [36] which has the space group Im-3m (and lattice parameter a≈2.97 Å) and is depicted by a red circle. The two BCC phases have almost identical lattice parameters resulting in peak overlap of these crystal structures causing the XRD peaks to exhibit leaning 'shoulders' and peak-splitting.

Figure 6.41: shows the Thermo-Calc predictions for $V_{0.35}Cr_{0.33}Mn_{0.02}Fe_{0.12}W_{0.18}$ using the TCHEA4 and SSOL4 databases. The predicted equilibrium phases using both databases are very similar. For both databases, the main phase is a BCC phase (disordered for the SSOL4 prediction and ordered for TCHEA4). Both databases also predicted a σ phase at lower temperatures (below 500 °C for SSOL4 and below 1000 °C for TCHEA4) in moderate to low proportions.

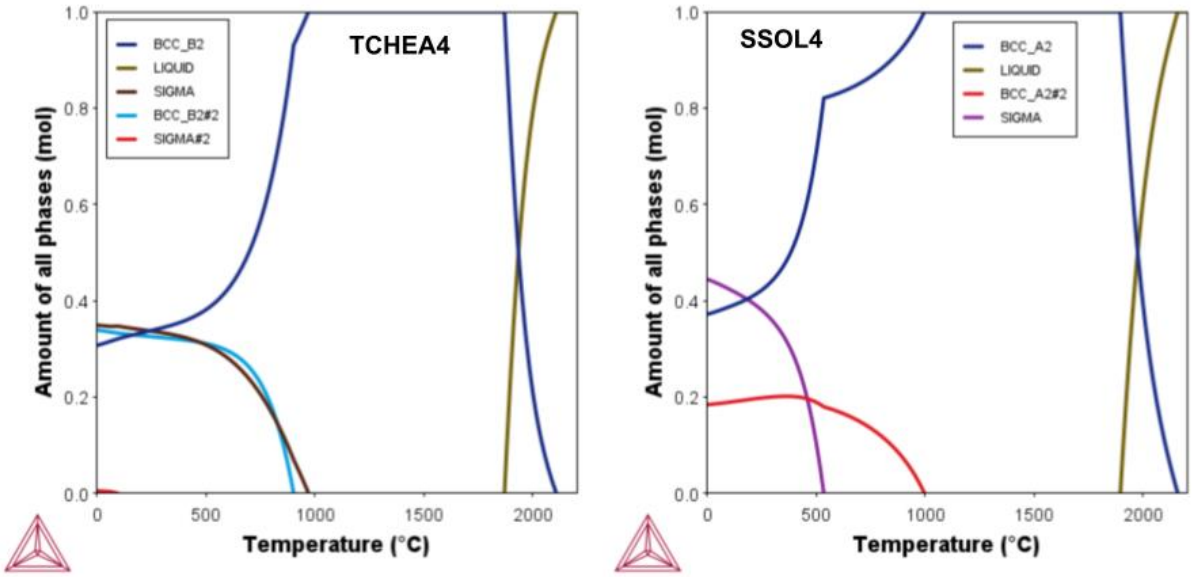

Figure 6.41: The Thermo-Calc predictions for $V_{0.35}Cr_{0.33}Mn_{0.02}Fe_{0.12}W_{0.18}$ using the SSOL4 and TCHEA4 databases

The main BCC phase coincides with the observed phase identified in the experimental XRD pattern.

Figure 6.42 shows the SEM-BSE micrographs of the as-cast VCrMnFeW which display a fine dendritic microstructure with three different regions of contrast: white regions representing dendrites, grey regions depicting the interdendritic regions, and black regions surrounding the dendritic and interdendritic regions. The black regions resemble precipitation of lower atomic mass elements around the dendritic regions which given their arrangement may be located at grain boundaries.

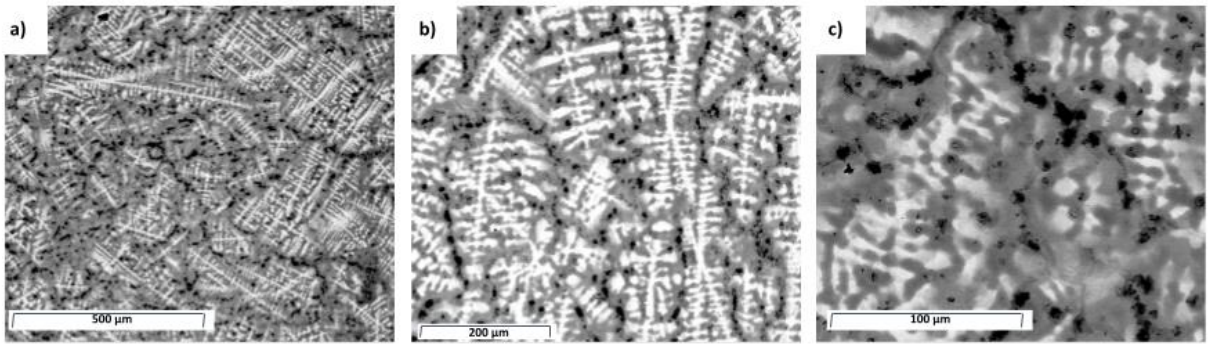

Figure 6.42: SEM-BSE micrograph of the *as-cast* $V_{0.35}Cr_{0.33}Mn_{0.02}Fe_{0.12}W_{0.18}$ *at magnification a) x1200, b) x3000, and c) x6000*

Table 6.22 displays the three different areas of contrast with the chemical compositions determined using SEM-EDX point scans. Much like VCrFeTa, which also has three distinct

regions of contrast; the white, grey, and black areas vary slightly in chemical composition showing some evidence of microsegregation.

Table 6.22: Elemental concentrations (at%) of the three different regions of the refined VCrMnFeW alloy in the as-cast state using SEM-EDX point scans (averaged from 5 separate point scans from each region). The corresponding Thermo-Calc predictions of the equilibrium phases for each regional composition are also stated. The averaged XRF values of the overall VCrMnFeW composition is included for comparison.

	White region (at%)	**Grey region (at%)**	**Black region (at%)**	**Overall Alloy (at%)**
V	30±2.8	50±1.1	64±10.4	35
Cr	1.1±0.3	3±0.4	3±0.8	33
Mn	0.1±0.17	0.2±0.3	0.1±0.1	2
Fe	1.2±0.5	6±0.8	20±4.7	12
W	68±3.4	41±1.7	13±7.2	18
Thermo-Calc predictions (SSOL4)	BCC A2	BCC A2	BCC A2	BCC A2 σ

These point scan compositions were calculated in Thermo-Calc for an estimate of phases that would likely occur between these elements. For all three regions, a stable single-phase BCC phase was predicted which corroborates with the experimental XRD pattern. Therefore, the elemental microsegregation of the as-cast VCrMnFeW may also reflect the overlapping of two very similar BCC peaks. The white precipitation around the dendrites, the interdendritic region, is rich in only vanadium (30 at%) and tungsten (68 at%). From the V-W binary phase diagram (discussed in Chapter 5: Alloy Design) the isomorphous system only forms a BCC phase across all temperatures. This is also in agreement with the Thermo-Calc predictions of this specific composition as determined from the point scans.

Figure 6.43 displays a representative SEM-EDX spectra collected from one of the point scans for the as-cast VCrMnFeW. The main peak corresponding to manganese (at around 6 keV) can be clearly observed. The overlapping peaks at around 0.5 keV are affiliated with Mn, Cr, Fe, and V. However, the peak at approximately 6 keV is due solely to the presence of manganese with no overlapping of other peaks affiliated with another element.

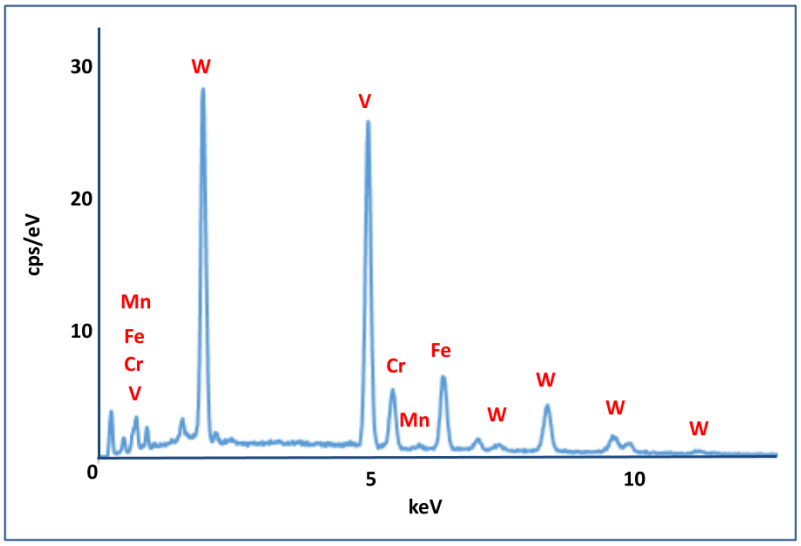

Figure 6.43: SEM-EDX spectra from the as-cast $V_{0.35}Cr_{0.33}Mn_{0.02}Fe_{0.12}W_{0.18}$

This confirms that the energy window applied was sufficient to gather data for the elemental concentrations of manganese. It is worth noting that the concentration of manganese (2 at%) in this alloy is relatively small and so is difficult to accurately quantify using the SEM-EDX point scans, due to the resolution of the EDX detector. So, whilst the point scans could not quantify an amount of manganese, the presence of manganese peaks (although relatively very low in intensity) in the point scan spectra confirms that manganese content was taken into consideration.

Figure 6.44 shows the SEM-EDX elemental maps of the as-cast VCrMnFeW displaying the elemental distribution. Coinciding with the black precipitation, there appears to be brighter areas of vanadium and iron (indicating enrichment of these elements in these regions). In these same regions, there is a darker contrast of tungsten, revealing a depletion of this element.

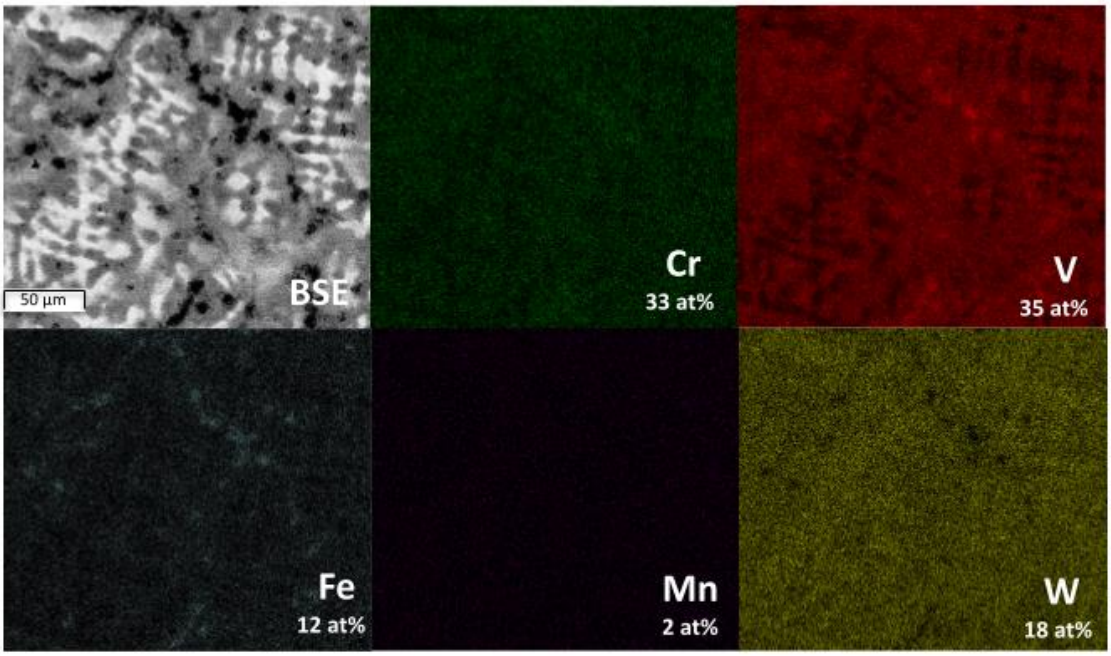

Figure 6.44: SEM-EDX elemental maps *as-cast* $V_{0.35}Cr_{0.33}Mn_{0.02}Fe_{0.12}W_{0.18}$ *at magnification a) x6000*

Whilst the amount of manganese could not be quantified using the point scans, the SEM-EDX elemental maps do reveal a homogenous dispersal of manganese. The SEM-EDX elemental maps also highlight an inverse relationship between tungsten and vanadium which was also quantified using the point scans. In the black precipitation regions, there is a high concentration of vanadium (64 at%) which coincides with a lower concentration of tungsten (13 at%). In the white interdendritic region, this area is enriched in tungsten (68 at%) and lacking in vanadium (30 at%) compared to the other regions.

6.8.2. 1400 °C, 18 hours

Figure 6.45 displays the experimental XRD pattern of VCrMnFeW after heat treating at 1400 °C for 18 hours and reveals the single BCC phase analogous to $Mn_{0.16}Mo_{0.84}$ [37] with a space group of Im-3m (229) and a lattice parameter of a≈3.12 Å.

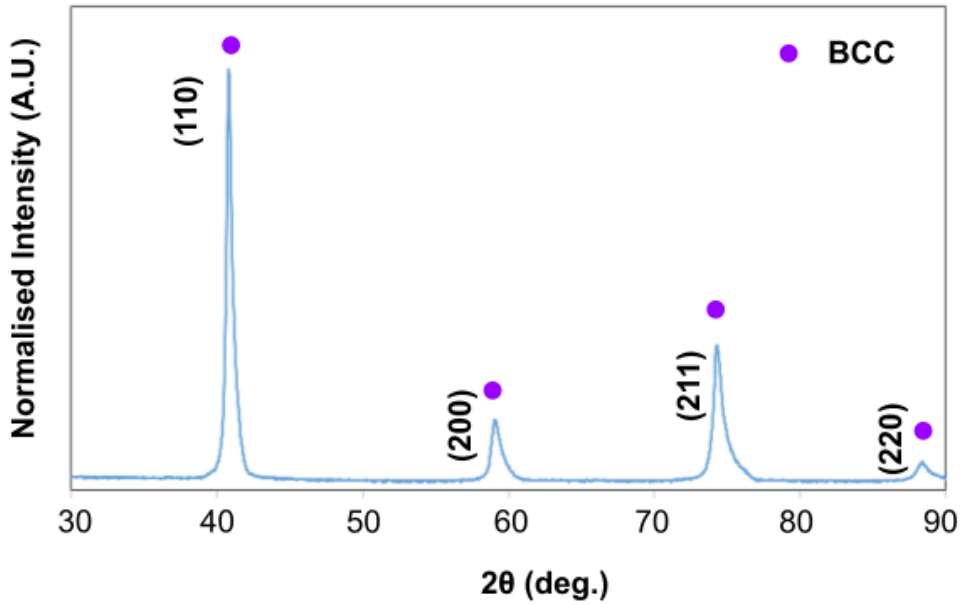

Figure 6.45: XRD pattern of $V_{0.35}Cr_{0.33}Mn_{0.02}Fe_{0.12}W_{0.18}$ after heat treatment at 1400 °C for 18 hours

After a shorter high-temperature heat treatment, 1400 °C for 18 hours, the alloy obtained a single-phase BCC structure and displayed sharp peaks with sloped edges. However, there is no splitting of the peaks in the XRD pattern unlike the as-cast sample.

Figure 6.46 shows the SEM-BSE micrographs of the 'homogenised' VCrMnFeW which demonstrate a black region forming along grain boundaries and some precipitation (of the same contrast) within these boundaries on the scale of 10 μm. Unlike the as-cast sample, which had three different regions of contrast, in the 'homogenised' sample there appears to only be two different regions.

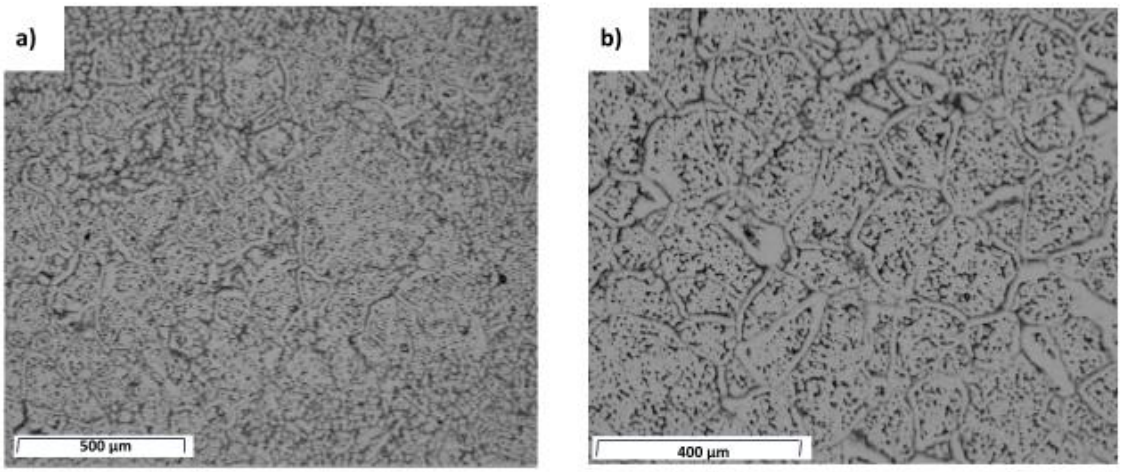

Figure 6.46: SEM-BSE micrograph of $V_{0.35}Cr_{0.33}Mn_{0.02}Fe_{0.12}W_{0.18}$ after heat treatment at 1400 °C for 18 hours at magnification a) x190 and b) x300

Figure 6.47 displays the SEM-EDX elemental maps which highlight a small amount of elemental segregation. The black region indicative of the grain boundaries and precipitation within the grains appears to be enriched in a higher content of vanadium and chromium. Iron, manganese, and tungsten all represent a fairly homogenous elemental distribution.

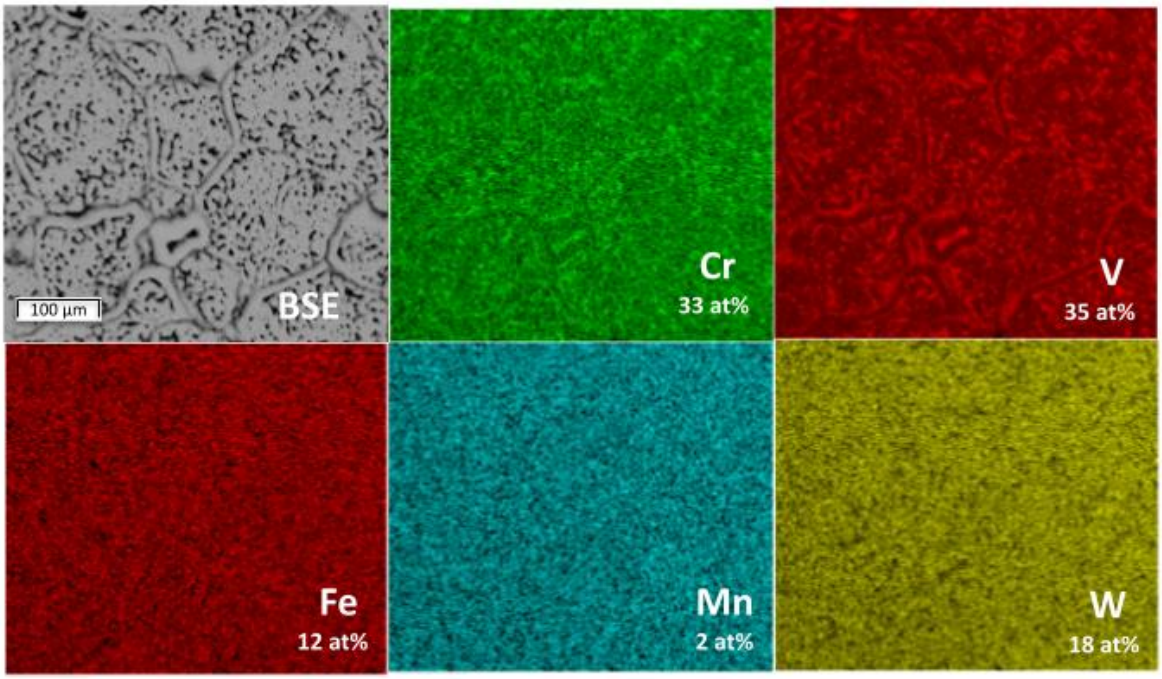

Figure 6.47: SEM-EDX elemental maps as-cast $V_{0.35}Cr_{0.33}Mn_{0.02}Fe_{0.12}W_{0.18}$ at magnification x450

In order to reduce the V-Cr enrichment, a further heat treatment was applied, at a higher temperature and for a longer duration. From Table 6.6, 1400 °C is only 0.58 T_m of the homogenisation temperature which is slightly below the limit for homogenising VCrMnFeW. A higher temperature heat treatment, at 1500 °C (the maximum allowable temperature in this work), would result in a homogenisation temperature of 0.63 T_m which is in the lower limit and is more likely to result in a successful homogenisation of the alloy.

6.8.3. 1500 °C, 48 hours

Figure 6.48 shows the SEM-BSE micrographs of the 'homogenised' VCrMnFeW (heat treated at 1500 °C for 48 hours). Much like the lower temperature homogenisation treatment, there are areas of defined black precipitates which follow regions of the grain boundaries.

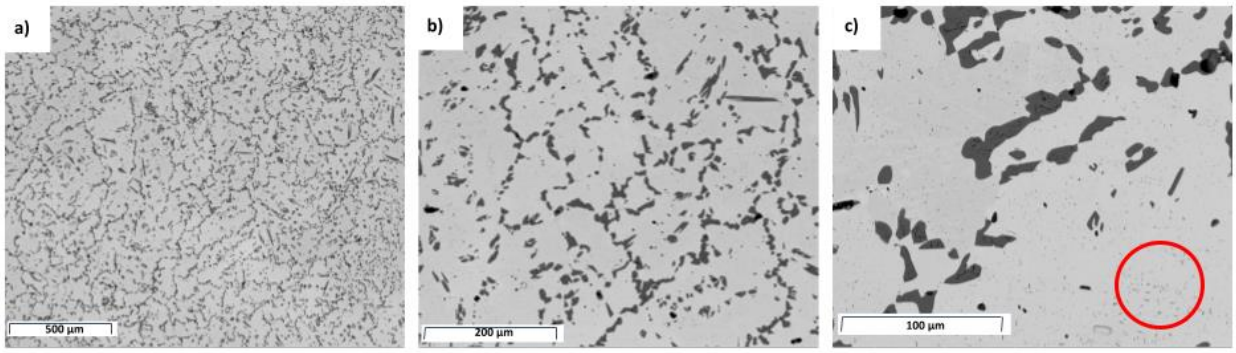

Figure 6.48: SEM-BSE micrograph of $V_{0.35}Cr_{0.33}Mn_{0.02}Fe_{0.12}W_{0.18}$ after heat treatment at 1500 °C for 100 hours at magnification a) x150, b) x500, and c) x1300

As the temperature of the homogenisation treatment is increased and prolonged (to 1500 °C for 48 hours) the vanadium and chromium segregation is exacerbated. Precipitation around the grains with a dispersal of fine precipitates (around a micron in size) within the grains (shown by the red circle) is evident from the SEM-BSE micrographs. A similar morphology of precipitates was identified by Barron et el [38] in a range of ternary V-Cr-Mn-(Ti) alloys. They observed a light grey matrix (BCC) with darker precipitates, where the quaternary alloys had much finer precipitates. For the ternary alloys, the precipitates were depleted in Mn and Cr and contained large amounts of oxygen.

Figure 6.49 shows the SEM-EDX elemental maps which reveal the black precipitates to be rich in vanadium and chromium, and completely void in iron and tungsten. It is also feasible that a small amount of manganese also comprises these precipitates.

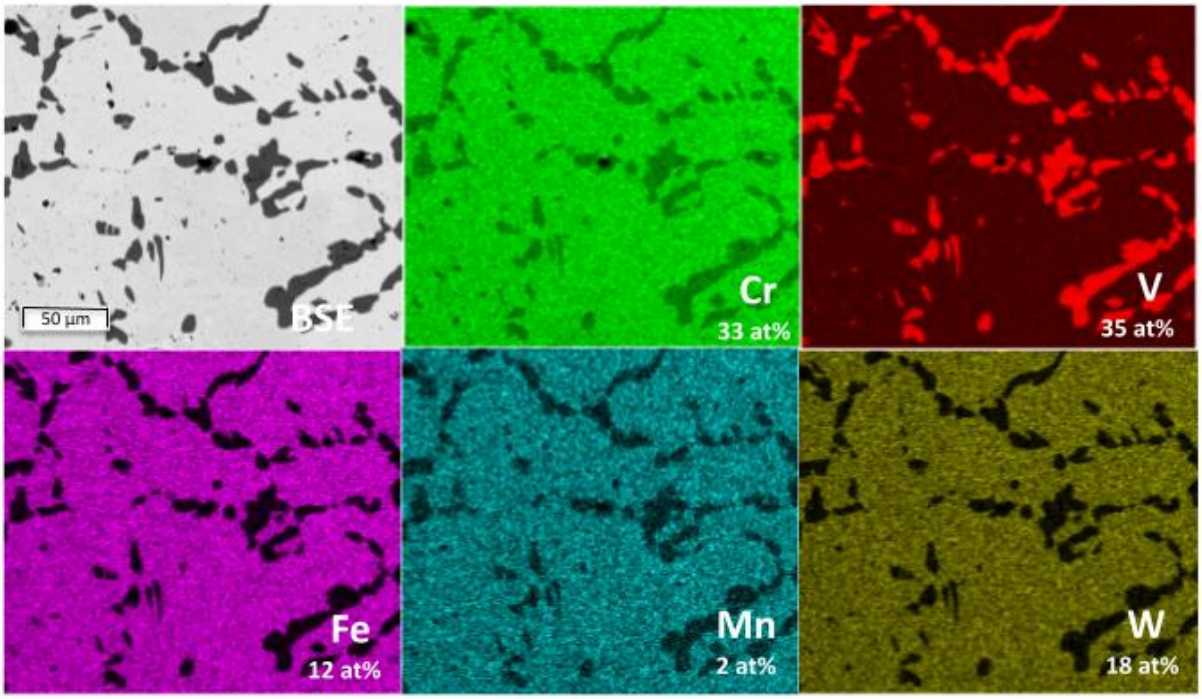

Figure 6.49: SEM-EDX elemental maps $V_{0.35}Cr_{0.33}Mn_{0.02}Fe_{0.12}W_{0.18}$ after heat treatment at 1500 °C for 100 hours at magnification x1300

Whilst the 'homogenised' VCrMnFeTaW alloy demonstrated the loss of vanadium-rich precipitates compared to the as-cast state, the 'homogenised' VCrMnFeW displayed the exacerbated formation and stability of vanadium-based precipitation. This is analogous to the work discussed in Section 4.6. where the homogenisation of VCrMoW was considered. Figure 6.50 shows the SEM-BSE micrographs for VCrMoW heat treated at 1600 °C for 72 hours.

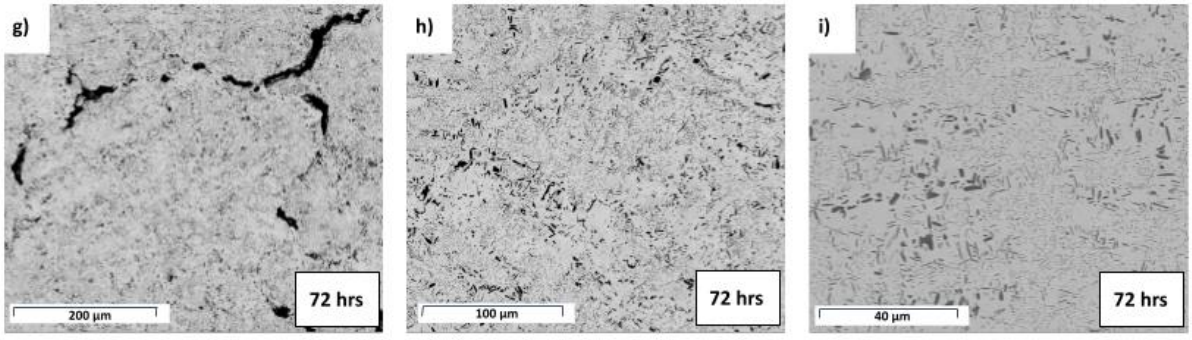

Figure 6.50: SEM-BSE micrographs of VCrMoW heat treated at 1600 °C for 72 hours at varying magnifications

These micrographs are clearly comparable to VCrMnFeW also homogenised at high temperature where larger precipitates surround finer, more dispersed precipitation. Additionally, both precipitates, from the homogenised VCrMnFeW and VCrMoW, are rich in vanadium and depleted in tungsten.

Figure 6.51 displays the experimental XRD pattern of the 'homogenised' VCrMnFeW and (much like the as-cast state) exhibits two very similar BCC phases (akin to the structures in the as-cast section and are represented by the same symbols). The third phase has a tetragonal crystal structure with a space group P42/mnm (136) and is analogous to Re_3V [39] and is represented by an orange triangle.

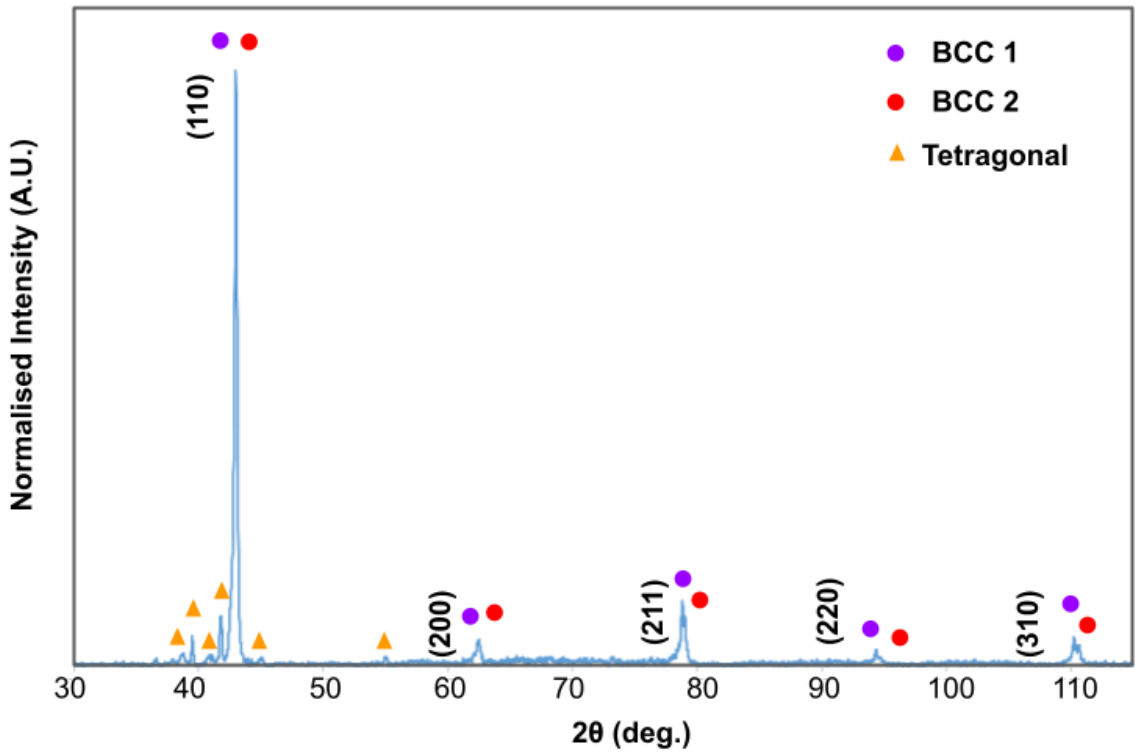

Figure 6.51: XRD pattern of $V_{0.35}Cr_{0.33}Mn_{0.02}Fe_{0.12}W_{0.18}$ after heat treatment at 1500 °C for 100 hours

The details of these analogous XRD phases and their parameters are listed in Table 6.23.

Table 6.23: The three phases identified by the experimental XRD of the 'homogenised' VCrMnFeW. These are derived from the analogous structures which have the same XRD pattern to the phases found experimentally.

	BCC1	**BCC2**	**Tetragonal**
Space group	Im-3m (229)	Im-3m (229)	P42/mnm (136)
Prototype	$Fe_{0.5}Rh_{0.5}$	$Fe_{0.5}Al_{0.5}$	σCrFe
Name	Hexagonal C14 Laves	E93 Structure	σ Phase D8b Structure
Structure	BCC A2	BCC A2	σ
Pearson symbol	cI2	cI2	tP30
Lattice parameter (Å)	a≈2.98 Å	a≈2.97 Å	a≈9.36 Å c≈4.86 Å

The XRD pattern reveals the same two BCC phases evident in the as-cast phase, in addition to a tetragonal phase with a space group P42/mnm (analogous to the σCrFe which appears in the Cr-Fe binary phase diagram and is discussed further in Chapter 5: Alloy Design). The tetragonal crystal structure is indicative of a σ phase.

Table 6.24 displays the quantitative elemental composition of the regions defined in the SEM-BSE of the 'homogenised' VCrMnFeW using SEM-EDX point scans.

Table 6.24: Elemental concentrations (at%) of the three different regions of the 'homogenised' VCrMnFeW alloy using SEM-EDX point scans (averaged from 5 separate point scans from each region). The corresponding Thermo-Calc predictions of the equilibrium phases for each regional composition are also stated. The averaged XRF values of the overall VCrMnFeW composition is included for comparison.

	White (at%)	**Black (at%)**	**Alloy composition (at%)**
N	-	-	14
V	29±0.6	90±0.1	33
Cr	39±0.6	10±0	29
Mn	0.6±1.1	-	2
Fe	16±0.3	0.5±0	11
W	15±0.3	0.8±0.1	11
Thermo-Calc predictions	BCC	BCC	BCC A2

As with the other alloys in this study, the quantitative determination of manganese was unable to be detected in either contrast region. However, as indicated by the SEM-EDX elemental maps whilst manganese is primarily in the predominant white region of the alloy, a small amount may be present in the black V-Cr rich precipitates. Therefore, it is reasonable to establish that the black precipitation correlates with a vanadium, chromium (and small amount of manganese) enriched phase as reinforced by the SEM-EDX elemental maps. A significant amount of nitrogen was also detected by the EDX area scans. However, it was unable to be determined in which region nitrogen was a contaminant. Additionally, the composition of the white region, likely to be the BCC matrix, shows some deficiencies in tungsten and surplus in iron compared to the total alloy composition. The differences may be representative of the error involved in the EDX detector and may be relative to the other regional compositions.

Interestingly the black precipitates contain 90 at% of vanadium, and this is also the case for VCrMoW homogenised at 1600 °C for 48 hours, where the precipitates also contained 92 at% of vanadium. The likeness between these two alloys in the as-cast state and homogenised conditions may suggest that VCrMnFeW may also demonstrate the similar qualities of radiation damage tolerance upon heavy ion implantation. Both VCrMnFeW and VCrMoW readily form two stable BCC phases, of which in the as-cast state VCrMoW exhibited excellent resistance to room temperature ion implantation. Whilst upon intermediate annealing, VCrMoW the BCC phases transformed into a BCC, orthorhombic, and a tetragonal phase, VCrMnFeW showed some tetragonal formation at high temperatures. Regardless, the mechanisms of which resisted radiation in the as-cast metastable phases of VCrMoW may also be appropriate for VCrMnFeW.

Figure 6.52 shows the isothermal V-Cr-Mn ternary phase diagram calculated for 1500 °C using the SSOL4 database of Thermo-Calc. As indicated in the diagram a stable BCC solid solution at all concentrations. There is no evidence of a σ phase at high concentrations of chromium. However, this is likely due to insufficient data at these concentrations.

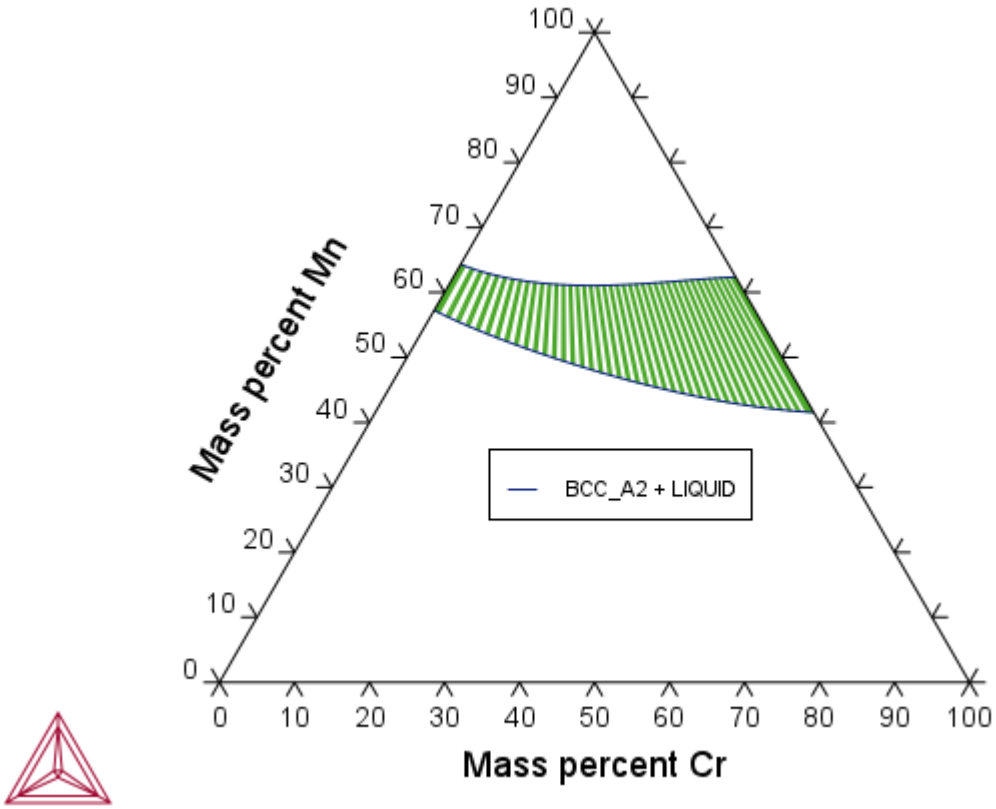

Figure 6.52: The isothermal V-Cr-Mn ternary phase diagram calculated for 1500 °C using the SSOL4 database of Thermo-Calc.

Krapivka, Firstov, [19] have suggested that for alloys with higher proportions of binary pairs that form σ phases, the likelihood of the formation of a σ phase in the alloy is increased. For this alloy, almost all the binary pairs contain a σ phase in the binary phase diagrams, thus suggesting a higher probability of the formation of this phase. The propensity of the σ phase in the binary phase diagrams and Thermo-Calc predictions is discussed in detail in the previous Chapter 5: Alloy Design.

Figure 6.41 shows the Thermo-Calc predictions of the equilibrium phases, using both the TCHEA4 and SSOL4 databases, of $V_{0.35}Cr_{0.33}Mn_{0.02}Fe_{0.12}W_{0.18}$. These predictions reveal the minor formation of a σ phase (0.2 mol) at low temperatures (below 1000 °C).

Table 6.25 lists the relative concentration of components in the σ phase present in $V_{0.35}Cr_{0.33}Mn_{0.02}Fe_{0.12}W_{0.18}$ using the SSOL4 database. Thermo-Calc predicts this σ phase to be predominantly formed of iron, chromium, vanadium, manganese, then tungsten (in descending order of concentration).

Table 6.25: Thermo-Calc predictions of the elemental concentrations of the C15 Laves phase and the σ phase for $V_{0.35}Cr_{0.33}Mn_{0.02}Fe_{0.12}W_{0.18}$.

Phase	Amount of component in the phase from the largest concentration to smallest
σ phase	Fe>Cr>V>Mn>W

This is contradictory from the experimental characterisation of 'homogenised' VCrMnFeW where the SEM-EDX point scans report the black precipitates surrounding the grains to be composed mainly of vanadium and chromium with a small possible addition of manganese and nitrogen.

An alternative theory may be that the black precipitates may form a stable BCC phase in accordance with the experimental XRD pattern. Precipitation consisting of purely $V_{0.9}Cr_{0.1}$, as detected by the SEM-EDX point scans, has been confirmed using Thermo-Calc predictions (and the V-Cr binary phase diagram) to be a BCC phase. The white region may represent the second BCC phase (displayed in the experimental XRD pattern) whilst the tetragonal phase, which may include a small amount of nitrogen, may be the smaller precipitation finely dispersed across the entire alloy. This region is unable to be quantitatively assessed due to the resolution restrictions in the SEM microscope. Further investigation using higher resolution techniques, including TEM, is required to resolve these phases.

Another consideration that needs to be considered is the low temperature formation of the σ phase. In the binary phase diagrams and in the Thermo-Calc predictions, the σ phase is only present at temperatures below 1000 °C due to the ordered σ phase becoming unstable at higher temperatures. The homogenisation heat treatment at 1500 °C should be sufficiently high enough for this phase to not form, however the XRD pattern for the homogenised alloy confirms the presence of a tetragonal phase. It has been postulated that at high temperatures the stability of the BCC phase overrides that of the σ phase due to the solid solution phases having higher configurational entropy thereby minimising the Gibbs free energy of the BCC solid solution [40]. However, this is not observed in VCrMnFeW; after homogenisation there is not expected to be any σ formation. On the other hand, it is known that in V-containing alloys the σ phase can form at higher temperatures [41]. Stepanov et al [42] reported the structural and mechanical properties of a series of $CoCrFeMnNiV_x$ alloys where the volume fraction of the σ phase proportional to the cumulative chromium and vanadium concentration. In this study, the vanadium and chromium atoms significantly distort the FCC solid solution and so post-annealing these elements are forced to the grain boundaries to reduce stresses. The higher concentration of vanadium and chromium at the grain boundaries forms a BCC phase

which transforms to the observed σ phase during cooling. For VCrMnFeW a similar process may occur, where the vanadium and chromium are displaced from the BCC matrix to the grain boundaries where the elemental concentrations are high enough to form the σ phase.

Further investigation of the formation of the σ phase in VCrMnFeW and the temperature-dependence of this secondary phase is investigated in Chapter 7: VCrMnFeW using high temperature X-ray diffraction.

6.8.4. 700 °C, 100 hours

Figure 6.53 displays the experimental XRD pattern of VCrMnFeW heat treated at 700 °C for 100 hours. The XRD pattern exhibits a single BCC phase is analogous to $Fe_{0.5}Rh_{0.5}$ [35] with a space group Im-3m (and lattice parameter a≈2.98 Å) and is represented by a purple circle.

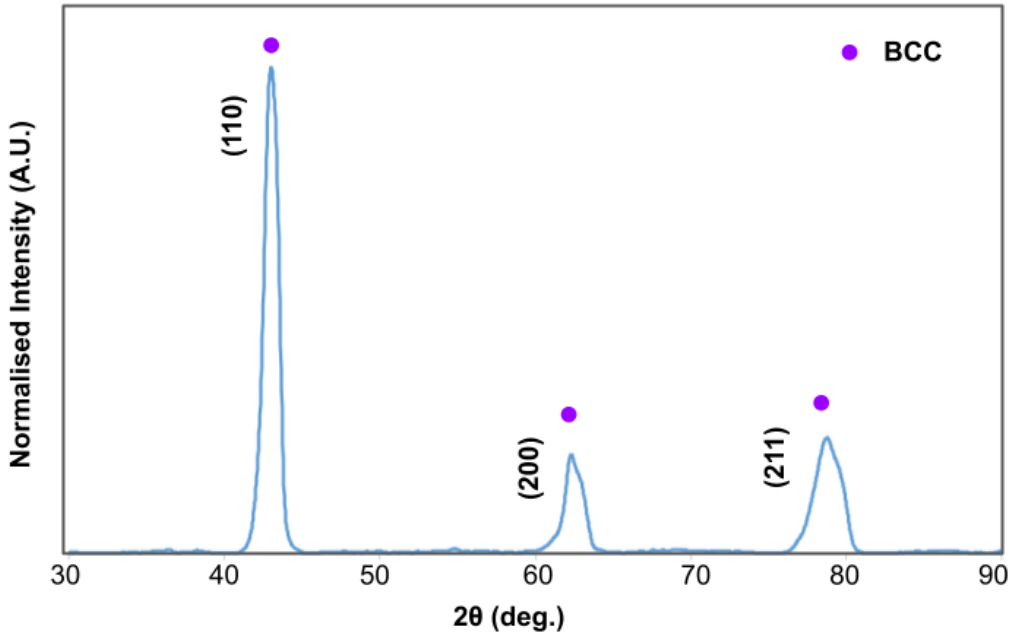

Figure 6.53: XRD pattern of $V_{0.35}Cr_{0.33}Mn_{0.02}Fe_{0.12}W_{0.18}$ after heat treatment at 700 °C for 100 hours

The peaks are sharp and narrow and are similar to the 1400 °C 'homogenised' sample. There is no evidence of a tetragonal phase in the XRD pattern.

Figure 6.54 shows the SEM-BSE micrographs and SEM-EDX elemental maps of VCrMnFeW heat treated at 700 °C for 100 hours. The micrographs display a globular dendritic microstructure with darker precipitates within the dendrites.

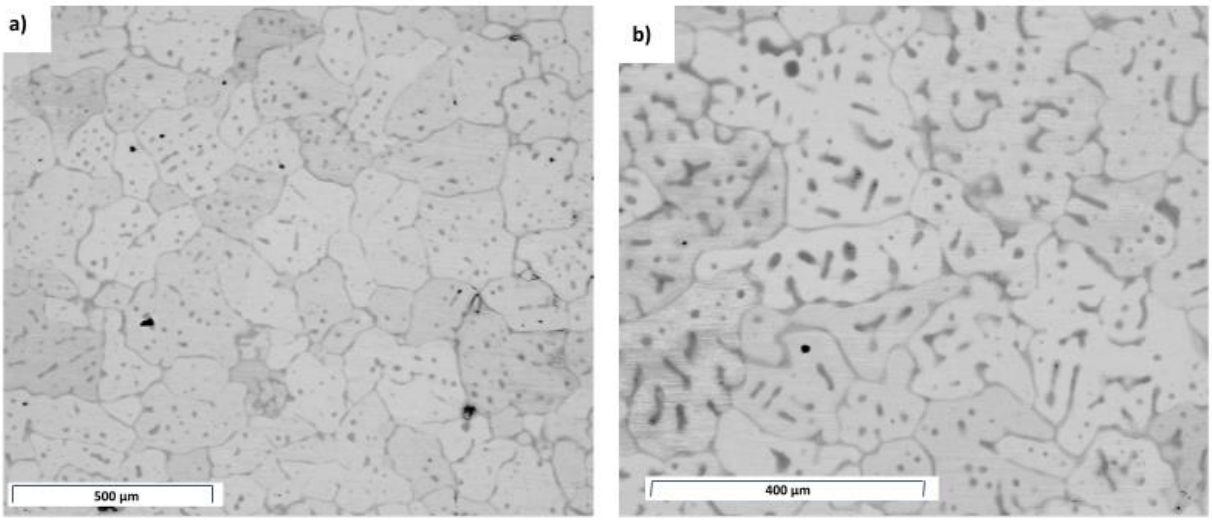

Figure 6.54: SEM-BSE micrograph of $V_{0.35}Cr_{0.33}Mn_{0.02}Fe_{0.12}W_{0.18}$ after heat treatment at 700 °C for 100 hours at magnification a) x200 and b) x400

These precipitates are larger than in the 1500 °C sample and are approximately 20-50 µm in length.

Figure 6.55 shows the SEM-EDX elemental maps of $V_{0.35}Cr_{0.33}Mn_{0.02}Fe_{0.12}W_{0.18}$ after heat treatment at 700 °C for 100 hours

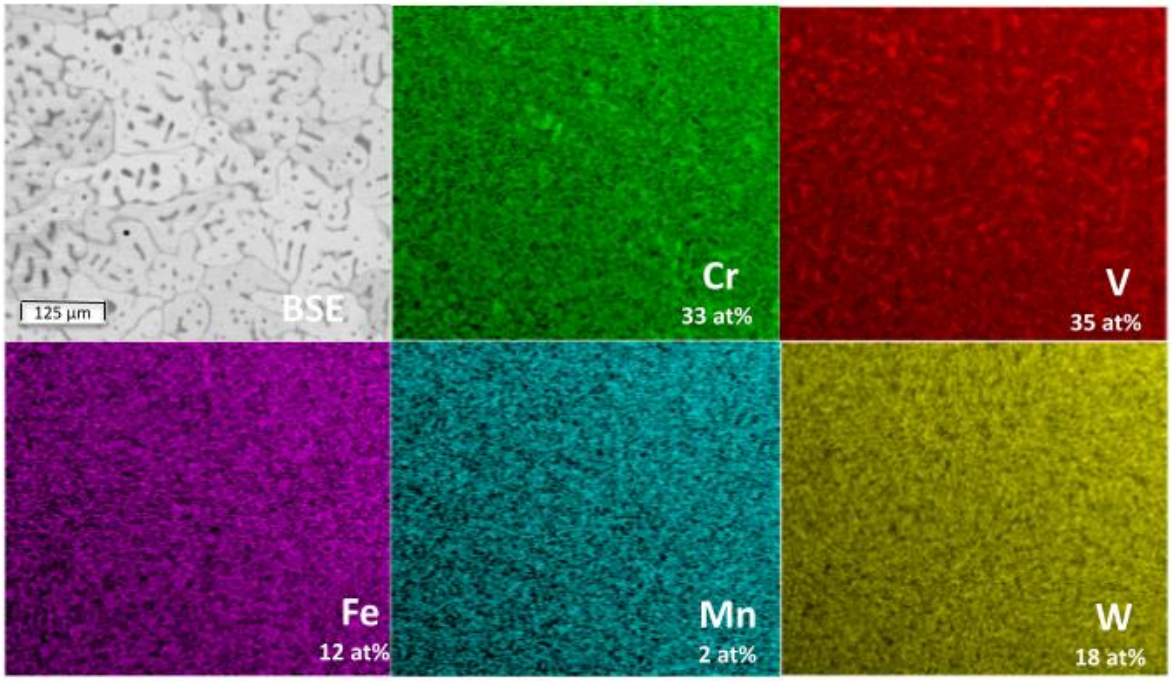

Figure 6.55: SEM-EDX elemental maps $V_{0.35}Cr_{0.33}Mn_{0.02}Fe_{0.12}W_{0.18}$ after heat treatment at 700 °C for 100 hours at magnification x400

The SEM-EDX elemental maps reveal that the interdendritic precipitate regions are enriched in predominantly vanadium and chromium which reflects the same elemental distribution as the sample heat treated at 1500 °C for 48 hours.

6.8.5. 500 °C, 100 hours

Figure 6.56 shows the experimental XRD pattern for VCrMnFeW heat treated at 500 °C for 100 hours and exhibits two BCC phases (with space groups Im-3m) which match the two BCC phases observed in the XRD pattern of the as-cast VCrMnFeW.

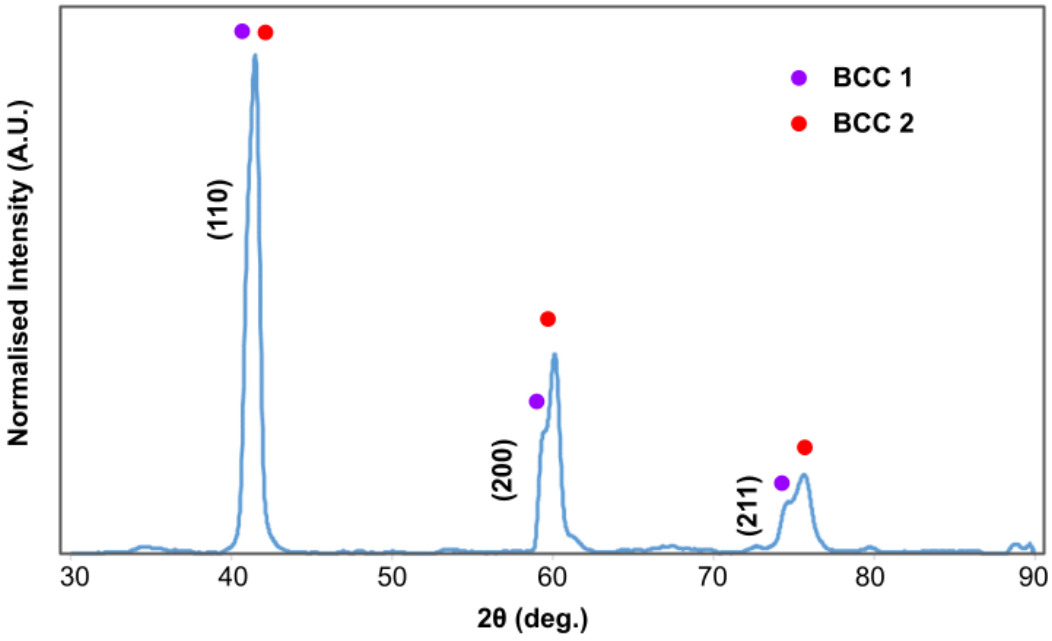

Figure 6.56: XRD pattern of $V_{0.35}Cr_{0.33}Mn_{0.02}Fe_{0.12}W_{0.18}$ after heat treatment at 500 °C for 100 hours

As mentioned in a previous section, one of the design aims for the alloy compositions VCrMnFeW and VCrMnTaW was for the evaluation of the substitution of iron and tantalum. In the as-cast state, VCrMnTaW displays a single BCC phase as identified by experimental XRD. The BCC phase analogous to $V_{0.5}W_{0.5}$ [25] has a space group Im-3m (229) and a lattice parameter a≈3.09 Å. Substitution of tantalum for iron, resulting in the alloy VCrMnFeW results in a lattice contraction as observed by XRD; the lattice parameters of the two BCC phases of the as-cast VCrMnFeW is a≈2.98 Å and 2.97 Å. These phases and lattice parameters are also retained after heat treatment at 500 °C for 100 hours. The increase in lattice parameter from VCrMnFeW to VCrMnTaW is consistent with the increased atomic radii of Fe (0.1241 nm) to Ta (0.1430 nm). A comparative study by Jiang et al [43] demonstrated that the addition of $W_{0.25}$ to $CrFeNi_2V_{0.5}$ increased the lattice parameter of the FCC phase from a = 3.5892 Å (for to $CrFeNi_2V_{0.5}$) to a = 3.6329 Å (for to $CrFeNi_2V_{0.5}$ $W_{0.25}$). They attributed this increase to the addition of tungsten atoms dissolving in the FCC lattice.

Figure 6.57 shows the SEM-BSE micrographs of VCrMnFeW heat treated at 500 °C for 100 hours which display the typical dendritic microstructure with surrounding grain boundaries (as indicated by the red arrow).

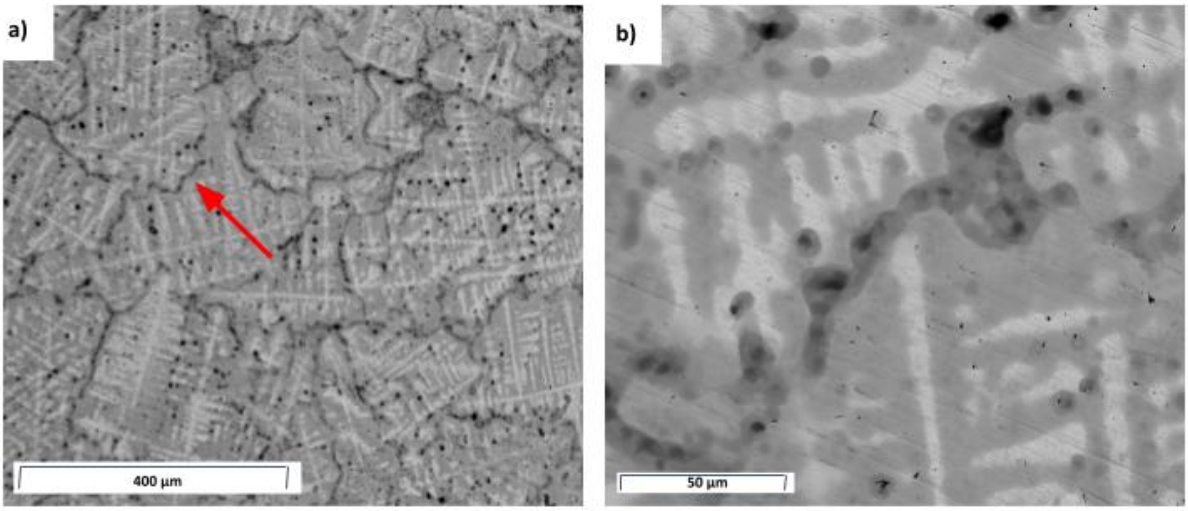

Figure 6.57: SEM-BSE micrograph of $V_{0.35}Cr_{0.33}Mn_{0.02}Fe_{0.12}W_{0.18}$ after heat treatment at 500 °C for 100 hours at magnification a) x300 and b) x1700

Figure 6.58 shows the SEM-EDX elemental maps of VCrMnFeW heat treated at 500 °C for 100 hours. The white contrast dendrites are surrounded by darker grey interdendritic regions. The lighter contrast dendrites are richer in tungsten (which has the higher atomic mass) and relatively lower in concentration of the other elements. The grey interdendritic regions are abundant in chromium, vanadium, iron, and manganese whilst being devoid in tungsten.

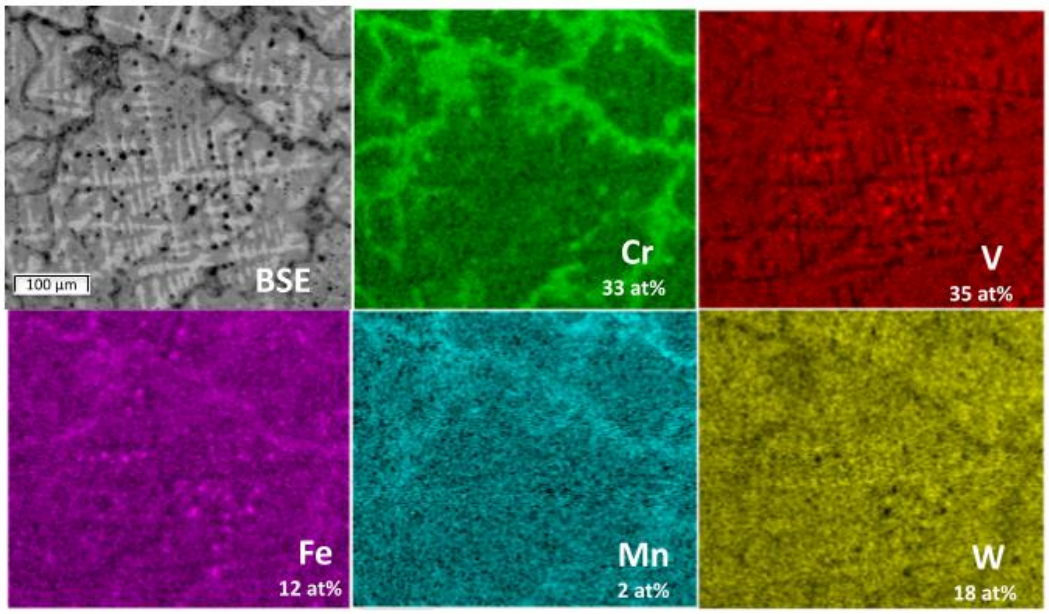

Figure 6.58: SEM-EDX elemental maps $V_{0.35}Cr_{0.33}Mn_{0.02}Fe_{0.12}W_{0.18}$ after heat treatment at 500 °C for 100 hours at magnification x650

The SEM-BSE micrographs exhibit the same morphology and typical microstructural formation observed in the as-cast VCrMnFeW, indicating that this low temperature heat treatment was inadequate in promoting any thermally-induced changes to the microstructure or phases compared to the as-cast VCrMnFeW.

Overall, for the two lower temperature heat treatments, 500 °C and 700 °C for 100 hours, there is minimal change from the as-cast alloy. This may be due to the BCC phase(s) being the most stable formation at these low temperatures therefore justifying the lack of intermetallic compound and secondary phase formation. However, the lack of refinement of the dendritic microstructure and retainment of elemental segregation suggests that further processing is required to achieve a favourable grain microstructure. Alternatively, 100 hours at these temperatures may be insufficient enough time to promote the formation of equilibrium phases. Importantly, for both of these lower temperature heat treatments, there is no evidence of a tetragonal phase indicating that the formation of this ordered σ phase occurs at higher temperatures. The Thermo-Calc predictions of the VCrMnFeW overall alloy composition (using the SSOL4 database) indicate the start of the precipitation of a σ phase from 1000 °C (rising to 0.2 mol at room temperature) increasing in concentration upon cooling to room temperature. To accurately determine the initial formation of this phase, high-temperature X-ray diffraction (HT-XRD) is used. This technique can also be used to determine the thermal stability of the phases up to intermediate temperatures (1000 °C). The HT-XRD of the as-cast VCrMnFeW is examined in Chapter 7: VCrMnFeW.

6.9. Microhardness

Vickers microhardness testing is often applied for a quick and efficient method for the general assessment of the strength of a material. A full description of this method and the conditions and parameters used can be seen in Chapter 3: Experimental Methods. Due to the nature of this technique, the indent size is on the order of microns, a comprehensive evaluation of the alloy's overall hardness is measured. Many of these alloys, as discussed in the previous section, are multiphase in nature and as the indent is too large for site-specific regions (i.e., within precipitates, or dendritic arms) only the hardness of the overall alloy was able to be calculated.

Table 6.26 displays the average Vickers microhardness values for the high entropy alloys in this work. The as-cast, 'homogenised', and low temperature heat treated samples were tested

for their Vickers microhardness. An average of ~10 indents in a random arrangement across the entire sample.

Table 6.26: The average Vickers microhardness (HV1) values for the alloys investigated in this work collected from an averaged value from ten indents across the samples. The as-cast samples and the different heat-treated conditions of the alloys are also included alongside the standard deviation error.

Alloy Composition	As-cast (HV)	1500 °C 48 hrs (HV)	1400 °C 18 hrs (HV)	700 °C 100 hrs (HV)	500 °C 100 hrs (HV)
$V_{35}Cr_{33}Mn_2Fe_{12}W_{18}$	775±82	826±71	734±1.1		714±61
$V_{46}Cr_3Mn_1Ta_{10}W_{40}$	632±0.1			724±0.2	642±0.1
$V_{21}Cr_{18}Mn_9Fe_{17}Ta_{20}W_{15}$		1020±0.8			
$V_{36}Cr_{18}Fe_8Ta_{17}W_{21}$	693±0.5	1407±61			
$V_{26}Cr_{17}Fe_{32}Ta_{25}$	826±0.3				

The alloy composition with the highest hardness post-heat treatment (1407 HV) is for VCrFeTaW after annealing at 1500 °C for 48 hours. This may be associated with the lamellae microstructure with the tetragonal, FCC, and primitive phases as identified by the experimental XRD pattern. Fine lamellae microstructures of high entropy alloys have been demonstrated to typically display higher strength and hardness than that of coarse dendritic microstructures [44]. VCrMnFeW also displayed an increase in hardness post-homogenisation heat treatment. As-cast VCrMnFeW had a hardness of 775 HV and after heat treating at 1500 °C for 48 hours the hardness increased to 826 HV. A more homogeneous composition leads to a hardening effect due to solid-solution strengthening and precipitation strengthening. This increase can also be attributed to the formation of the brittle σ phase. In conventional alloys the inherent brittleness of the σ phase is derivative of the topologically close-packed structure which inhibits dislocation nucleation and movement [45].

Figure 6.59 shows the optical micrographs of the ‘homogenised’ VCrMnFeW and ‘homogenised’ VCrFeTaW alloys post-indentation. Small cracks leading from the indent can be observed in VCrMnFeW indicating a tendency for brittleness in these areas, whereas for VCrFeTaW there are no observable cracks.

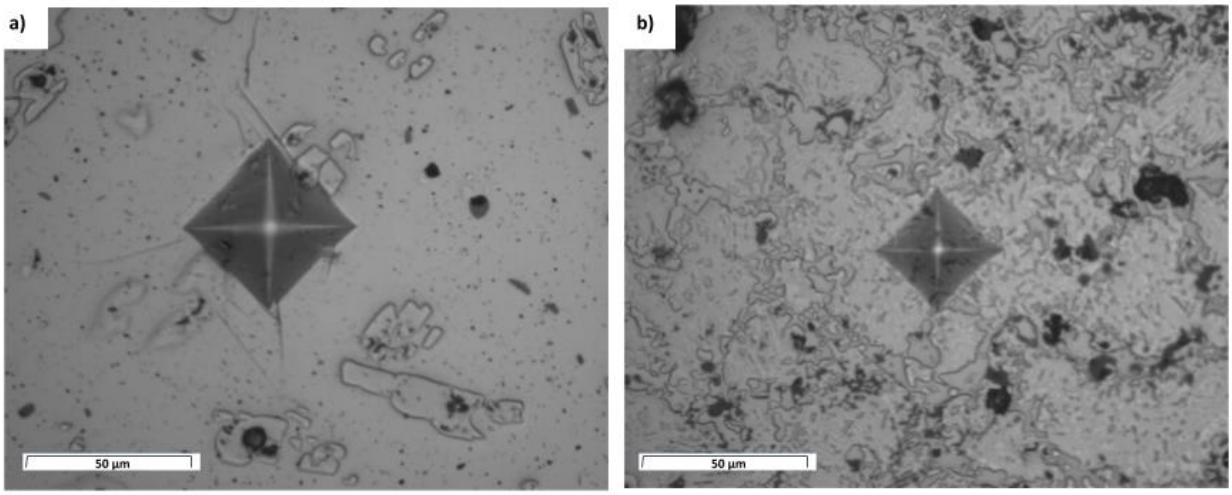

Figure 6.59: Optical micrographs of the a) 'homogenised' VCrMnFeW and b) 'homogenised' VCrFeTaW after hardness indenting at x40 magnification.

The lack of cracking of the VCrFeTaW 'homogenised' alloy, even with a high hardness of 1407 HV suggests that the lamella microstructure with the σ phase may be not as brittle as the spherical σ phase of the 'homogenised' VCrMnFeW. Furthermore, recent research of multiphase high entropy alloys has suggested that multicomponent σ phases may not be as brittle as the conventional stoichiometric intermetallic compounds [45], [46]. For the 'homogenised' VCrFeTaW the SEM-EDX point scan data reveals that the σ phase is likely to be composed of $Ta_{36}Fe_{29}V_{18}Cr_{12}$ whilst the 'homogenised' VCrMnFeW σ phase is predicted to be composed of mostly V-Cr (with maybe a small amount of manganese). Therefore, due to the multicomponent nature of the σ phase in the 'homogenised' VCrFeTaW, this may reveal the lack of brittle cracks in the optical micrographs. For VCrMnFeW, the homogenisation heat treatment, while still evident of some elemental segregation, is mostly successful. The loss of the dendritic microstructure and preservation of a BCC matrix is beneficial however, the precipitation of a secondary phase, a brittle σ phase, can be somewhat detrimental to the mechanical performance of the alloy.

6.10. Conclusion

Table 6.27 summarises the phase evolution of the five alloys (in the as-cast and heat-treated conditions) assessed in this work. The Thermo-Calc predictions of the major phases for each alloy is also included. From this table it can be identified that only one alloy, VCrMnTaW, was able to retain a single BCC phase upon thermal annealing.

Table 6.27: Summary of phases identified by experimental XRD for the as-cast and heat-treated alloys.

Alloy	State	Phase1	Phase2	Phase3
$V_{35}Cr_{33}Mn_2Fe_{12}W_{18}$	**As-cast**	**BCC** Im-3m	**BCC** Im-3m	
	1400 °C 18 hrs	**BCC** Im-3m		
	1500 °C 48 hrs	**BCC** Im-3m	**BCC** Im-3m	**Tetragonal** σCrFe (D8b) P42/mnm
	700 °C 100 hrs	**BCC** Im-3m		
	500 °C 100 hrs	**BCC** Im-3m	**BCC** Im-3m	
	TCHEA4	**BCC B2**	**σ**	
	SSOL4	**BCC A2**	**σ**	
$V_{46}Cr_3Mn_1Ta_{10}W_{40}$	**As-cast**	**BCC** Im-3m		
	700 °C 100 hrs	**BCC** Im-3m		
	500 °C 100 hrs	**BCC** Im-3m		
	TCHEA4	**BCC B2**	**μ**	
	SSOL4	**BCC A2**		
$V_{21}Cr_{18}Mn_9Fe_{17}Ta_{20}W_{15}$	**As-cast**	**FCC** Zincblende (B3)	**FCC** Heusler (L21)	**FCC** C15 Laves

		F43m	Fm-3m	Fd-3m
	1500 °C 48 hrs	**FCC** $NiTi_2$ Fd-3m	**FCC** Heusler (L21) Fm-3m	
	TCHEA4	**BCC B2**	**C14 Laves**	**C15 Laves** **μ**
	SSOL4	**BCC A2**	**C15 Laves**	**σ**
$V_{36}Cr_{18}Fe_8Ta_{17}W_{21}$	**As-cast**	**BCC** Im-3m	**BCC** Im-3m	**BCC** Im-3m
	1500 °C 48 hrs	**Tetragonal** $Mn_{12}Th$ (D2b) I4/mmm	**FCC** Fe_3W_3C (E93) Fd-3m	**Primitive** Perovskite (E21) Pm-3m
	500 °C 100hrs	**BCC** Im-3m	**BCC** Im-3m	
	TCHEA4	**BCC B2**	**C15 Laves**	**μ**
	SSOL4	**BCC A2**	**C15 Laves**	**σ**
$V_{26}Cr_{17}Fe_{32}Ta_{25}$	**As-cast**	**Hexagonal** C14 Laves P63/mmc		
	1500 °C 48 hrs	**Hexagonal** C14 Laves P63/mmc	**FCC** Fe_3W_3C (E93) Fd-3m	
	TCHEA4	**C15 Laves**	**σ**	**BCC B2** **C14 Laves**
	SSOL4	**BCC A2**	**C15 Laves**	**σ**

6.10.1. As-Cast

From Chapter 5: Alloy Design, the alloys were designed, using several design tools, to obtain single phase BCC solid solutions. The inconsistencies of the melting process, in correspondence with disparate alloying elements, resulted in alloy compositions that deviated from the designed high entropy alloys. Re-calculation of the HEA empirical parameters and Thermo-Calc simulations revealed that the fabricated alloys were still predicted to form a BCC solid solution. Characterisation of the as-cast condition alloys revealed that only VCrMnFeW, VCrMnTaW, and VCrFeTaW formed either a single BCC phase or multiple BCC phases. Interestingly VCrMnFeTaW formed three FCC phases, despite none of the constituents having an FCC crystal structure. Whilst very few single-phase HCP HEAs have been experimentally verified, VCrFeTa, in the as-cast condition had a single HCP phase, despite not being predicted by any of the design tools.

Whilst the experimental Vickers microhardness value were generally lower than the theoretical hardness (calculated using the rule of mixtures) they showed a corresponding increase in hardness with increasing atomic size difference. This is most likely attributed to the increase in atomic size misfit of the lattice, causing lattice distortion which results in an increase in relative overall hardness.

6.10.2. High Temperature Heat Treatment

The first heat treatment applied to the alloys was to determine if successful homogenisation of the microstructure could be obtained. These novel high entropy alloys contained relatively high amounts of refractory metals which increased the calculated melting point of the alloys. This, in turn, increased the required homogenisation temperature, however, due to the facilities available only 1400 °C and 1500 °C heat treatments were possible.

Whilst elemental homogenisation was not achieved and none of the alloys displayed a typical grain structure post-homogenisation, observation of the SEM micrographs of all of the high temperature treated alloys did reveal a change in the microstructures in comparison to the as-cast condition. Additionally, all of the alloys heat treated at 1500 °C underwent phase transformations showing that the as-cast phases were not thermally stable at these high temperatures. The microhardness values of the high temperature alloys shows a considerable increase in hardness from the as-cast condition. For VCrMnFeW this may be likely due to the precipitation of the brittle σ phase, also evident by the cracking observed post-indentation in the optical micrographs.

6.10.3. Low Temperature Heat Treatment

For VCrMnFeW and VCrMnTaW the low temperature heat treatment of the alloys revealed very little change from the as-cast condition as observed from the SEM micrographs. This may be likely due to the longer heat treatment duration needed to reach equilibrium conditions. Successful homogenisation of the alloys followed by subsequent low temperature ageing heat treatments is required to observe the extent of precipitation of intermetallic compounds and secondary phase formation.

6.10.4. Design Strategy

In Chapter 5: Design of Novel High Entropy Alloys, several design processes were adopted for the refinement of equimolar low activation high entropy alloys. The alloy compositions were refined to adhere to melting restrictions and to minimise secondary phases. In this chapter, the validation of these design process can be undertaken.

The Thermo-Calc predictions of the alloy compositions, for the most part, were inaccurate in predicting the majority phases of the as-cast and heat-treated alloys. However, for $V_{46}Cr_3Mn_1Ta_{10}W_{40}$, which has the overall lowest entropy (9.19 $JK^{-1}mol^{-1}$), both databases successfully predicted the formation of a BCC phase. This may be likely due to VCrMnTaW having a composition comparable to that of a conventional alloy – vanadium and tungsten compose most of the alloy with small amounts of the other constituents. The highest configurational entropy alloy, $V_{21}Cr_{18}Mn_9Fe_{17}Ta_{20}W_{15}$ (14.64 $JK^{-1}mol^{-1}$) displayed three separate FCC phases in the as-cast condition and two FCC phases post-homogenisation treatment. Both databases failed to predict any FCC phase formation at any temperature or even in small concentrations. The presence of interstitial contaminants may also be the key reason for the discrepancies here. It can be tentatively suggested that for the higher configurational entropy alloys in this work, the Thermo-Calc predictions of stable phases were found to be lacking. Comparison between the two thermodynamic databases reveals that the TCHEA4 database consistently predicts the formation of an ordered BCC B2 phase (in some cases even as the majority phase), whilst the SSOL4 database will predict a disordered BCC A2 phase in place of an ordered phase.

6.10.5. Candidate Plasma-Facing Material

Whilst VCrMnTaW was the only alloy in this study to retain a single BCC phase upon heat treatment. However, a high temperature homogenisation treatment was unavailable for this alloy composition, so it is currently unknown whether the as-cast BCC phase is stable at elevated temperatures. Furthermore, $V_{46}Cr_3Mn_1Ta_{10}W_{40}$ has the overall lowest entropy (9.19 $JK^{-1}mol^{-1}$) of all the fabricated alloys in this work. Therefore, the most promising alloy for the

investigation of potential armour materials is $V_{35}Cr_{33}Mn_2Fe_{12}W_{18}$ which demonstrated a stable BCC at high and low temperature heat treatments. These experimental findings also correlated with the HEA empirical parameters predictions and the Thermo-Calc simulations. Additionally, the comparison of VCrMnFeW with VCrMoW demonstrated that further research is required to determine if VCrMnFeW could also be radiation damage tolerant to heavy ion implantation. Both alloys in the as-cast state exhibited two BCC phases (for VCrMoW this was hypothesised to result from the overlapping of two similar BCC phases resulting in the observation of a single BCC phase with broad peaks). And for VCrMoW, this metastable as-cast phase was shown to have excellent radiation resistance discussed in Section 4.5. Therefore, further research is required to see if there are any similarities between the two alloys. However, a difference between the two alloys is shown in the homogenisation of VCrMnFeW which indicated the small formation of the σ phase. Therefore, the stability of the σ phase formed at high temperatures is detailed in Chapter 7: HT-XRD of VCrMnFeW.

6.11. References

[1] Senkov, O.N., Wilks, G.B., Miracle, D.B., Chuang, C.P. and Liaw, P.K., 2010. Refractory high-entropy alloys. Intermetallics, 18(9), pp.1758-1765.

[2] Khalajzadeh, V. and Beckermann, C., 2020. Simulation of shrinkage porosity formation during alloy solidification. Metallurgical and Materials Transactions A, 51(5), pp.2239-2254.

[3] Khalajzadeh, V., Carlson, K.D., Backman, D.G. and Beckermann, C., 2017. A pore-centric model for combined shrinkage and gas porosity in alloy solidification. Metallurgical and Materials Transactions A, 48(4), pp.1797-1816.

[4] Zhang, A., Guo, Z., Jiang, B., Du, J., Wang, C., Huang, G., Zhang, D., Liu, F., Xiong, S. and Pan, F., 2021. Multiphase and multiphysics modeling of dendrite growth and gas porosity evolution during solidification. Acta Materialia, 214, p.117005.

[5] Wei, Q., Shen, Q., Zhang, J., Chen, B., Luo, G. and Zhang, L., 2018. Microstructure and mechanical property of a novel ReMoTaW high-entropy alloy with high density. International Journal of Refractory Metals and Hard Materials, 77, pp.8-11.

[6] Nagase, T., Mizuuchi, K. and Nakano, T., 2019. Solidification microstructures of the ingots obtained by arc melting and cold crucible levitation melting in TiNbTaZr medium-entropy alloy and TiNbTaZrX (X= V, Mo, W) high-entropy alloys. Entropy, 21(5), p.483.

[7] Laurent-Brocq, M., Akhatova, A., Perrière, L., Chebini, S., Sauvage, X., Leroy, E. and Champion, Y., 2015. Insights into the phase diagram of the CrMnFeCoNi high entropy alloy. Acta Materialia, 88, pp.355-365.

[8] Nasledov, D.N. and Gorí͡ũ̃nova, N.A. eds., 1965. Soviet Research in New Semiconductor Materials. Springer.

[9] Graf, T., Casper, F., Winterlik, J., Balke, B., Fecher, G.H. and Felser, C., 2009. Crystal structure of new Heusler compounds. Zeitschrift für anorganische und allgemeine Chemie, 635(6-7), pp.976-981.

[10] Buschow, K.H.J., 1982. Crystallization of amorphous Zr1− xCox alloys. Journal of the Less Common Metals, 85, pp.221-231.

[11] Balema, V.P., Pecharsky, A.O., Ellis, T.W. and Pecharsky, V.K., 2000. Preparation and electrochemical properties of some (Sc1− xTix) Ni alloys. Journal of alloys and compounds, 296(1-2), pp.67-71.

[12] Romaka, V.V., Rogl, P., Romaka, L., Stadnyk, Y., Grytsiv, A., Lakh, O. and Krayovskii, V., 2013. Peculiarities of structural disorder in Zr-and Hf-containing Heusler and half-Heusler stannides. Intermetallics, 35, pp.45-52.

[13] Hmel N., Dmytriv G. "Mn solubility in binary compound Ti2Co at 1070 K". Visn. L'viv. Derzh. Univ., Ser. Khim. 2013, 54, 52.

[14] Bhowmik, A., Jones, C.N., Edmonds, I.M. and Stone, H.J., 2012. Effect of Mo, Al and Si on the microstructure and mechanical properties of Cr–Cr2Ta based alloys. Journal of alloys and compounds, 530, pp.169-177.

[15] Gao, M.C. and Alman, D.E., 2013. Searching for next single-phase high-entropy alloy compositions. Entropy, 15(10), pp.4504-4519.

[16] Gao, M.C., Zhang, B., Guo, S.M., Qiao, J.W. and Hawk, J.A., 2016. High-entropy alloys in hexagonal close-packed structure. Metallurgical and Materials Transactions A, 47(7), pp.3322-3332.

[17] Zhao, Y.J., Qiao, J.W., Ma, S.G., Gao, M.C., Yang, H.J., Chen, M.W. and Zhang, Y., 2016. A hexagonal close-packed high-entropy alloy: The effect of entropy. Materials & Design, 96, pp.10-15.

[18] Zhang, Y., Zuo, T.T., Tang, Z., Gao, M.C., Dahmen, K.A., Liaw, P.K. and Lu, Z.P., 2014. Microstructures and properties of high-entropy alloys. Progress in Materials Science, 61, pp.1-93.

[19] Krapivka, N.A. and Firstov, S.A., 2017. High-entropy alloys: Interrelations between electron concentration, phase composition, lattice parameter, and properties. Physics of Metals and Metallography, 118(10), pp.970-981.

[20] Stein, F. and Leineweber, A., 2020. Laves phases: a review of their functional and structural applications and an improved fundamental understanding of stability and properties. Journal of Materials Science, pp.1-107.

[21] Zhang, B., Gao, M.C., Zhang, Y. and Guo, S.M., 2015. Senary refractory high-entropy alloy CrxMoNbTaVW. Calphad, 51, pp.193-201.

[22] Leo, A., Hansch, C. and Elkins, D., 1971. Partition coefficients and their uses. Chemical reviews, 71(6), pp.525-616.

[23] Brando, M., Kerkau, A., Todorova, A., Yamada, Y., Khuntia, P., Förster, T., Burkhard, U., Baenitz, M. and Kreiner, G., 2016. Quantum Phase Transitions and Multicriticality in Ta (Fe1− x V x) 2. Journal of the Physical Society of Japan, 85(8), p.084707.

[24] Holleck, H. and THUMMLER, F., 1967. TERNARY COMPLEX CARBIDES NITRIDES AND OXIDES WITH PARTIALLY COMPLETED TI2NI-STRUCTURE. MONATSHEFTE FUR CHEMIE, 98(1), p.133.

[25] Gladyshevskii, E.I., Fedorov, T.F., Skolozdra, R.V. and Gorshkova, L.V., 1967. System WV-Si. Soviet Powder Metallurgy and Metal Ceramics, 6(5), pp.406-408.

[26] van Arkel, A.E., 1926. Over den bouw van mengkristallen. Laboratoria NV Philips' Gloeilampenfabrieken.

[27] Lomnytska, Y., Babizhetskyy, V., Oliynyk, A., Toma, O., Dzevenko, M. and Mar, A., 2016. Interaction of tantalum, chromium, and phosphorus at 1070 K: Phase diagram and structural chemistry. Journal of Solid State Chemistry, 235, pp.50-57.

[28] Martens, H.E. and Duwez, P., 1951. Phase Relationships in the Iron-Chromium-Vanadium System. JET PROPULSION LAB PASADENA CA.

[29] Tan, Y.Y., Su, M.Y., Xie, Z.C., Chen, Z.J., Gong, Y., Zheng, L.R., Shi, Z., Mo, G., Li, Y., Li, L.W. and Wang, H.Y., 2021. Chemical composition dependent local lattice distortions and magnetism in high entropy alloys. Intermetallics, 129, p.107050.

[30] Kusma, J.B. and Laube, E., 1965. Die Kristallstrukturen von YAg 2, YAu 2 und YZn 12. Monatshefte für Chemie und verwandte Teile anderer Wissenschaften, 96(5), pp.1496-1502.

[31] Josien, F.A. and Mary, Y., 1967. REDUCTION OF NICKEL OXIDE BY TUNGSTEN CARBIDE. A NEW DOUBLE CARBIDE NI2W4C. REVUE DE CHIMIE MINERALE, 4(3), p.699.

[32] Filip’ev, V.S. and Fesenko, E.G., 1961. Preparation and Unit Cell of Ä 2 Ç IB II O 6 Compounds. Kristallografiya, 6(5), pp.770-772.

[33] Davey, W.P., 1925. Precision measurements of the lattice constants of twelve common metals. Physical Review, 25(6), p.753.

[34] Drake, B.L., Grandjean, F., Kangas, M.J., Okudzeto, E.K., Karki, A.B., Sougrati, M.T., Young, D.P., Long, G.J. and Chan, J.Y., 2010. Crystal growth, transport, and the structural and magnetic properties of Ln4FeGa12 with Ln= Y, Tb, Dy, Ho, and Er. Inorganic chemistry, 49(2), pp.445-456.

[35] Hasegawa, H., 1987. Electronic structures and local magnetic moments in ferromagnetic and antiferromagnetic FexRh1− x alloys. Journal of magnetism and magnetic materials, 66(2), pp.175-186.

[36] Stein, F., Vogel, S.C., Eumann, M. and Palm, M., 2010. Determination of the crystal structure of the ε phase in the Fe–Al system by high-temperature neutron diffraction. Intermetallics, 18(1), pp.150-156.

[37] Pipitz, E., and R. Kieffer. "EINFLUSS VON LEGIERUNGSZUSATZEN AUF FESTIGKEITSEIGENSCHAFTEN UND REKRISTALLISATION VON VAKUUMGESINTERTEM MOLYBDAN." ZEITSCHRIFT FUR METALLKUNDE 46, no. 3 (1955): 187-194.

[38] Barron, P.J., Carruthers, A.W., Fellowes, J.W., Jones, N.G., Dawson, H. and Pickering, E.J., 2020. Towards V-based high-entropy alloys for nuclear fusion applications. Scripta Materialia, 176, pp.12-16.

[39] Tylkina et al. Proc. Acad. Sci. USSR (Chem. Sec.) 1960, 131, 247.

[40] Tsai, M.H., Yuan, H., Cheng, G., Xu, W., Jian, W.W., Chuang, M.H., Juan, C.C., Yeh, A.C., Lin, S.J. and Zhu, Y., 2013. Significant hardening due to the formation of a σ phase matrix in a high entropy alloy. Intermetallics, 33, pp.81-86.

[41] Baker, H. and Okamoto, H., 1992. ASM Handbook. Vol. 3. Alloy Phase Diagrams. ASM International, Materials Park, Ohio 44073-0002, USA, 1992. 501.

[42] Stepanov, N.D., Shaysultanov, D.G., Salishchev, G.A., Tikhonovsky, M.A., Oleynik, E.E., Tortika, A.S. and Senkov, O.N., 2015. Effect of V content on microstructure and mechanical properties of the CoCrFeMnNiVx high entropy alloys. Journal of Alloys and Compounds, 628, pp.170-185.

[43] Jiang, H., Han, K., Qiao, D., Lu, Y., Cao, Z. and Li, T., 2018. Effects of Ta addition on the microstructures and mechanical properties of CoCrFeNi high entropy alloy. Materials Chemistry and Physics, 210, pp.43-48.

[44] Jiang, H., Huang, T.D., Su, C., Zhang, H.B., Han, K.M. and Qin, S.X., 2020. Microstructure and Mechanical Behavior of CrFeNi 2 V 0.5 W x (x= 0, 0.25) High-Entropy Alloys. Acta Metallurgica Sinica (English Letters), pp.1-7.

[45] Chung, D.H., Liu, X.D. and Yang, Y., 2020. Fracture of σ phase containing Co–Cr–Ni–Mo medium entropy alloys. Journal of Alloys and Compounds, 846, p.156189.

[46] Jo, Y.H., Choi, W.M., Kim, D.G., Zargaran, A., Lee, K., Sung, H., Sohn, S.S., Kim, H.S., Lee, B.J. and Lee, S., 2019. Utilization of brittle σ phase for strengthening and strain hardening in ductile VCrFeNi high-entropy alloy. Materials Science and Engineering: A, 743, pp.665-674.

Chapter 7: HT-XRD of VCrMnFeW

7.1. Introduction

The detailed experimental characterisation of the as-cast alloy compositions designed in Chapter 5: Design of Novel Low Activation High Entropy Alloys was investigated and assessed in regard to their suitability as plasma-facing materials. The stability of the phases identified in the as-cast conditions a range of temperatures and durations were also evaluated. From this analysis, detailed in Chapter 6: Experimental Assessment of Novel High Entropy Alloys, the alloy composition, $V_{0.35}Cr_{0.33}Mn_{0.02}Fe_{0.12}W_{0.18}$, was established as a potential candidate material for structural components of advanced nuclear fusion reactors. In this chapter, further analysis of $V_{0.35}Cr_{0.33}Mn_{0.02}Fe_{0.12}W_{0.18}$ (hereon referred to as VCrMnFeW) using detailed characterisation techniques (high-temperature X-ray diffraction) is conducted to investigate the stability of the microstructure and phases of the as-cast alloy.

7.2. Methodology

Several heat treatments of the as-cast VCrMnFeW were explored to establish the stability of the as-cast BCC phases. Extensive annealing treatments at various temperatures are not always feasible due to time constraints and the requirements of large amounts of sample. X-ray diffraction (XRD) combined with in situ high-temperature capabilities is a tool used to investigate structural transformations and thermodynamic stability of phases. The in situ thermal observation of as-cast VCrMnFeW was used to determine any temperature-dependent crystal lattice transformations quickly and efficiently across a wide range of temperatures. For this work, an as-cast sample of VCrMnFeW was mechanically crushed into a fine powder and placed into a narrow silica capillary. This sample was then analysed under vacuum in the PANalytical Xpert^3 with a furnace attachment. The full outline of the experimental procedure is detailed in Chapter 3: Experimental Methodology. The as-cast powder sample was heated from room temperature (25 °C) to 1000 °C and the sample was isothermally held at every 100 °C increments and XRD data were collected at these temperatures. Once the maximum operating temperature (1000 °C) was reached, the sample was cooled to room temperature with XRD data being collected again at every 100 °C increments until the furnace reached 100 °C.

7.3. Results and Discussion

Figure 7.1 shows the HT-XRD data collected for the as-cast VCrMnFeW powder sample on heating from room temperature to 1000 °C.

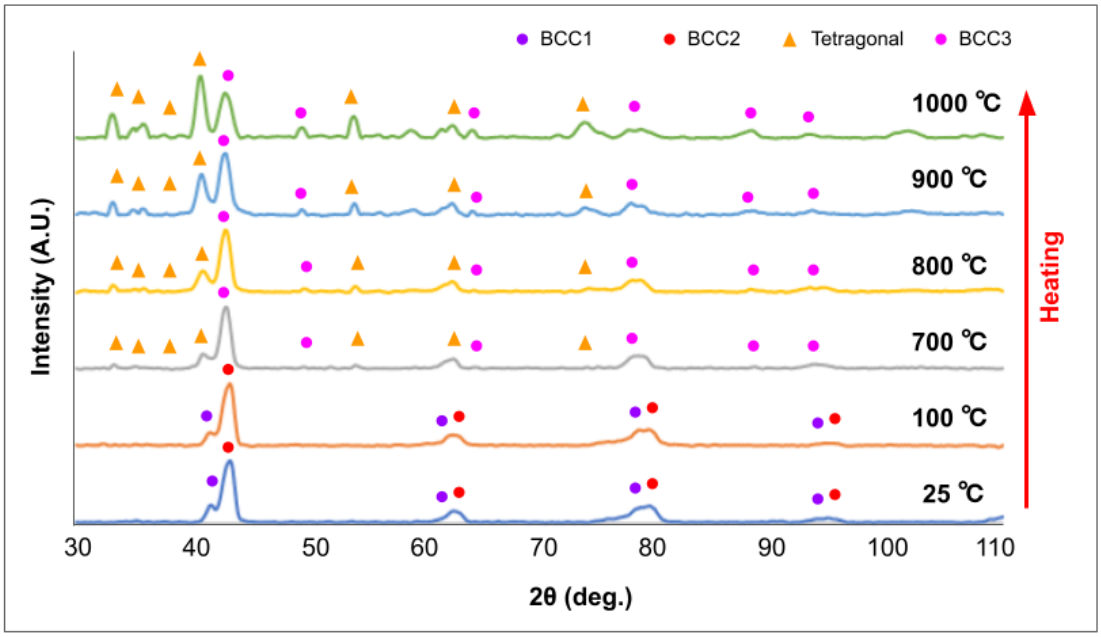

Figure 7.1: Experimental XRD patterns for the as-cast VCrMnFeW from room temperature on heating to 1000 °C.

The experimental XRD pattern is observed at room temperature to have two distinct BCC phases (space group Im-3m) with similar lattice parameters. Comparison with the as-cast XRD data collected at ambient room temperature (as shown in Chapter 6: Experimental Assessment of Novel High Entropy Alloys) highlights some differences in the XRD peaks. Figure 7.2 shows the as-cast ambient room temperature of the bulk VCrMnFeW.

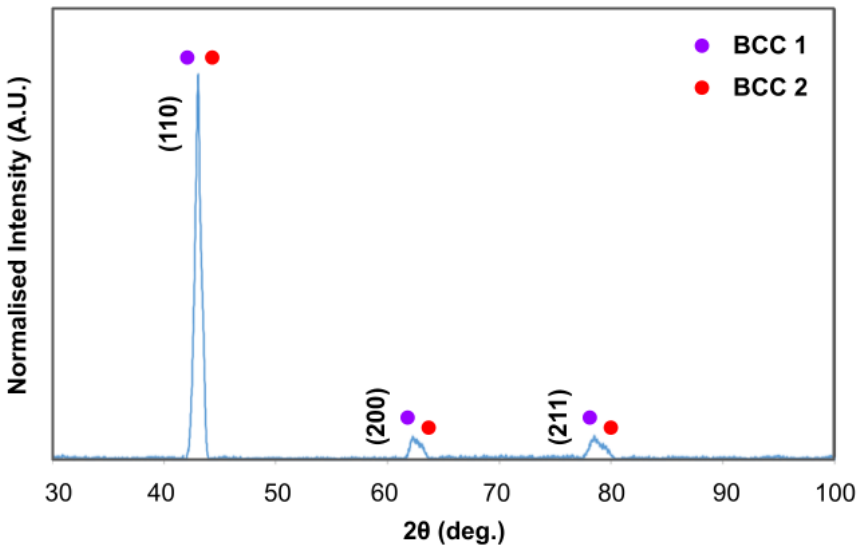

Figure 7.2: XRD pattern of bulk as-cast VCrMnFeW at room temperature

Observation of the HT-XRD VCrMnFeW at room temperature reveals two BCC phases, with two distinct peaks at around 40 °2θ, whereas in the as-cast bulk VCrMnFeW experimental XRD pattern taken at ambient room temperature this initial peak at 42 °2θ is a sharp single peak. This difference may be characterised by the variation in resolution of the XRD diffractometers. The HT-XRD was performed using a PANalytical Xpert^3 diffractometer which has a higher resolution and therefore there is a resolution of broader peaks into multiple defined peaks. At increasing 2θ both the bulk material and powdered sample display broad, sloping peaks (indicative of two overlapping similar BCC peaks).

For the HT-XRD data, on heating from 200 °C to 600 °C, the XRD pattern remains unchanged - two BCC phases remain with no further precipitation. For clarity, this data is not included in the composite Figure 7.1. From 700 °C, one BCC phase decomposes whilst an additional phase precipitates; small peaks corresponding to a tetragonal crystal structure (space group I4/mmm) are thermally-induced and become more prominent and higher in intensity with increasing temperature up to 1000 °C. This tetragonal crystal structure, as discussed in depth in Chapter 6: Experimental Assessment of Novel High Entropy Alloys, is consistent with the σ phase. Interestingly, whilst the formation of the σ phase begins to appear from 700 °C, from the bulk analysis of VCrMnFeW heat treated at a range of temperatures, there is no formation of a σ phase at the 700 °C or 1400 °C heat treatments. Figure 7.3 shows the XRD patterns of the bulk VCrMnFeW after heat treating at 700 °C and 1400 °C. Both patterns display a single BCC phase without any indication of the formation of a σ phase. These results are in direct conflict with the HT-XRD data and are discussed in the cooling section of the chapter.

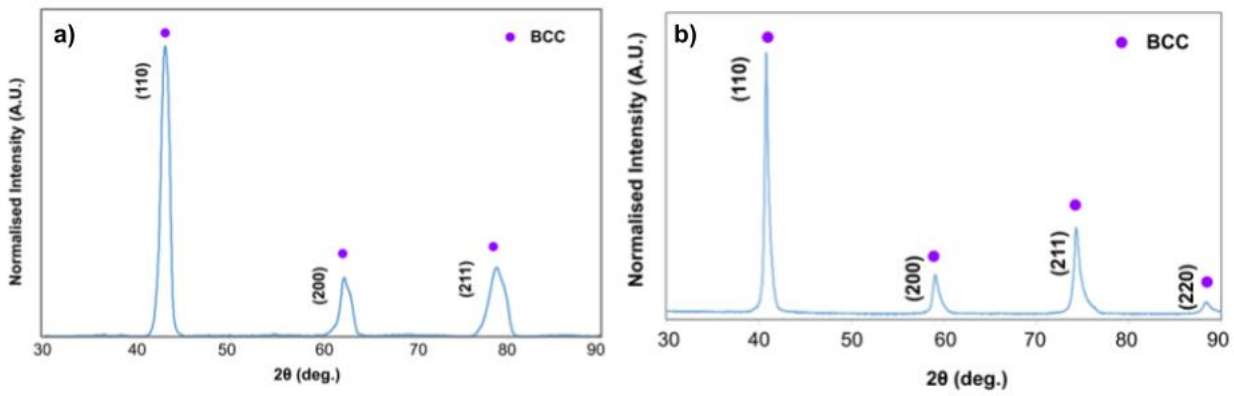

Figure 7.3: Experimental XRD patterns of bulk VCrMnFeW after heat treatment at a) 700 °C for 100 hours and b) 1400 °C for 18 hours

Figure 7.4 shows the HT-XRD data collected for the as-cast VCrMnFeW powder sample on cooling from 1000 °C to room temperature.

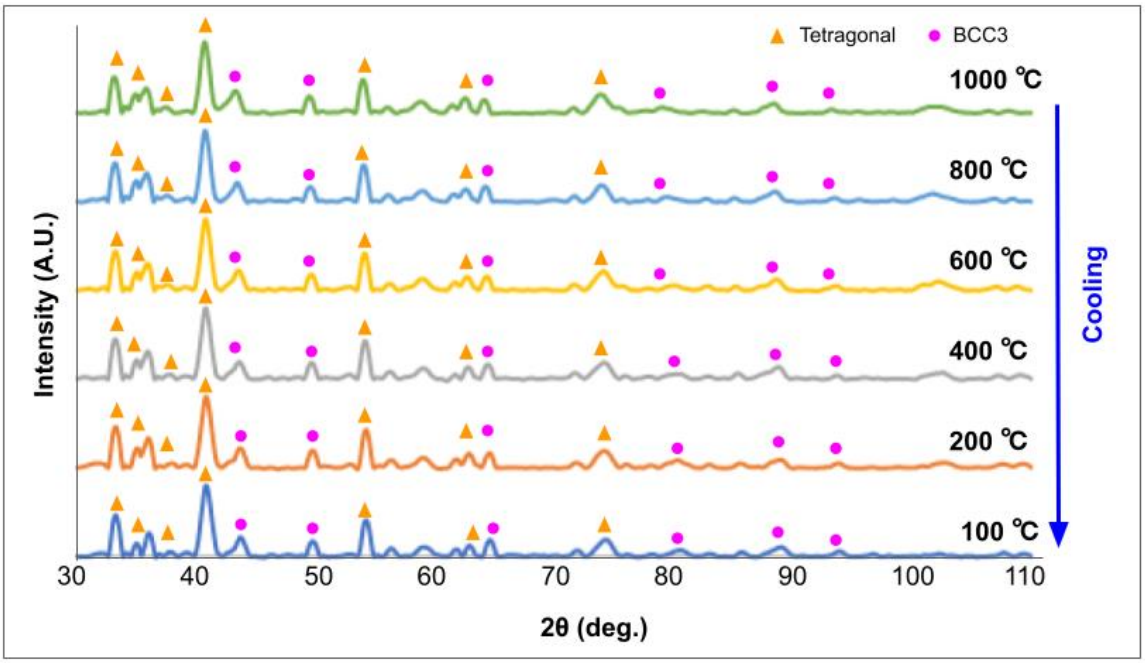

Figure 7.4: Experimental XRD patterns for the as-cast VCrMnFeW from room temperature on heating to 1000 °C.

Compilation of XRD data collected from the sample upon slow cooling from 1000 °C to room temperature reveals that the precipitation of the σ phase remains stable, does not decompose at lower temperatures, and there is no significant shift in any of the peaks. This irreversible phase transformation from BCC to σ begins upon heating at approximately 700 °C and persists upon further heating to 1000 °C and upon subsequent cooling to room temperature.

A similar irreversible phase transformation was observed by Gandy et al [1] where, upon heating to above 400 °C, a single-phase BCC high entropy alloy, SiFeVCr, similarly formed a stable σ phase. The σ phase detected in SiFeVCr was theorised to derive from the Fe-Cr binary phase diagram and is based on the tetragonal crystal structure with a P4/mnm space group. This coincides with the phases identified in the bulk as-cast VCrMnFeW homogenised at 1500 °C. Figure 7.5 shows the XRD pattern of the bulk VCrMnFeW which identifies two BCC phases (space group Im-3m) and a σ phase (space group P4/mnm).

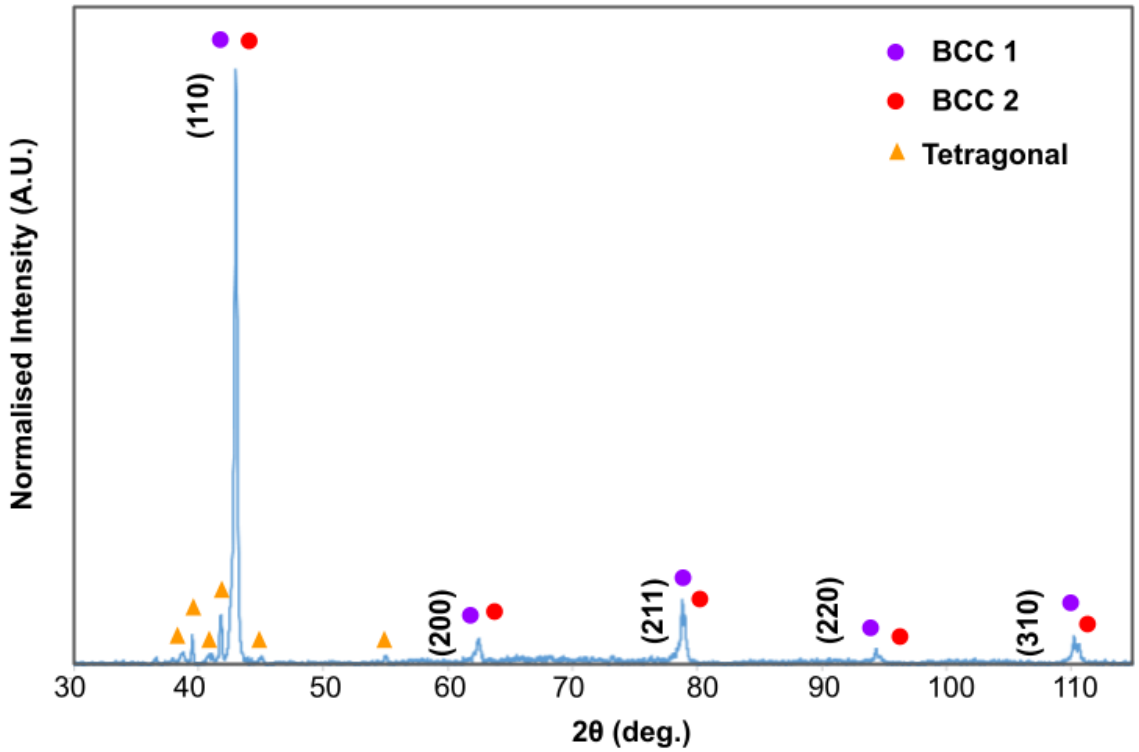

Figure 7.5: Experimental XRD pattern of the bulk VCrMnFeW heat treated at 1500 °C for 48 hours.

However, from the data collected using the HT-XRD method, the space group that best matches the σ phase in the XRD pattern corresponds with a tetragonal crystal structure with an I4/mmm space group. This lattice structure is the same as the σ phase identified in the homogenised VCrFeTaW (with a prototype $Mn_{12}Th$ D2b structure). The SEM-EDX point scans revealed that this phase was likely composed of a near equimolar composition of VCrFeTa (and mostly tantalum and iron-rich). The difference in space groups between the bulk and powdered samples may be due to a variation between the compositions of the σ phases; the powder sample may be more multi-component in nature (much like the I4/mmm phase observed in VCrFeTaW) and the homogenised bulk sample may be composed of a majority V-Cr with small amounts of manganese (as discussed in Chapter 6: Matrix of Alloys). The disparity between the σ phases may have arisen from the differences in cooling rates between the annealed sample and the HT-XRD powder sample. The bulk sample annealed at 1500 °C

for 48 hours was immediately followed by quenching in room temperature water upon removal from the furnace; this aims to kinetically trap high-temperature phases. However, it cannot be ascertained if 48 hours is sufficient time for the formation of equilibrium phases at 1500 °C. For powder HT-XRD the sample is much smaller compared to the bulk sample heat treated in a furnace, and so will need less time to reach equilibrium conditions. Additionally, the HT-XRD furnace attachment has a limit of 1000 °C and so assumptions of phase transformations above this temperature, specifically at 1500 °C, cannot be made. As discussed previously, the resolution of the equipment in both XRD techniques varies and so the appearance of additional smaller peaks is likely to be observed during the HT-XRD and can be identified as a secondary phase, whilst for the bulk samples, this secondary phase may not be readily discernible from the background noise.

7.4. Conclusion

Overall, the HT-XRD results generally reflect those of the annealing treatments conducted on bulk samples of VCrMnFeW in Chapter 6: Experimental Assessment of Novel High Entropy Alloys. The as-cast bulk sample corresponds with the room temperature HT-XRD pattern, and the bulk homogenised experimental XRD pattern coincides with the additional formation of the σ phase at intermediate-higher temperatures. Overall, there is an irreversible phase transformation of VCrMnFeW from two BCC phases to a BCC phase and a σ phase and this is reflected in the HT-XRD results.

However, there are some discrepancies between the two XRD methods which may be attributed to chemical homogeneity between the two samples. The bulk samples heat-treated at 500 °C and 700 °C reveal a BCC single-phase with no indication of σ phase precipitation. Whilst for the 700 °C powder sample using HT-XRD, there are very small peaks correlating to the σ phase indicating the start of the precipitation of this secondary phase. Additionally, there could also be some differences in chemical homogeneity between the two different samples arising from the VAM process. The observation of this σ phase using HT-XRD may be due to the resolution of the diffractometer or due to the smaller sample size being able to reach equilibrium conditions much quicker. At 800 °C the peaks corresponding to the tetragonal crystal structure are more defined and higher in intensity concluding that the formation of the σ phase can be reasonably observed. Annealing VCrMnFeW at 800 °C in a furnace for a long duration will likely precipitate the thermally-induced σ phase. It is likely that a smaller sized sample and a heat treatment exceeding 100 °C is required for observation of the σ phase.

7.5. References

[1] Gandy, A.S., Jim, B., Coe, G., Patel, D., Hardwick, L., Akhmadaliev, S., Reeves-McLaren, N. and Goodall, R., 2019. High temperature and ion implantation-induced phase transformations in novel reduced activation Si-Fe-V-Cr (-Mo) high entropy alloys. Frontiers in Materials, 6, p.146.

Chapter 8: Conclusion and Future Work

8.1. Summary

This thesis has successfully assessed several alloy design processes for the investigation of low activation high entropy alloys that form stable BCC solid solutions. The aim of this work was to design a series of potential plasma-facing materials based on low activation and refractory high entropy alloys. The design processes used in this work were evaluated and verified using characterisation techniques to determine the thermal stability of phases formed.

The foundation work set out in Chapter 4 for the novel alloy $V_{2.5}Cr_{1.2}WMoCo_{0.04}$, investigated the stability of the metastable multi-BCC phase high entropy alloy. Whilst this alloy contained high activation elements, including molybdenum (and so is rendered unsuitable for nuclear fusion applications) all the refractory elements demonstrated complete immiscibility with one another and so promotes the formation of a BCC structure solid solution. Nonetheless, $V_{2.5}Cr_{1.2}WMoCo_{0.04}$ demonstrated excellent radiation resistance despite having a dendritic microstructure and exhibiting elemental segregation. Following a longer duration heat treatment at 1187 °C, three equilibrium phases formed – a BCC phase, an orthorhombic phase, and a tetragonal phase. Therefore, whilst the as-cast phases were retained after 5 MeV Au^{2+} ion implantation up to 40 dpa and showed tolerance against irradiation, interestingly these phases are not necessarily the most thermally stable. Furthermore, mechanical testing suggests that significant resistance against radiation hardening, and embrittlement may be due to self-healing and recombination of radiation-induced defects. Additional thermal treatments to reduce the elemental segregation showed the precipitation of a mostly vanadium-rich BCC phase and with longer duration of heat treatment this phase became enriched in tungsten. From these thermal studies, it was clear that a longer duration homogenisation treatment should be applied for high entropy alloys higher in tungsten content to reach equilibrium conditions.

After the successful display of radiation damage tolerance of the refractory high entropy alloy $V_{2.5}Cr_{1.2}WMoCo_{0.04}$, the same alloy design methods used in Chapter 4 were employed to identify promising low activation alloy compositions with similar radiation resistance. Potential refractory elements were highlighted, based on low activation properties and high temperature capabilities. A range of suitable alloy systems were designed for the assessment of high entropy alloy design parameters. One of these parameters, maximisation of configuration entropy, was probed using the designed alloy VCrMnFeTaW which has all the considered

elements in one alloy. Substitution of elements (Ta and Fe) for the alloys VCrMnFeW and VCrMnTaW will also investigate the effects of different elemental properties on phase formation. Elemental combination which could potentially promote the formation of unwanted brittle intermetallic phases were evaluated using available assessed binary phase diagrams. The σ phase and the Laves phase both readily form in high entropy alloys and are encouraged by increasing the constituents of these phases in the alloy (i.e., equimolar compositions may be too high concentration for some elements). For example, V, Cr, Fe, and Ta can all readily form a σ phase. Therefore, some elemental limitations must be made to discourage this. Additionally, due to the available manufacturing processes, some volatile elements can pose problematic issues during the melting process. High melting point elements (like tungsten) and low boiling point elements (like manganese) must be reduced. The alloys VCrFeTa and VCrFeTaW were designed. Thermo-Calc simulations were performed of the proposed high entropy alloy systems with consideration of these constraints. Overall, the refinement processes resulted in a series of novel low activation high entropy alloy compositions (deviated from equimolar compositions) suitable for consideration for application as plasma-facing materials.

These alloys were experimentally assessed for thermal stability – high temperature homogenisation treatments and intermediate longer duration heat treatments were applied for the investigation of microstructural changes. The HEA empirical parameters were assessed for the formation of a single BCC phase, however, only $V_{46}Cr_3Mn_1Ta_{10}W_{40}$ was identified to have a single BCC phase in the as-cast state. $V_{21}Cr_{18}Mn_9Fe_{17}Ta_{20}W_{15}$ surprisingly displayed three distinct FCC phases despite not being predicted an FCC phase in the Thermo-Calc simulations or HEA empirical parameters. Upon high temperature heat treatment these transformed in two FCC phases. $V_{36}Cr_{18}Fe_8Ta_{17}W_{21}$ exhibited three BCC phases in the observed, however upon high temperature homogenisation these phases transformed into a σ, FCC, and primitive structure phases. Unusually, $V_{26}Cr_{17}Fe_{32}Ta_{25}$ in the as-cast state exhibited a single C14 Laves phase and demonstrated the highest hardness value – likely attributed to the dendritic microstructure. Also, as a general trend, the increase in atomic size difference between the elements of the alloy strongly correlated with an increase in hardness values. This was credited to increase in atomic size misfit of the lattice causing a consequential increase in overall hardness. Upon heat treatment, significant formation of an inherently brittle stoichiometric σ phase causes an increase in the overall hardness. This was observed for VCrMnFeW where subsequent cracking was observed from optical micrographs. The lack of cracking from indents for the homogenised VCrFeTaW was attributed to the multiphase σ phase which is theorised to be more ductile than its counterpart. Furthermore, for all the alloys in this study, 1500 °C for 48 hours was insufficient time for the homogenisation of elemental

segregation. Additionally, for the lower temperature heat treatment there was little change observed from the as-cast condition from the XRD and SEM results.

Overall, the assessment of two thermodynamic databases SSOL4 and TCHEA4 of Thermo-Calc could be undertaken by comparison with experimental results. For the most part, for alloy compositions nearing equimolar compositions, the Thermo-Calc predictions were inaccurate. The alloy with the lowest configurational entropy, VCrMnTaW, proved to be the most successful predictions whilst the highest configurational entropy alloy VCrMnFeTaW were the most incorrect. This is likely due to the tendency of conventional alloy compositions to be used in Thermo-Calc.

The alloy with the greatest potential for use as a plasma-facing alloy is $V_{35}Cr_{33}Mn_2Fe_{12}W_{18}$. In the as-cast condition, the alloy exhibited a typical dendritic microstructure with elemental segregation (tungsten enrichment in the dendrite arms and a higher vanadium content in the interdendritic regions) much like VCrMoW, with two very similar BCC phases. Additionally, the morphology of the microstructure of VCrMnFeW homogenised at 1400 °C resembled that of VCrMoW with a grey BCC matrix and additional fine precipitation. It is hypothesised that these precipitates may be a BCC phase or an additional tetragonal phase, observed by XRD. Further TEM analysis is required to determine the exact crystal structure. HT-XRD revealed that this tetragonal phase is an irreversible phase transformation which begins to form at around 700 °C upon heating from room temperature. The similarities between VCrMnFeW and VCrMoW suggests that VCrMnFeW in the as-cast condition may also demonstrate similar radiation damage resistance.

Thermal stability of a BCC solid solution is incredibly important for plasma-facing material, as precipitation of brittle phases during service is detrimental to the mechanical performance of the component. Whilst VCrMoW wasn't thermally stable as a single BCC phase, this metastable phase did show some promising radiation damage tolerance. Microstructural investigation of the thermal stability of a system of novel low activation refractory high entropy alloys revealed a promising alloy VCrMnFeW which has demonstrated similar potential for radiation resistance.

8.2. Future Work

The fundamental investigations of the designed alloys in Chapter 6 and Chapter 4 gave insight into the stability of the as-cast phases at higher and lower temperatures. However, detailed

below are some further experiments that can be conducted for the assessment of these materials for fusion applications.

- A higher temperature homogenisation heat treatment (ideally around 1700 °C) for the assessment of reduction of elemental segregation. This is required for the successful homogenisation of the alloys, then further ion implantation of these homogenised alloys will assess the radiation resistance of these equilibrium phases. Investigation of a BCC solid solution upon irradiation will be useful for the examination of radiation resistance of high entropy alloys.
- For the durability of the BCC phases (for the alloys VCrMnFeW, VCrMnTaW, and VCrFeTaW) a long-term annealing treatment at an intermediate temperature (around 1000 °C) is needed to determine the equilibrium phases likely to form in service conditions. Due to the equipment available, a longer duration heat treatment was not possible due to the type of furnace required. Attainment of equilibrium phases will allow for the study of further precipitation that may occur at lower temperatures and the morphology of these phases. This will be critical in assessing if these phases will be detrimental in mechanical performance.
- Transmission electron microscopy (TEM) studies of VCrMnFeW homogenised at 1500 °C for 48 hours for the determination of crystallographic information of the observed σ phase. As identified in Chapter 6, the experimental XRD suggested the formation of a high temperature σ phase. However, observation of the SEM-BSE micrographs revealed difficulties in allocating this σ phase due to the resolution of the SEM technique.
- Further mechanical testing at elevated temperatures of the novel high entropy alloys is needed to establish relative strength. Small punch testing on 3 mm diameter samples would be ideal for the small, fabricated ingots (Charpy testing is often impractical for VAM samples due to the small dimensions of the ingots produced). Important mechanical data, including tensile properties and DBTT, can be derived for the assessment of these alloys as plasma-facing components.
- Heavy ion implantation at elevated temperatures, followed by subsequent TEM studies are essential for the understanding of fundamental radiation-induced defect damage mechanisms for low activation high entropy alloys. Further ion implantation of both as-cast alloys and thermally annealed alloys in this study is key for identifying potential radiation damage tolerant materials for nuclear fusion applications.